

©Copyright 2017  
Bradley Ross Markle

Climate dynamics revealed in ice cores:  
advances in techniques, theory, and interpretation

Bradley Ross Markle

A dissertation  
submitted in partial fulfillment of the  
requirements for the degree of

Doctor of Philosophy

University of Washington

2017

Reading Committee:

Eric Steig, Chair

Gerard Roe

Edwin Waddington

Program Authorized to Offer Degree:  
Department of Earth and Space Sciences

University of Washington

**Abstract**

Climate dynamics revealed in ice cores:  
advances in techniques, theory, and interpretation

Bradley Ross Markle

Chair of the Supervisory Committee:  
Professor Eric Steig  
Department of Earth and Space Sciences

Ice cores from the polar ice sheets provide detailed histories of Earth's climate. Interpreting past climate dynamics from ice-core records requires understanding how the climate system influences the geochemical proxies preserved in the ice. Models of physical climate processes have always formed the basis of climate-proxy interpretations. In this thesis I investigate how atmospheric transport of moisture toward the poles influences the water-isotope ratios of Antarctic precipitation as well as the amount of aerosols that reach the ice sheets. I refine interpretations of these geochemical proxies and the relationships between them. These interpretations help us better understand past climate dynamics, including changes in mid- and high-latitude temperatures and changes in the patterns of atmospheric circulation in the Southern Hemisphere. I make use of new high-resolution proxy records from a West Antarctic ice core and use both simple and complex physical models to better understand the relationships between the climate, moisture transport, and the geochemical proxies. This work improves our understanding of the spatial pattern and timing of climate changes in the Southern Hemisphere over the last 70,000 years.

## TABLE OF CONTENTS

	Page
Chapter 1: Introduction . . . . .	1
Chapter 2: Nonlinear temperature reconstructions with the Simple Water-Isotope Model . . . . .	15
Chapter 3: Global atmospheric teleconnections during Dansgaard-Oeschger events	102
Chapter 4: The great atmospheric washing machine: reconciling water, aerosols, and climate . . . . .	137
Appendix A: Onset of deglacial warming in West Antarctica driven by local orbital forcing . . . . .	181

## ACKNOWLEDGMENTS

The author wishes to express sincere appreciation to the many people and institutions who have supported this work. I'd first like to thank my adviser, Eric Steig, for his guidance, support, and friendship. I am also indebted to the members of my thesis committee, Gerard Roe, Edwin Waddington, Cecilia Bitz, and Luanne Thompson, for their advice, assistance, and for many fruitful discussions. My fellow graduate students in Earth and Space Sciences and the Program on Climate Change have been a tremendous source of camaraderie and learning. I particularly want to thank Spruce Schoenemann, T.J. Fudge, Emma Kahle, and Joel Pedro as well as all the wonderful people of the Juneau Icefield Research Program. I want to thank Andy Schauer and acknowledge the support of  $\Delta^*$  IsoLab, as well as the Seattle ARCS Foundation. I'd like to thank the University of Washington for the opportunity to pursue this research. Finally, I want to express my deep gratitude to my friends and family.

## **DEDICATION**

to my parents, Linda and Doug

Chapter 1  
**INTRODUCTION**

# CLIMATE DYNAMICS REVEALED IN ICE CORES: ADVANCES IN TECHNIQUES, THEORY, AND INTERPRETATION

BRADLEY ROSS MARKLE

## 1. INTRODUCTION

This thesis investigates climate dynamics as recorded in ice cores. This work is a part of the West Antarctic Ice Sheet (WAIS) Divide Ice Core Project and is a study of the water-isotope records from that core, in particular. In this first chapter I will outline the scope of the thesis. I start by providing a brief introduction to the study of water-isotope ratios in ice cores and the types of paleoclimate variability that this proxy has been used to understand. More-detailed introductions to these topics are found in the individual chapters. I next provide some background information for the WAIS Divide Ice Core Project and describe some of the unique opportunities presented by these records. I then outline the structure of this thesis and the topics addressed in the individual chapters, which are written as stand-alone manuscripts. Finally, I offer some concluding remarks about this thesis and future work.

**1.1. Ice cores and water isotopes.** Ice cores from the world's ice caps and ice sheets provide detailed histories of Earth's climate. Since the first projects recovering deep ice cores in the 1950s and 1960s, the ratios of stable isotopes of water have been the foundational proxy for past climate variability [Langway, 1958, Gonfiantini, 1959, Dansgaard, 1964]. Water isotope ratios in vapor and precipitation record the integrated condensation history of that water through the atmosphere, a process fundamentally connected to temperature [Dansgaard, 1964]. A well established theoretical framework for the water-isotope distillation process has allowed the interpretation of ice-core water-isotopes records as temperature proxies [Dansgaard, 1964, Merlivat and Jouzel, 1979, Jouzel and Merlivat, 1984, Ciais and Jouzel, 1994], the quantification of climate changes on orbital timescales (e.g. Jouzel et al. [2007]), and the discovery of dramatic millennial-scale variability (e.g. Dansgaard [1987]).

The classic water-isotope parameters  $\delta^{18}O$  and  $\delta D$  quantify the relative amount of heavy and light isotopologues within a water sample. For example, in the case of the oxygen isotopes,

$$\delta^{18}O = \frac{{}^{18}R_{sample}}{{}^{18}R_{standard}} - 1 \quad (1)$$

where  $R$  represents the number ratio of heavy to light isotopologues,  $^{18}R = ^{18}O/^{16}O$ , in a water sample and in a standard, typically Vienna Standard Mean Ocean Water.

A second-order water-isotope parameter, the deuterium excess [Dansgaard, 1964], is the weighted difference between the  $\delta D$  and  $\delta^{18}O$  ( $d_{xs} = \delta D - 8 \times \delta^{18}O$ ) and adds additional insight to climatic interpretations. The deuterium excess is sensitive to evaporation source-region conditions and has been used to improve quantitative estimates of Antarctic surface temperature changes [Vimeux et al., 2002] and to understand variability in Antarctic moisture-source regions [Stenni et al., 2004]. However, recent research has suggested potential issues with the underlying definition of the deuterium-excess parameter [Uemura et al., 2012] which may bias both of these types of interpretation.

The processes through which the climate transitions between glacial and interglacial states is an important topic in paleoclimate research. Records of temperature variability from Antarctic water-isotope records spanning tens of thousands of years have not only provided detailed histories of the the climate’s glacial cycles [Jouzel et al., 2007], but have also allowed the testing of hypothesis of the underlying physics [Huybers and Denton, 2008]. In conjunction with the concentration of greenhouse gases measured in the same Antarctic ice cores, these records have demonstrated the coevolution of Earth’s temperature and atmospheric composition [Petit et al., 1999, Shakun et al., 2012]. However, important questions about the phasing of deglaciations between the hemispheres and across Antarctica have persisted.

Millennial-scale climate events with surprisingly abrupt features were identified in Greenland ice core water-isotope records [Dansgaard et al., 1982, Dansgaard, 1987, Grootes et al., 1993] and subsequently in other paleoclimate archives from around the world [Sachs and Lehman, 1999, Deplazes et al., 2013]. These climate anomalies, known as Dansgaard-Oeschger events, each have counterparts observed in Antarctic ice-core water-isotope records [Barbante et al., 2006], known as Antarctic Isotope Maximum events, which have a distinctly different temporal character [Blunier et al., 1998]. Changes in the ocean’s heat transport are thought to link the temperature variations in each hemisphere [Stocker and Johnsen, 2003] though there are significant questions as to the phasing between the hemispheres [Wolff et al., 2010] as well as the potential role of atmospheric changes in addition to those of the ocean [Cane and Clement, 1999].

**1.2. West Antarctic Ice Sheet Divide Ice Core Project.** In the mid 2000s the U.S. ice core community began drilling a deep ice core at the West Antarctic Ice Sheet Divide. Drilling of the main core was completed in the 2010-2011 field season to a depth of 3405 m. The deepest recovered ice is approximately 68,000 years old [Buizert et al., 2015]. The goal of the project was to uncover a record of Antarctic climate over the last glacial cycle with unprecedented detail. While East Antarctic sites have yielded the longest ice-core records of Earth’s climate [Jouzel

et al., 2007], they have not provided the same level of temporal resolution and age-scale precision as their Greenland counterparts owing to their colder temperatures and lower accumulation rates. At an elevation of 1766 m, the modern temperature and accumulation rate at WAIS Divide are similar to Greenland sites [WAIS Divide Project Members et al., 2013], promising an analogous record from the Southern Hemisphere. These traits lead to a higher resolution in the WAIS Divide record than those from East Antarctica. Additionally, these traits lead to a smaller and more precisely determined age difference between the gas and ice phases of the core ( $\Delta$ age, Buizert et al. [2015]), which allows the synchronization of the WAIS Divide record to those from Greenland.

Annual layers are detectable in the WAIS Divide core for over 30,000 years [WAIS Divide Project Members et al., 2013] and form the basis for part of the chronology [Fudge et al., 2016a]. This also allows a quantification of the accumulation rate that is independent of the water isotope record. We showed that the relationship between water isotopes and accumulation rate in the WAIS Divide record is not fixed through time, as commonly assumed in Antarctic ice-core records, but varies on millennial timescales [Fudge et al., 2016b]. I contributed to the development of the deep age scale for WAIS Divide, in particular by identifying constraints on the accumulation rates for the site below the annual-layer counted portion of the core [Buizert et al., 2015].

Measuring the water isotope ratios of the WAIS Divide ice core was a joint effort between the University of Washington (UW) and the University of Colorado at Boulder (CU). At CU, water isotopes were measured by a new method of continuous flow analysis (CFA) which allows sub-centimeter resolution and the characterization of high-frequency variability in the record. I participated in these high-resolution measurements, contributing to the refinement of the method [Jones et al., 2017a] and the measurement and determination of isotope diffusion lengths calculated from the high resolution measurements [Jones et al., 2016]. I played a key role in a new study making use of these measurements which identifies a novel teleconnection between changes in Northern Hemisphere ice sheet and climate variability in the high latitudes of the Southern Hemisphere [Jones et al., 2017b].

At the University of Washington, we made complementary discrete measurements of water isotope ratios by laser spectroscopy, at half-meter resolution throughout the core (methods described in Steig et al. [2013]). This so-called “low-resolution” version of the record is itself the highest resolution Antarctic stable-isotope record to cover this interval of Earth’s climate history, providing temporal resolution better than 20 years per sample through the last deglaciation and better than 40 years per sample throughout the entire record. This record forms the foundation of my PhD research. Parallel measurements of the water isotopes at two labs enabled the assessment of the new CFA technique and demonstrated the

robustness of the record. We have shown that the discrete measurements are critical for the calculation and verification of the second-order water-isotope parameter deuterium excess [Jones et al., 2017a].

## 2. STRUCTURE OF THESIS

This thesis makes use of the unique opportunity presented by the WAIS Divide ice core and the water-isotope records in particular. I examine how climate dynamics are imprinted upon the ice-core records through atmospheric moisture transport. Water transport in the atmosphere is the fundamental process driving the distillation of water isotopes [Dansgaard, 1964]. It is also a critical aspect of the Earth’s climate system; a significant fraction of the total heat transported by the climate system in the mid-to-high latitudes is achieved through the transport of moisture in the atmosphere [Hartmann, 2015].

**2.1. Chapter 2.** I first develop a simple one-dimensional Rayleigh-type water-isotope distillation model. This model is based on existing models in the literature (e.g. Merlivat and Jouzel [1979], Ciais and Jouzel [1994], Kavanaugh and Cuffey [2003]), though several parameterizations are updated with recent empirical constraints, and the logical consistency of others parameterizations is refined. This model is then used to examine the temperature-dependence of water isotopes in Antarctic precipitation. In particular, I test the assumption of linearity in the relationships among  $\delta^{18}O$ , deuterium excess, evaporation-source temperature, and condensation temperature, which is widely used in quantitative temperature-reconstructions [Vimeux et al., 2002, Stenni et al., 2004].

This study compliments previous work that has shown issues in the definition of the deuterium excess parameter [Uemura et al., 2012]. My results show that a nonlinearly-defined deuterium excess parameter is a more faithful proxy for moisture-source region changes.

I next use the model to reconstruct ice-core site temperatures and evaporation-source temperatures for several Antarctic ice-core records, taking into account the nonlinearities in water-isotope distillation as resolved in the simple model. The isotope-based temperature reconstruction for WAIS Divide is shown to agree with an independent estimate from the borehole temperature profile [Cuffey et al., 2016]. The non-linear temperature reconstructions are compared to traditional linear reconstructions based on the same model. The traditional linear reconstruction technique is shown to work well for ice-core site temperatures; however the linear technique introduces potentially large biases into the reconstruction of evaporation-source temperature variability. Finally, I use the nonlinear temperature-reconstructions to investigate the spatial pattern of warming in the Southern Hemisphere since the Last Glacial Maximum.

**2.2. Chapter 3.** In the third chapter I further bolster arguments for the redefinition of the deuterium excess parameter. In addition to the simple Rayleigh-type model analyses discussed in Chapter 2, I here conduct analyses using results from multiple unforced runs of the isotope-enabled ECHAM4.6 General Circulation Model (GCM). These analyses confirm that the fundamental relationship between  $\delta^{18}O$  and  $\delta D$  is not linear and that a nonlinear definition of the deuterium excess parameter,  $d_{ln}$ , is a more faithful proxy for evaporation-source region sea-surface temperatures (SSTs). I compare the WAIS Divide deuterium excess records (both linear and nonlinear definitions) to those from other high-resolution East Antarctic sites, including the EPICA Dronning Maud Land (EDML) and EPICA Dome Concordia (EDC) cores [Stenni et al., 2010]. The records of the linear definition of the excess parameter,  $d_{xs}$ , from the three cores are divergent at all time scales, while the  $d_{ln}$  records show significantly more coherent variability. The differences in the linear definition of the parameter are shown to be related to biases originating from changes in the overall depletion at each ice core site. These results have substantial implications for our understanding of past changes in Southern Hemisphere source-region conditions. By redefining the parameter to a more physically-justified form, I find a zonally coherent pattern of source region changes at multi-millennial and orbital timescales.

Building upon the above insights into the deuterium excess parameter, I investigate millennial variability in the WAIS Divide water-isotope records. I compare the  $d_{ln}$  record from WAIS Divide to other records of millennial scale climate change during the last glacial period. Variability in deuterium excess in Antarctic ice cores arises from changes in moisture source region conditions. Because moisture is transported to Antarctic ice-core sites through the atmosphere, this variability may arise from changes in Southern Ocean surface conditions and from changes in atmospheric circulation. Atmospheric circulation, in particular the location of the storm tracks, influences the spatial distribution of evaporation sources that contribute to precipitation at an ice-core site. I investigate this process using moisture-tagged control runs of the Community Atmospheric Model. I quantify the likely influence of both sea-surface temperatures and storm-track changes on the WAIS Divide deuterium excess record.

I show that at millennial timescales the WAIS Divide  $d_{ln}$  record shows variability similar to both the Northern Hemisphere Dansgaard-Oeschger (DO) events and the Southern Hemisphere AIM events. This combination of DO-like and AIM-like variability is readily explained by changes in Southern Ocean sea surface temperatures that follow the AIM-like temporal pattern of variability and changes in the latitude of the SH storm tracks that follow the DO-like pattern of variability.

This finding is in agreement with proposed atmospheric teleconnections that link the position of tropical convection to abrupt temperature changes in the North Atlantic region [Cheng et al., 2007] and in turn the location of tropical convection to the position of the Southern Hemisphere storm tracks [Ceppi et al., 2013]. These

results complement another study in which I played a key role. In WAIS Divide Project Members et al. [2015], we demonstrated the existence of a centennial-scale time lag between the abrupt DO events in the Northern Hemisphere and the initiation of change in Antarctic temperature, a result we attribute to timescales associated with ocean circulation. In contrast, my results show that deuterium excess in the WAIS Divide core shows anomalies in phase with the NH DO events, with no more than decadal-scale time lags. In this chapter I demonstrate that in addition to oceanic teleconnections that operate during millennial climate variability, atmospheric teleconnections couple climate variations between the NH and SH high latitudes.

**2.3. Chapter 4.** In addition to the stable isotopes of water, a variety of impurities are routinely measured in polar ice cores. These impurities record the deposition of aerosols, such as dust and sea salts, and have been used to study many aspects of the climate system, from biogeochemical processes to atmospheric circulation [Mayewski et al., 1997]. Among these impurities, the concentrations of dust particles and related terrestrial elements like Ca, have been used to constrain past changes in the aerosol loading of the atmosphere, windiness and aridity in dust-source regions, and other aspects of climate [McGee et al., 2010, Mayewski et al., 1997, Petit et al., 1981]. Dust concentrations in Antarctic ice show orders-of-magnitude changes during glacial cycles [Lambert et al., 2008]. In contrast ocean sediment core records of dust-flux changes at lower latitudes generally show only 2- to 5-fold changes over the same climate transitions [Harrison et al., 2001]. It has been noted that the ice-core concentrations of dust and elements such as Ca, are not only extremely well correlated with each other [Mahowald et al., 1999], but also strongly covary with the ice-core  $\delta^{18}O$  records [Lambert et al., 2008]. Marine-sourced sea-salt aerosols also show large changes across millennial and orbital timescales in ice-core records, though the source of these changes is debated [Wolff et al., 2006, Petit and Delmonte, 2009].

I examine the relationships between the high-resolution records of water isotopes and impurities from the WAIS Divide ice core. Much previous research has focused on changes in source-region emissions as the dominant driver of aerosol variability through time. In this chapter I investigate the role of the rain-out process in driving variability in both aerosols and water-isotope ratios in air masses reaching Antarctica. I use the simple water-isotope model described in Chapter 2 and an equivalently simple aerosol rain-out model. I show that the process of moisture transport and removal of moisture and aerosols from the atmosphere predicts a negative and exponential relationship between aerosols and water isotope ratios, exactly as observed in ice-core records. Further, I show that the glacial-interglacial change in rain-out consistent with the water-isotope record should lead to orders-of-magnitude variability in aerosols reaching Antarctica.

This coherent understanding of water-isotope and aerosol variability has several important implications. First, it constrains the magnitude of possible changes in

aerosol source emissions. Next, it suggests changes in the magnitude and spatial pattern of the atmosphere's aerosol burden through time, which have direct and indirect effects on the radiative forcing of the climate system. Finally, because water isotopes and aerosols are both influenced by the poleward transport of moisture, their relationships can be used to constrain changes in this process as well as related aspects of the climate system such as the pole-to-equator temperature gradient.

**2.4. Appendix.** In the Appendix, I include a study, WAIS Divide Project Members et al. [2013], that examines the timing of the onset of deglacial warming in West Antarctica and compares that timing to existing records from East Antarctica. We show that the WAIS Divide  $\delta^{18}O$  record indicates that significant deglacial warming began in West Antarctica several thousand years before any detectable changes are observed in East Antarctic records. These results are in line with the timing of changes in relevant orbital forcing parameters [Huybers and Denton, 2008], and suggest that West Antarctica responds more quickly to global climate changes than East Antarctica.

I played a key role in this study and was involved in the primary interpretations of the data and writing the manuscript. I helped to produce and quality control the primary dataset, the WAIS Divide  $\delta^{18}O$  record. I designed the statistical algorithms used to detect significant change in the ice core records. Variations of these algorithms are used again in subsequent studies to which I contributed including Fudge et al. [2016b] and Jones et al. [2017b].

### 3. SYNTHESIS

Together, the chapters of this thesis investigate climate dynamics in the past, as recorded in ice cores. Ice-core records are possible because the ice sheets steadily accumulate water precipitated from the atmosphere. It is through the atmospheric transport of this water toward the poles that many climate processes are recorded in the ice sheets. Using a quantitative understanding of moisture transport through the atmosphere, I investigate how this process influences the water-isotope ratios of precipitation and the amount of aerosols that reach the ice sheets. This thesis makes extensive use of multiple geochemical-proxy data sets and the objective analysis of those data sets to discern signal from noise. I use both simple and complex models to understand the relationship between the climate system and our geochemical measurements. This thesis lays the theoretical groundwork for future self-consistent multi-proxy climate reconstructions.

Global-scale moisture transport occurs down meridional temperature gradients. Changes in the ratios of water isotopes record this down-gradient transport. Through a quantitative model of the water-distillation process, I investigate how information about the hemispheric temperature gradient may be extracted from ice-core records of water-isotope ratios. These records allow the quantification of changes

in the meridional temperature-gradient (Chapter 2) and the determination of phasing between temperature changes across Antarctica (Appendix 1) and between the hemispheres (e.g. WAIS Divide Project Members et al. [2015]).

The hemispheric temperature gradient is not the only aspect of climate influencing the transport of moisture to ice-core sites on the ice sheets. Changes in the patterns of atmospheric circulation can alter the way water is transported through these temperature gradients as well as how much moisture is delivered to specific locations. In this thesis, I show that changes in atmospheric circulation are imprinted on the water-isotope ratios of Antarctica precipitation (Chapter 3). The records from the WAIS Divide ice core reveal abrupt changes in the location of the Southern Hemisphere storm tracks during the last glacial period. Changes in atmospheric circulation may also be the source of the complex relationship between water-isotope ratios and snow accumulation that we identified in the WAIS Divide ice-core records [Fudge et al., 2016b].

The isotopes of water are not the only atmospheric constituents affected by the transport and progressive removal of moisture from the atmosphere. A variety of aerosols are transported to the ice sheets through the atmosphere and are influenced by the same process. I show that this hydrologic process drives a characteristic relationship between water-isotope and aerosol records in ice cores (Chapter 4). The strong influence of the rain-out process on these atmospheric constituents is evidenced by the high covariance between these otherwise distinct proxy records.

#### 4. FUTURE WORK

The different water-isotope ratios and aerosols measured in ice cores are all affected by the transport and removal of moisture from the atmosphere, but each in slightly different ways. While the  $\delta D$  and  $\delta^{18}O$  of Antarctic precipitation are each strongly influenced by the total distillation and thus temperature at final precipitation over the ice sheet, their weighted difference, the deuterium excess, is more strongly influenced by conditions during the initial evaporation from the ocean. The amount of terrestrial calcium and marine sodium that reaches Antarctica are both moderated by the rain-out process during transport. But owing to their different starting locations and source dynamics they are subjected to different segments of this rain-out pathway. By examining the shared and unshared variability among these proxy records we have an opportunity to quantify their common process, moisture transport in the atmosphere, as well as to constrain variability in processes unique to each individual proxy.

Building from the work comprising this thesis, a self-consistent model that incorporates both water isotopes and aerosols will allow improved multi-proxy climate reconstructions. The inclusion of additional proxies allows for the reconstruction of additional climate parameters. As demonstrated in Chapter 2, the addition of

$^{17}\text{O}_{\text{excess}}$  to an isotope model in principle allows the reconstruction of relative humidity during evaporation, as well as the traditionally reconstructed evaporation and precipitation temperature histories. Likewise the addition of aerosols to a self-consistent model would provide more constraints on the spatial pattern of these temperature changes, as well as the opportunity to reconstruct additional parameters such as aerosol source strengths. By fixing the temperature reconstructions to latitudinal grids and making use of multiple synchronized ice core records, we could more precisely reconstruct polar amplification in the past (as mentioned in Chapters 2 and 4) as well as changes in the location of moisture sources related to shifts in the position of the storm tracks (as done for a single location in Chapter 3). The chapters of this thesis lay the groundwork for such multi-parameter climate reconstructions using simplified multi-proxy models.

## REFERENCES

- Chester C Langway. A 400 meter deep ice core in Greenland: Preliminary report. *Journal of Glaciology*, 3(23):217–217, 1958.
- R Gonfiantini. Oxygen isotope variations in Antarctic snow samples. *Nature*, 184:1557–1558, 1959.
- W. Dansgaard. Stable isotopes in precipitation. *Tellus*, 16(4):436–468, 1964. doi: 10.3402/tellusa.v16i4.8993. URL <http://dx.doi.org/10.3402/tellusa.v16i4.8993>.
- Liliane Merlivat and Jean Jouzel. Global climatic interpretation of the deuterium-oxygen 18 relationship for precipitation. *Journal of Geophysical Research: Oceans*, 84(C8):5029–5033, 1979.
- Jean Jouzel and Liliane Merlivat. Deuterium and oxygen 18 in precipitation: Modeling of the isotopic effects during snow formation. *Journal of Geophysical Research: Atmospheres*, 89(D7):11749–11757, 1984.
- Philippe Ciais and Jean Jouzel. Deuterium and oxygen 18 in precipitation: Isotopic model, including mixed cloud processes. *Journal of Geophysical Research: Atmospheres*, 99(D8):16793–16803, 1994.
- Jean Jouzel, Valérie Masson-Delmotte, Olivier Cattani, Gabrielle Dreyfus, Sonia Falourd, Georg Hoffmann, Bénédicte Minster, J Nouet, Jean-Marc Barnola, Jérôme Chappellaz, et al. Orbital and millennial Antarctic climate variability over the past 800,000 years. *Science*, 317(5839):793–796, 2007.
- W Dansgaard. Ice core evidence of abrupt climatic changes. In *Abrupt climatic change*, pages 223–233. Springer, 1987.
- F Vimeux, K M Cuffey, and J Jouzel. New insights into Southern Hemisphere temperature changes from Vostok ice cores using deuterium excess correction. *Earth and Planetary Science Letters*, 2002.
- Barbara Stenni, Jean Jouzel, V Masson-Delmotte, Regine Röthlisberger, Emiliano Castellano, Olivier Cattani, Sonia Falourd, SJ Johnsen, Antonio Longinelli, JP Sachs, et al. A late-glacial high-resolution site and source temperature record

- derived from the EPICA Dome C isotope records (East Antarctica). *Earth and Planetary Science Letters*, 217(1):183–195, 2004.
- R Uemura, V Masson-Delmotte, J Jouzel, A Landais, H Motoyama, and B Stenni. Ranges of moisture-source temperature estimated from Antarctic ice cores stable isotope records over glacial–interglacial cycles. *Climate of the Past*, 8(3):1109–1125, 2012.
- Peter Huybers and George Denton. Antarctic temperature at orbital timescales controlled by local summer duration. *Nature Geoscience*, 1(11):787–792, 2008.
- Jean-Robert Petit, Jean Jouzel, Dominique Raynaud, Narcisse I Barkov, J-M Barnola, Isabelle Basile, Michael Bender, J Chappellaz, M Davis, G Delaygue, et al. Climate and atmospheric history of the past 420,000 years from the Vostok ice core, Antarctica. *Nature*, 399(6735):429–436, 1999.
- Jeremy D Shakun, Peter U Clark, Feng He, Shaun A Marcott, Alan C Mix, Zhengyu Liu, Bette Otto-Bliesner, Andreas Schmittner, and Edouard Bard. Global warming preceded by increasing carbon dioxide concentrations during the last deglaciation. *Nature*, 484(7392):49–54, 2012.
- Willi Dansgaard, HB Clausen, N Gundestrup, CU Hammer, SF Johnsen, PM Kristinsdottir, and Niels Reeh. A new Greenland deep ice core. *Science*, 218(4579):1273–1277, 1982.
- PM Grootes, Minze Stuiver, JWC White, S Johnsen, and J Jouzel. Comparison of oxygen isotope records from the GISP2 and GRIP Greenland ice cores. *Nature*, 366(6455):552–554, 1993.
- Julian P Sachs and Scott J Lehman. Subtropical north atlantic temperatures 60,000 to 30,000 years ago. *Science*, 286(5440):756–759, 1999.
- Gaudenz Deplazes, Andreas Lückge, Larry C Peterson, Axel Timmermann, Yvonne Hamann, Konrad A Hughen, Ursula Röhl, Carlo Laj, Mark A Cane, Daniel M Sigman, et al. Links between tropical rainfall and North Atlantic climate during the last glacial period. *Nature Geoscience*, 6(3):213–217, 2013.
- Carlo Barbante, J-M Barnola, Silvia Becagli, J Beer, M Bigler, Claude Boutron, T Blunier, E Castellano, O Cattani, Jérôme Chappellaz, et al. One-to-one coupling of glacial climate variability in Greenland and Antarctica. *Nature*, 444(7116):195–198, 2006.
- T Blunier, J Chappellaz, J Schwander, A Dällenbach, B Stauffer, TF Stocker, D Raynaud, J Jouzel, lammer Clausen, CU Hammer, et al. Asynchrony of Antarctic and Greenland climate change during the last glacial period. *Nature*, 394(6695):739–743, 1998.
- Thomas F Stocker and Sigfùs J Johnsen. A minimum thermodynamic model for the bipolar seesaw. *Paleoceanography*, 18(4), 2003.
- Eric W Wolff, Jérôme Chappellaz, Thomas Blunier, Sune Olander Rasmussen, and Anders Svensson. Millennial-scale variability during the last glacial: The ice core record. *Quaternary Science Reviews*, 29(21):2828–2838, 2010.

- Mark Cane and Amy C Clement. A role for the tropical Pacific coupled ocean-atmosphere system on Milankovitch and millennial timescales. Part II: Global impacts. *Mechanisms of global climate change at millennial time scales*, pages 373–383, 1999.
- C Buizert, K M Cuffey, J P Severinghaus, D Baggenstos, T J Fudge, E J Steig, B R Markle, M Winstrup, R H Rhodes, E J Brook, T A Sowers, G D Clow, H Cheng, R L Edwards, M Sigl, J R McConnell, and K C Taylor. The WAIS Divide deep ice core WD2014 chronology; Part 1: Methane synchronization (68–31 ka BP) and the gas age–ice age difference. *Climate of the Past*, 11(2):153–173, February 2015.
- WAIS Divide Project Members et al. Onset of deglacial warming in West Antarctica driven by local orbital forcing. *Nature*, 500(7463):440–444, 2013.
- Tyler J Fudge, Joseph R McConnell, Ken C Taylor, Kees C Welten, Thomas E Woodruff, Edward J Brook, Marc W Caffee, Nelia W Dunbar, Olivia J Maselli, Daniel R Pasteris, et al. The WAIS Divide deep ice core WD2014 chronology-Part 2: Annual-layer counting (0-31-ka-BP). *Climate of the Past*, 12(3):769, 2016a.
- TJ Fudge, Bradley R Markle, Kurt M Cuffey, Christo Buizert, Kendrick C Taylor, Eric J Steig, Edwin D Waddington, Howard Conway, and Michelle Koutnik. Variable relationship between accumulation and temperature in West Antarctica for the past 31,000 years. *Geophysical Research Letters*, 43(8):3795–3803, 2016b.
- Tyler R Jones, James WC White, Eric J Steig, Bruce H Vaughn, Valerie Morris, Vasileios Gkinis, Bradley R Markle, and Spruce W Schoenemann. Improved methodologies for continuous-flow analysis of stable water isotopes in ice cores. *Atmospheric Measurement Techniques*, 10(2):617, 2017a.
- TR Jones, KM Cuffey, JWC White, EJ Steig, C Buizert, BR Markle, JR McConnell, and M Sigl. Water Isotope Diffusion in the WAIS Divide Ice Core During the Holocene and Last Glacial. *Journal of Geophysical Research: Earth Surface*, 2016.
- T. R. Jones, W. H. G. Roberts, E. J. Steig, K. M. Cuffey, B. R. Markle, and J. W. C. White. Southern Hemisphere Climate Variability Forced by Northern Hemisphere Ice Sheet Topography. In Review, *Nature*, 2017b.
- Eric J Steig, Qinghua Ding, James WC White, Marcel Küttel, Summer B Rupper, Thomas A Neumann, Peter D Neff, Ailie JE Gallant, Paul A Mayewski, Kendrick C Taylor, et al. Recent climate and ice-sheet changes in West Antarctica compared with the past 2,000 years. *Nature Geoscience*, 6(5):372–375, 2013.
- Dennis L Hartmann. *Global physical climatology*, volume 103. Newnes, 2015.
- J L Kavanaugh and Kurt M Cuffey. Space and time variation of  $\delta^{18}\text{O}$  and  $\delta\text{D}$  in Antarctic precipitation revisited. *Global Biogeochemical Cycles*, 17(1):n/a–n/a, February 2003.
- Kurt M Cuffey, Gary D Clow, Eric J Steig, Christo Buizert, TJ Fudge, Michelle Koutnik, Edwin D Waddington, Richard B Alley, and Jeffrey P Severinghaus.

- Deglacial temperature history of West Antarctica. *Proceedings of the National Academy of Sciences*, 113(50):14249–14254, 2016.
- B Stenni, V Masson-Delmotte, E Selmo, Hans Oerter, Hanno Meyer, R Röthlisberger, J Jouzel, O Cattani, S Falourd, Hubertus Fischer, et al. The deuterium excess records of EPICA Dome C and Dronning Maud Land ice cores (east Antarctica). *Quaternary Science Reviews*, 29(1):146–159, 2010.
- Wei Cheng, Cecilia M Bitz, and John C H Chiang. Adjustment of the Global Climate to an Abrupt Slowdown of the Atlantic Meridional Overturning Circulation. *Ocean Circulation: Mechanisms and Impacts-Past and Future Changes of Meridional Overturning*, 173, 2007.
- Paulo Ceppi, Yen-Ting Hwang, Xiaojuan Liu, Dargan M W Frierson, and Dennis L Hartmann. The relationship between the ITCZ and the Southern Hemispheric eddy-driven jet. *Journal of Geophysical Research: Atmospheres*, 118(11):5136–5146, June 2013.
- WAIS Divide Project Members et al. Precise inter-polar phasing of abrupt climate change during the last ice age. *Nature*, 520(7549):661–665, 2015.
- P A Mayewski, L D Meeker, and M S Twickler. Major features and forcing of high-latitude northern hemisphere atmospheric circulation using a 110,000-year-long glaciochemical series. *Oceans*, 1997.
- David McGee, Wallace S Broecker, and Gisela Winckler. Gustiness: The driver of glacial dustiness? *Quaternary Science Reviews*, 29(17–18):2340–2350, 2010.
- J R Petit, M Briat, and A Royer. Ice age aerosol content from East Antarctic ice core samples and past wind strength. *Nature*, 1981.
- F Lambert, B Delmonte, J R Petit, M Bigler, P R Kaufmann, M A Hutterli, T F Stocker, U Ruth, J P Steffensen, and V Maggi. Dust-climate couplings over the past 800,000 years from the EPICA Dome C ice core. *Nature*, 452(7187):616–619, April 2008.
- Sandy P Harrison, Karen E Kohfeld, Caroline Roelandt, and Tanguy Claquin. The role of dust in climate changes today, at the last glacial maximum and in the future. *Earth-Science Reviews*, 54(1-3):43–80, June 2001.
- Natalie Mahowald, Karen Kohfeld, Margaret Hansson, Yves Balkanski, Sandy P Harrison, I Colin Prentice, Michael Schulz, and Henning Rodhe. Dust sources and deposition during the last glacial maximum and current climate: A comparison of model results with paleodata from ice cores and marine sediments. *Journal of Geophysical Research: Oceans (1978–2012)*, 104(D13):15895–15916, July 1999.
- Eric W Wolff, Hubertus Fischer, Felix Fundel, Urs Ruth, Birthe Twarloh, Geneviève C Littot, R Mulvaney, Regine Röthlisberger, Martine De Angelis, Claude F Boutron, et al. Southern ocean sea-ice extent, productivity and iron flux over the past eight glacial cycles. *Nature*, 440(7083):491–496, 2006.

Jean-Robert Petit and B Delmonte. A model for large glacial–interglacial climate-induced changes in dust and sea salt concentrations in deep ice cores (central Antarctica): Palaeoclimatic implications and prospects for refining ice core chronologies. *Tellus B*, 61(5):768–790, 2009.

## Chapter 2

**NONLINEAR TEMPERATURE RECONSTRUCTIONS WITH  
THE SIMPLE WATER-ISOTOPE MODEL**

# NONLINEAR TEMPERATURE RECONSTRUCTIONS WITH THE SIMPLE WATER-ISOTOPE MODEL

BRADLEY R MARKLE AND ERIC J STEIG

ABSTRACT. Stable water-isotope ratios in polar ice are important archives of past climate variability. Using models, we can interpret records of water-isotope variability in ice cores as changes in condensation temperature over the ice sheet and evaporation temperature at the moisture source. Traditionally water isotope-temperature inversions assume linear relationships between water isotopes in precipitation and temperature variability. Here we investigate these relationships with a simple water-isotope model. We find that there are important nonlinearities in the relationships between water isotopes and their condensation and evaporation temperatures. These nonlinearities influence the interpretation of source-region temperatures in particular. We describe a reconstruction technique that accounts for the nonlinearities incorporated in the simple model. We then reconstruct Antarctic surface temperatures, condensation temperatures, and source-region evaporation temperatures for a number of Antarctic ice-core records. Our reconstructions constrain the pattern and magnitude of polar amplification in the past and reveal asymmetries in the temperature histories of East and West Antarctica.

## 1. INTRODUCTION

Stable-isotope ratios of water have been the foundational proxy of polar paleoclimate research for over half a century (Dansgaard, 1964; Gonfiantini, 1959; Langway, 1958). Stratigraphic records of water-isotope ratios in the ice sheets have provided our most detailed records of Earth's climate history, extending tens and hundreds of thousands of years into the past (Dansgaard et al., 1969; Petit et al., 1999). Primarily driven by temperature variations, water-isotope ratios measured in ice cores can provide insight into the past magnitudes and spatial patterns of climate warming and cooling, as well as the links and phasing between climate changes across the globe (Barbante et al., 2006; Masson-Delmotte et al., 2006; WAIS Divide Project Members et al., 2013, 2015). The quantitative reconstruction of temperature variations from ice-core water-isotope records is aided by detailed knowledge of the fractionation processes that drive water-isotope variability (Jouzel et al., 1982; Merlivat and Jouzel, 1979). Generally, water-isotope ratios in polar precipitation depend strongly on the temperature at the site of precipitation (Jouzel et al., 1997; Petit et al., 1999)

and evaporation (Vimeux et al., 2002). Both evaporation and precipitation temperature can be reconstructed from ice-core records, if scaling relationships between the isotope values and temperatures can be determined (Kavanaugh and Cuffey, 2002; Stenni et al., 2010; Vimeux et al., 2002). Here, we examine the widely used assumption of linearity in the scaling relationship between water-isotope ratios and temperature. We find that accounting for known non-linearities in water-isotope fractionation processes can improve quantitative temperature reconstructions.

The atoms in water have five stable isotopes including the  $^{18}\text{O}$ ,  $^{17}\text{O}$ , and  $^{16}\text{O}$  isotopes of oxygen and the  $^2\text{H}$  (deuterium,  $D$ ) and  $^1\text{H}$  isotopes of hydrogen. The ratio of their abundance in a water sample, e.g.  $^{18}R = ^{18}\text{O}/^{16}\text{O}$ , can be measured in ice and is typically expressed in  $\delta$  notation\*, e.g.  $\delta^{18}\text{O}$ . Changes in water-isotope ratios are driven by fractionation during phase changes (Craig, 1961). The isotopic values of polar precipitation record the integrated condensation history of moisture transported to the ice sheets (Dansgaard, 1964; Epstein et al., 1963; Gonfiantini, 1965) which is fundamentally linked to temperature (Criss, 1999; Dansgaard, 1964). The quantitative interpretation of ice-core water-isotope records as paleothermometers is supported by physically-based models of water-isotope distillation (Dansgaard, 1964; Jouzel et al., 1982; Merlivat and Jouzel, 1979) and empirical evidence of the strong correlation between the water-isotope ratios and temperature of precipitation (Jouzel et al., 1997; Masson-Delmotte et al., 2008; Petit et al., 1999).

**1.1. Temperature reconstructions.** The simplest approach to quantitatively interpreting ice-core water-isotope records is to assume a linear scaling between the water-isotope values in precipitation and temperature during condensation, based on empirical correlations between  $\delta^{18}\text{O}$  (or  $\delta D$ ) and surface temperature from observations (Jouzel et al., 1997; Petit et al., 1999). There is however a distinction between the water-isotope temperature “spatial slope”, that is the relationship measured at surface sites, and the “temporal slope”, this relationship at a single point through time (Jouzel et al., 1997). Further, in addition to the cumulative fractionation characterized by the temperature at precipitation, water isotope ratios in vapor are influenced by conditions during initial evaporation from the ocean. Of particular importance is the  $\delta$  ( $\delta^{18}\text{O}$  and  $\delta D$ ) values of the ocean, the temperature during evaporation, and the occurrence of kinetic fractionation during evaporation, which is driven by sub-equilibrium relative humidity and influenced by sea surface temperature and windspeed (Jouzel et al., 1982; Merlivat and Jouzel, 1979).

A more complex approach to reconstructing temperatures from water isotope records is to account for the combined influence of both evaporation temperature and

---

\*Delta notation reflects the measured ratios with respect to a known standard,  $\delta_x = \frac{R_x - R_{std}}{R_{std}}$  and are typically reported in ‰. See Equation 7 in Section 2.2 for further details.

condensation temperature on the final values of Antarctic precipitation. The deuterium excess is the weighted difference between  $\delta^{18}O$  and  $\delta D$ ,  $d_{xs} = \delta D - 8 \times \delta^{18}O$ , and aims to quantify the effects of kinetic fractionation (Dansgaard, 1964; Merlivat and Jouzel, 1979). With these two measured constraints,  $\delta^{18}O$  and  $d_{xs}$ , it is possible to solve a system of equations for variations in both the condensation temperature over the ice-core site and the evaporation temperature at the moisture source (Kavanaugh and Cuffey, 2002; Vimeux et al., 2002). In this system of equations, changes in water-isotope parameters,  $\Delta\delta^{18}O$  and  $\Delta d_{xs}$ , are driven by changes in site and source temperature,  $\Delta T_{site}$  and  $\Delta T_{source}$ :

$$\Delta\delta^{18}O = \gamma_1\Delta T_{site} + \gamma_2\Delta T_{source} \quad (1)$$

$$\Delta d_{xs} = \beta_1\Delta T_{site} + \beta_2\Delta T_{source} \quad (2)$$

The  $\beta$  and  $\gamma$  parameters are the partial derivatives of  $\delta^{18}O$  and  $d_{xs}$  with site and source temperature, respectively. These parameters are typically diagnosed for each ice-core site from water-isotope distillation models (Kavanaugh and Cuffey, 2002; Stenni et al., 2010; Uemura et al., 2012; Vimeux et al., 2002). Once these slopes are established, the equations may be inverted for  $\Delta T_{site}$  and  $\Delta T_{source}$ , and records of  $\delta^{18}O$  and  $d_{xs}$  variability used to reconstruct variability in Antarctic surface temperatures and evaporation conditions over the Southern Ocean (Stenni et al., 2010; Uemura et al., 2012; Vimeux et al., 2002).

**1.2. Nonlinearities in isotope fractionation.** The linear temperature reconstruction approach described above depends on the  $\beta$  and  $\gamma$  parameters, the slopes between water-isotope values and temperatures at the evaporation and condensation site. Further these reconstructions depend on those slopes being fixed through time and linear throughout the range of reconstructed temperatures. While it is widely known that the underlying distillation physics are not linear processes (Criss, 1999; Dansgaard, 1964), it is assumed that the relationships are sufficiently close to linear that variability within some range is insignificant to the reconstruction (Vimeux et al., 2002).

How important are these assumptions? There are some indications that these slopes are not linear. For example, the  $\beta$  and  $\gamma$  parameters diagnosed from models often differ between different ice-core sites (e.g. Stenni et al. (2010) and Uemura et al. (2012)). It is of course reasonable to expect these relationships to vary between locations. However, if the relationships depend on the current conditions of the site, this implies that if the site's conditions change, so should the relationships. If the slope  $\beta_1 = \partial d_{xs} / \partial T_{site}$  depends on  $T_{site}$ ,  $\beta_1$  is by definition nonlinear.

Another potential issue is the deuterium excess parameter, which is influenced by nonlinear biases (Markle et al., 2017; Uemura et al., 2012) owing to its definition. The origin of the linear slope in the definition of deuterium excess comes from an empirical fit to global precipitation measurements (Dansgaard, 1964). However, a linear relationship between  $\delta^{18}O$  and  $\delta D$  is not fundamental (Craig, 1961). Equilibrium fractionation alone drives a nonlinear relationship between  $\delta^{18}O$  and  $\delta D$  (e.g. Markle et al. (2017)). The definition of the  $\delta$  value require that as water is increasingly depleted, the values of  $\delta^{18}O$  and  $\delta D$  must converge toward the point -1000‰, -1000‰, requiring increasing nonlinearity with increasing depletion.

While the effect of source-region conditions on deuterium excess of evaporation is close to linear for the vapor at initial evaporation (Merlivat and Jouzel, 1979; Uemura et al., 2008), the signal is not linearly preserved as the moisture is transported toward the deposition site on the ice sheet. Kinetic fractionation that occurs during transport (Jouzel et al., 1982) alters the deuterium excess of the vapor as does equilibrium fractionation, owing to biases in the linear definition (Markle et al., 2017). Thus the slope relating  $d_{xs}$  to evaporation and condensation site temperatures should vary as a function of the total depletion experienced at a site.

Some of these issues have recently been addressed by redefining the deuterium excess parameter (Markle et al., 2017; Uemura et al., 2012). (Uemura et al., 2012) fit a second-order polynomial to a compilation of  $\delta^{18}O$  and  $\delta' D$  data, where  $\delta'_x = \ln(1 + \delta_x)$  (see Equation 8 in Section 2.2 for further details):

$$\delta' D = A \times (\delta^{18}O)^2 + B \times \delta^{18}O + C \quad (3)$$

This relationship defines a phenomenological, non-linear deuterium excess parameter (Uemura et al., 2012), (hereafter called the “logarithmic definition” owing to the use of  $\delta'$  values):

$$d_{ln} = \delta' D - (A \times (\delta^{18}O)^2 + B \times \delta^{18}O) \quad (4)$$

with coefficients  $A = -28.5$  and  $B = 8.47$  for unitless  $\delta'$  values (that is  $\delta^{18}O = 0.040$  not 40‰).

By fitting to the climatological mean this definition of the deuterium excess reduces the influence of kinetic fractionation during transport and the nonlinear biases inherent to the linear definition and is a more faithful proxy for source-region conditions (Markle et al., 2017; Uemura et al., 2012).

The same distillation physics that lead to biases in the linear definition of the deuterium excess parameter, could in principle lead to biases in the linear temperature reconstruction technique used throughout the literature and described above. This is likely to be particularly true at the coldest sites in East Antarctica, where

the precipitation is extremely depleted and the nonlinearities associated with isotope distillation are most pronounced.

We first construct a simple water-isotope model in Section 2. Our model is based on existing Rayleigh-type distillation models (Jouzel et al., 1982; Merlivat and Jouzel, 1979), with several improvements in the representation of the environmental conditions and updates to the fractionation scheme. In Section 3 we compare the model’s results to modern observations and in Section 4 we investigate the linearity of relationships between modeled water-isotope values and site and source temperatures. We then propose a nonlinear temperature reconstruction technique, and compare reconstructed histories to previously published results using the linear inversion (Section 5). Finally, we use these nonlinear water isotope-based temperature reconstructions to examine past patterns of temperature variability (Section 6).

## 2. SIMPLE WATER-ISOTOPE MODEL

We here describe a simple numerical Rayleigh-type distillation model for water isotopes. The Simple Water-Isotope Model (SWIM) is based on existing models (Ciais and Jouzel, 1994; Criss, 1999; Jouzel and Merlivat, 1984; Kavanaugh and Cuffey, 2003; Merlivat and Jouzel, 1979). We make several additions compared to previous models including updated fractionation factors, and resolve inconsistencies between aspects of water transport and water-isotope fractionation. The model considers one-dimensional temperature pathways from initial evaporation through progressive condensation and distillation. We account for kinetic and equilibrium fractionation of the  $^2H/^1H$ ,  $^{18}O/^{16}O$ , and  $^{17}O/^{16}O$  ratios of water.

We will first describe the physical transport of moisture in the model (Section 2.1) and the relationships between environmental conditions, such as temperature and relative humidity, that influence water-isotope fractionation and moisture removal. We then describe the processes that drive water-isotope fractionation (Section 2.2), starting with evaporation of water from the ocean (Section 2.3), and followed by the distillation of water as it is transported from the evaporation site to final precipitation on the ice sheet (Section 2.4).

**2.1. Environmental trajectory.** We first describe the environmental pathway of moisture transport from evaporation over the midlatitude oceans to precipitation over the ice sheet. The fractionation of water-isotope ratios occurs during evaporation and condensation (Criss, 1999). After initial evaporation, moist air parcels are cooled as they are transported from the midlatitudes toward the pole, driving condensation and fractionation (Dansgaard, 1964). We consider isolated pathways through temperature space defined by an initial surface air temperature,  $T_0$ , and a final condensation temperature,  $T_c$ :  $\vec{T} = (T_0, T_0 - dT, T_0 - 2dT, \dots, T_c)$ . We use Euler numerics where,

$$\frac{dx_i}{dT_i} \approx \frac{x_i - x_{i-1}}{T_i - T_{i-1}} \quad (5)$$

with sufficiently small  $dT = T_i - T_{i-1}$ , where  $x$  is the variable of interest.

**2.1.1. Source-region conditions.** The air temperature ( $T_0$ ), sea surface temperature ( $SST$ ), and relative humidity ( $RH$ ) during initial evaporation determine the isotopic composition of the vapor over the ocean. We use climatological correlations to find initial values of  $SST_0$  and  $RH_0$  given a specified initial air temperature,  $T_0$ . We calculate climatological correlations between global surface air temperature over oceans,  $T_a$ , and the  $SST$  and surface  $RH$  using the 1980-2010 annual mean climatological fields from the NCEP/NCAR reanalysis project (Kalnay et al., 1996). The relationships are fit by 9<sup>th</sup>-order polynomials (Figure 1). The high order fits are required to accurately capture the shape of the observed relationships, including the asymptote of  $SST$  at the sea water freezing point.

Relative humidity gradients in the modern climate are fairly weak, and while highly variable on short timescales  $RH$  appears largely invariant on timescales longer than interannual (Dai, 2006; Vimeux et al., 2002). To first approximation,  $RH$  is tied to local temperature within the mid-latitude sources of Antarctic moisture.

The appropriate values of  $SST_0$  and  $RH_0$  are calculated given a specified  $T_0$  and the climatological fits. The sensitivity of the model to these fits is analyzed below. We examine whether these fits depend on the underlying reanalysis data set, making the same calculations based on the ERA-Interim reanalysis (Dee et al., 2011). Both reanalysis data sets give similar results. We find significant differences in the  $T_a - to - SST$  fits between the Northern and Southern Hemispheres for air temperatures between  $5^\circ$  and  $-15^\circ\text{C}$ , as seen in Figure 1. We find no major hemispheric differences for the  $T_a - to - RH$  fit. In this study we will use the Southern Hemisphere fits from here on.

To examine the sensitivity of the climatological fits to zonal asymmetry, we compare  $T_a - to - SST$  and  $T_a - to - RH$  fits calculated from zonally averaged data and fits calculated from the full resolution fields. The fits are not meaningfully different, though the full resolution clearly leads to a larger spread around the fit.

We next investigate the dependence of the  $T_a$ ,  $SST$ , and  $RH$  relationships on seasonality. We find relatively small differences in the fits between  $T_a$  and  $SST_0$  for different seasons and somewhat larger seasonal differences in the  $T_a$  and  $RH_0$  relationship, as seen in Figure 2. Unless otherwise noted we use the annual average fits hereafter, though we test the sensitivity of the water-isotope values of evaporation to these seasonal differences below.

The normalized relative humidity at the evaporation site is the critical driver of kinetic fractionation of water isotopes (Merlivat and Jouzel, 1979; Risi et al., 2010).

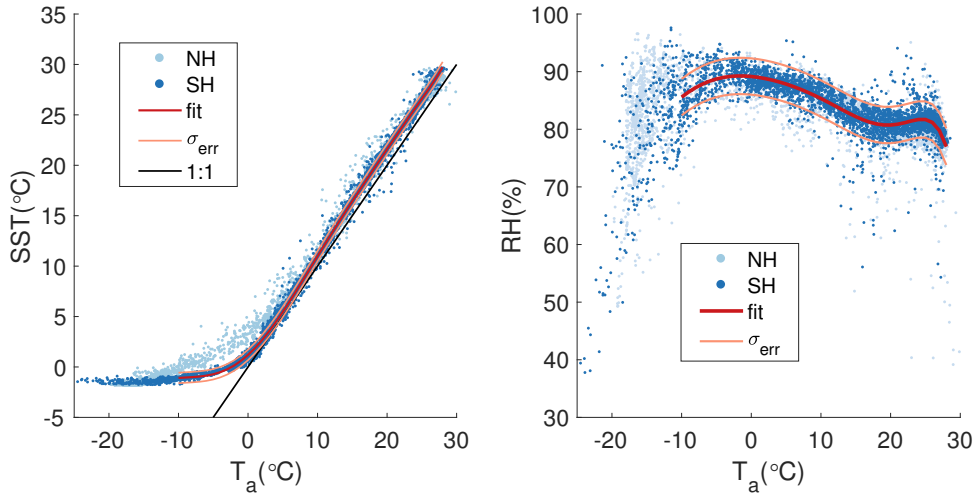


**Figure 1.** Climatological correlations between  $T_a$ ,  $SST$ , and  $RH$ . Left: Annual mean climatological surface air temperature,  $T_a$ , and sea surface temperature,  $SST$ , from the NCEP/NCAR reanalysis (Kalnay et al., 1996). Light blue dots are Northern Hemisphere (NH) grid points, while dark blue dots are Southern Hemisphere (SH) grid points. The polynomial fit for the SH is in red. The error estimate on the fit,  $\sigma_{err}$  in orange, is the standard deviation of the misfit in the model. The 1:1 line is shown in black. Right: same as on the left but for the surface air temperature over ocean,  $T_a$ , and surface relative humidity ( $RH$ ) over oceans.

Normalized relative humidity,  $RH_n$ , quantifies the surface moisture gradient and is calculated as:

$$RH_n = \frac{RH \times e_s(T_a)}{e_s(SST)} \quad (6)$$

where  $e_s(T_a)$  and  $e_s(SST)$  are the saturated vapor pressures of air at the surface air temperature and at the sea surface, respectively.  $RH$  and  $RH_n$  may be varied explicitly in this model, as discussed later. In general we use the climatological relationships described above. The advantage of these relationships is that when investigating the influence of changing site and source temperatures, SWIM allows for  $SST$ ,  $RH$ , and  $RH_n$  values that vary with the specified initial air temperatures, following the correlations in the known climate.

2.1.2. *Transport.* After evaporation at initial air temperature,  $T_0$ , and surface pressure,  $P_0$ , moisture is transported toward the pole in isolation, cooling and condensing

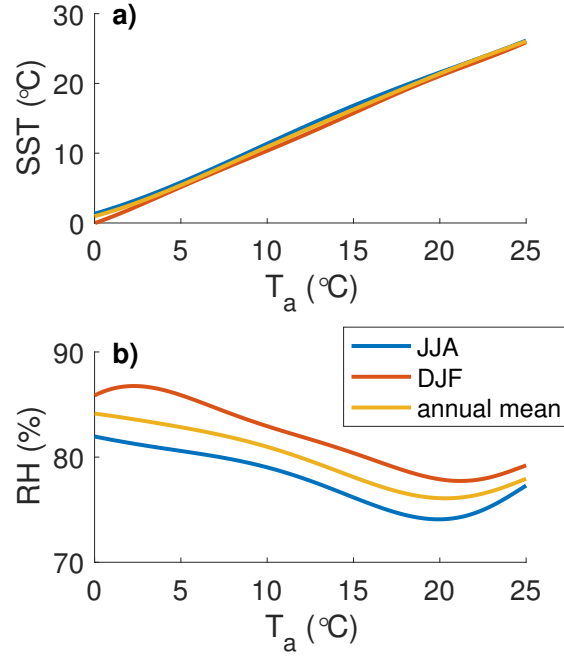


**Figure 2.** Relationships between  $T_a$ ,  $SST$ , and  $RH$  in different seasons in the ERA-interim reanalysis data set for the Southern Hemisphere. a) Relationship between  $T_a$  and  $SST$  for the annual average (yellow), the December, January, February (DJF) season (red), and the June, July, August (JJA) season (blue). b) same as a) but for the relationship between  $T_a$  and  $RH$ .

along the way. Several physical details of the cooling pathway are important to the cumulative condensation and water-isotope fractionation, including the air pressure and saturated vapor pressure which together define the saturated mixing ratio, the presence of liquid water and ice in the parcel, and the degree of supersaturation. The air parcel is cooled pseudoadiabatically defining a pressure trajectory,  $P$ , that depends on  $T$ . As the air parcel cools, moisture above saturation is removed and the latent heat released during the phase change keeps the air parcel warmer than in an otherwise equivalent isobaric pathway. For sensitivity studies an alternate isobaric pathway may be specified in the model, though it is less realistic; the pseudoadiabatic pathway is used hereafter. We calculate a pseudoadiabat following the iterative routine described in (Bakhshaii and Stull, 2013) but taking into account the saturated vapor pressures of both ice and liquid water condensate that is formed and removed from the air parcel.

We calculate the temperature dependence of the latent and specific heats, and saturated vapor pressures of ice and liquid water (Murphy and Koop, 2005; Murray, 1966). The saturated vapor pressures and the air pressure,  $P$ , define a saturated mixing ratio for both ice,  $r_{s,i}$ , and liquid water  $r_{s,l}$ , at any point along the cooling pathway,  $r_s = \frac{R_d}{R_{wv}} \times \frac{e_s}{P - e_s}$ , where  $\frac{R_d}{R_{wv}}$  is the ratio of gas constants of water vapor and dry air.

Condensed water in the atmosphere does not abruptly transition from all liquid to all ice at the 0°C isotherm. Rather, air parcels are mixed in phase (Ciais and Jouzel, 1994). The ice fraction of condensate smoothly increases as temperatures decrease below freezing (Hu et al., 2010). Many models, including isotope-enabled GCMs, approximate the temperature dependence of cloud ice-liquid fraction as piecewise linear functions (Hu et al., 2010). Some water-isotope models use more realistic smoothly varying error integrals (Ciais and Jouzel, 1994; Kavanaugh and Cuffey, 2003). Using satellite measurements, Hu et al. (Hu et al., 2010) derive polynomial relationships between cloud temperature and liquid-ice fractions. As shown in Figure 3, the observation-based relationships preserve significantly more liquid water at colder temperatures than previously used parameterizations such as the error integral between 0°C and -40°C employed by (Kavanaugh and Cuffey, 2003). Further, Hu et al. (c.f. Figure 6, (Hu et al., 2010)) show that over the Southern Ocean and over snow and ice surfaces the cloud liquid water content is higher at a given temperature than in the global average. We use a fit based on the relationship found over the Southern Ocean and over land snow/ice surfaces in (Hu et al., 2010). Because of the influence of mixed phase vapor pressures on kinetic fractionation, the satellite-derived mixing curves are an important constraint on the model.

The effective specific heat at constant pressure  $c_{p,eff}$ , latent heat,  $L_{eff}$ , saturated vapor pressure,  $e_{s,eff}$ , and saturated mixing ratio,  $r_{s,eff}$ , for a mixed-phased air parcel are calculated based on the temperature dependent parameter for the liquid and ice phases individually and the mixing fractions of each phase (Kavanaugh and Cuffey, 2003). For example,  $r_{s,eff} = r_{s,i} \times \text{fraction}_{ice} + r_{s,l} \times \text{fraction}_{liq}$ , where  $r_{s,i}$  and  $r_{s,l}$  are the saturated mixing ratios of ice and liquid, respectively, and  $\text{fraction}_{ice}$  and  $\text{fraction}_{liq}$  are the temperature dependent fractions of condensate that are in the ice and liquid phase, determined by the satellite observations of (Hu et al., 2010).

The presence of both ice and liquid condensate in the cloud dictates a supersaturation of vapor over ice due to the difference in liquid and ice vapor pressures (Jouzel and Merlivat, 1984). The supersaturation is a critical variable in the kinetic fractionation of water isotopes (Jouzel and Merlivat, 1984). The mixed phase nature of the condensate has a strong influence on the supersaturation, but is not the only factor. For example, a paucity of condensation nuclei may lead to additional

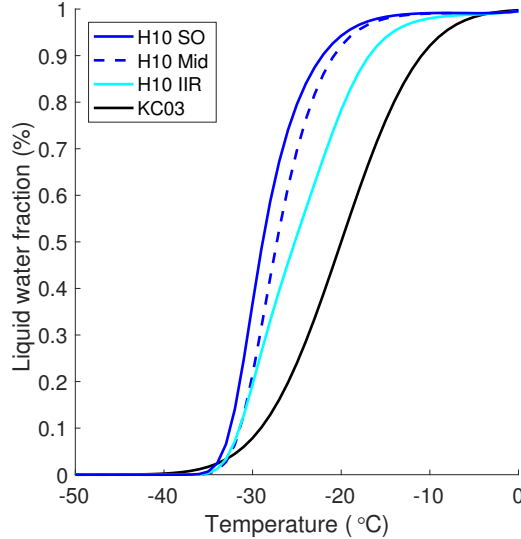


**Figure 3.** Liquid fraction of cloud condensate ( $\text{fraction}_{liq}$ ) as a function of temperature. The solid blue line is based on the relationship found by (Hu et al., 2010) (H10) for liquid fraction over the Southern Ocean and land based ice (SO). The dashed blue and cyan lines are globally averaged estimates from Hu et al based on midlevel cloud temperature (Mid) and IIR estimated cloud temperatures (IIR), respectively. These estimates are less suitable for the mid and high latitudes of the Southern Hemisphere, but may be useful to other applications. The black line is the error integral used in the (Kavanaugh and Cuffey, 2003) (KC03) intermediate complexity model. Note that  $\text{fraction}_{ice} = 1 - \text{fraction}_{liq}$ .

super saturation at cold temperatures (Tegen and Fung, 1994). The influence of supersaturation on the behavior of modeled water-isotope ratios is discussed in detail below (Section 2.4.2). However it is important to note here that the supersaturation dictates the threshold for removal of condensation from the atmosphere and thus relationship between total moisture,  $q$ , and temperature of the pathway. In most water-isotope models (e.g. Kavanaugh and Cuffey (2003)) and including General Circulation Models (GCMs) (e.g. Schoenemann et al. (2014)), the supersaturation of the physical transport path and that dictating fractionation of water isotopes are not self consistent. This leads to discrepancies in the relationship between modeled water-isotope ratios and the surrounding environmental conditions. In SWIM, the supersaturation of vapor over ice is parameterized and self consistent between the physical transport path and water-isotope fractionation (Section 2.4.2).

Moisture is removed along the temperature pathway owing to the changes in saturated mixing ratio. For a given change in temperature between steps,  $dT$ ,  $-dq(dT) = dr_{s,eff}(dT)$ . We do not consider reevaporation of falling precipitation. Our assumption of pseudoadiabtic pathways is consistent with air parcels that do not mix during transport and are not recharged by evaporation. However, the total moisture reaching an ice-core site is not well defined by a single isolated pathway, since the Southern Hemisphere atmosphere is well mixed by the Westerlies and baroclinic waves. Thus for any individual ice-core site we consider an ensemble of temperature pathways defined by the distribution of relevant moisture-source temperatures and the site's surface temperature.

The distribution of moisture-source temperatures reflects the combination of the spatial pattern of evaporation and the broad sampling of the Southern Ocean by the atmospheric circulation. The range of moisture-source temperatures for an ice-core site may be estimated simply as a reasonable range of Southern Ocean surface temperatures with no explicit weighting, or with explicit weighting derived from reanalysis (Markle et al., 2012; Sodemann and Stohl, 2009) or moisture-tagged GCMs (Markle et al., 2017). Annual mean moisture-source distributions (MSD) as a function of latitude are diagnosed from a water tagged control run of the Community Atmosphere Model (CAM) general circulation model for East and West Antarctic sites (details are given in Markle et al. (2017)), shown in Figure 4. Moisture from a wide range of source latitudes influences any given ice-core site. These MSDs define the relative weighting of appropriate source conditions.

*2.1.3. Condensation site conditions.* The modeled pathway is cooled from initial evaporation temperature to subsequent condensation temperatures. However we are often interested in the surface temperature of a site and its variability, rather than the condensation temperature. For much of the world, one may simply assume a lapse rate from the surface to the condensation level. Antarctica however, has strong inversions such that temperature aloft in the troposphere is often warmer than the surface (Connolley, 1996). Masson-Delmotte et al. (2008) review the relationship between the condensation temperature and the surface temperature over Antarctica. They compare the surface temperature and the weighted annual mean condensation temperature in both ERA-40 reanalysis (1980-2002) and MAR, a 40km resolution mesoscale model forced by ERA-40 (c.f. Figure 8, Masson-Delmotte et al. (2008)). In both models the upper bound of the Antarctic surface temperature to condensation temperature relationship appears to be set by the inversion temperature. They calculate a best fit slope of the surface to condensation temperature relationship as  $0.67^{\circ}\text{C}/^{\circ}\text{C}$  in the ERA-40 data, consistent with previous work and assumptions used in Raleigh-type distillation models (Connolley, 1996; Jouzel and Merlivat, 1984). In both tERA-40 and MAR however, condensation temperatures are on average colder

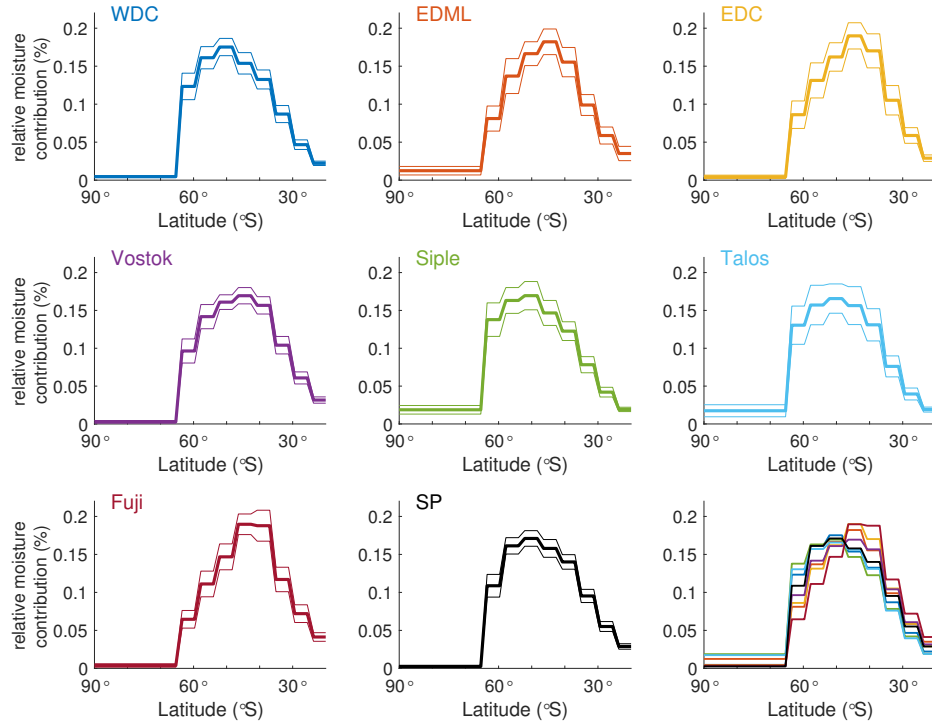


**Figure 4.** Moisture Source Distributions (MSDs) for Antarctic deep ice-core sites. MSDs were calculated from a 30 yr moisture-tagged control run of the CAM model (Markle et al., 2017). Bold lines show the relative contribution of 9 latitudinal bins in the Southern Ocean as evaporation sources for the total annual average moisture falling at eight Antarctic ice-core sites. The thin lines show the  $\pm 1\sigma$  variability in the MSDs associated with inter-annual variability. The MSDs for all sites are superimposed in the lower left plot. One can see the more northern mean latitude of East Antarctic moisture sources (e.g. that of EPICA Dome Concordia (EDC), EPICA Dronning Maud Land (EDML), Vostok, Fuji, South Pole (SP), and Talos Dome) compared to West Antarctic moisture sources (e.g. West Antarctic Ice Sheet Divide (WDC), and Siple Dome).

than the peak inversion temperature. This makes physical sense; the peak inversion temperature is the upper limit of possible condensation temperatures, but it is possible for precipitation to occur at colder temperatures as well. The range of condensation temperature in the higher resolution MAR model includes colder temperature than in the lower resolution reanalysis, including temperatures as cold as

the surface, suggests that greater model resolution leads to colder average condensation temperatures (Masson-Delmotte et al., 2008). The strength of the Antarctic inversion diminishes with increasing temperature (Connolley, 1996), and relatively warm Antarctic surface temperatures (e.g.  $> -20^\circ\text{C}$ ) are associated with condensation temperatures colder than the surface temperature (Masson-Delmotte et al., 2008).

Over the Antarctic continent, we use a simple relationship,  $T_c = 0.75T_s - 6^\circ\text{C}$ . This relationship maintains a linear assumption as used in previous studies (Jouzel and Merlivat, 1984; Masson-Delmotte et al., 2008), but better captures the lower condensation temperatures of the high resolution MAR analysis in Masson-Delmotte et al. (2008) compared to previous assumptions based on the peak inversion temperature (Figure 5). For relatively mild surface temperatures, this fit results in condensation temperatures that are colder than the surface, in line with observations and modeling (Connolley, 1996; Masson-Delmotte et al., 2008). The relationship between surface and condensation temperature may be less well constrained in the absence of the inversion layer.

**2.2. Isotope fractionation.** In this section we outline the water-isotope fractionation scheme used in SWIM. We use conventional notation in which  $R$  is the number ratio of heavy to light isotopes of a species in a sample, for example  $^D R = \frac{^2\text{H}}{^1\text{H}}$  and  $^{18}R = \frac{^{18}\text{O}}{^{16}\text{O}}$ . The isotopic content of a water sample is reported in delta notation:

$$\delta_x = \frac{R_x - R_{std}}{R_{std}} \quad (7)$$

where  $R_x$  is the ratio in the sample and  $R_{std}$  is the ratio in a known standard, typically Vienna Standard Mean Ocean Water (VSMOW). For R values of SMOW we use  $^{18}R_{SMOW} = 0.00200520$ ,  $^{17}R_{SMOW} = 0.0003799$ , and  $^D R_{SMOW} = 0.00015576$  (Criss, 1999). In some instances it will be useful to define a logarithmic definition of of the delta values,

$$\delta'_x = \ln(1 + \delta_x). \quad (8)$$

Fractionation is the change in relative distribution of heavy and light isotopes of an element between phases. For example, consider two phases of water, liquid and vapor, at equilibrium with each other. The ratio of the rarer and heavier  $^{18}\text{O}$  isotope to the common and lighter  $^{16}\text{O}$  isotope is larger in the liquid phase compared to the vapor phase, that is  $^{18}R_l > ^{18}R_v$ . This is due to the reduced vibrational energy of the heavier isotope and the greater bond forces of the lower energy phase (Criss,

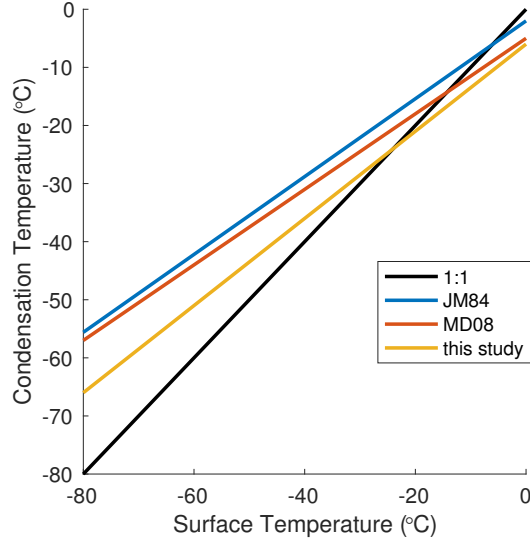


**Figure 5.** Relationship between surface temperature and condensation temperature. Black line shows the 1:1 line. The blue line shows the relationship between surface temperature and inversion temperature used in Jouzel and Merlivat (1984) (JM84), and the red line shows the best fit of condensation temperature to surface temperature in the ERA-40 reanalysis found by Masson-Delmotte et al. (2008) (MD08). The yellow line shows the estimate of the relationship between surface temperature and condensation temperature used in this study. This fit is based on the high-resolution MAR analysis in MD08, which shows a lower average condensation temperature than the ERA-40 analysis.

1999). The ratio of  $R$  values between phases is known as a fractionation factor,  $\alpha$ . For example, the fractionation factor between liquid and vapor phases for  $\delta^{18}\text{O}$  is:

$${}^{18}\alpha_{l-v} = \frac{\left(\frac{{}^{18}\text{O}}{{}^{16}\text{O}}\right)_{\text{liquid}}}{\left(\frac{{}^{18}\text{O}}{{}^{16}\text{O}}\right)_{\text{vapor}}} = \frac{{}^{18}R_l}{{}^{18}R_v} \quad (9)$$

The equilibrium fractionation factors between liquid and vapor,  ${}^{18}\alpha_{l-v, eq}$  and  ${}^D\alpha_{l-v, eq}$ , as well as those between vapor and ice,  ${}^{18}\alpha_{i-v, eq}$  and  ${}^D\alpha_{i-v, eq}$ , are temperature dependent and determined empirically. We use the temperature-dependent relationships summarized by Criss (1999) with updates for the temperature dependent fractionation factor for ice-vapor equilibrium found by Lamb et al. (2017).

Ellehoj et al. (2013) found much stronger temperature dependence of the vapor-ice equilibrium fractionation factors than previous work (e.g. Merlivat and Nief (1967)). For very cold temperatures, where this stronger temperature dependence is most pronounced, it is difficult to reproduce the observed relationship between  $\delta^{18}O$  and  $\delta D$  in our model when using the Ellehoj et al. (2013) fractionation factors. However, the more recent study by Lamb et al. (2017), was not able to reproduce these very large  $\alpha_{eq}$  at low temperatures, instead finding a temperature relationship much closer to previous studies (Merlivat and Nief, 1967).

**2.3. Evaporation from the ocean.** The isotopic values of vapor evaporating from the ocean are determined, in part, by the isotopic values of the sea water. By definition, globally averaged seawater has  $\delta$  values near 0 ‰. However the  $\delta^{18}O$  of seawater ( $\delta^{18}O_{sw}$ ) in the Southern Ocean, the region of Antarctic moisture sources, is in general less than 0 ‰, with a mean around -0.3 ‰, (Schmidt et al., 1999). Some previous literature (e.g. Uemura et al. (2012)) has assumed that  $\delta D_{sw} = 8 \times \delta^{18}O_{sw}$ . We use the observed correlation between  $\delta^{18}O_{sw}$  and  $\delta D_{sw}$  from a compilation of global measurements (Schmidt et al., 1999) to find an initial  $\delta D_{sw}$  given a specified initial  $\delta^{18}O_{sw}$ . We use an initial  $\delta^{18}O_{sw} = -0.3$  ‰. We investigate the sensitivity of the model to these initial conditions and allow for the initial  $\delta_{sw}$  to change with climate mean state. We assume a  $^{17}O_{xs}$  of sea water equal to 0.

Fractionation occurs during the initial evaporation of water from the ocean. At equilibrium, i.e. saturation, the vapor will be isotopically lighter than the underlying surface water ( $\alpha_{l-v,eq} > 1$ ). The atmosphere above the global oceans is not at saturation on average, with relative humidities typically around 80% (Hartmann, 2015). Because of this steady-state disequilibrium, significant kinetic (non-equilibrium) fractionation occurs during evaporation. Kinetic fractionation is especially important for the deuterium excess of vapor and precipitation.

The amount of kinetic fractionation depends both on the relative humidity and the wind speed at the air-ocean interface during evaporation (Merlivat and Jouzel, 1979). The effective fractionation factor associated with diffusion and turbulence can be written,

$$\alpha_{diff} = \left( \frac{D}{D^*} \right)^n \quad (10)$$

where  $D$  and  $D^*$  are the diffusivities of the light and heavy isotopes, respectively (Merlivat and Jouzel, 1979). The exponent  $n$  ranges in value from 0 to 1 and relates to the wind regime, speed, and the ratio of turbulent and molecular diffusion. For the diffusive fractionation between  $H_2^{18}O$  and  $H_2^{16}O$  during initial evaporation, the fractionation factor  $^{18}\alpha_{diff}$  equals 1.0 for pure turbulence and 1.0028 for pure molecular diffusion (Barkan and Luz, 2007; Merlivat and Jouzel, 1979).

Following Kavanaugh and Cuffey (2003), we do not explicitly consider surface wind speeds or changes in windspeed in the model. Instead we use the phenomenological results of Uemura et al. (2008) and Uemura et al. (2010) for  $^{18}\alpha_{diff}$ , who estimate the parameter based on measurements of  $\delta D$ ,  $\delta^{18}O$ , and  $\delta^{17}O$  in vapor above the Southern Ocean. Uemura et al. (2010) find a value of  $^{18}\alpha_{diff} = 1.007 \pm 0.0013$  and  $1.008 \pm 0.0018$ , when optimizing for observations of  $d_{xs}$  and  $^{17}O_{xs}$  of vapor, respectively. These results are within uncertainty of each other and of independent analysis by Pfahl and Wernli (2009) which found a value of 1.0076. We use a default value of  $^{18}\alpha_{diff} = 1.007$  and test the sensitivity of the model to the parameter below.

The diffusive fractionation factor between hydrogen and deuterium,  $^D\alpha_{diff}$  may be determined experimentally by measuring the relationship between diffusive fractionation factors (Luz et al., 2009; Merlivat, 1978):

$$\phi_{diff} = \frac{^D\alpha_{diff} - 1}{^{18}\alpha_{diff} - 1} \quad (11)$$

Merlivat (1978) found a mean value for  $\phi_{diff}$  of 0.88 based on laboratory evaporation studies. Luz et al. (2009) found that the value of  $\phi_{diff}$  depends on the evaporation temperature, ranging between 0.73 and 1.06 for temperatures between 10°C and 69.5°C. We use a piecewise linear function based on the results of Luz et al. (2009) to relate  $\phi_{diff}$  and evaporation temperature, and thus  $^D\alpha_{diff}$  to  $^{18}\alpha_{diff}$ . For evaporation temperatures outside the experimental range ( $< 10^\circ\text{C}$ ) of Luz et al. (2009), we use the experimentally determined value at 10°C ( $\phi_{diff} = 1.06$ ). The differences in SWIM model results for evaporation with a temperature dependent  $\phi_{diff}$  and a constant  $\phi_{diff} = 0.88$ , are small ( $< 1\%$  for initial  $\delta D$  of vapor). We use the estimates of  $\phi_{diff}$  from Luz et al. (2009) but not their estimates for  $\alpha_{diff}$ . Because the laboratory experiments were conducted in conditions with low  $RH$  and no wind, the Southern Ocean measurements of  $\alpha_{diff}$  by Uemura et al. (2008) and Uemura et al. (2010) are better suited to our purposes. The influence of flow regime on  $\phi_{diff}$ , characterized by the exponent  $n$  in Equation 10, is negligible (Luz et al., 2009).

For the fractionation of the rarer oxygen isotope ratio,  $\frac{^{17}O}{^{16}O}$ , we use the following relationships, which are backed both by theory and empirical observation (Barkan and Luz, 2005, 2007):  $^{17}\alpha_{eq} = ^{18}\alpha_{eq}^{0.529}$  for vapor and liquid in equilibrium, and  $^{17}\alpha_{diff} = ^{18}\alpha_{diff}^{0.518}$  for vapor diffusion.

The relationship between the initial R value of the vapor and the ocean due to kinetic fractionation depends on the normalized relative humidity during evaporation,  $RH_n$ , the equilibrium and diffusive fractionation factors,  $\alpha_{l-v,eq}$  and  $\alpha_{diff}$ . Following

Criss (1999) and Luz et al. (2009) this can be written,

$$\alpha_{evap} = \frac{R_o}{R_e} = \frac{\alpha_{eq}\alpha_{diff}(1 - RH_n)}{1 - \alpha_{eq}RH_n\frac{R_v}{R_o}} \quad (12)$$

where  $R_o$  and  $R_v$  are the isotopic ratios of the ocean water and the water vapor in the atmospheric boundary layer, respectively.  $R_e$  is the ratio of the evaporate, the net vapor lost to the atmosphere and is not directly measurable. It is the net value between the outgoing and incoming moisture to the atmosphere in the steady state for a given relative humidity (Criss, 1999).

If we assume that the only source of vapor to the boundary layer is the local evaporate, we may equate  $R_v$  and  $R_e$  and solve Equation 12 for  $R_v$  (Criss, 1999; Merlivat and Jouzel, 1979; Risi et al., 2010):

$$R_v = \frac{R_o}{\alpha_{eq} \times (\alpha_{diff} + RH_n(1 - \alpha_{diff}))} \quad (13)$$

The modeled isotopic composition of vapor evaporated from the ocean is shown in Figure 6. This “local” closure assumption is within the range of observations of water isotopes in vapor over the Southern Ocean ( $\delta^{18}O$ ,  $\delta D$ , and  $d_{xs}$  from Uemura et al. (2008) and Liu et al. (2014),  $^{17}O_{xs}$  from Uemura et al. (2010)). However, the validity of the local closure assumption under certain conditions is in question (Risi et al., 2010; Uemura et al., 2010). In addition to moisture from the ocean surface, the boundary layer may receive moisture from convection, subsidence, and reevaporation of precipitation. Risi et al. (2010) explored this issue extensively, using a model that takes into account these other sources of moisture. They show that the closure assumption leads to vapor that is too enriched in both  $\delta D$  and  $\delta^{18}O$ , and too low in  $d_{xs}$ , and that these offsets are a function of environmental conditions (Risi et al., 2010). The comparison of SWIM model results to observations are in agreement with these findings (Figure 6). The closure assumption appears near the upper limit of the observations. This is physically reasonable since an ocean-only source is an end member scenario for local evaporation. Most of the data lie below the modeled line, possibly reflecting contributions from other sources of evaporation.

We investigate the utility of the local closure assumption, by considering closure globally rather than locally, as outlined by Criss (1999). In a global steady state of evaporation and precipitation, the evaporate from the ocean is the ultimate source of vapor. The mean ocean has  $\delta$  values of about 0‰, and global average precipitation has  $\delta^{18}O = -4.5‰$  and  $\delta D = -26.7‰$ , (Craig and Gordon, 1965). Following (Criss, 1999), in the global average steady state the delta values of precipitation must reflect the net loss by evaporate from the ocean. Thus globally, the ratio of  $\left(\frac{R_o}{R_e}\right)_{global}$  is

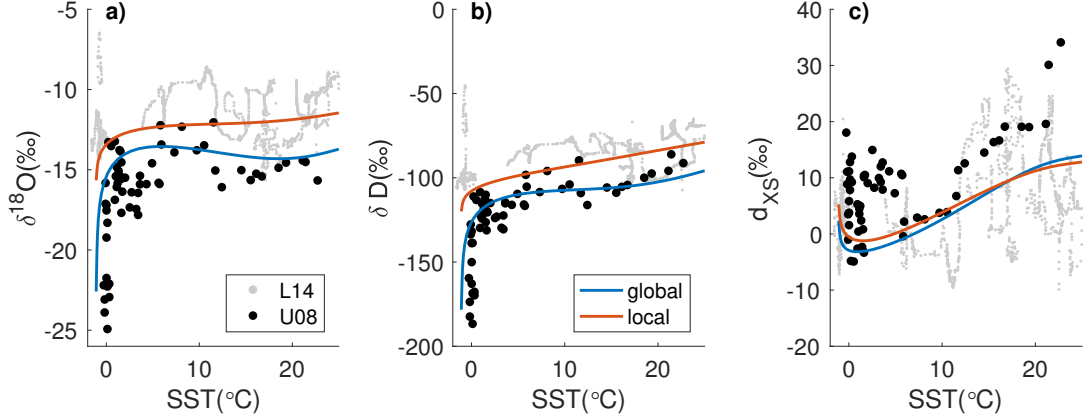


**Figure 6.** Modeled isotopic values of evaporation compared to Southern Ocean vapor measurements. a) Modeled  $\delta^{18}O$  versus  $SST$  using the “local” closure assumption (red line) and “global” closure assumption (blue line). Black dots are discrete vapor measurements from the Southern Ocean made by Uemura et al. (2008), while grey dots are continuous Southern Ocean vapor measurements made by Liu et al. (2014). b) Same as a) but for modeled  $\delta D$  versus  $SST$ . c) Same as a) but for modeled  $d_{xs}$  versus  $SST$ . Model results use the annual average NCEP/NCAR  $SST$  and  $RH$  climatology. The vertical tails at low  $SST$  in panels a) and b) result from the fact that  $SST$ s asymptote to the freezing point of seawater while air temperatures may continue to decrease.

1.0267 for  $\delta D$  and 1.0045 for  $\delta^{18}O$ . Next, instead of equating  $R_e$  and  $R_v$  locally, we define a global  $\bar{\alpha}_{evap} = \left(\frac{R_o}{R_e}\right)_{global}$ , and solve for  $R_v$ . Substitution into Equation 12 and rearranging leads to:

$$R_v = R_o \left(1 - \frac{\alpha_{eq} \alpha_{diff} (1 - RH_n)}{\bar{\alpha}_{evap}}\right) (\alpha_{eq} RH_n)^{-1} \quad (14)$$

We will call this the “global closure” assumption, in contrast to the more frequently used “local closure” assumption described above. The global closure assumption is of course valid globally, though is arguably a blunt approach for local evaporation. Despite this, it makes a useful and simple approximation, which matches observational data well. Modeled evaporation using both closure assumptions are compared to isotopic measurements of Southern Ocean vapor in Figure 6. The local closure assumption is generally near the upper bounds of the observational  $\delta^{18}O$  and  $\delta D$  data,

reflecting the end member conditions implied by this assumption. The global closure assumption results in more depleted  $\delta D$  and  $\delta^{18}O$  values of initial vapor compared to the local closure assumption, in line with the limitations of the local assumption found by Risi et al. (2010), and in agreement with observations.

A few caveats are important to discuss. The available observations are not sufficient to distinguish between the appropriateness of these two assumptions. The observational data are from single season cruises, with evaporation conditions changing daily (Liu et al., 2014; Uemura et al., 2008). Our model on the other hand aims to represent general climatology. Furthermore, the utility of both closure assumptions depends on the mean state, and may thus change with time. The appropriate values for  $\left(\frac{R_o}{R_e}\right)_{global}$  used in the global closure will certainly change as ice sheets grow and decay. The degree to which local closure is applicable to any site likely depends on the patterns of atmospheric circulation, which may change. Regardless, local closure always represents an end member of possible evaporative conditions. The differences between these assumptions during initial evaporation have limited influence of the reconstructions presented below. Both methods result in similar initial  $d_{excess}$  values of vapor and, while there are differences in the initial  $\delta D$  and  $\delta^{18}O$  of vapor, the relative dependence of either on SST is similar. We consider the choice of closure assumption to be a source of uncertainty in temperature reconstructions and discuss those uncertainties below.

The deuterium excess parameter is critical to water isotope based temperature reconstructions. In Figure 7 we compare modeled  $d_{xs}$  of vapor and modeled  $^{17}O_{xs}$  of vapor to Southern Ocean vapor observations. We use the observed values of  $T_0$ ,  $SST_0$ , and  $RH_0$  at the time of the vapor measurements (Liu et al., 2014; Uemura et al., 2008), rather than our model climatology, to test the model’s ability to accurately reproduce the excess parameters.

When using the observed  $T_0$ ,  $SST_0$ , and  $RH_0$  values, the modeled relationships between  $d_{xs}$  and  $SST_0$  and  $RH_0$  are in excellent agreement with observations. Likewise the modeled relationship between  $^{17}O_{xs}$ ,  $SST_0$ , and  $RH_0$  are in good agreement with observations. This provides confidence that our model is capturing the influence of source conditions on water isotope behavior and can thus be used to reconstruct source conditions.

We next test the sensitivity of initial evaporation to several model parameters discussed above. We test model sensitivity to the choice of climatology and seasonality (Figure 8), and the uncertainty in the climatological fits between surface temperature, SST, and RH (Figure 9). Modeled evaporation sensitivity to the value of  $\alpha_{diff}$  is shown in Figure 10 and to the initial  $\delta^{18}O_{sw}$  of the ocean in Figure 11. In all cases the modeled sensitivity to these parameterizations and uncertainties are relatively

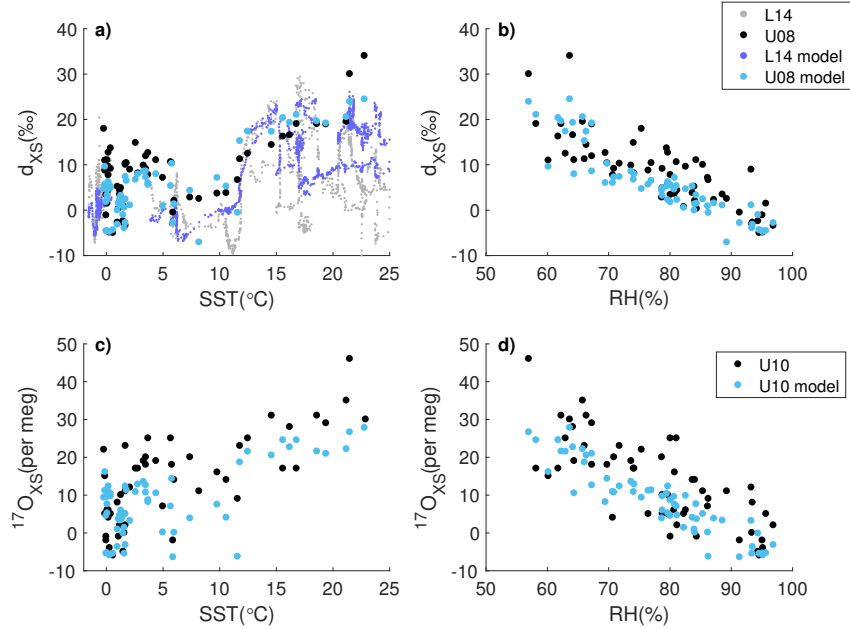


**Figure 7.** Comparison of modeled and observed isotope excess parameters and relationship to source-region conditions. a) Observed  $d_{xs}$  and  $SST$  relationship in Southern Ocean vapor from Uemura et al. (2008) (black dots, U08) and Liu et al. (2014) (grey dots, L14). SWIM model results for evaporation under  $SST$  and  $RH$  conditions observed coincident with vapor measurements of Uemura et al. (cyan dots, U08 model), and Liu et al. (purple dots, L14 model). b) Same as a) but for modeled and observed  $d_{xs}$  to  $RH$  relationship from observations of Uemura et al. The Liu et al. observations and model show a similar trend and are omitted for visual clarity. c) Observed  $^{17}O_{xs}$  and  $SST$  relationship in Southern Ocean vapor from Uemura et al. (2010) (black dots, U10), and SWIM model results run under observed sea surface conditions (cyan dots, U10 model). d) Same as c) but for observed and modeled  $^{17}O_{xs}$  and  $RH$  relationship in Southern Ocean vapor.

small compared to the observed natural variability in the observations (Liu et al., 2014; Uemura et al., 2008).

**2.4. Distillation.** We next discuss the distillation of water isotopes as the vapor initially evaporated out of the ocean is transport to the ice sheet. As the air parcel is cooled, moisture condenses and water fractionates. The essential differential equation for Rayleigh distillation (Criss, 1999; Dansgaard, 1964; Rayleigh, 1902) is:

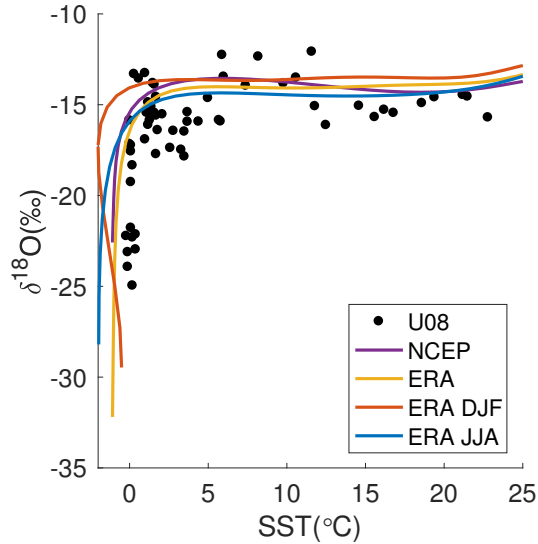


**Figure 8.** Sensitivity of modeled  $\delta^{18}\text{O}$  of vapor to the seasonality of evaporation. We use four different 30yr climatologies from different reanalysis data sets to determine the correlation between  $SST$  and  $RH$  used during initial evaporation: NCEP/NCAR annual average (purple); ERA-Interim annual average (yellow); ERA-Interim December January February (DJF, red); and ERA-Interim June July August (JJA, blue). Model results are not meaningfully different at SSTs warmer than  $0^\circ\text{C}$ . Black dots are the Southern Ocean vapor measurements of Uemura et al. (2008) (U08).

$$\frac{d\ln(R)}{d\ln(f)} = \alpha - 1 \quad (15)$$

where  $R$  and  $\alpha$  are the isotopic ratio and fractionation factor. The variable  $f$  is the fraction of initial water vapor remaining in the air parcel,  $f = \frac{q}{q_0}$ . As discussed in Section 2.1.2,  $q$  at any temperature along the pathway is found by integrating the changes in the saturated mixing ratio  $r_s$  owing to pseudoadiabatic cooling (Dansgaard, 1964) from the source. Thus,

$$f = \frac{q}{q_0} = \frac{r_s}{r_{s,0}} \quad (16)$$

2.4.1. *Equilibrium and kinetic fractionation during transport.* In general, condensation occurs in the model at saturation, and thus the temperature dependent  $\alpha_{eq}$  is used in Equation 15. However at cold conditions there may be supersaturation of

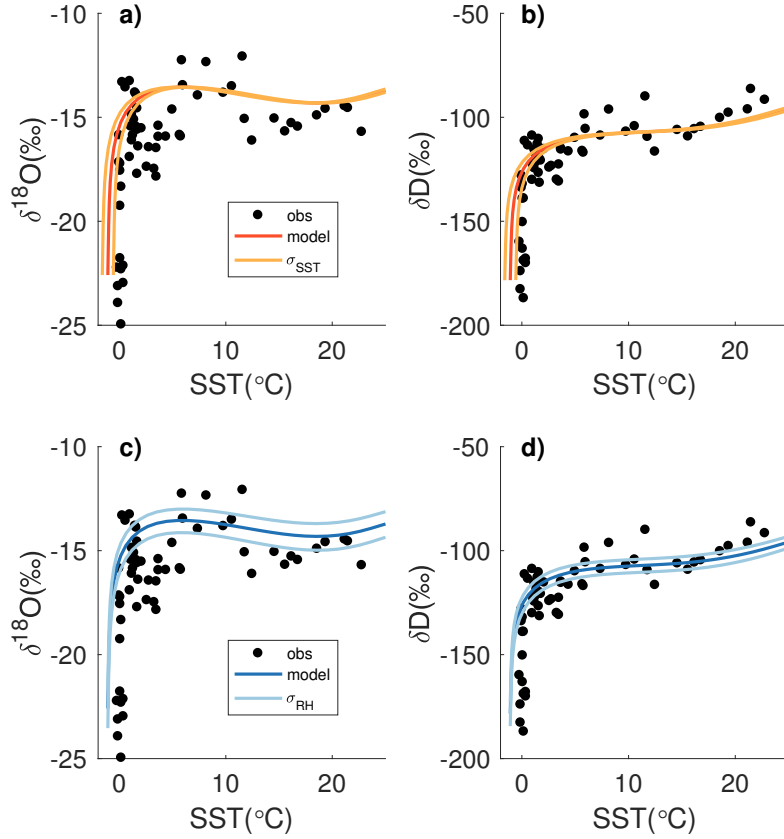


**Figure 9.** Sensitivity of modeled  $\delta^{18}O$  and  $\delta D$  of vapor to uncertainty in the reanalysis-based fits between climatological  $T_a$ ,  $SST$ , and  $RH$  in the NCEP/NCAR reanalysis. a) and b) show modeled isotope vapor relationship to uncertainty in the climatological  $T_a$ -to- $SST$  relationship. Red lines show model run using the central estimate of the fit, orange lines show the spread expected with  $\pm\sigma_{err}$  of the fit as shown in Figure 1. c) and d) are the same as a) and b) but showing the central estimate (dark blue) and spread associated with  $\pm\sigma_{err}$  (light blue) in the climatological  $T_a$ -to- $RH$  relationship shown in Figure 1. In all panels, black dots are the Southern Ocean vapor measurements of Uemura et al. (2008) (obs).

vapor over ice leading to additional kinetic fractionation. Following previous models (Jouzel and Merlivat, 1984), the total fractionation,  $\alpha_{tot}$  factor is written:

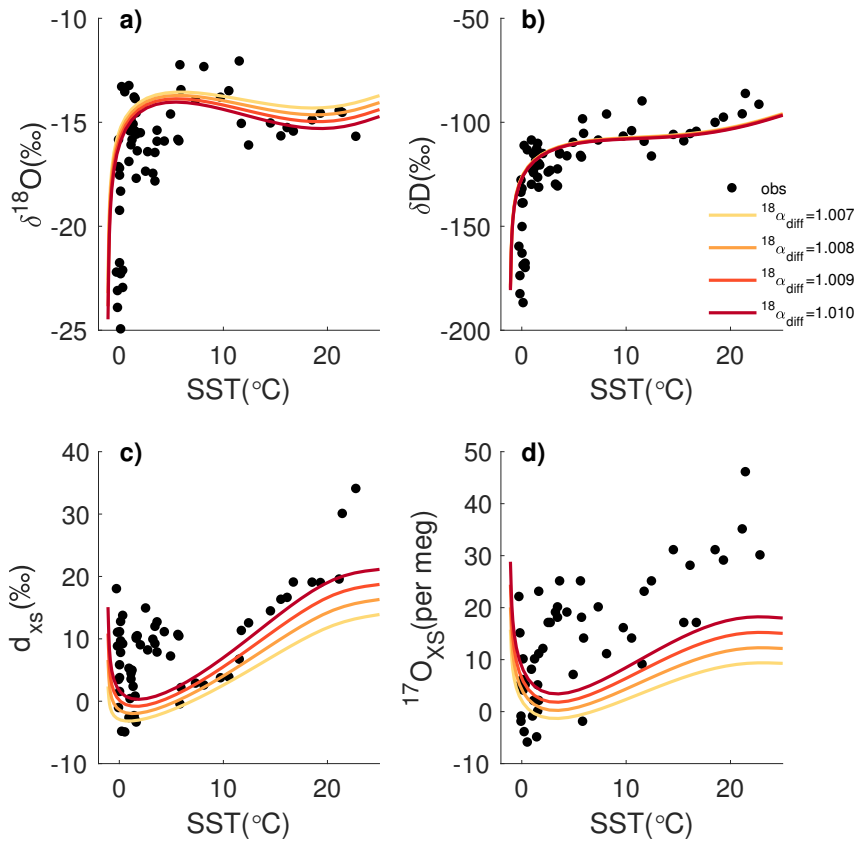


**Figure 10.** Sensitivity of modeled isotope values of vapor to  $^{18}\alpha_{diff}$ . We test a range of  $^{18}\alpha_{diff}$  values from 1.007 to 1.010. In panels a-c), black dots are the Southern Ocean vapor measurements of Uemura et al. (2008) and Uemura et al. (2010) in panel d).

$$\alpha_{tot} = \alpha_{eq}\alpha_k \quad (17)$$

Equation 15 thus becomes:

$$d \ln(R) = (\alpha_{tot} - 1)d \ln(f) \quad (18)$$

Following Kavanaugh and Cuffey (2003), the effective fractionation factors for the mixed-phase portion of the transport pathway depend on the mixing fractions of ice and liquid with temperature.

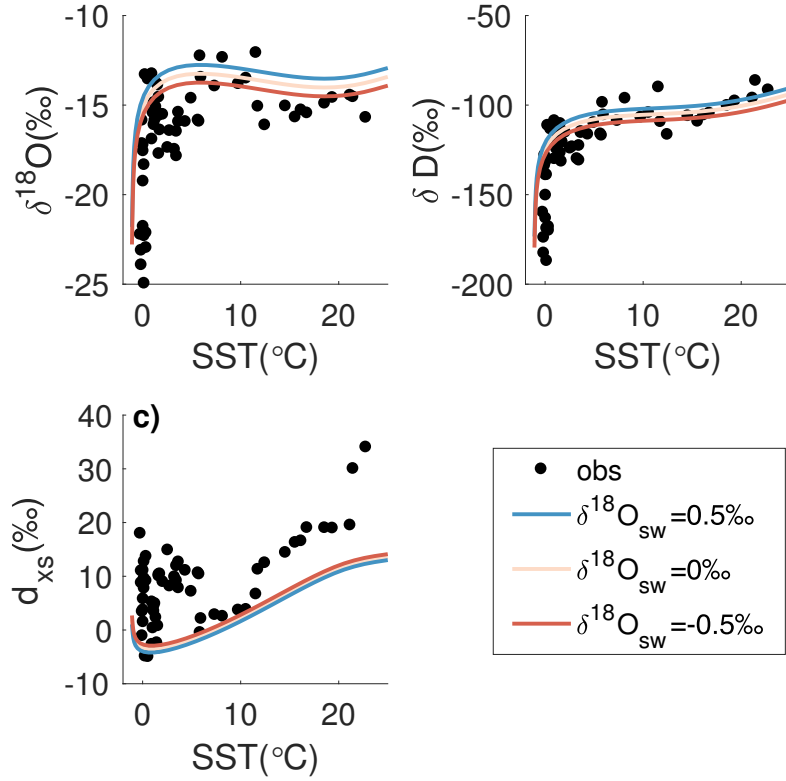


**Figure 11.** Sensitivity of modeled isotope values of vapor to the  $\delta^{18}O_{sw}$  of sea water. Values of  $\delta^{18}O_{sw}$  from  $-0.5\text{‰}$  to  $0.5\text{‰}$  are specified, representing most of the global variance in  $\delta^{18}O_{sw}$ . Values of  $\delta D_{sw}$  are determined based on correlations of  $\delta^{18}O_{sw}$  and  $\delta D_{sw}$  from observations (Schmidt et al., 1999).

$$\alpha_{eff} = \alpha_{l-v, tot} \times \text{fraction}_{liq} + \alpha_{i-v, tot} \times \text{fraction}_{ice} \quad (19)$$

The kinetic modification factor,  $\alpha_k$  in Equation 17, is related to the supersaturation of vapor over ice,  $S_i$ :

$$\alpha_k = \frac{S_i}{\alpha_{eq} \times \frac{D}{D^*} (S_i - 1) + 1} \quad (20)$$

Following Jouzel and Merlivat (1984), we use the ratio of diffusivities for oxygen isotopes  $\frac{D^{16}}{D^{18}} = 1.0285$ , during moisture transport, representative of pure molecular diffusion and ignoring the negligible ventilation effect. Likewise for the ratio of

diffusivities of hydrogen isotopes, we use  $\frac{D^1}{D^2} = 1.0251$ . These values imply a constant  $\phi_{diff}$  during transport equal to 0.88 (Jouzel and Merlivat, 1984), rather than the temperature dependent  $\phi_{diff}$  used in the evaporation scheme. We prefer this value for simplicity and consistency with earlier work and for a lack of experimental measurements of  $\phi_{diff}$  at the colder temperatures experienced during transport.

It is possible that condensation conditions may not represent pure molecular diffusion or that the temperature dependence of  $\phi_{diff}$  found by Luz et al. (2009) may extend to the cold temperatures experienced during transport. As discussed above, we use piecewise linear fits to the measurements of  $\phi_{diff}$  in Luz et al. (2009) for the relatively warm temperatures of initial evaporation. We believe there is little justification however for extrapolating these observations to the very low temperatures experienced during transport, which is far outside the experimental sample. Between 10°C and 69.5°C, (Luz et al., 2009) find that  $\phi_{diff}$  had a maximum value of 1.06 (at 10°C) and a minima of 0.73 (at 39.9°C), a total range of 0.33. Linearly extrapolating from their measurements at 10°C and 20.1°C to a condensation temperature of -50°C leads to a  $\phi_{diff}$  of 2.3678, a change in  $\phi_{diff}$  over 4 times larger than the total spread of their actual measurements (which themselves span nearly 60°C). This implies a very strong non-linearity in  $\phi_{diff}$  which is not supported by the measurements. For example, extrapolating  $\phi_{diff}$  from the 10°C and 20.1°C measurements in the other direction, one would incorrectly estimate a  $\phi_{diff}$  at 39.9°C that is a nearly factor of 2 different than the actual measurement.

It is possible to implement any temperature-dependent diffusivity in the model. As discussed below, we use the temperature dependent supersaturation function to tune the model to observations of  $\delta D$  and  $\delta^{18}O$  in precipitation. The combined influence of supersaturation and diffusivities drives the kinetic fractionation factor as seen in Equation 20, which determines the  $\delta D$  to  $\delta^{18}O$  relationship in precipitation. The model may be tuned using either a constant or temperature-dependent  $\phi_{diff}$ , the latter simply requiring a stronger compensating temperature dependence in the supersaturation function. The behavior of fractionation in the model is similar in either case.

*2.4.2. Supersaturation.* The supersaturation of vapor over ice, is a critical parameterization in water-isotope distillation models. The true relationship of supersaturation to environmental conditions is the result of complex cloud microphysics (Hong et al., 2004). Because of its strong influence on water-isotope fractionation and the uncertainty in the underlying physics, the supersaturation is often parameterized to depend on temperature and used to tune water-isotope models to observations (Jouzel and Merlivat, 1984; Kavanaugh and Cuffey, 2003; Schoenemann et al., 2014); indeed it is the primary tuning knob used in this model. Jouzel and Merlivat (1984)

parametrized the supersaturation as a function of temperature and note that available water-isotope data could not distinguish among possible functional forms of the parameterization (e.g. linear, exponential, etc.). Their linear parameterization,  $S_i = a - b \times T$ , has been used extensively in water-isotope models since.

We use the linear supersaturation parameterization of Jouzel and Merlivat (1984),

$$S_i = a - b \times T \quad (21)$$

Setting  $a = 1$ , we find  $b = 0.00525^\circ\text{C}^{-1}$  to match observations well (see Section 2.5). It is important to note that the prescribed mixing of liquid and ice in the cloud, and the pseudoadiabatic transport pathway described above, imply a supersaturation of vapor over ice that follows the blue curve shown in Figure 12.b, which is inconsistent with that prescribed in Equation 21. The presence of both liquid and ice phases in a cloud is not the only source of supersaturation. The lack of condensation nuclei, for example, allows supersaturation to remain high in very cold, ice-only conditions (Hong et al., 2004), rather than returning to unity as the cloud becomes entirely ice-phase.

The model can be run with two different supersaturations, one relevant to water-isotope fractionation and another to transport and precipitation, an “inconsistent” scenario. The modeled relationship between temperature and  $\delta^{18}\text{O}$  for this scenario is shown in Figure 13. While physically unsatisfying, this is not uncommon; even water-isotope enabled GCMs often use a prescribed supersaturation in the water-isotope fractionation scheme that is disconnected from the model’s own microphysical schemes. However, because the supersaturation experienced by the transport dictates the relationship of temperature and moisture removal (quantified by  $f$  in water isotope distillation), this inconsistency influences the water isotope-temperature relationship in the ice-phase portion of the model.

We explore resolutions to the inconsistency described above as well as its influence on model results. We will consider two additional scenarios in which water-isotope fractionation and the transport path experience the same supersaturation function: 1) the supersaturation function is dictated by the ice and liquid-water fraction in the air parcel; and 2) the supersaturation is specified by the linear parameterization with temperature. In these scenarios the supersaturation used in the calculation of water-isotope fractionation and the removal of moisture from the air parcel is the same, in contrast to the “inconsistent” scenario described above.

In the first consistent scenario, the supersaturation is dictated by the mixed ice and liquid vapor pressures in the pseudoadiabatic pathway. We’ll call this the “ILS consistent” scenario (for ice-liquid supersaturation). In this case, the supersaturation returns to unity once the cloud is fully ice-phase (Figure 12), in contrast to the case in which supersaturation is parameterized as a function of temperature. Because there is no supersaturation in the completely ice-phase portion of the cloud, there is

no kinetic fractionation. The modeled relationship between temperature and  $\delta^{18}O$  for this scenario is shown in Figure 13. The resulting relationship between  $\delta^{18}O$  and  $\delta D$  in this scenario is not consistent with observations. The data imply a slope of  $\partial\delta^{18}O/\partial\delta D$  that is not compatible with equilibrium fractionation alone in the ice-only portion of the pathway.

In the second consistent scenario, we use the traditional linear parameterization for the supersaturation influencing water-isotope fractionation (Equation 21, Figure 12). Further, moisture is removed from the pseudoadiabatic pathway only when the it reaches supersaturation as prescribed by the linear parameterization, by dictating an effective saturated mixing ratio where  $r_{s,eff}/r_{s,i} = S_i$ . We will call this a “consistent linear” scenario. The modeled relationship between temperature and  $\delta^{18}O$  for this scenario is shown in Figure 13. In this case kinetic fractionation occurs in the ice-only portion of the pathway. However, in contrast to the “inconsistent” scenario described above, here the supersaturation that dictates the removal of moisture from the air parcel and the fractionation conditions driving  $\delta$  values are self-consistent.

The relationship between  $\delta^{18}O$  and  $\delta D$  in observations suggests that kinetic fractionation occurs at very cold temperatures (e.g. Jouzel and Merlivat (1984)). These water-isotope data suggest that the supersaturation driving water-isotope fractionation is *below* that implied by the simple pseudoadiabatic pathway in the mixed-phase portion of the pathway and *above* unity in the ice-only portion (Figure 12). The simple linear parameterization of supersaturation with temperature proposed by Jouzel and Merlivat (1984) achieves this.

The modeled relationship between condensation temperature and  $\delta^{18}O$  in the “inconsistent” and “ILS consistent” scenarios have somewhat complex curvature (Figure 13). In comparison, the “consistent linear” scenario results in a far smoother relationship between temperature and the  $\delta^{18}O$  of precipitation. The curvature in the “inconsistent” scenario in Figure 13 is in part due to curvature in the slope of  $f$  with temperature,  $d\ln(f)/dT$ , that arises from the bell-like supersaturation function, and in part due to the inconsistency between the supersaturation experienced by the water isotopes and that experienced by the transport. The curvature in the “ILS consistent” scenario results from the model transitioning between equilibrium-only fractionation, equilibrium and kinetic fractionation, and then back to equilibrium-only as the cloud becomes all ice-phase and the supersaturation returns to unity.

From here on, we use the “consistent linear” scenario in which water-isotope fractionation and the rainout process experience the same supersaturation as dictated by the linear parametrization with temperature (Equation 21). Ensuring self-consistent supersaturation in the isotope fractionation and the temperature dependences of  $f$  yields a smooth  $\delta^{18}O$  to temperature relationship, which is supported by observations.

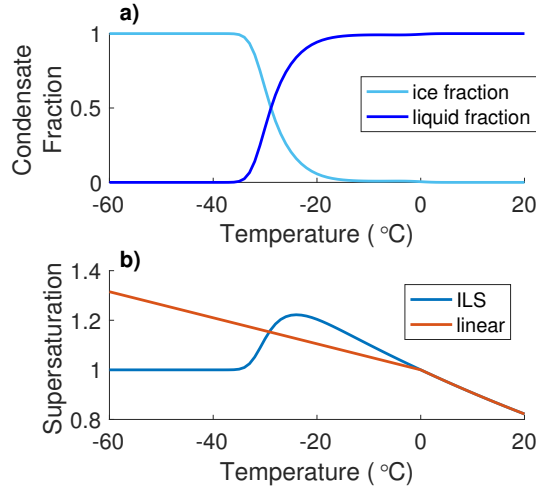


**Figure 12.** Supersaturation of vapor over ice. a) Fractions of ice (cyan) and liquid (blue) condensate as a function of temperature. Curves are derived from satellite based measurements (Hu et al., 2010) as discussed in Section 2.1.2. b) Supersaturation as a function of temperature. The blue curve shows supersaturation based solely on the saturated vapor pressures of ice and liquid, and the mixing fractions based on the curves shown in panel a), and the pseudoadiabatic assumption (“ILS”). The red curve shows the linear parameterization of supersaturation (“linear”) used in the model,  $S_i = 1 - 0.00525 \times T$ . The “inconsistent” scenario described in the text uses the “linear” supersaturation in the water-isotope fractionation scheme and the “ILS” supersaturation to determine the removal of moisture from the air parcel. The “ILS consistent” scenario uses the “ILS” supersaturation for both purposes, while the “consistent linear” scenario uses the “linear” supersaturation for both purposes.

**2.5. Tuning the Simple Water-Isotope Model.** We use the supersaturation function as the primary tuning knob in this model owing to its importance in kinetic fractionation (Equation 20) and thus the relative values of  $\delta D$  and  $\delta^{18}O$  in precipitation. Given insufficient observational and physical constraints on its true form, we parameterize the supersaturation as a linear function of temperature (Jouzel and Merlivat, 1984) as discussed above,  $S_i = a + b \times T$ , set  $a = 1$  and tune the slope,  $b$ .

**2.5.1. Primary Tuning Procedure.** Our target for the tuning procedure is the relationship between  $\delta$  values of precipitation. We do not tune the model to match water-isotope values of precipitation to temperature or any other environmental variable. Rather we tune the model via the supersaturation function to yield the proportion

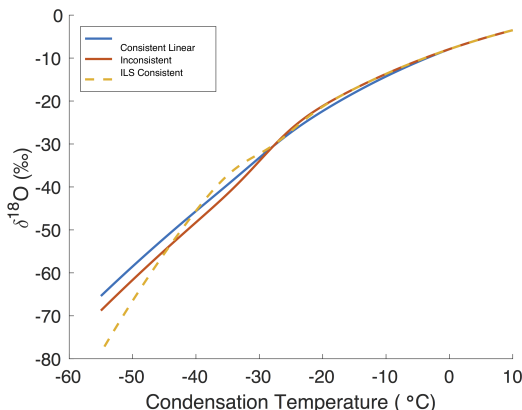


**Figure 13.** Modeled relationship between  $\delta^{18}O$  and condensation temperature using three different supersaturation scenarios described in the text: “consistent linear”, in which the water isotopes and the transport (which determines the  $T_c$ -to- $f$  relationship) experience the same linear supersaturation parameterization, the red curve in Figure 12.b; “inconsistent” in which the water isotopes experience the linear supersaturation parameterization and the transport experiences the supersaturation dictated by the ice-liquid mixing fractions, the blue curve labeled “ILS” in Figure 12.b; and “ILS consistent” in which both the water isotopes and transport experience the “ILS” supersaturation. The “consistent linear” scenario leads to the smoothest, most realistic temperature dependence of  $\delta^{18}O$ .

of kinetic and equilibrium fractionation that results in the observed relationship between  $\delta D$  and  $\delta^{18}O$  in global precipitation. We use a target observational data set, described in Section 2.5.4, that includes water isotope measurements from precipitation around the globe, with its most depleted samples being primarily Antarctic.

The global relationship between  $\delta D$  and  $\delta^{18}O$  has been identified as approximately a slope of 8, as codified in the historical definition of the deuterium excess parameter (Dansgaard, 1964). However the approximate slope of 8 is not fundamental (Craig, 1961); as discussed in Section 1.2 the true relationship is nonlinear (Markle et al., 2017; Uemura et al., 2012). Uemura et al. (2012) find a phenomenological fit between  $\delta' D$  and  $\delta^{18}O$  in a global data set of precipitation (note the logarithmic  $\delta'$  notation following Equation 8). They use a 2<sup>nd</sup> order polynomial fit, which is the basis for the logarithmic deuterium excess parameter (Markle et al., 2017; Uemura et al., 2012) (Equation 4). From Equation 15, we can see that true relationship between  $\delta D$  and  $\delta^{18}O$  depends on the ratio of  $\exp(P\alpha_{tot})/\exp(^{18}\alpha_{tot})$ , where each  $\alpha_{tot}$  itself is a nonlinear function of temperature as outlined throughout Section 2.4. The ratio of exponential

functions can be estimated to any arbitrary degree of accuracy with a polynomial function.

Our modern data set includes several new sets of measurements in addition to those used in Uemura et al. (2012). We find similar coefficients in a 2<sup>nd</sup>-order polynomial fit between  $\delta^{18}O$  and  $\delta'D$  in our larger data set compared to those found by Uemura et al. (2012); we find  $A = -29.2$  and  $B = 8.45$  for the fit (see Equation 3 and Equation 4). Because these coefficients are not significantly different than those previously published, and for consistency with that work, we from here on use the coefficients found by Uemura et al. (2012) ( $A = -28.5$  and  $B = 8.47$ ). We tune the model to match the observed  $d_{ln}$  to  $\delta^{18}O$  relationship in our target data set, using the Uemura et al. (2012) definition of  $d_{ln}$ .

We run the SWIM model to produce an ensemble of temperature trajectories representing a range of possible evaporation and condensation temperatures ( $T_0$  varies from 5 to 25°C;  $T_c$  from 5 to -50°C). We then compare the resulting cloud of modeled  $\delta^{18}O$ ,  $\delta'D$ , and  $d_{ln}$  of precipitation to the observational data set. This is quantified by a 2<sup>nd</sup>-order polynomial fit to the cloud of  $\delta'D$  and  $\delta^{18}O$  values of precipitation resulting from the ensemble of temperature trajectories.

We perform the routine iteratively, adjusting the  $b$  value in the supersaturation parameterization, to minimize the difference between the modeled  $\delta'D$  and  $\delta^{18}O$  relationship and the Uemura et al. (2012) fit to global observations (Equation 4). The model is tuned when the parameters of the polynomial fit of modeled  $\delta'D$  and  $\delta^{18}O$  ( $A^*$  and  $B^*$ ) have the smallest residual to the parameters of the fit to modern observations ( $A$  and  $B$ , given above). This is easily visualized in a plot of  $\delta^{18}O$  and  $d_{ln}$  (e.g. Figure 14.a), as the target  $\delta^{18}O$ -to- $d_{ln}$  relationship is flat buy definition.

For the SWIM model using the local closure assumption and the NCEP/NCAR reanalysis data set for source region correlations, we find an optimal tuning of  $S_i = 1 - b \times T$ , for  $b = 0.00525 \text{ } ^\circ\text{C}^{-1}$  as shown in Figure 14. Model results from rejected values of  $b$  are shown in Figure 15b and c. These values of  $b$  are rejected because the coefficients of the fit to resultant  $\delta'D$  and  $\delta^{18}O$  have larger summed difference to the observe fit's coefficients than the optimal value.

While this tuning process is able to match the observed relationship between  $\delta'D$  and  $\delta^{18}O$  well, there are several limitations and it should not in principle lead to a 2<sup>nd</sup>-order polynomial fit between  $\delta'D$  and  $\delta^{18}O$  that is identical to the observed fit (Equation 4). The primary limitation is the weighting of modeled and target data points.

The individual  $\delta'D$  and  $\delta^{18}O$  values of within our target data set should not receive equal weighting in the comparison to the modeled values. The observational data points represent a variety of timescales from sub-seasonal to several year averages. Further the sites are neither evenly nor randomly distributed over the Antarctic

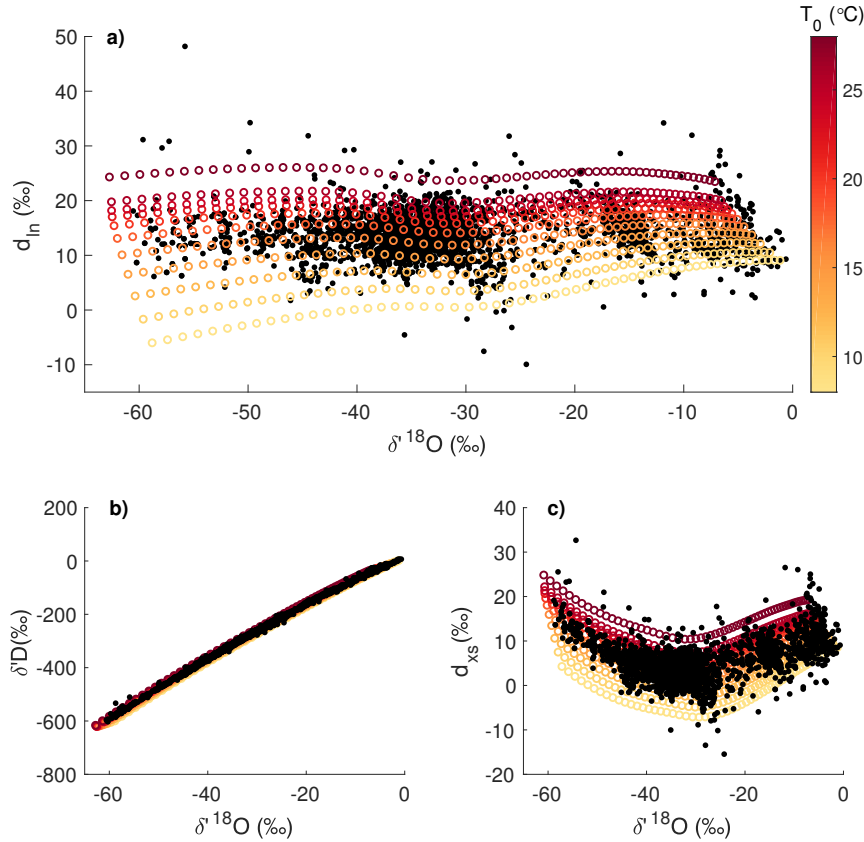


**Figure 14.** Tuning SWIM with linear supersaturation parameterization. **a)** The modeled  $\delta^{18}O$  and  $d_{ln}$  of precipitation (colored circles), for a range of condensation and evaporation temperatures. Color shading shows source region evaporation temperature in °C. Black dots are the target data set as described in the text. Modeled results are for the optimized supersaturation parameterization ( $S_i = 1 - b \times T$ ,  $b = 0.00525^\circ\text{C}^{-1}$ ) using the local closure assumption and the NCEP/NCAR reanalysis data set for source region correlations. **b)** Same as panel **a)** for the modeled and target  $\delta^{18}O$  and  $\delta D$  of precipitation. **c)** Same as panel **a)** for the modeled and target  $\delta^{18}O$  and  $d_{xs}$  of precipitation.

continent, which may bias the observational data set toward the climate conditions of oversampled sites.

Further, the sites represented in the observational data set have different moisture source distributions. As shown in Figure 16, the mean latitude of evaporation for

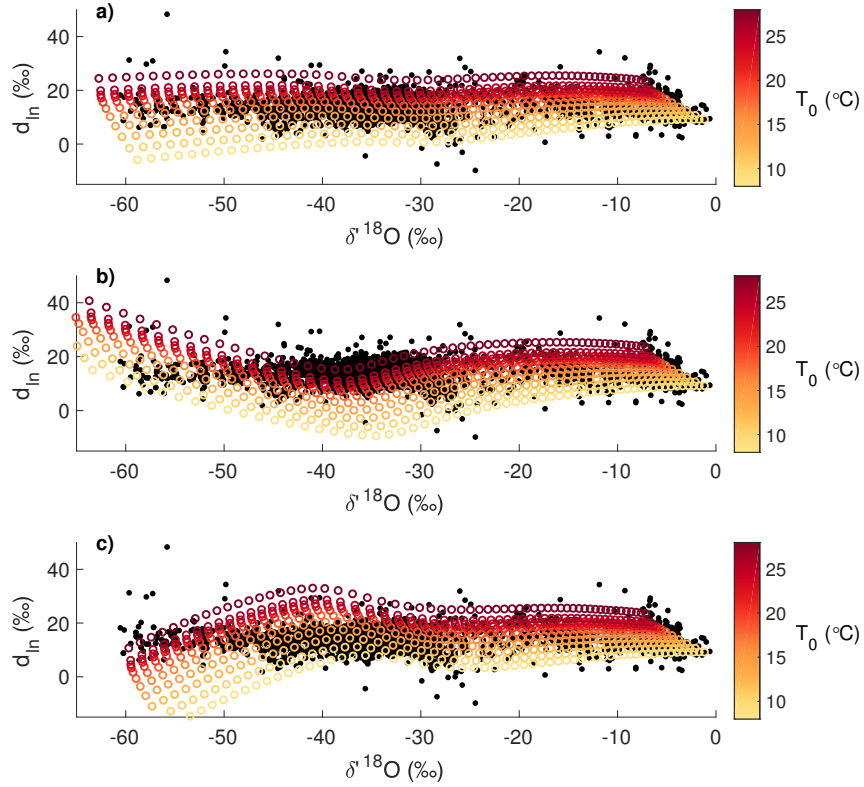


**Figure 15.** Comparison of tuned and rejected supersaturation parameterizations,  $S_i = 1 - b \times T$ . **a)** Tuned example:  $b = 0.00525^\circ\text{C}^{-1}$ . Same as in Figure 14a. The modeled  $\delta^{18}\text{O}$  and  $d_{ln}$  of precipitation (colored circles) and target data set (black dots). Color shading shows source region evaporation temperature in  $^\circ\text{C}$ . **b)** Same as panel **a)**, but for a rejected tuning:  $b = 0.003^\circ\text{C}^{-1}$ . The modeled  $d_{ln}$  curve upward strongly with  $\delta^{18}\text{O}$ , incongruently with the target data. **c)** Same as panel **a)**, but for another rejected tuning:  $b = 0.007^\circ\text{C}^{-1}$ . The modeled  $d_{ln}$  curve downward strongly with  $\delta^{18}\text{O}$  and incongruently with the target data.

moisture, and thus average evaporation temperature, can vary between different Antarctic sites. Thus the appropriate weighting of model realizations with different initial  $T_0$  should vary within our cost function depending on the site of the target data. Without knowing the true moisture source distribution for each site *a priori* it is difficult to assign appropriate weighting to the cost function. This issue can

be understood visually in Figure 14. While the definition of  $d_{ln}$  results in a flat relationship with  $\delta^{18}O$  in the global average, we should expect that the modeled precipitation along lines of equal  $T_0$  (circles with the same color in Figure 14) may curve somewhat as some sites will have different average evaporation temperatures. This curvature should be small however, as moisture-tagged GCM results (Figure 16) suggest the difference in average moisture evaporation latitude between Antarctic site is modest. In spite of these limitations the tuning procedure reproduces the observed isotope relationships well. But we should not expect that the simple model fit the observed data perfectly.

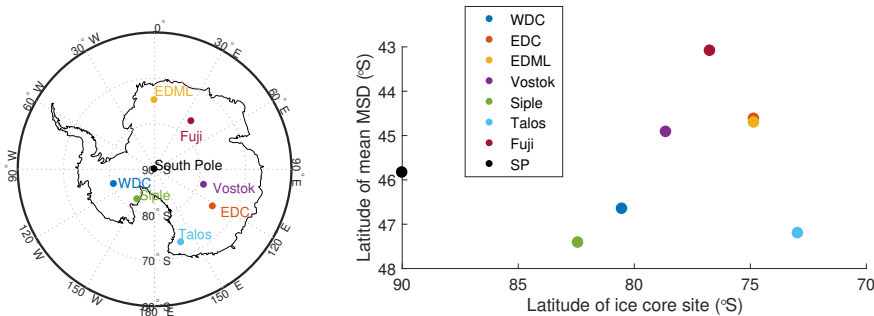


**Figure 16.** Left) Map of Antarctica showing ice-core sites mentioned throughout the text. Right) Weighted mean latitude of moisture source distributions (MSDs, as shown in Figure 4 for each ice-core site. Moisture source distributions are calculated from a water tagged control run of CAM4 as described in Markle et al. (2017).

We do not tune the model to observations of  $^{17}O_{xs}$ , owing to insufficient target data. However, due to its sensitivity to kinetic fractionation, the  $^{17}O_{xs}$  of precipitation strongly depends on the parameterization of supersaturation (Schoenemann et al., 2014). A comparison of surface  $^{17}O_{xs}$  measurements to our model results with optimized  $b$ , as well as two rejected values of  $b$  are shown in Figure 17. Given large uncertainties in the limited  $^{17}O_{xs}$  measurements available, this is not as strong a constraint on the model as the observed  $d_{ln}$ .

The model tuning is not particularly sensitive to the reanalysis data set used for correlations of the initial evaporation conditions nor the season of evaporation. The model is however sensitive to which closure assumption is used. The use of different fractionation factors or diffusivities within the model will require different values of  $b$  for optimal tuning.

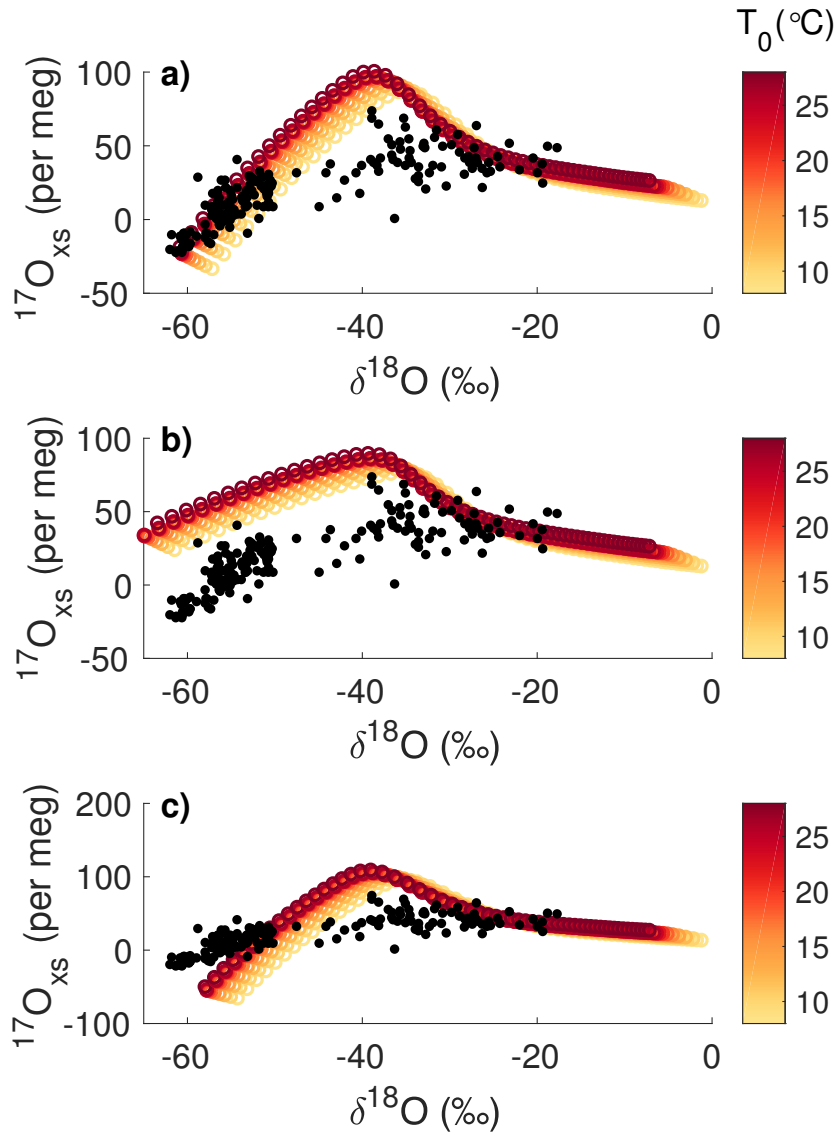


**Figure 17.** Same as in Figure 15, but for the modeled  $\delta^{18}\text{O}$  and  $^{17}\text{O}_{xs}$  of precipitation, for three possible supersaturation parameterizations: panel a)  $b = 0.00525^\circ\text{C}^{-1}$ ; panel b)  $b = 0.003^\circ\text{C}^{-1}$ ; and panel c)  $b = 0.007^\circ\text{C}^{-1}$ .

2.5.2. *Nonlinear supersaturation parameterization.* The temperature dependence of the supersaturation function is important for the deuterium excess which quantifies the amount of kinetic fractionation that occurs during the integrated pathway. We tune the supersaturation to match the modern mean state deuterium excess as described above. When using the model to interpret out-of-sample intervals, such as the Last Glacial Maximum, the temperature dependence of the supersaturation becomes critical.

We explore the sensitivity of the model to a nonlinear parametrization of supersaturation with temperature,  $S_i = a - b \times T - c \times T^2$ . Only very small values of the second-order term,  $c$ , those of order  $5 \times 10^{-6} \text{ }^\circ\text{C}^{-2}$ , are reconcilable with the observed  $\delta^{18}\text{O}$  to  $\delta D$  (or  $\delta^{18}\text{O}$  to  $d_{ln}$ ) relationship. Higher-order dependence (e.g. terms with  $T^3$  and higher orders) is vanishingly small. However, if the physical source of the high supersaturation at very cold conditions is related to the absence of condensation nuclei there may be reason to think that supersaturation won't continue to linearly increase as temperature decreases. There will eventually be diminishing returns as the atmosphere becomes increasingly clean. In such a case a small, but positive  $c$  parameter that gradually decrease the slope in  $S_i$  with decreasing temperature could be expected (e.g. Figure 18). A  $c$  value of  $1 \times 10^{-6} \text{ }^\circ\text{C}^{-2}$ , leads to model results with a marginally flatter  $\delta^{18}\text{O}$ -to- $d_{ln}$  relationship (Figure 19) than the linear parameterization (Figure 14). The modern data cannot readily distinguish whether the added complexity of the nonlinear parameterization is a better fit than the simple linear parameterization. For this reason, the linear parameterization may be the most justifiable choice, though the uncertainty associated with this parameterization on temperature reconstructions will be examined below.

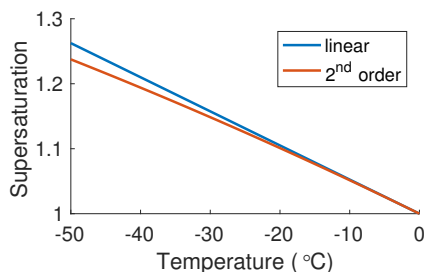


**Figure 18.** Supersaturation of vapor over ice as a function of two different parameterizations: the traditional linear parameterization,  $S_i = a - b \times$ , with tuned  $b = 0.00525 \text{ }^\circ\text{C}^{-1}$  (in blue); and a 2<sup>nd</sup>order polynomial parameterization,  $S_i = a - b \times T - c \times T^2$ , with tuned values  $b = 0.00525 \text{ }^\circ\text{C}^{-1}$  and  $c = 0.0001 \text{ }^\circ\text{C}^{-2}$ .

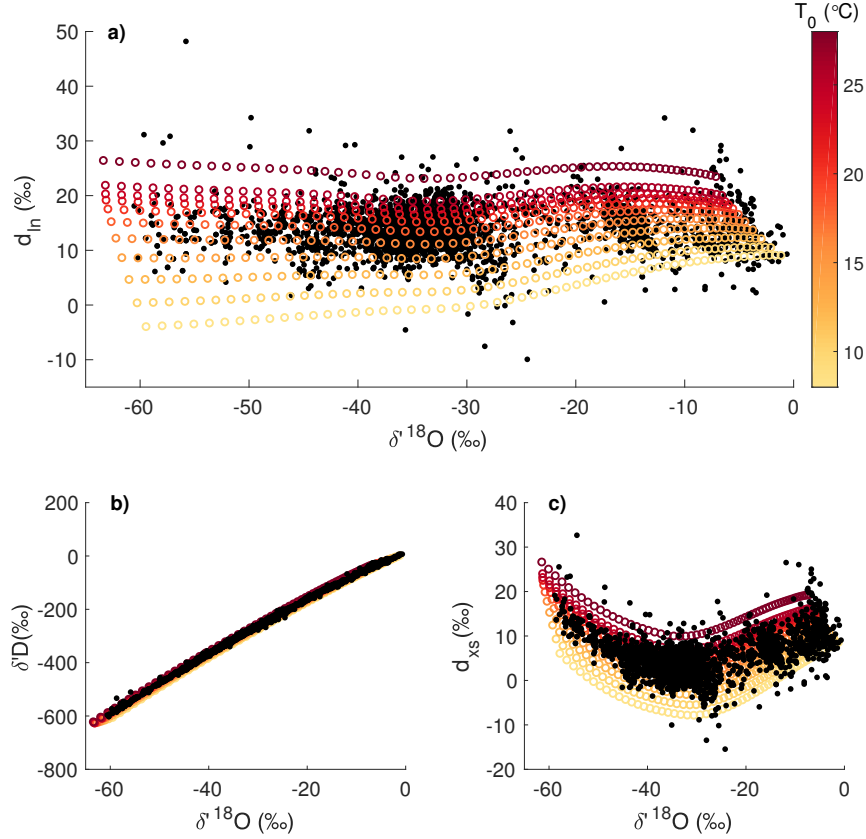


**Figure 19.** Tuning SWIM with non-linear supersaturation parameterization. Same as Figure 14, but using a 2<sup>nd</sup> order polynomial parameterization for the supersaturation,  $S_i = a - b \times T - c \times T^2$ , with tuned values  $b = 0.00525^\circ\text{C}^{-1}$  and  $c = 0.0001^\circ\text{C}^{-2}$ , as shown in Figure 18.

2.5.3. *Alternate supersaturation considerations.* In principle it is possible to solve for a function of the supersaturation such that the modeled slope,  $\partial\delta^D/\partial\delta^{18}O$ , is the same nonlinear function of  $\delta^{18}O$  as the best fit to modern data encapsulated by the  $d_{ln}$  definition. This can be achieved, following Equation 15, by equating  $D^{\alpha_{tot} - 1/18\alpha_{tot} - 1}$  to the observed nonlinear slope of  $\partial\ln(DR)/\partial\ln(^{18}R)$ , substituting each  $\alpha_{tot}$  for the combined equations outlined in Section 2.4 which depend on the temperature-dependent fractionation factors and  $S_i$ , and finally solving the resultant quadratic equation for  $S_i$  as a function of the fractionation factors and the observed slope of  $\partial\ln(DR)/\partial\ln(^{18}R)$ . There are two issues with such an approach in practice. The first is that the influence of  $S_i$  on fractionation in the model varies with the fraction of ice in the cloud. The

solutions to the above problem are not stable as the ice fraction approaches zero. Secondly, as discussed above, the modern data do not reflect a consistent set of initial conditions, or a single moisture transport pathway. Moisture reaching any single location in Antarctica has a broad distribution of evaporation source latitudes and temperatures, and different locations have overlapping but possibly distinct moisture source distributions. The observed modern slope,  $\partial\delta^D/\partial\delta^{18}O$ , reflects the mixing of many different evaporation source temperatures, and a mix whose relative weighting likely varies as a function of  $\delta^{18}O$ . Thus tuning the model to reproduce this observed slope exactly, without *a priori* knowledge of the appropriate weighting, is not justified.

2.5.4. *Compilation of global precipitation data.* Throughout this study we use a compilation of water isotope measurements from surface snow to evaluate the Simple Water-Isotope Model. The bulk of this compilation is that published by (Masson-Delmotte et al., 2008). We include additional published surface snow and precipitation measurements from the GNIP database (IAEA, 2001), from surface traverses at Dome A (Pang et al., 2015; Xiao et al., 2013), Dahe et al. (1994), and a  $^{17}O_{xs}$  compilation from Schoenemann et al. (2014).

We also include previously unpublished measurements from a transect of snow pits and shallow firn cores across the main divide of the West Antarctic Ice Sheet. Samples from five sites were collected spanning 80 km across the ice flow divide in the 2012/13 summer season. Samples were measured at IsoLab, University of Washington, Seattle WA, USA. Measurement techniques are described in Markle et al. (2017). Measurements were made using laser spectroscopy (Picarro L2120-i analyzer). Data are reported relative to the VSMOW (Vienna Standard Mean Ocean Water) standard, and normalized to SLAP. Finally we include previously unpublished surface snow measurements from the Juneau Icefield in South East Alaska. Snow samples were collected from shallow snow pits and fresh precipitation over several summer seasons (2012, 2015, 2016) and measured in the field and at the University of Alaska, Fairbanks, using laser spectroscopy (LGR DLT-100 v2).

### 3. MODERN RELATIONSHIPS

The modeled relationship between the water-isotope ratios of precipitation and condensation temperature for pathways with a range of initial evaporation temperatures, is shown in Figure 20. We convert the modeled condensation temperature to Antarctic surface temperatures following the method described in Section 2.1.3. We show the modeled relationship between the  $\delta^{18}O$  and  $\delta D$  of precipitation against Antarctic surface temperatures in Figure 21. We compare the modeled results against a compilation of modern surface temperature and surface precipitation isotopic values (Masson-Delmotte et al., 2008). The model shows excellent agreement with

the observed water isotope-temperature relationship. Note that we only tune the model for the observed relationship between  $\delta^{18}O$  and  $\delta D$ , not their relationships to temperature.

There is sensitivity in the modeled isotope-surface temperature relationship arising from the conversion of condensation temperature to surface temperature discussed in Section 2.1.3. The light blue line in Figure 22 shows the model results using the  $T_c$ -to- $T_s$  relationship described in Section 2.1.3. The dashed line shows the result if we assume that the condensation temperature follows the peak inversion temperature following Jouzel and Merlivat (1984). For the coldest sites (where the inversion is generally strongest), this assumption results in isotopic values that are on average less depleted than observed and generally defines the upper limit of the observations. The solid black line in Figure 22 shows the model results if we assume that the condensation temperature equals the surface temperature,  $T_c = T_s$ . The comparison shown in Figure 22 is consistent with the arguments in Section 2.1.3. The peak inversion temperature sets an upper limit for possible condensation temperatures, however significant condensation occurs at temperatures colder than the peak inversion but warmer than the surface. At warmer Antarctic surface temperatures (those approaching  $0^\circ\text{C}$ ), the inversion is weak and condensation occurs at temperatures aloft that are colder than the surface.

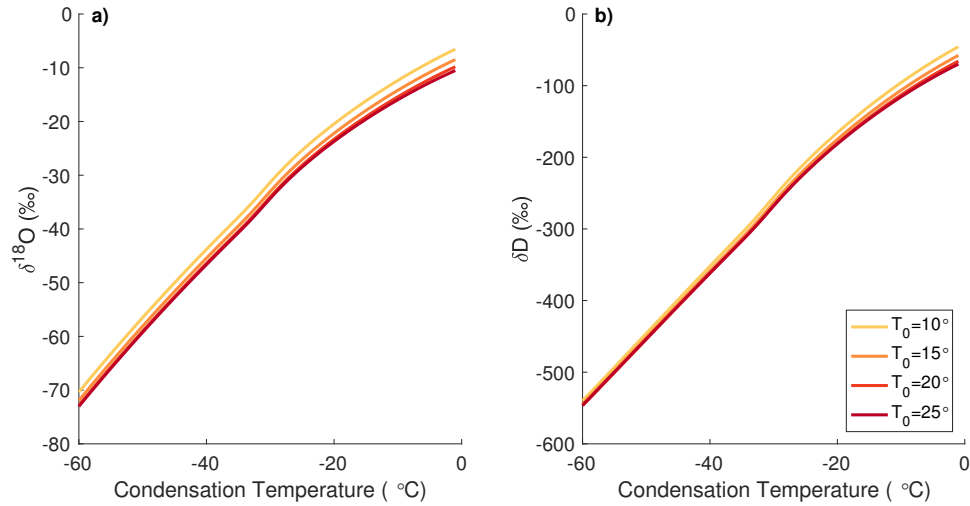


**Figure 20.** **a)** Modeled relationship between condensation temperature and  $\delta^{18}O$  for a range of initial evaporation temperatures ( $T_0$ , colored lines). **b)** Same as panel **a)** but for the modeled relationship between condensation temperature and  $\delta D$  of precipitation.

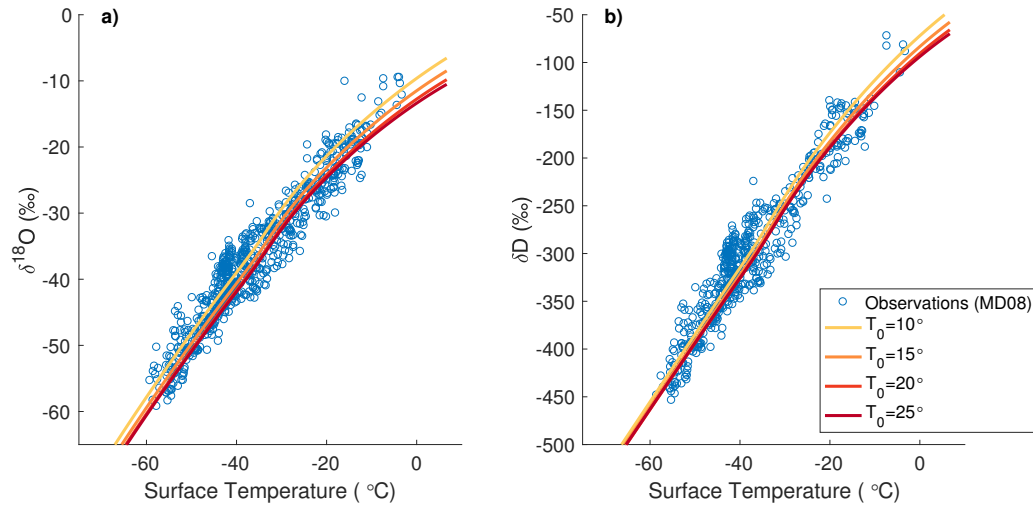


**Figure 21.** **a)** Modeled relationship between surface temperature and  $\delta^{18}\text{O}$  for a range of initial evaporation temperatures ( $T_0$ , colored lines). Observations of modern surface temperatures and  $\delta^{18}\text{O}$  of precipitation from a compilation of Antarctic surface samples (Masson-Delmotte et al., 2008) (MD08, blue circles). **b)** Same as panel **a)** but for the modeled and observed relationship between surface temperature and  $\delta\text{D}$  of precipitation.

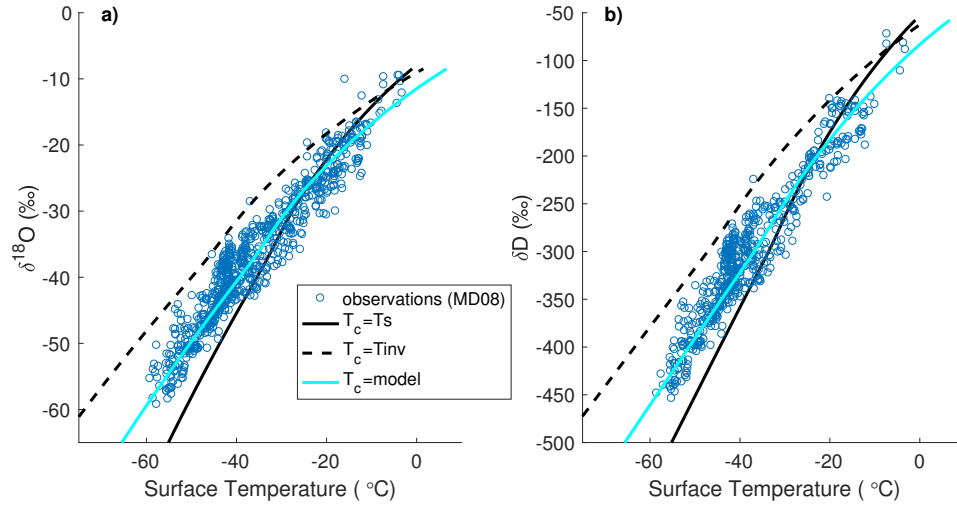


**Figure 22.** Comparison of modeled  $\delta^{18}\text{O}$  to surface temperature relationship for different possible scalings between surface temperature and condensation temperature. Observations of modern surface temperatures and  $\delta^{18}\text{O}$  (panel **a**) and  $\delta\text{D}$  (panel **b**) of precipitation from a compilation of Antarctic surface samples (Masson-Delmotte et al., 2008) (MD08, blue circles). Water isotopes are modeled from an initial evaporation temperature,  $T_0 = 15^\circ\text{C}$ , to a series of condensation temperatures, which are then converted to surface temperature assuming: the scaling described in Section 2.1.3,  $T_c = 0.75T_s - 6$  (cyan line); the condensation temperature equals the surface temperature ( $T_c = T_s$ , black line); and condensation temperature equals the inversion temperature ( $T_{inv} = T_s$ , black dashed line), as used elsewhere in the literature (Jouzel and Merlivat, 1984; Masson-Delmotte et al., 2008).

4. TEMPERATURE SENSITIVITY

To investigate the sensitivity of water-isotope ratios of Antarctic precipitation to site and source conditions, we run SWIM through a large ensemble of pathways defined by all likely values of  $T_0$  and  $T_c$ . We define the sets of possible evaporation temperatures,  $T_0 = \{T_{0(1)}, T_{0(2)}, \dots, T_{0(m)}\}$ , and condensation temperatures,  $T_c = \{T_{c(1)}, T_{c(2)}, \dots, T_{c(n)}\}$ . These sets of boundary conditions define a model parameter space:

$$\mathbf{T}_{m,n} = \begin{pmatrix} \vec{T}_{1,1} & \vec{T}_{1,2} & \cdots & \vec{T}_{1,n} \\ \vec{T}_{2,1} & \vec{T}_{2,2} & \cdots & \vec{T}_{2,n} \\ \vdots & \vdots & \ddots & \vdots \\ \vec{T}_{m,1} & \vec{T}_{m,2} & \cdots & \vec{T}_{m,n} \end{pmatrix}$$

in which each element of  $\mathbf{T}$  is a temperature trajectory

$$\vec{T}_{i,j} = (T_{0(i)}, T_{0(i)} - dT, T_{0(i)} - 2dT, \dots, T_{c(j)}).$$

SWIM is then run for each temperature pathway in the ensemble, generating a state space of the water isotopic values of precipitation for all combinations of boundary conditions. For example, the  $\delta^{18}O$  of precipitation under all boundary conditions is an  $m \times n$  matrix,

$$\delta^{18}\mathbf{O}_{m,n} = \begin{pmatrix} \delta^{18}O_{1,1} & \delta^{18}O_{1,2} & \cdots & \delta^{18}O_{1,n} \\ \delta^{18}O_{2,1} & \delta^{18}O_{2,2} & \cdots & \delta^{18}O_{2,n} \\ \vdots & \vdots & \ddots & \vdots \\ \delta^{18}O_{m,1} & \delta^{18}O_{m,2} & \cdots & \delta^{18}O_{m,n} \end{pmatrix}$$

whose elements,  $\delta^{18}O_{i,j}$ , are the modeled isotopic values of precipitation resulting from the temperature trajectory  $\vec{T}_{i,j}$ . The sampling of the parameter space can be run at arbitrarily high resolution in the temperature parameter space;  $\Delta T_0 = T_{0(i)} - T_{0(i+1)}$  and  $\Delta T_c = T_{c(j)} - T_{c(j+1)}$ . Results presented here are run at a resolution of  $\Delta T_0 = \Delta T_c = 0.1^\circ C$ , requiring approximately 200,000 modeled temperature trajectories to fill the parameter space of  $0^\circ C \leq T_0 \leq 25^\circ C$ ,  $-80^\circ C \leq T_c \leq 0^\circ C$ .

The modeled isotopic state spaces are easily visualized as functions of evaporation and condensation temperature. We present these results as “maps” whose  $x$  and  $y$  coordinates are the condensation and evaporation temperatures, respectively, and whose  $z$  or color dimension is the  $\delta^{18}O$  of precipitation (Figure 23),  $\delta D$  of precipitation (Figure 24),  $d_{xs}$  of precipitation (Figure 26),  $d_{ln}$  of precipitation (Figure 25), and  $^{17}O_{xs}$  of precipitation (Figure 27).

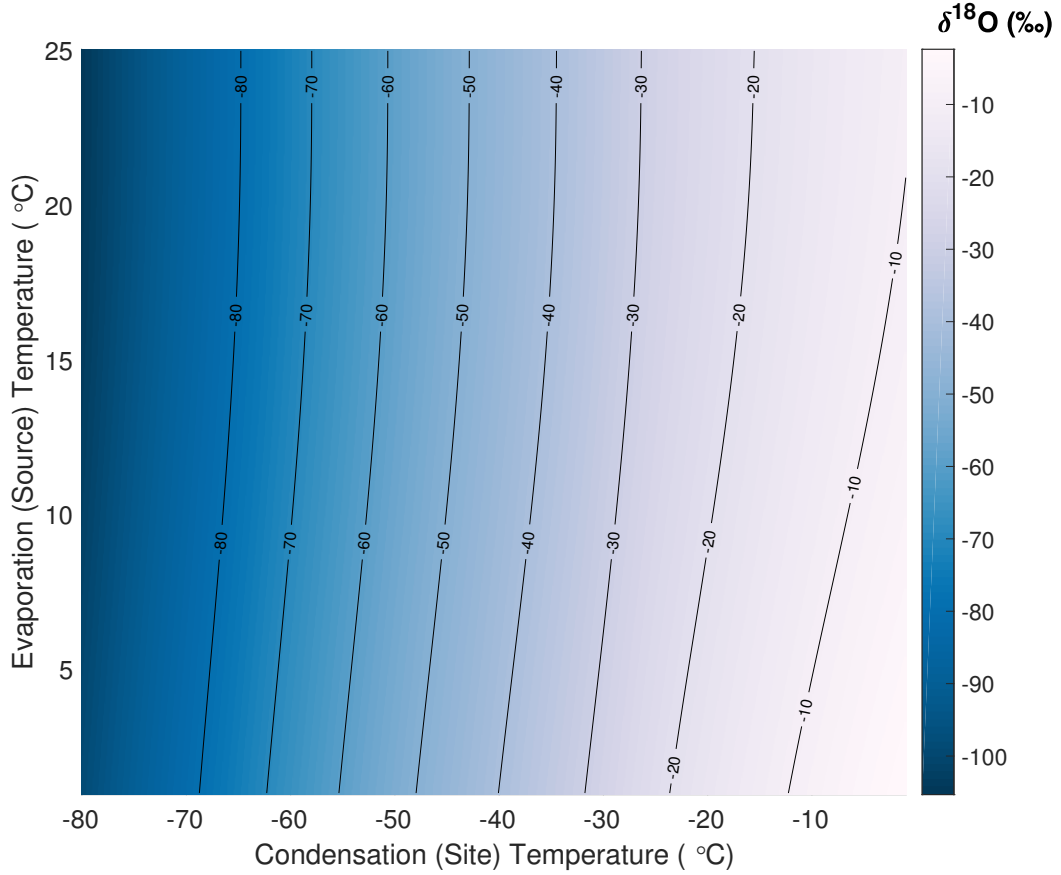


**Figure 23.** The  $\delta^{18}O$  state space as a function of the boundary conditions  $T_c$ , the condensation temperature at a hypothetical ice-core site, and  $T_0$ , the evaporation temperature at the moisture source. Surface shading and contour lines are the  $\delta^{18}O$  of precipitation in units of ‰.

In Figure 23, one can see that the predominant slope in the  $\delta^{18}O$  “surface” is in the direction of the condensation temperature (the  $x$ -axis), that is the lines of equal  $\delta$  values are largely parallel to the evaporation temperature axis. This emphasizes the strong dependence of  $\delta^{18}O$  on the condensation temperature which underlies its widespread use as a paleotemperature proxy. Indeed  $\delta^{18}O$  is nearly linear with condensation temperature. The map for the  $\delta D$  of precipitation (Figure 24) is qualitatively similar to that of  $\delta^{18}O$ ; both are quite linear in with condensation site temperature. However the slopes are not strictly linear. The slope of  $\delta^{18}O$  in precipitation to condensation temperature clearly depends on the absolute value of the

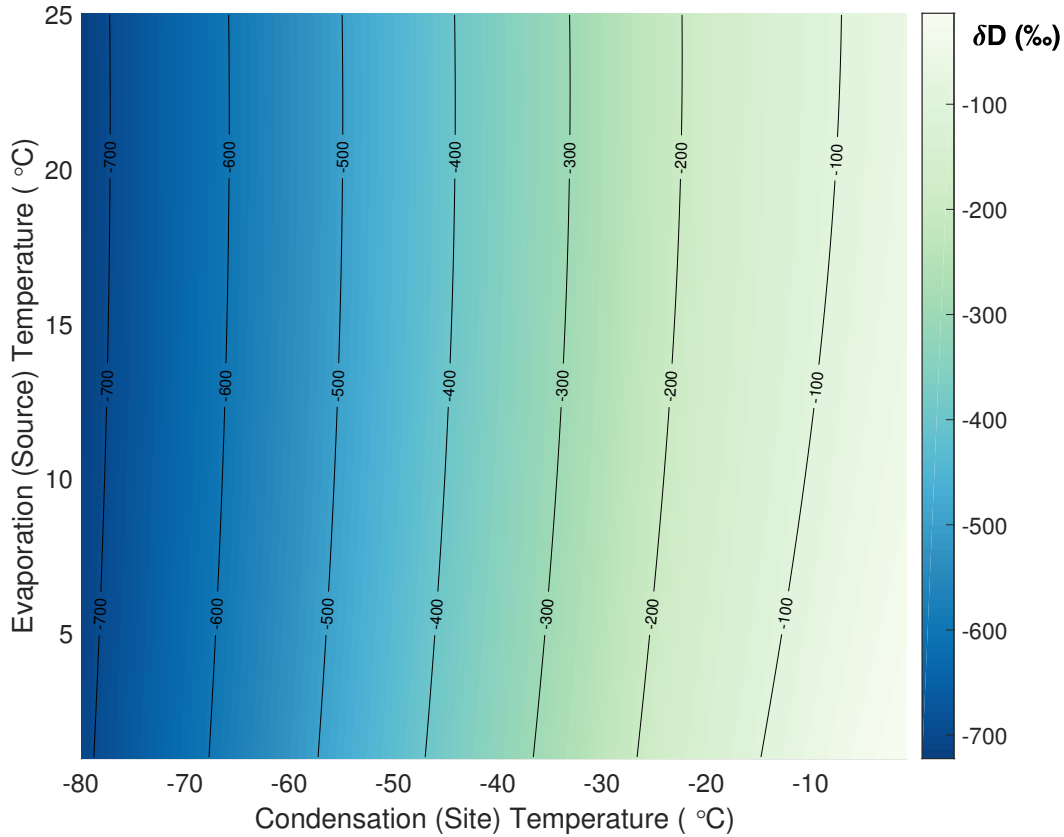


**Figure 24.** The  $\delta D$  state space as a function of the boundary conditions  $T_c$ , the condensation temperature at a hypothetical ice-core site, and  $T_0$ , the evaporation temperature at the moisture source. Surface shading and contour lines are the  $\delta D$  of precipitation in units of ‰.

condensation temperature; at lower condensation temperatures the contour lines of  $\delta^{18}O$  in precipitation become closer together. Further the slope of  $\delta^{18}O$  to evaporation source temperature depends on the absolute values of both the evaporation and condensation temperatures. This can be seen in the changing angle of the contour lines with respect to either axis.

The modeled surface of the  $d_{xs}$  relationship is much less mono-axial compared to that of  $\delta^{18}O$ , showing strong slopes along both the condensation temperature and evaporation temperature axes (Figure 26). The modeled  $d_{ln}$  surface also shows dependence on both the condensation temperature and evaporation temperature

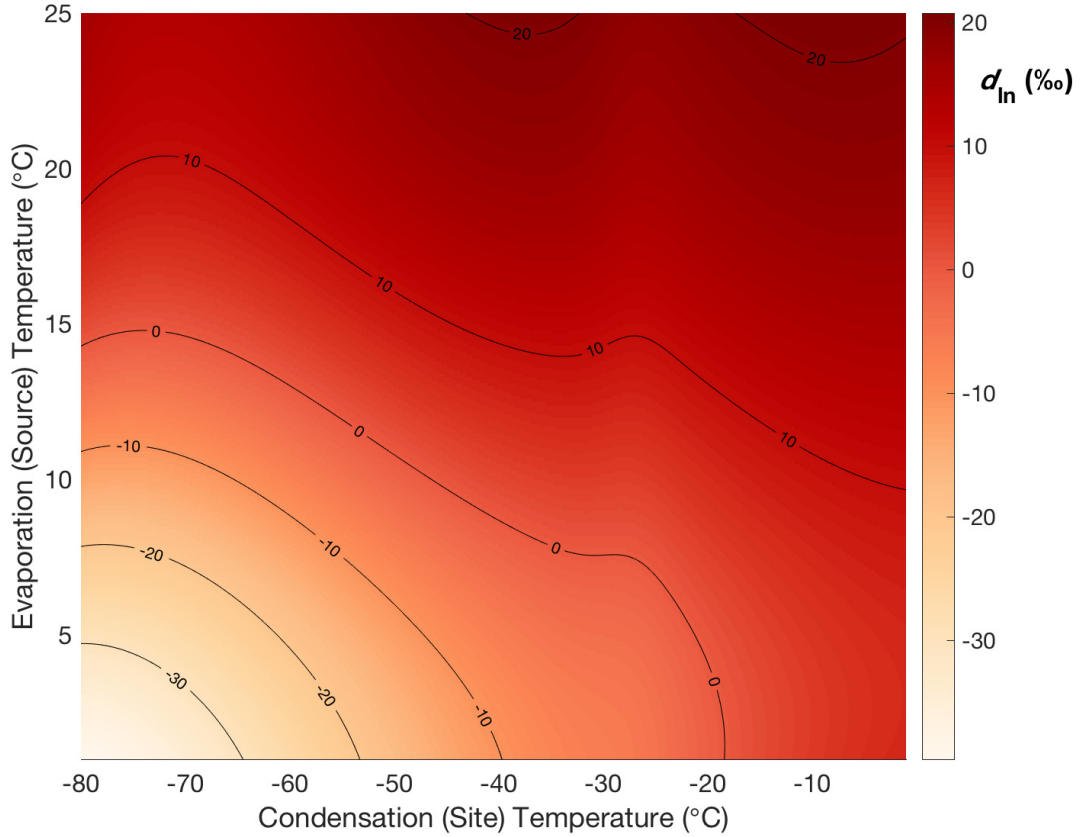


**Figure 25.** The  $d_{ln}$  (Equation 4) state space as a function of the boundary conditions  $T_c$ , the condensation temperature at a hypothetical ice-core site, and  $T_0$ , the evaporation temperature at the moisture source. Surface shading and contour lines are the  $d_{ln}$  of precipitation in units of ‰.

axes (Figure 25). In comparison to  $d_{xs}$ , the lines of equal  $d_{ln}$  depend much more strongly on the evaporation temperature. In particular, at the coldest condensation temperatures, the  $d_{xs}$  surface slopes strongly with the condensation temperature. This reflects the strong influence of kinetic fractionation and the nonlinear bias built in to the historical linear definition of deuterium excess (Markle et al., 2017; Uemura et al., 2012). These results demonstrate how the logarithmic definition of the deuterium excess parameter ( $d_{ln}$ ) is a much more faithful proxy for source-region

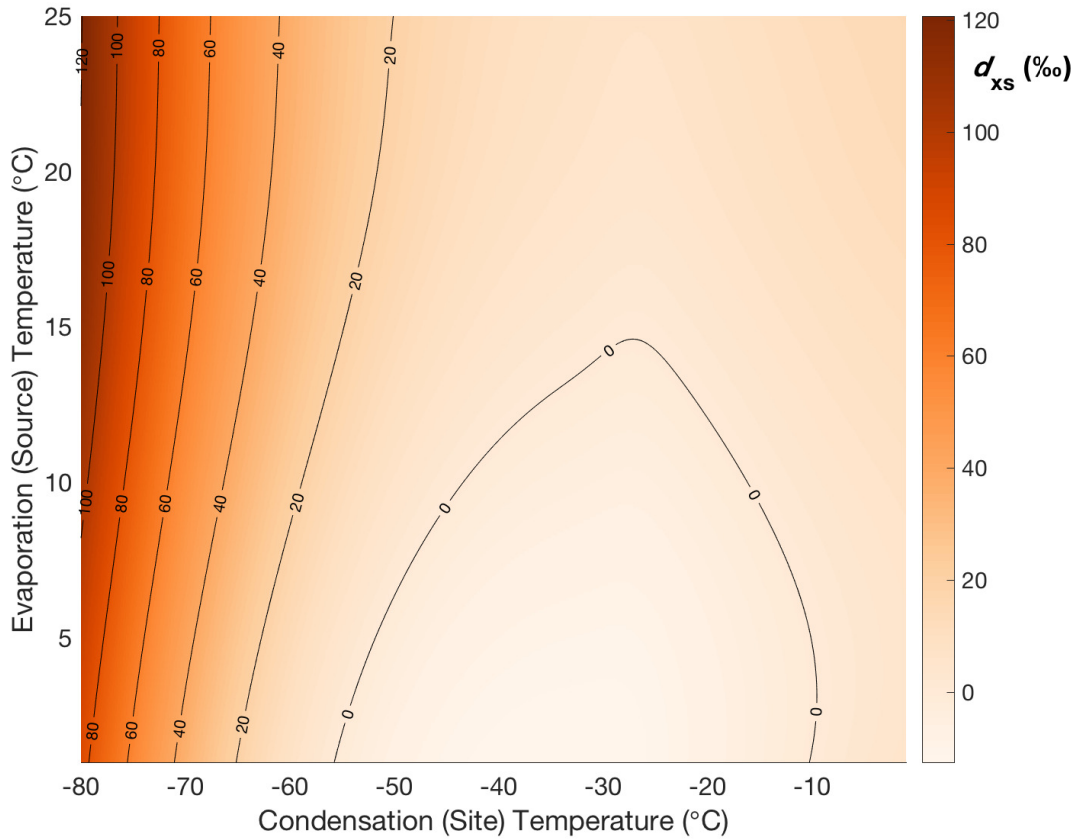


**Figure 26.** The  $d_{xs}$  ( $d_{xs} = \delta D - 8 \times \delta^{18}O$ ) state space as a function of the boundary conditions  $T_c$ , the condensation temperature at a hypothetical ice-core site, and  $T_0$ , the evaporation temperature at the moisture source. Surface shading and contour lines are the  $d_{xs}$  of precipitation in units of ‰.

conditions than the linear definition ( $d_{xs}$ ). Even at very low condensation temperatures, the  $d_{ln}$  still depends strongly on the initial evaporation temperature, whereas the linear  $d_{xs}$  becomes almost solely dependent on condensation temperature.

The modeled isotope surfaces presented here are not linear planes, nor necessarily monotonic along either axis. The linear inversion technique described in Section 1.1 is based on the linearization of the relationships between  $\delta^{18}O$ ,  $d_{xs}$ , condensation temperature, and evaporation temperature. It assumes the  $\beta$  and  $\gamma$  parameters in Equations 1 and 2, are fixed and linear for the range of reconstructed  $\Delta T_{site}$  and  $\Delta T_{source}$ .

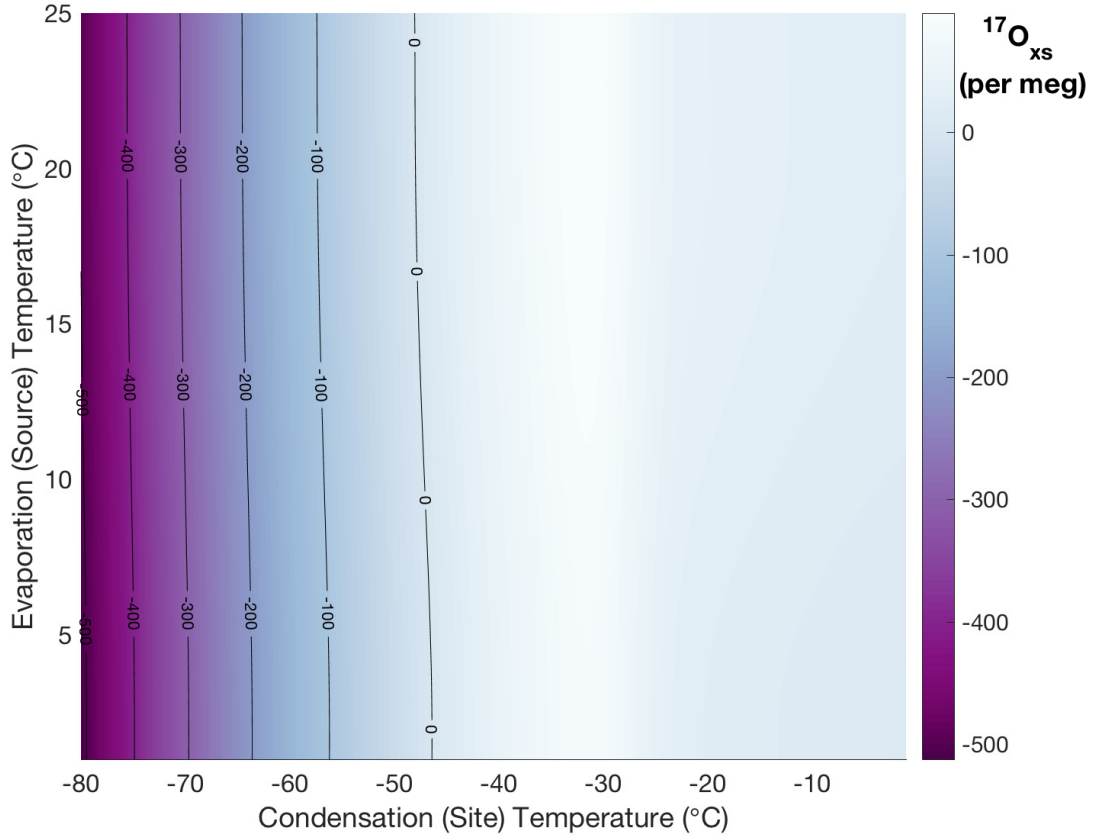


**Figure 27.** The  $^{17}O_{xs}$  state space as a function of the boundary conditions  $T_c$ , the condensation temperature at a hypothetical ice-core site, and  $T_0$ , the evaporation temperature at the moisture source. Surface shading and contour lines are the  $^{17}O_{xs}$  of precipitation in units of per meg.

Our results in Figures 23 and 26 demonstrate that the assumption of linearity in these slopes is problematic. The parameters  $\gamma_1$  and  $\gamma_2$  in Equation 1, represent the slopes  $\frac{\partial \delta^{18}O}{\partial T_c}$  and  $\frac{\partial \delta^{18}O}{\partial T_0}$  in Figure 23, respectively. The slope of  $\delta^{18}O$  along the condensation temperature axis,  $\frac{\partial \delta^{18}O}{\partial T_c}$ , remains fairly constant through most of the range though is clearly somewhat nonlinear at warmer condensation temperatures. The evaporation temperature dependence,  $\frac{\partial \delta^{18}O}{\partial T_0}$ , also varies across the surface.

These same considerations are far more dramatic for the  $d_{xs}$  of Antarctic precipitation. As seen in Figure 26, the slopes  $\frac{\partial d_{xs}}{\partial T_c}$  and  $\frac{\partial d_{xs}}{\partial T_0}$  (equivalent to  $\beta_1$  and  $\beta_2$  in Equation 2, respectively), are strikingly variable across the surface. Indeed  $d_{xs}$

has a saddle at moderate condensation site temperatures meaning  $\frac{\partial d_{xs}}{\partial T_c}$  changes sign. One can see in Figures 23 and 26 that, depending on the evaporation and condensation temperatures appropriate to a site, the use of constant  $\beta$  and  $\gamma$  parameters in isotope-based temperature reconstructions may be valid only under very narrow ranges of  $\Delta T_{site}$  and  $\Delta T_{source}$ .

The issue of variable slopes is implicit in previous work. (Uemura et al., 2012) for example, following (Stenni et al., 2010) used an isotope model to calculate the relevant  $\beta$  and  $\gamma$  parameters for several East Antarctic ice-core sites. Using the same model, they calculated different scalings for each site due to each site's different environmental conditions. By assuming constant slopes for each site, they do not consider the possibility that one site's conditions may have been more like another's in the past. Recognizing this as well as the inability of their model to simultaneously match observed site temperature and  $\delta$  values, Uemura et al. create several reconstructions for the Dome Fuji site utilizing different linearizations of the model. They do not however attempt a reconstruction that accounts for the nonlinearities in the water isotope-temperature relationships.

Using the established isotope temperature reconstruction framework (Equations 1 and 2), where relative isotopic change (e.g.  $\Delta\delta^{18}O$  and  $\Delta d_{xs}$ ) is considered to be driven by relative change in the site and source conditions ( $\Delta T_{site}$  and  $\Delta T_{source}$ ), the solution to the above issues is not obvious. The nonlinearities in the slopes of the isotope surfaces depend on the absolute condensation and evaporation temperatures. These absolute temperatures are not known *a priori*; indeed they are the target of the reconstruction. Accounting for these nonlinearities in the current framework is thus difficult. We next present a novel water isotope-based temperature reconstruction framework, which utilizing SWIM, takes into account all the inherent non-linearities in the water-isotope fractionation process as represented within the model.

## 5. NONLINEAR TEMPERATURE RECONSTRUCTIONS

**5.1. Reconstruction method.** In analogy to the established linear temperature reconstruction framework (Equations 1 and 2), the results of the SWIM presented in Figures 23 through 27 are equivalent to a system of nonlinear equations that relate the isotopic values of precipitation to  $T_0$  and  $T_c$ . The full set of nonlinear relationships that underlies the modeled isotope surfaces are encapsulated by the numerical model described in Section 2. We consider the sets of evaporation and condensation temperatures  $\mathbf{T}_0$  and  $\mathbf{T}_c$ , respectively, that form the boundary conditions of  $\mathbf{T}$ . Each element of  $\delta^{18}\mathbf{O}$ , has a corresponding element in  $\mathbf{T}_0$  and  $\mathbf{T}_c$ . We can then project either boundary condition onto any pair of axes defined by any two isotope state spaces, e.g.  $\delta^{18}\mathbf{O}$  and  $d_{ln}$ . These define a new set of "maps" whose  $x$  and  $y$  axes are, for example,  $\delta^{18}O$  and  $d_{ln}$ , and whose  $z$  axes are  $T_c$  and  $T_0$  as shown in Figure 28.

To reconstruct  $T_c$  and  $T_0$  we simply use a pair of  $\delta^{18}O$  and  $d_{ln}$  measurements and interpolate to the modeled relationship between  $\delta^{18}O$  and  $d_{ln}$ , and  $T_c$  or  $T_0$ . This is in essence a lookup table; one uses the water-isotope coordinates to read the value of  $T_c$  and  $T_0$  off the map in Figure 28. For example, a snow sample from a site with a  $\delta^{18}O$  value of  $-30\text{‰}$  and a  $d_{ln}$  value of  $0\text{‰}$ , has a condensation temperature of  $\approx -29.6^\circ\text{C}$ . While previous reconstruction methods (e.g. (Kavanaugh and Cuffey, 2002; Stenni et al., 2010; Vimeux et al., 2002)) linearize the slopes calculated by a water-isotope model, this method accounts for the nonlinearities in the slopes.

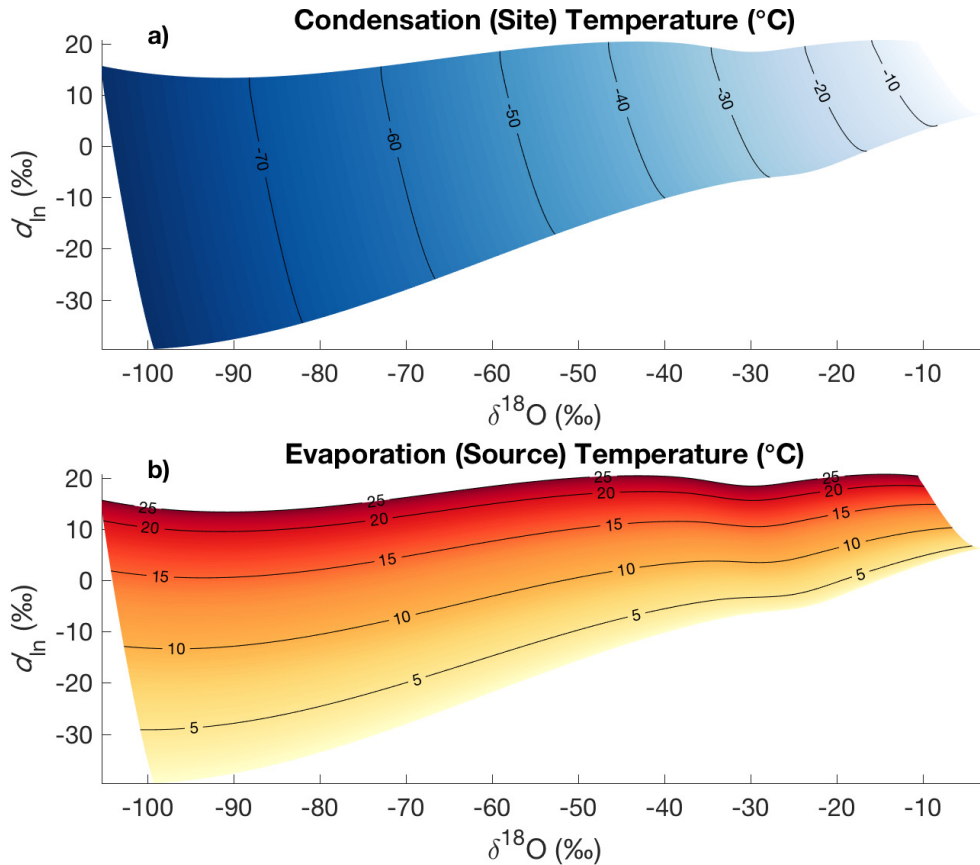


**Figure 28.** Boundary condition surfaces of against modeled  $d_{ln}$  and  $\delta^{18}O$  of precipitation. **a)** Surface shading and contours show condensation site temperature,  $T_c$  in  $^\circ\text{C}$ , as a function of  $d_{ln}$  and  $\delta^{18}O$  of precipitation at a site. **b)** Surface shading and contours show evaporation source temperature,  $T_0$  in  $^\circ\text{C}$ , as a function of  $d_{ln}$  and  $\delta^{18}O$  of precipitation at a site.

Note that any two pairs of isotopic parameters may be used to solve for  $T_0$  and  $T_c$ . The example in Figure 28 uses  $\delta^{18}O$  and  $d_{ln}$  of precipitation as the known axes, but it is possible to project  $T_c$  and  $T_0$  onto axes defined by  $\delta^{18}O$  and  $\delta D$  (Figure 29), or  $\delta^{18}O$  and  $d_{xs}$  (Figure 30). In principle, even  $\delta^{18}O$  and  $^{17}O_{xs}$  are possible coordinates (Figure 31).

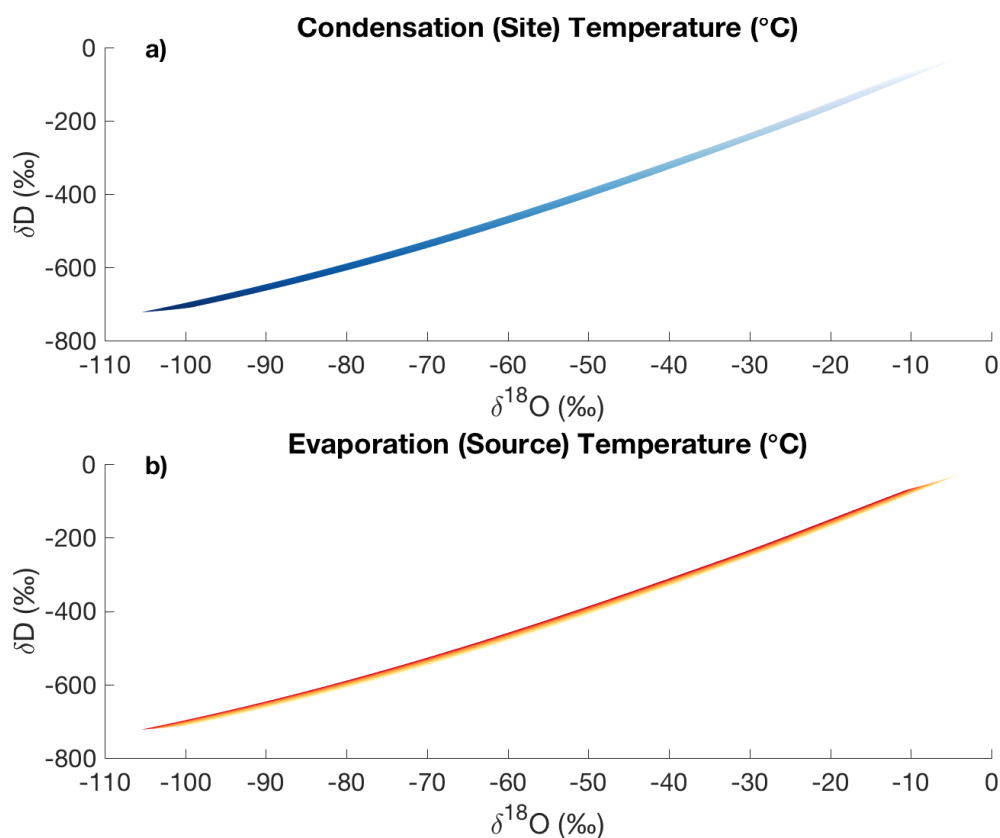


**Figure 29.** Boundary condition surfaces plotted against modeled  $\delta^{18}O$  and  $\delta D$  of precipitation. **a)** Surface shading and contours show condensation site temperature,  $T_c$  in  $^{\circ}C$ , as a function of  $\delta^{18}O$  and  $\delta D$  of precipitation at a site. **b)** Surface shading and contours show evaporation source temperature,  $T_0$  in  $^{\circ}C$ , as a function of  $\delta^{18}O$  and  $\delta D$  of precipitation at a site.

However, in practice  $\delta^{18}O$  and  $d_{ln}$  (or  $\delta D$  and  $d_{ln}$ ) are the optimal isotope parameters to use for temperature reconstruction. This result is counterintuitive. It might seem reasonable that since the only unique information among the quantities  $\delta^{18}O$ ,  $\delta D$ ,  $d_{xs}$ , and  $d_{ln}$ , are the underlying  $\delta^{18}O$  and  $\delta D$  measurements ( $d_{xs}$  and  $d_{ln}$  being

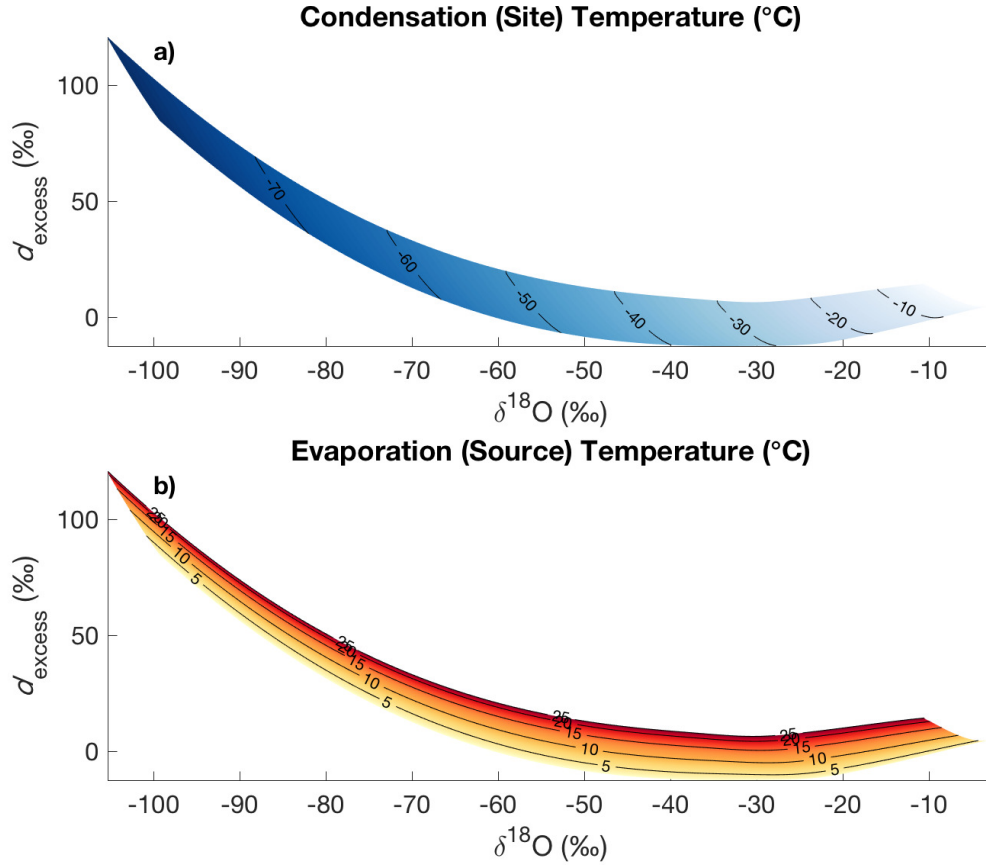


**Figure 30.** Boundary condition surfaces of against modeled  $d_{xs}$  and  $\delta^{18}\text{O}$  of precipitation. **a)** Surface shading and contours show condensation site temperature,  $T_c$  in  $^{\circ}\text{C}$ , as a function of  $d_{ln}$  and  $\delta^{18}\text{O}$  of precipitation at a site. **b)** Surface shading and contours show evaporation source temperature,  $T_0$  in  $^{\circ}\text{C}$ , as a function of  $d_{xs}$  and  $\delta^{18}\text{O}$  of precipitation at a site.

derivatives of those), any combination of those parameters will be equally good for the purposes of reconstruction (Uemura et al., 2012). This is not the case however. In comparing Figures 28, 29, and 30 it can be seen that for a given range of variability in either  $d_{ln}$ ,  $\delta D$ , or  $d_{xs}$ , the isotherms of  $T_0$  are most separated along the  $d_{ln}$  axis and that the isotherms of  $T_0$  remain nearest to perpendicular to the  $d_{ln}$  axis compared to the axes defined by  $\delta D$  or  $d_{xs}$ .

Consider two mean values of  $\delta^{18}\text{O}$  and  $\delta D$  from the same sample, with normally distributed uncertainties  $\sigma_{18}$  and  $\sigma_D$ , respectively. These uncertainties may arise

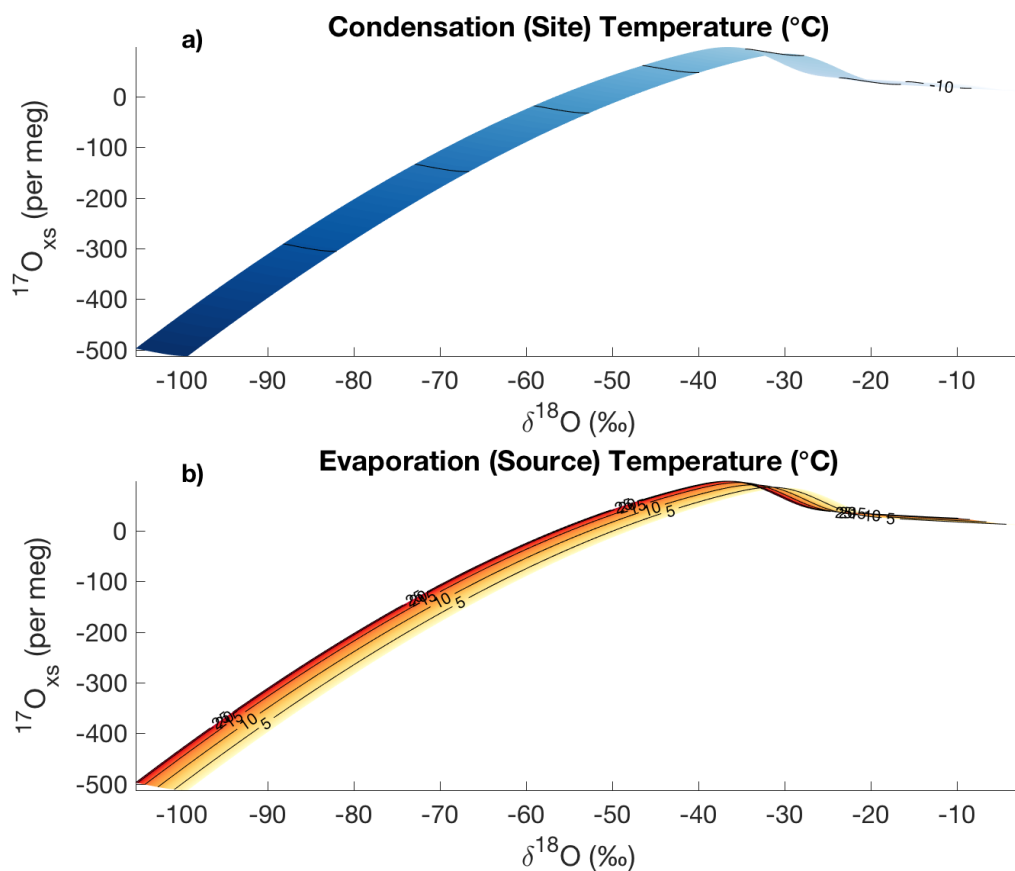


**Figure 31.** Boundary condition surfaces of against modeled  $\delta^{18}\text{O}$  and  $^{17}\text{O}_{xs}$  of precipitation. **a)** Surface shading and contours show condensation site temperature,  $T_c$  in  $^{\circ}\text{C}$ , as a function of  $\delta^{18}\text{O}$  and  $^{17}\text{O}_{xs}$  of precipitation at a site. **b)** Surface shading and contours show evaporation source temperature,  $T_0$  in  $^{\circ}\text{C}$ , as a function of  $\delta^{18}\text{O}$  and  $^{17}\text{O}_{xs}$  of precipitation at a site.

from measurement uncertainty or be uncertainty in the mean  $\delta$  value for some time or depth range represented by that sample. These uncertainties translate into uncertainties in the  $d_{xs}$  and  $d_{ln}$  values of the sample,  $\sigma_{xs}$  and  $\sigma_{ln}$ , respectively. The propagation of these uncertainties is not straightforward in the case of  $d_{ln}$  and is discussed in detail in the Supplement Section S1. We consider the use of these

mean isotopic values and their uncertainties in the estimation of  $T_0$  using coordinates of  $\delta^{18}O$  and  $\delta D$  (Figure 32.a),  $\delta^{18}O$  and  $d_{xs}$  (Figure 32.b), and  $\delta^{18}O$  and  $d_{ln}$  (Figure 32.c).

The uncertainty in the position of the measurement along both the  $x$  axis ( $\delta^{18}O$ ) and  $y$  axis ( $\delta D$ ,  $d_{xs}$ , or  $d_{ln}$ ) combine to give the total uncertainty in the position on the  $T_0$  surface, shown as the targets in (Figure 32.a-c). The total combined uncertainty in the estimation of  $T_0$  is shown as probability density functions (PDFs) for each method in Figure 32.d. All estimates yield the same mean value of reconstructed  $T_0$ , however the widths of the probability density functions are different for each method. The  $\delta D$  method yields the broadest PDF and thus most uncertain reconstruction. While the PDFs for the  $d_{xs}$  and  $d_{ln}$  reconstructions are similar, the  $d_{ln}$  reconstruction has a significantly narrower PDF and thus more confident reconstruction. The reason for this result can be seen in Figure 32. Again, compared to other  $y$  axes the  $T_0$  isotherms are most separated along, and most perpendicular to the  $d_{ln}$  axis. The separation of isotherms along the  $d_{ln}$  axis is important, though compared to the  $d_{xs}$  axis, the effect is in part compensated by the broadening of the  $d_{ln}$  PDF due to the propagation of  $\sigma$ . However the angle of the isotherms to the  $y$ -axis is significant. Given a normal distribution of uncertainty along the  $y$  axis, perpendicular isotherms of the variable we wish to reconstruct will result in the narrowest possible distribution of that uncertainty across isotherms. However, if the angle between the isotherms deviates from perpendicular, as in the case with  $d_{xs}$  toward the left end of the  $x$ -axis (more depleted in  $\delta^{18}O$ ), that uncertainty will be spread across a wider range of isotherms. The axis of the influence of  $T_0$  on  $d_{xs}$  (and  $\delta D$ ) is rotated with respect to its axis of variability (its definition).

The above reasoning is of course ultimately tied to the same reason that  $d_{ln}$  provides a better qualitative proxy of source region changes: the initial imprint of the source conditions are better preserved in  $d_{ln}$  than  $d_{xs}$ . The unfaithfulness of the historical definition of the parameter is the result of nonlinear biases from the linear slope of the definition, the nonlinear nature of equilibrium fractionation, and the cumulative influence of kinetic fractionation during transport (Markle et al., 2017).

Note that the above arguments apply not only to uncertainty in the mean  $\delta$  and excess values of individual samples, but also to the mean values of a time period of interest. If we wish to know the mean site and source temperatures of the LGM for example, given mean and standard deviations of  $\delta^{18}O$  and  $\delta D$  through the interval, we can make more precise reconstructions using  $\delta^{18}O$  and  $d_{ln}$  than using  $\delta^{18}O$  and  $d_{xs}$ .

**5.2. Absolute temperature reconstructions.** An advantage of the reconstruction technique presented here is that we are able to reconstruct absolute evaporation and condensation temperatures, not just relative changes as in the linear technique.

We next reconstruct modern surface temperatures and evaporation source temperatures for seven different Antarctic deep ice-core sites for which there are  $\delta^{18}O$  and  $d_{ln}$  records. The records include WDC (Markle et al., 2017; WAIS Divide Project Members et al., 2013) and Siple Dome (Brook et al., 2005) from West Antarctica (the Siple Dome deuterium excess record has not yet been published), as well as the EDML (Stenni et al., 2010), EDC (Stenni et al., 2010), Vostok (Vimeux et al., 2002), Dome Fuji (Uemura et al., 2012), and Talos Dome (Stenni et al., 2011) records from East Antarctica.

Because we tune the our model only to fit the relationships between isotope parameters and not to the relationship between isotopes and temperature, our ability to reconstruct modern site temperatures from isotope measurements is a useful check on our model’s fidelity. Figure 33 shows the reported annual average site temperature of the seven different ice-core sites as well as our reconstructed site temperature averaged over most recent 100 years of each ice core. In the case of Vostok and EDML, the most recent one hundred years are not available; our “modern” averages represent 400-500 years ago and 1200-1300 years ago, for those cores respectively. For several sites (e.g. WDC, EDML, and Vostok) is accurate to within  $1^{\circ}C$ . Our reconstruction overestimates the observed modern temperature for some sites (e.g. Talos Dome) by as much as  $6.5^{\circ}C$ , though this is within the spread of observed water isotope-to-temperature relationships as seen in Figure 21. Given the  $40^{\circ}C$  range of observed modern site temperatures, and simplifications used in the model, this is an acceptable level of agreement.

The observation that our reconstructions may overestimate surface temperatures, may point to spatial heterogeneity in the strength of the Antarctic inversion or its relationship to the condensation level. The error in our estimates may arise from other sources as well, including the absence of processes within our model that are important at a given site. Talos Dome (Stenni et al., 2011) for example is both very high in elevation and near to the Antarctic coast. Our reconstruction suggests that the average condensation temperature for precipitation at Talos is warmer than would be expected given its average annual surface temperature. The sites’ local climate may make it significantly different from the continent on average, for example being exposed to warmer oceanic storms compared to interior sites of similar elevation. Reconstructions based both on the global and local closure assumptions give similar results. For the paleoclimate reconstructions presented below we use the local assumption as the global assumption is likely not valid in past mean states.

The exact moisture source locations for each ice-core site are not known *a priori*. However the evaporation temperature reconstructions show modern moisture-source temperatures in the range of  $12^{\circ}$  to  $22^{\circ}C$  for all cores. Given the modern latitudinal surface temperature gradient over the Southern Ocean, this temperature range puts the mean latitudes of Antarctic moisture sources between  $30^{\circ}S$  and  $50^{\circ}S$ , in excellent

agreement with calculations of the moisture source distributions, shown in Figure 4. In Figure 34, we plot the reconstructed modern evaporation source temperature as a function of the mean latitude of the modeled moisture source distribution (MSD) for each core site shown in Figure 4. The local and global closure assumptions lead to different absolute values of the average reconstructed evaporation temperature, though the entire range is plausible for Southern Hemisphere air temperatures over the ocean. There is a general trend of increasing reconstructed evaporation temperature with more equatorward modeled MSD, as expected. The relationship between modeled MSD latitude and reconstructed evaporation temperature for both EDML and EDC appear distinct from that of the other sites.

### 5.3. Comparison of linear and nonlinear reconstruction techniques.

5.3.1. *Temperature reconstruction using SWIM.* Nonlinearities are present in the slopes between water-isotope values of precipitation and the temperature boundary conditions. However, are these changes in slope large enough to influence temperature reconstructions? If the changes in slope are small within the range of temperatures changes experienced by moisture arriving at an ice-core site, then accounting for these nonlinearities will not significantly alter temperature reconstructions.

To test the importance of accounting for these nonlinearities we compare the nonlinear reconstructions to traditional linear reconstructions of relative changes in condensation and evaporation temperature. Following previous studies (e.g. Uemura et al. (2012)), we calculate linear regressions of relative changes in  $T_c$  and  $T_0$  to relative changes in  $\delta^{18}O$  and  $d_{xs}$  to find the  $\beta$  and  $\gamma$  coefficients in Equations 1 and 2. If the nonlinearities in the temperature-isotope relationships are large, the value of the calculated  $\beta$  and  $\gamma$  coefficients will depend on the absolute values of  $\delta^{18}O$  and  $d_{xs}$ . Thus the appropriate  $\beta$  and  $\gamma$  coefficients may change between different core sites or over the range of isotope values within a single core.

We illustrate this point by calculating the  $\beta$  and  $\gamma$  coefficients for the WAIS Divide site, using subsets of SWIM results for  $\delta^{18}O$  and  $d_{xs}$  values representative of those in the WAIS Divide ice core (WDC). We find different values of the  $\beta$  and  $\gamma$  coefficients if we conduct the regression on  $\delta^{18}O$  and  $d_{xs}$  values representative of the entire WDC record ( $\gamma_1 = 1.12$ ,  $\gamma_2 = -0.26$ ,  $\beta_1 = -0.32$ ,  $\beta_2 = 1.03$ ), those representative of the Holocene portion of the core ( $\gamma_1 = 1.29$ ,  $\gamma_2 = -0.2$ ,  $\beta_1 = -0.31$ ,  $\beta_2 = 0.8$ ) or those representative of the Glacial portion of the core ( $\gamma_1 = 1.12$ ,  $\gamma_2 = -0.33$ ,  $\beta_1 = -0.4$ ,  $\beta_2 = 1.26$ ). In particular,  $\beta_2$  changes by over 50% between the Glacial and the Holocene. This issue was also explored by Uemura et al. (2012), who used linear regression of results from a water-isotope model (of comparable complexity to SWIM) to make temperature reconstructions for different East Antarctic ice cores. They found that their temperature reconstructions depended on what set of model

results were used in their linear regressions, though they did not attempt to nonlinear reconstructions or connect those differences to nonlinearities in the underlying slopes.

We reconstruct relative changes in moisture-source and ice-core site condensation temperature for WDC using the three sets of the  $\beta$  and  $\gamma$  coefficients found above. We first correct all records for changes in the isotopic composition of seawater (Bintanja and Van de Wal, 2008),  $\delta^{18}O_{sw}$ , following the method outlined in Uemura et al. (2012) and Stenni et al. (2010). In Figure 35 we compare the residuals between these three sets of linear reconstructions and relative changes in the non-linear reconstructions for WDC. The differences between linear and nonlinear-reconstruction techniques are fairly small for relative changes in the ice core site temperature, on the order of  $\pm 0.5^\circ C$  for WDC. This reflects the largely linear relationship between  $\delta^{18}O$  and  $T_c$ . However, it is clear that the residuals are correlated with the actual temperature reconstructions (Figure 35.b). This results from the temperature dependent nonlinearities in the water isotope-temperature relationships and is expected. The error in a linear estimation of a nonlinear process will be proportional to the absolute value of the estimation.

The residuals between the linear and nonlinear-reconstruction techniques for evaporation source temperature changes are larger than those for the condensation temperature, on the order of  $\pm 1^\circ C$ . The degree to which an ice core site is affected by these nonlinearities depends on its unique history of absolute temperatures and associated  $\delta^{18}O$  and  $d_{xs}$  values. The difference in evaporation source temperature residuals is even larger for East Antarctic sites like Dome Fuji (Figure 36), on the order of  $\pm 2^\circ C$ , though the residuals in ice core site temperature are smaller at these sites. While the differences in the linear and nonlinear-reconstruction techniques do not substantially change interpretations of ice-core site temperature changes, they may clearly influence the interpretation of evaporation source temperature changes, since the errors introduced by the linear method ( $\pm 2^\circ C$ ) are a significant fraction of the total variability in reconstructed evaporation temperature.

As shown above, the relationship between  $\delta^{18}O$  and  $T_c$  is largely linear across a wide range of values of  $T_c$  and regardless of evaporation temperature. The ice core site temperature reconstructions from the linear and nonlinear reconstruction techniques have relatively small differences. However, as seen in Figure 35, there are some differences arising from slight nonlinearity in the  $\delta^{18}O$ -to- $T_c$  relationship, particularly for relatively warmer sites like those in West Antarctica. This nonlinearity can be seen in Figure 20. The primary source of this nonlinearity is the change in total fractionation factor as the air parcel transitions between liquid-only and ice-only condensate. The SWIM model retains liquid condensate at colder temperatures than previous models (e.g. Kavanaugh and Cuffey (2002)) in line with satellite measurements (Hu et al., 2010). This results in the transition of fractionation factors and nonlinearities in the  $\delta^{18}O$ -to- $T_c$  relationship at temperatures relevant to some

Antarctic sites such the West Antarctic Ice Sheet Divide. It is for this reason that the differences between the linear and non-linear reconstruction techniques are larger for West Antarctic compared to East Antarctic cores. It is important to note that because the SWIM model uses a consistent scenario for the supersaturation parameterization and the removal of moisture from the air parcel, the relationship between  $\delta^{18}O$  and  $T_c$  is actually more linear (smaller 2<sup>nd</sup> derivative, see Figure 13) than in other comparable models (e.g. Kavanaugh and Cuffey (2002)).

5.3.2. *Comparison to previous reconstructions.* We next reconstruct site and source temperatures for four East Antarctic ice-core records and compare to previously published linear reconstructions. We use records of  $\delta^{18}O$  and  $\delta D$  measurements (and calculate  $d_{xs}$  and  $d_{ln}$ ) from the Vostok (Jouzel et al., 1997; Uemura et al., 2012), EPICA Dome Concordia (EDC) (Stenni et al., 2004, 2010), EPICA Dronning Maud Land (EDML) (Stenni et al., 2010), and Dome Fuji records (Uemura et al., 2012). After sea water correction, we use the ice core  $\delta D$  and  $d_{xs}$  for the linear reconstruction, and  $\delta^{18}O$  and  $d_{ln}$  for the nonlinear reconstruction. The linear reconstruction parameters,  $\beta$  for  $d_{xs}$  and  $\gamma$  for  $\delta D$ , from several temperature reconstruction studies are compiled by Uemura et al. (2012) (c.f. Tables 1 and 2 in Uemura et al. (2012)). Previous reconstruction techniques solve for the source temperature,  $T_{source}$ , equivalent to our evaporation temperature,  $T_0$ , and for the site surface temperature,  $T_{site}$ . We convert our reconstructed condensation temperatures,  $T_c$ , to surface temperatures following the method in Section 2.1.3.

A comparison of relative changes in site and source temperatures are shown in Figure 37. The nonlinear reconstruction results of this study are shown in black, while published linear inversions for each core are shown in color. The difference between the results of this study and the previous temperature reconstructions arise from differences between the linear and nonlinear reconstruction techniques as well as differences in the underlying water-isotope models used for the estimation of scaling relationships. In most cases, the previously-published linear inversions overestimate changes in both site and source temperature compared to the nonlinear reconstruction. Some linear reconstructions are more similar to the nonlinear reconstruction than others; the linear reconstructions for EDC (Stenni et al., 2004, 2010), for example, are generally similar to the nonlinear reconstruction.

The over-estimation of reconstructed temperature change by the linear reconstruction makes physical sense. The largest source of nonlinearities in the water isotope to temperature boundary condition relationships are in the deuterium excess parameter,  $\partial d_{xs}/\partial T_c$  and  $\partial d_{xs}/\partial T_0$  (Figure 26). If one assumes these slopes are linear over a given range in  $T_0$  and  $T_c$ , when in reality they are nonlinear, one will attribute a given change in  $\Delta d_{xs}$  to a larger change in temperature than is actually required. This over estimate of the required temperature change will be distributed across

the reconstructed site and source temperatures in proportion to the values of the  $\beta$  and  $\gamma$  parameters. The same reasoning is true for nonlinearities in the relationships between  $\delta D$  or  $\delta^{18}O$  and the temperature boundary conditions, though as seen in Section 4, the nonlinearities in these slopes are much smaller.

The residuals between relative temperature change in the nonlinear and linear reconstructions are shown in Figure 38. Residuals in the site temperature reconstructions are on the order of  $\pm 2^\circ\text{C}$  (Figure 38.a). One can see that the variability in the time series of the residuals, is similar to the variability of the reconstructions, as seen above.

The previous reconstructions use a different scaling between surface and condensation than that used in this study (see Section 2.1.3). However, the differences between the nonlinear reconstruction and the linear reconstructions do not arise solely because of this different surface-condensation temperature scaling. The residuals between reconstructed condensation temperatures are shown in Figure 38b. These differences are somewhat damped compared to those of the surface temperatures, owing to different assumed slopes in the condensation to surface temperature relationship, but are of similar magnitude and the time series of the residuals are again correlated to the reconstructions themselves, pointing to nonlinear biases.

The residuals between the reconstructed evaporation temperature anomalies (Figure 38c) have a large spread ranging from about  $+3^\circ\text{C}$  to  $-5^\circ\text{C}$ . As discussed above the largest source of potential nonlinear biases are in the deuterium excess relationships to temperature, and should be greatest in the reconstruction of source temperatures. While the magnitude of source temperature residuals is comparable to those of site temperature, they are far more significant, representing anywhere from 50% to over 200% of the total reconstructed variability in the source temperature. This is related to the issues surrounding the qualitative interpretation of source region changes from  $d_{xs}$  versus  $d_{ln}$  (Markle et al., 2017; Uemura et al., 2012) (see Section 1.2) and ultimately a consequence of the same distillation effects.

**5.4. Reconstruction sensitivity.** The sensitivity of our reconstructions to uncertainty in model parameters within SWIM can be tested. We must distinguish here between uncertainty in the true value of a parameter in the modern climate, and the possibility that the effective value for a parameter may change through time. In the case of uncertainty in a parameter's modern value, it is appropriate to retune SWIM for the new parameter value (following the procedure in Section 2.5) before calculating the isotope state spaces for the reconstruction. For example, we may have uncertainty in the value of the effective diffusive fractionation factor  $^{18}\alpha_{diff}$  appropriate for the modern climate. We can investigate the sensitivity in our reconstruction technique to the value of this parameter by changing its value, re-tuning the model and recreating the isotope state spaces, and comparing the reconstructed

temperatures in each case. However, if we do not re-tune SWIM before calculating the isotope state spaces for the reconstruction, we risk introducing biases into our comparison of reconstructions. The differences between the reconstructions will reflect any difference in sensitivity caused by the new parameter as well as any biases in the new parameters' reproduction of the modern mean state (specifically the modern relationship between  $\delta D$  and  $\delta^{18}O$  in precipitation). In general the sensitivity of our reconstructions to these types of parameter uncertainties is small; once the model is tuned to match the modern  $\delta D$  and  $\delta^{18}O$ , its responses to changes in boundary condition temperatures are similar. On the other hand, if we are interested in the sensitivity of the model to possible changes in the effective value of a parameter with mean state, it is appropriate to change only that parameter and recalculate the isotope state spaces, without re-tuning. This acknowledges that while the modern mean state may be represented by one set of effective parameters, past mean states may have been represented by a different set of parameters.

The quality of the tuning itself may also introduce uncertainty into our reconstructions. In particular the behavior of  $d_{ln}$  at very cold temperatures is influenced by the supersaturation parameterization. As shown in Section 2.5 and Figure 15, we can constrain the possible values of the  $b$  parameter in the supersaturation function by comparison to modern data. However, we may not be able to rule out small differences in this parameter (e.g.  $b = 0.00525 \pm 0.0002 \text{ } ^\circ\text{C}^{-1}$ ) based on the modern data alone. Differences in our reconstructions owing to this magnitude of uncertainty in  $b$  are insignificant.

A potential source of uncertainty in our reconstruction technique is the local closure assumption used for evaporation. While this assumption has known limitations (Risi et al., 2010), it represents an end-member scenario for possible evaporative conditions. To investigate the sensitivity of the model to this assumption we have also considered a global closure assumption, following (Criss, 1999) and described in Section 2.3. While the global closure assumption is likely less valid for past mean states (it is based on the average  $\delta$  values of global sea water and precipitation, which change with mean state), it provides a useful tool for investigating the sensitivity of our reconstructions to the closure assumption.

Isotope state-spaces were created using both the local (as presented above) and global closure assumptions with all other parameters held fixed. Moisture condensation temperatures and evaporation source temperatures were reconstructed for the West Antarctic Ice Sheet Divide (WDC) ice core (Markle et al., 2017; WAIS Divide Project Members et al., 2013). The two closure methods produce different absolute site and source temperatures. The global closure assumption yields condensation temperatures that are on average  $1.1^\circ\text{C}$  warmer than those produced by the local

closure assumption, corresponding surface temperatures are  $1.5^{\circ}\text{C}$  warmer on average, and evaporation source temperatures are  $2.3^{\circ}\text{C}$  colder than those produced by the local closure assumption.

These differences are largely absolute offsets in temperature. The difference in the *relative* temperature changes reconstructed with each closure assumption is smaller. The difference in the reconstructed glacial-interglacial temperature change is  $0.25^{\circ}\text{C}$  for the condensation temperature,  $0.38^{\circ}\text{C}$  for the site temperature and  $1.0^{\circ}\text{C}$  for the evaporation source temperature.

**5.5. Three parameter reconstructions.** In the approach outlined above, we have considered the boundary conditions  $T_c$  and  $T_0$  to be the only independent variables. In particular we have assumed that the source region relative humidity,  $RH_0$ , is a dependent variable whose value is determined by climatological correlations to  $T_0$  as described in Section 2.1.1. Most previous linear reconstructions have calculated scaling factors based on fixed values of  $RH$  or the average of variation in  $RH$  over some range (Uemura et al., 2012; Winkler et al., 2012). While we do not assume that  $RH$  is fixed, we do assume it varies with source region temperature.

We can however relax this assumption. Following the method in Section 4 we allow  $T_c$ ,  $T_0$ , and  $RH_0$ , to all vary as independent variables:  $T_0 = \{T_{0(1)}, T_{0(2)}, \dots, T_{0(m)}\}$ ,  $T_c = \{T_{c(1)}, T_{c(2)}, \dots, T_{c(n)}\}$ , and  $RH_0 = \{RH_{0(1)}, RH_{0(2)}, \dots, RH_{0(q)}\}$ . We thus define a three dimensional parameter space  $\mathbf{Q}$ , whose planes are each the parameter space  $\mathbf{T}$  of temperature trajectories for fixed values of  $RH_0$ .

SWIM is then run through the three dimensional parameter space  $\mathbf{Q}$  to produce three dimensional isotope state spaces, e.g.  $\delta^{18}\mathbf{O}$ . To reconstruct three independent variables we clearly require three independent constrains;  $\delta^{18}\text{O}$  and  $d_{ln}$  alone are not sufficient as before. The  $^{17}\text{O}_{xs}$  can provide the necessary additional independent information.

Rather than the isotope surfaces described in Section 4, the SWIM results under this scenario are three dimensional isotope spaces dependent on each boundary condition. In analogy to Equations 1 and 2, these are equivalent to three dimensional nonlinear functions.

We can as before, project any boundary condition on to a set of three axes defined by the isotope state spaces. It is difficult to display these spaces (three isotope dimensions, one boundary condition dimension) on a two dimensional page. In Figure 39, we show a slice through one of these spaces along the  $\delta^{18}\text{O}$  and  $^{17}\text{O}_{xs}$  axes and at  $T_0 = 15^{\circ}\text{C}$ , with  $RH_0$  shown in color. In Figure 40, we show the same  $T_0 = 15^{\circ}\text{C}$  surface, projected into the three isotope dimensions,  $\delta^{18}\text{O}$ ,  $d_{ln}$ , and  $^{17}\text{O}_{xs}$ , with the color again showing  $RH_0$ . The full isotope state space, of course, includes all surfaces of  $T_0$ .

As before, the reconstruction technique is in essence as simple as finding the value of  $T_c$ ,  $T_0$ , and  $RH_0$  given measured values of  $\delta^{18}O$ ,  $d_{ln}$ , and  $^{17}O_{xs}$ , which uniquely locates any sample in these three dimensional spaces.

A preliminary three-parameter reconstruction based on data from the EDC ice core (Landais et al., 2012) is shown in Figure 41. While promising, this method currently has significant limitations. As we saw in Section 2.5, our model does not reproduce a state space for  $^{17}O_{xs}$  that is able to cover the full range of observed values. This may result from large uncertainties in the measurement of  $^{17}O_{xs}$  or from limitations in our model such as the absence of relevant processes. The  $^{17}O_{xs}$  of Antarctic precipitation in our model is sensitive to the degree of supersaturation. Both small changes in the supersaturation parameter, and uncertainties in the absolute value of  $^{17}O_{xs}$  (which has order of per meg), lead to relatively large changes in the absolute value of reconstructed source-region conditions ( $T_0$  and  $RH_0$ ). Further, preliminary testing suggests that there may be non unique solutions, that is a position in the three-isotope parameter space, defined by  $\delta^{18}O$ ,  $d_{ln}$ , and  $^{17}O_{xs}$ , does not necessarily lead to unique values of the boundary conditions due, for example, to the crossing of planes of equal  $T_0$  (or other boundary conditions). A potential solution to this could be path-dependent reconstructions in which the possible value of a reconstructed boundary conditions is limited by previous values. At present these tests serve only as a proof of concept of the three parameter reconstruction.

The approach we have outlined here is generally scalable. Additional quantities that are both influenced by aspects of the environmental pathway and measurable in an ice core, for example accumulation rate (Fudge et al., 2016), water isotope diffusion lengths (Johnsen et al., 2000), or the concentration of aerosols (Markle, 2017), may be added to the model. These extra constraints allow for the reconstruction of additional independent variables or parameters. Given  $n$  constraints from ice-core measurements, the model can produce  $n$  different  $n$ -dimensional state spaces, to reconstruct  $n$  independent variables. In addition to reconstructing independent variables like  $T_0$  or  $T_c$ , it is possible to use the same approach to optimize model parameters like the supersaturation. We leave this exciting though daunting task to future work.

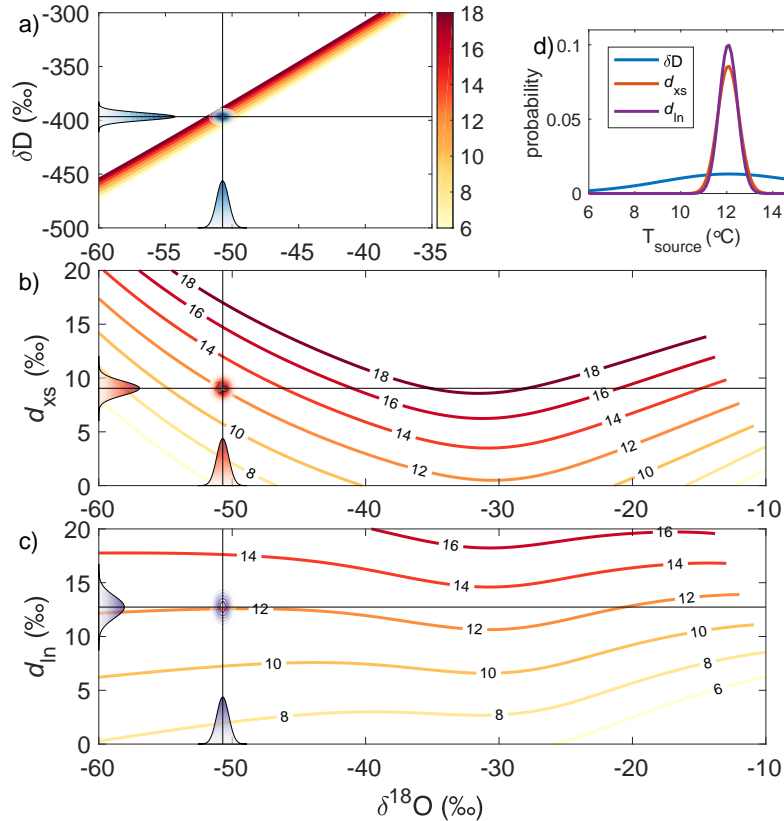


**Figure 32.** **a)** Evaporation source temperature,  $T_0$ , contours as a function of modeled  $\delta^{18}O$  and  $\delta D$  of precipitation, as in Figure 29. Uncertainty in  $\delta^{18}O$  and  $\delta D$  for an interval or sample are shown as PDFs of uncertainty along the respective axes. The intersection of these PDFs on the  $T_0$  surface result in a 2-dimensional PDF in the reconstructed value of  $T_0$ , shown as a target. **b)** Same as panel **a)** but for the evaporation source temperature projected on to the  $\delta^{18}O$  and  $d_{xs}$  axes. Uncertainties in  $\delta^{18}O$  and  $\delta D$  in panel **a)** are propagated into the PDF on the  $d_{xs}$  axis. **c)** Same as panel **a)**, but for the evaporation source temperature projected on to the  $\delta^{18}O$  and  $d_{ln}$  axes. Again, uncertainties in  $\delta^{18}O$  and  $\delta D$  in panel are propagated into the PDF on the  $d_{ln}$  axis, following the procedure in the Supplement Section S1. **d)** The uncertainty in the reconstructed evaporation source temperature ( $T_{source} = T_0$ ), owing to the weighting of the combined 2-dimensional PDFs from panels **a)** (in blue), **b)** (in red), and **c)** (in purple).

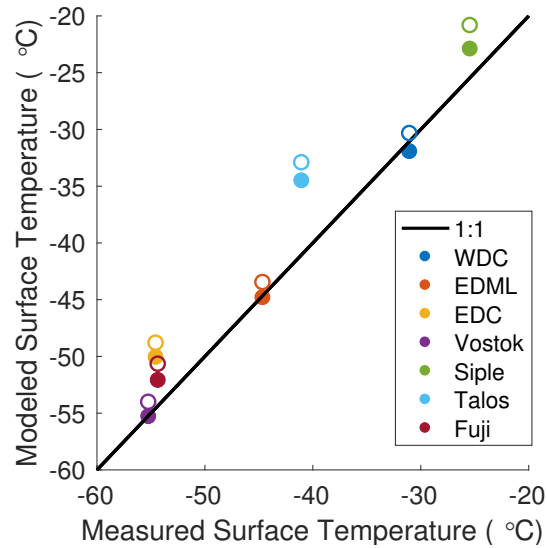


**Figure 33.** Comparison of observed and reconstructed modern surface temperatures for seven ice-core sites. Reconstructed modern surface temperatures are for the most recent hundred years of each ice core, except for Vostok and EDML, whose “modern” averages are for 400-500 years ago and 1200-1300 years ago, respectively, the most recent available water isotope measurements. Closed circles are for reconstructions based on the local closure assumption, open circles represent the global closure assumption. The 1:1 line is shown in black.

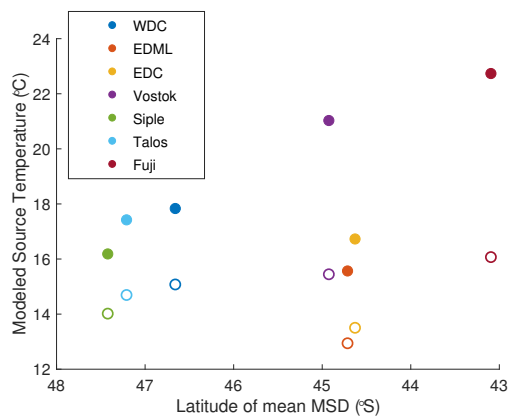


**Figure 34.** Comparison of reconstructed modern evaporation temperatures for seven ice-core sites against the mean latitude of the moisture source distribution for each site (Figure 4) calculated from a water tagged GCM experiment (Markle et al., 2017). Reconstructed modern evaporation temperatures are for the most recent hundred years of each ice core, except for Vostok and EDML, whose “modern” averages are for 400-500 years ago and 1200-1300 years ago, respectively, the most recent available water isotope measurements. Closed circles are for reconstructions based on the local closure assumption, open circles represent the global closure assumption. The 1:1 line is shown in black.

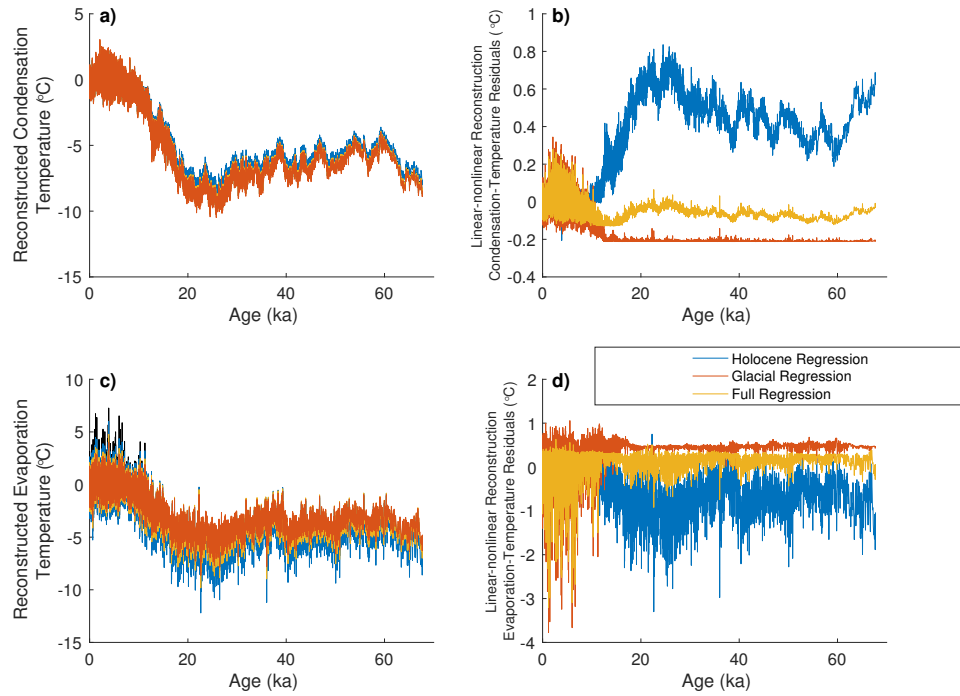


**Figure 35.** Comparison of linear and nonlinear reconstruction techniques for the WAIS Divide ice core. **a)** Relative changes in condensation temperature reconstructed using the nonlinear technique (black) and three linear techniques. The differences in the three linear reconstructions arise from range of modeled  $\delta^{18}O$  and  $d_{xs}$  values used in the linear regression to estimate the  $\beta$  and  $\gamma$  coefficients. The reconstruction resulting from the regression of Holocene-like values of  $\delta^{18}O$  and  $d_{xs}$  is shown in blue, from Glacial-like values in red, and for a regression of values representing the entire record is shown in yellow. Because the differences between techniques are small, and the total variability is large, the reconstructions are largely overlapping in this plot. **b)** The residuals between the three linear reconstructions and the nonlinear reconstruction of ice-core site condensation temperature. **c)** Same as for **a)** but for relative changes in the evaporation-source temperature. **d)** Same as **b)** but for the evaporation-source temperature reconstructions.

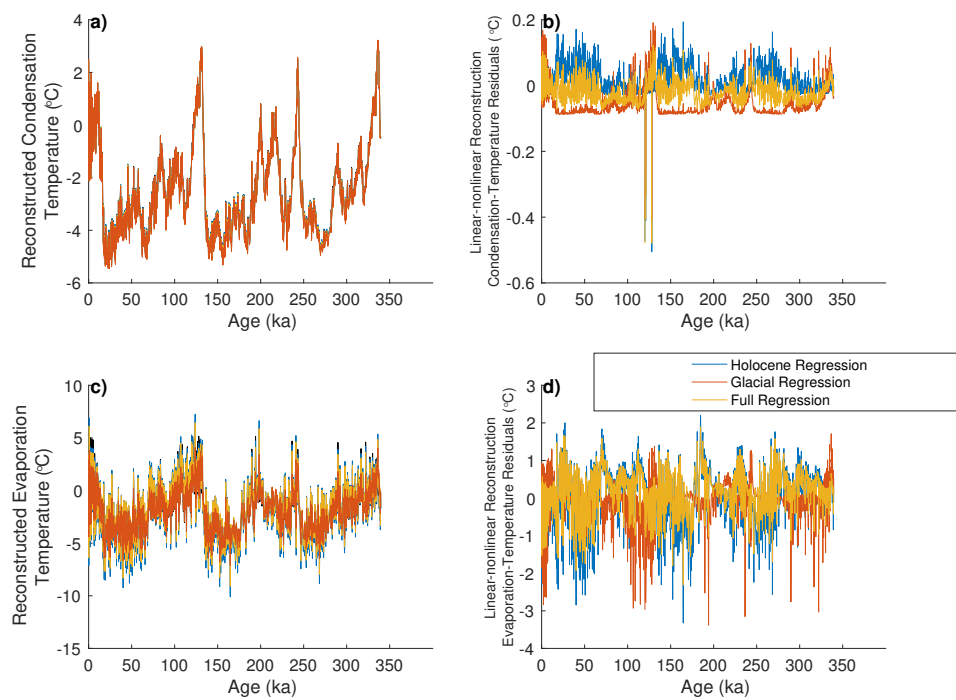


**Figure 36.** Same as Figure 35 but for the Dome Fuji ice core.

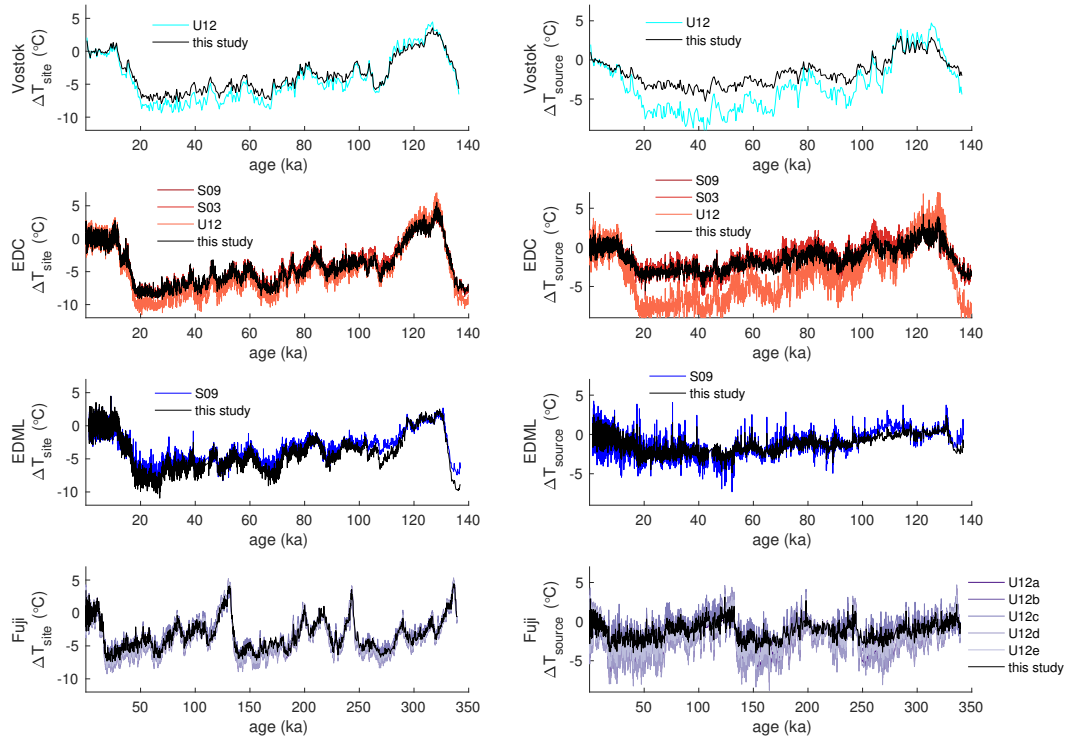


**Figure 37.** Reconstructions of relative change in Antarctic surface temperature ( $\Delta T_{site}$ , left panels) and source region evaporation temperature ( $\Delta T_{source}$ , right panels), for four East Antarctic ice-core site: Vostok, EDC, EDML, and Dome Fuji. The non linear reconstructions (this study) are shown in black while published linear reconstructions are shown for each site in color. The linear coefficients for the published reconstructions are compiled in (Uemura et al., 2012) (c.f. Tables 1 and 2). Linear methods labeled U12 for Vostok, EDC, and EDML were calculated by a simple Rayleigh-type model (Uemura et al., 2012). Reconstructions U12a-e for Dome Fuji represent a sensitivity study from Uemura et al. (2012). Reconstructions S03 and S09 are from Stenni et al. (2004) and Stenni et al. (2010).

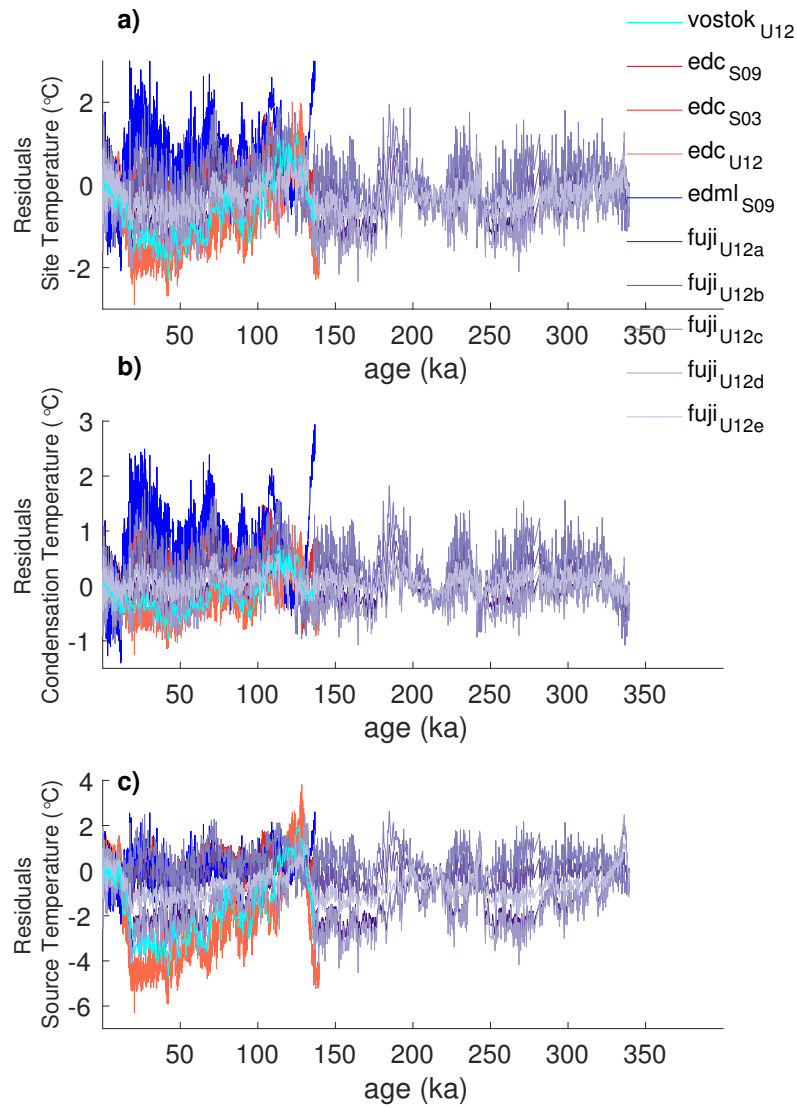


**Figure 38.** Residuals between the nonlinear reconstructions and all linear reconstructions shown in Figure 37. a) Site surface temperature residuals. b) Condensation temperature residuals. c) Evaporation source temperature residuals.

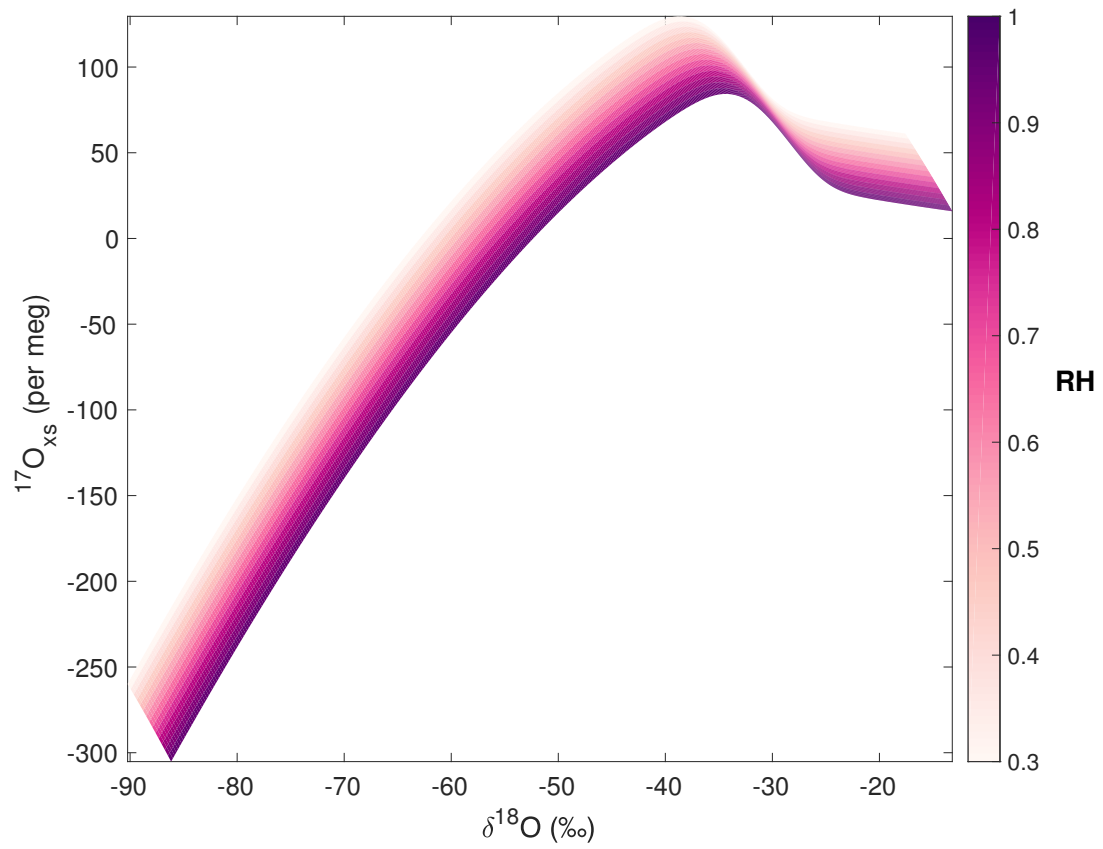


**Figure 39.** Relationship between modeled  $\delta^{18}\text{O}$  and  $^{17}\text{O}_{xs}$  of precipitation, for variability in  $RH_0$  at the evaporation source (shown in color), along the plane  $T_0 = 15^\circ\text{C}$ .

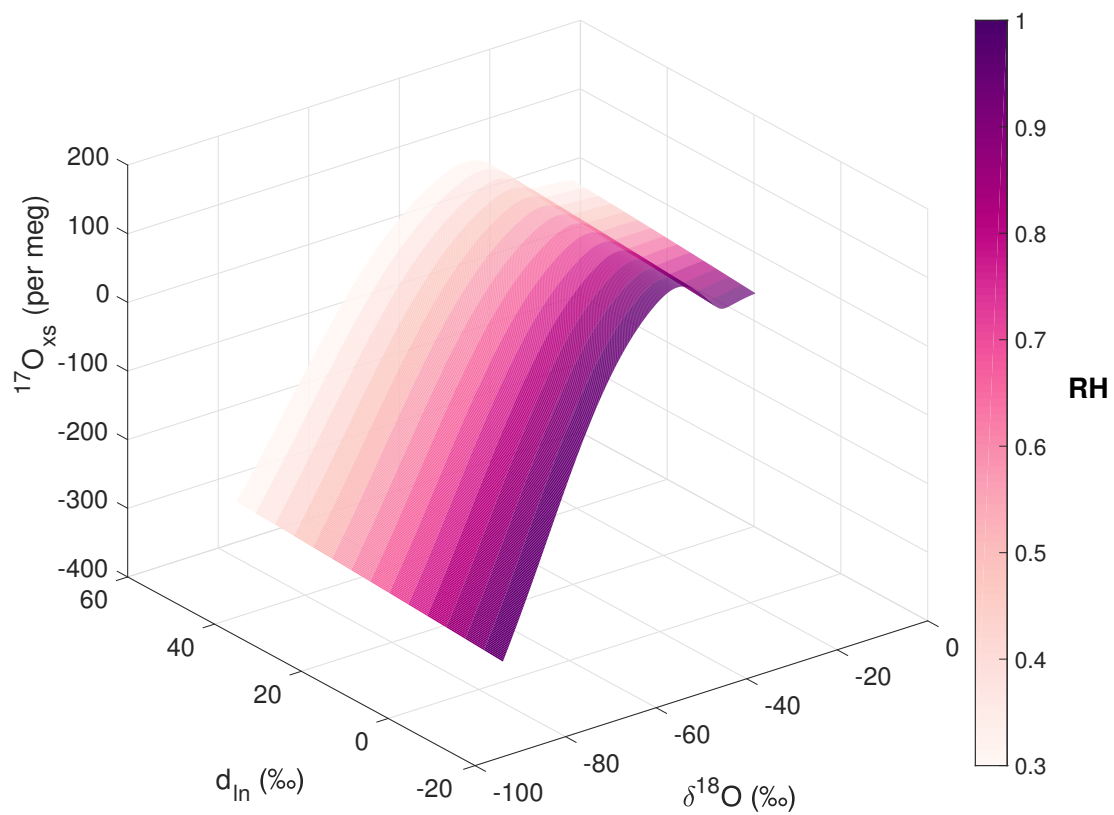


**Figure 40.** The same  $T_0 = 15$  plane, as in Figure 39, projected into three isotope dimensions,  $\delta^{18}\text{O}$ ,  $d_{ln}$ , and  $^{17}\text{O}_{xs}$ . Color axis shows the relative humidity ( $RH_0$ ) at the evaporation source

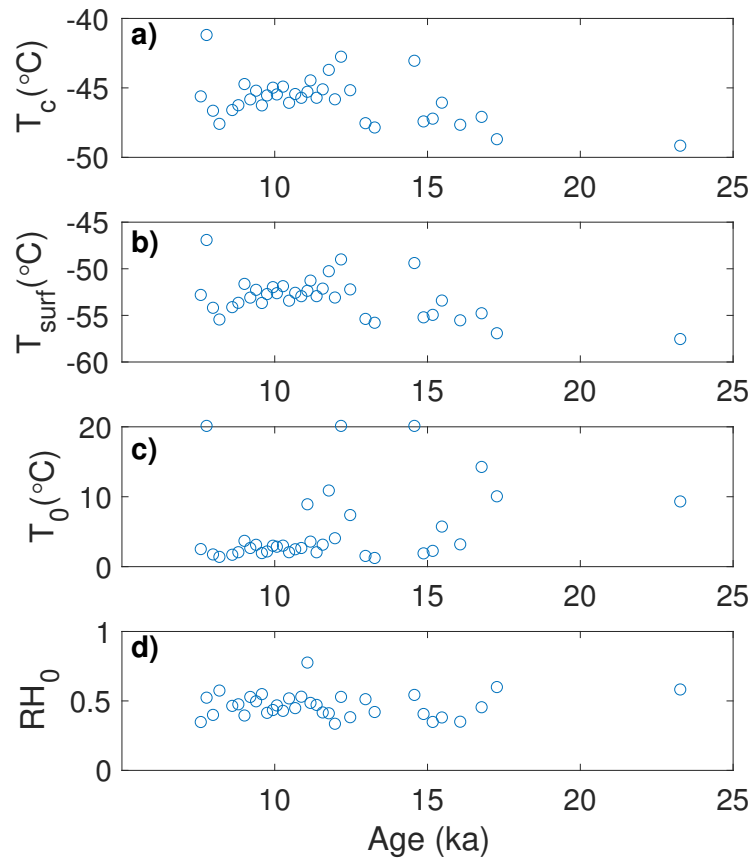


**Figure 41.** Preliminary results for three parameter inversion for EDC  $\delta^{18}O$ ,  $d_{ln}$ ,  $^{17}O_{xs}$  records. Reconstructed **a)** condensation temperature ( $T_c$ ), **b)** surface temperature ( $T_{surf}$ ), **c)** evaporation source temperature ( $T_0$ ), **d)** evaporation source relative humidity ( $RH_0$ ).

## 6. DISCUSSION

Using the nonlinear temperature-reconstruction technique on the seven ice core records described above, we have the opportunity to evaluate the spatial patterns of Antarctic site and moisture-source temperature changes through time. In Figures 42 and 43 we show the nonlinear reconstructions of Antarctic surface temperature and moisture source evaporation temperature for the seven ice-core records. At the WDC site in West Antarctica there is an independent estimate for the magnitude of glacial-interglacial temperature change from the borehole temperature profile (Cuffey et al., 2016). Our results are in good agreement with those findings, both in the absolute value of reconstructed temperatures as well as the magnitude of glacial-interglacial change. Cuffey et al. (2016) find  $11.3 \pm 1.8^\circ\text{C}$  warming at WDC during the deglaciation; we reconstruct  $10.9^\circ\text{C}$  of warming (measured as the difference between the average surface temperatures of 27-24 ka and 11-9 ka, for direct comparison to the results of Cuffey et al. (2016)). Our results are also in agreement with a third independent estimate of absolute temperature and glacial-interglacial change at WDC based on the diffusion lengths of water isotopes in the core calculated from high frequency variability (Holme, 2017).

**6.1. Polar amplification.** The spatial patterns of climate change are topic of interest in paleoclimate research. In particular the phenomenon of polar amplification, in which the poles experience greater temperature changes than the low latitudes, is an important aspect of both past and current climate change. We plot the magnitude of warming since the Last Glacial Maximum (LGM, 21-23 ka) for Antarctic surface temperatures and source evaporation temperatures for all ice-core records as a function of the reconstructed modern temperature in Figure 44. In Figure 45 we show the magnitude of glacial-interglacial change as a function of the latitude of the ice-core site and the mean latitude of the moisture source distribution for each site based on water tagged GCM simulations, as discussed above.

The magnitude of warming since the Last Glacial Maximum is calculated as the temperature difference between the average temperatures of the early holocene (EH, 9-11 ka) and Last Glacial Maximum. These intervals were chosen to minimize the potential influence of millennial changes during the LGM, which have variable magnitudes between sites, and of ice flow and elevation changes during the holocene (Stenni et al., 2011; WAIS Divide Project Members et al., 2013). We make no corrections to the records for elevation changes or ice flow, lacking constraints for all records. These effects are likely small in East Antarctica (Stenni et al., 2011), and smaller still in West Antarctica (WAIS Divide Project Members et al., 2013). There may be uncertainty in the relative magnitudes of these changes owing to offsets in the individual timescales of each record. While the relative magnitudes of interglacial changes depend on the exact time periods used in the differencing, the relative pattern across

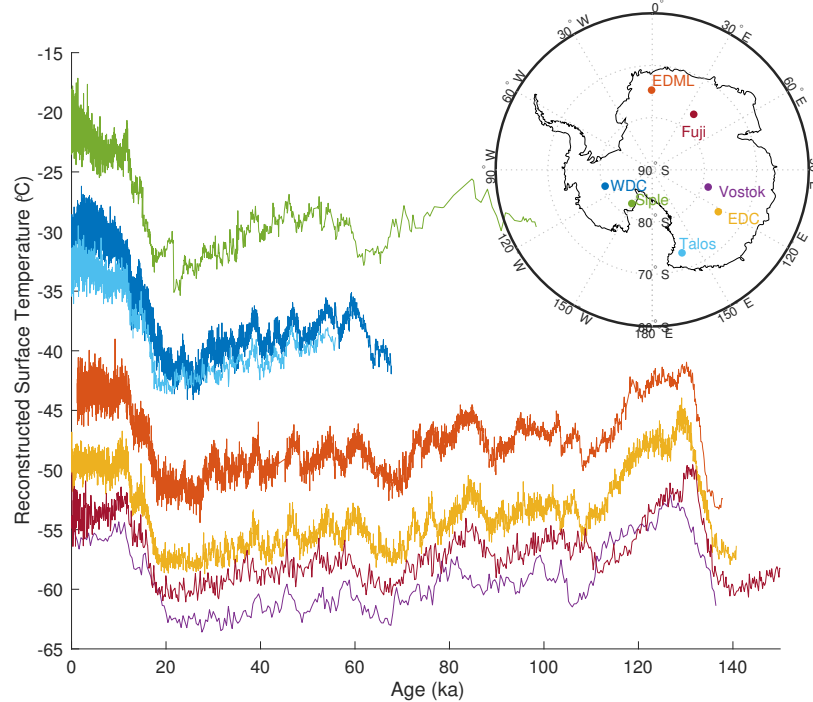


**Figure 42.** Reconstructed surface temperatures for seven ice-core sites: WDC, EDC, EDML, Siple dome, Vostok, Dome Fuji, and Talos Dome. Inset shows ice-core site locations on the continent.

the records is robust. Changes in evaporation temperatures may be influenced by changes in the atmospheric circulation which can shift the mean latitude of Antarctic moisture sources, though these effect are likely on the order of degrees of latitude (Markle et al., 2017).

It is clear from Figure 45 that the southern Pole warmed over twice as much as the Southern mid-latitudes since the Last Glacial Maximum. These results are in line with both modeling and other paleoclimate reconstructions of the pattern of polar amplification since the LGM (Masson-Delmotte et al., 2006; Otto-Bliesner et al., 2006). Notably, our reconstructions provide insight to the surface temperature changes in the midlatitude evaporation sources, where other paleoclimate records are rare.

The magnitude of glacial-interglacial warming is not constant across the Antarctic continent. As shown in Figure 46 sites with warmer modern temperatures, lower elevation, and higher latitude all show larger glacial-interglacial warming. The pattern

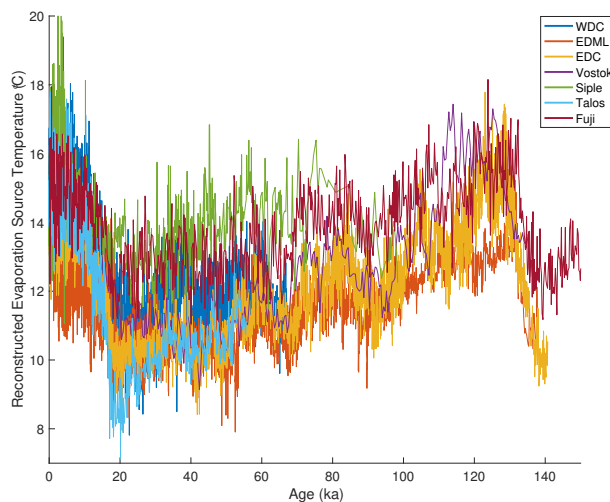


**Figure 43.** Reconstructed evaporation source temperatures for seven ice-core sites: WDC, EDC, EDML, Siple dome, Vostok, Dome Fuji, and Talos Dome.

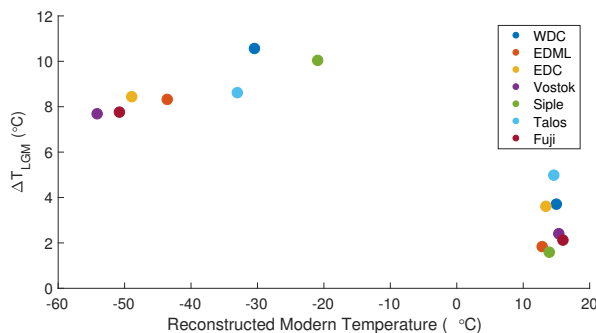


**Figure 44.** Reconstructed warming since the ( $\Delta T_{LGM}$ ) as a function of reconstructed modern temperature for Antarctic surface temperatures and moisture source evaporation temperatures. Glacial-interglacial change is the difference between the average ice-core site and evaporation-source temperatures from 9 to 11 ka and 21 to 23 ka.

largely breaks across the two main ice sheets: the lower, warmer, and higher latitude West Antarctic Ice sheet in the Pacific Sector shows greater glacial-interglacial temperature change than the higher, colder, and lower latitude East Antarctic sites. It is not yet clear what combination of these correlated physical features lead to the different magnitudes of warming between sites. The strong dependence of the

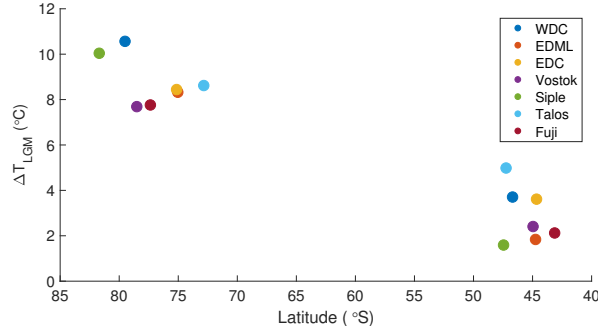


**Figure 45.** Reconstructed warming since the LGM ( $\Delta T_{LGM}$ ) as a function of latitude for Antarctic surface temperatures and moisture source evaporation temperatures. Latitudes represent modern ice-core sites and the mean latitude of the model derived moisture source distribution as described in the text. Glacial-interglacial change is the difference between the average ice-core site and evaporation-source temperatures from 9 to 11 ka and 21 to 23 ka.

magnitude of glacial-interglacial change on both site temperature and elevation may point to changes in the vertical structure of heating in the atmosphere, lapse rate changes, or ice sheet elevation changes.

The differences may also relate to the nature of West Antarctica’s climate and its position in the Pacific Sector. The spatial asymmetry in warming we find is in line with recent findings that West Antarctica is more sensitive to global climate changes than East Antarctica. For example the initiation of glacial-interglacial warming in West Antarctica began thousands of years before it began in East Antarctica (WAIS Divide Project Members et al., 2013). In the modern climate, West Antarctica has shown significant recent warming while East Antarctica has not (Steig et al., 2009), perhaps related to the sensitivity of West Antarctic climate to tropical atmospheric circulation (Steig et al., 2013).

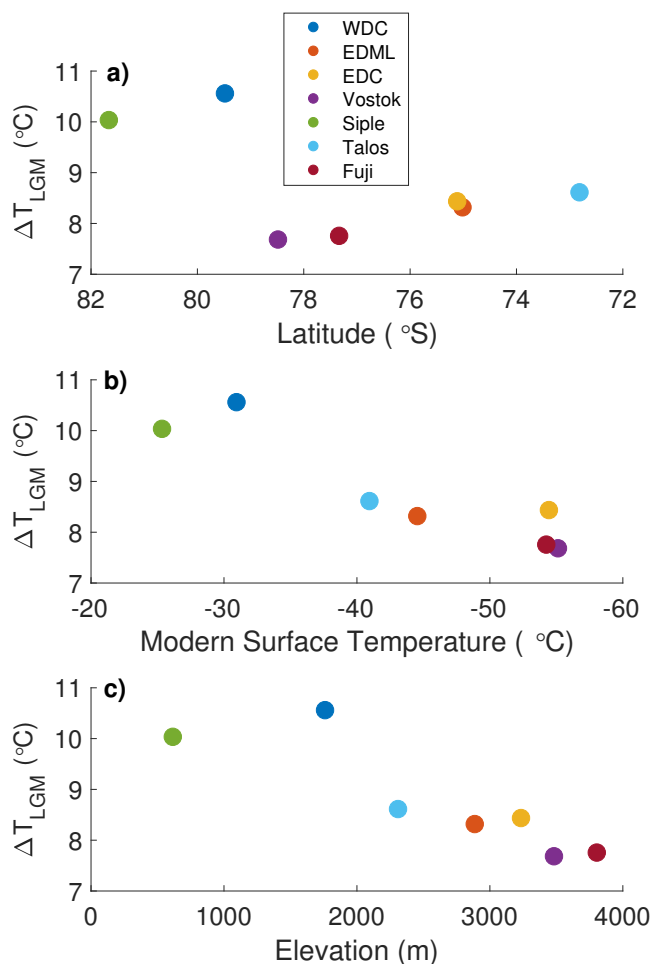


**Figure 46.** Reconstructed warming since the LGM ( $\Delta T_{LGM}$ ) as a function of modern ice-core site conditions. **a)** Glacial-Interglacial Antarctic surface temperature change versus modern ice-core site latitude. **b)** Glacial-Interglacial Antarctic surface temperature change versus observed modern site temperature. **c)** Glacial-Interglacial Antarctic surface temperature change versus modern ice-core site elevation. Glacial-interglacial change is the difference between the averages from 9 to 11 ka and 21 to 23 ka.

## 7. CONCLUSIONS

Ice-core records of the stable isotopes of water provide detailed histories of Earth's climate. Interpretation of these records requires understanding the relationships between fractionation processes and environmental conditions and is aided by models. When interpreting these records we may interpret them qualitatively as reflecting relative changes in ice-core site and moisture source-region conditions, or we could attempt to interpret them in terms of quantitative temperature changes.

In the first case,  $\delta^{18}O$  or  $\delta D$  are reliable indicators of relative change in condensation temperature. The assumption of a near-linear relationship is well justified, as shown in this study and previously. However, the linear definition of deuterium excess,  $d_{xs}$ , is unreliable as an indicator of relative evaporation-site temperature change, particularly at East Antarctic sites with very depleted  $\delta^{18}O$  and  $\delta D$  values. As shown in our analysis, nonlinearities in the slope of  $d_{xs}$  degrade its fidelity to evaporation temperature. In these cases, the logarithmic definition of the parameter,  $d_{ln}$  is a much more faithful proxy of evaporation temperature.

Alternatively, we can use empirical relationships or an isotope distillation model to make quantitative interpretations of water-isotope variability and to disentangle the combined influences of the source and site temperatures. To date all such water-isotope temperature inversions have, to my knowledge, assumed linear relationships. However, as shown here, this assumption is not valid. Even in the simplified water-isotope models that universally underly temperature reconstructions, there are nonlinearities in the isotope-temperature relationships. Ignoring these nonlinearities distorts reconstructed temperature variability. In the case of evaporation source temperature changes, these distortions may be a significant fraction of the total reconstructed variability.

There is significant debate regarding the interpretation of spatial versus temporal slopes in the water isotope-temperature relationship (e.g. Jouzel et al. (1997)). These discussions are conceptually useful. However, while space and time are obvious coordinates through which to understand climate, they are not necessarily the most relevant grids for water-isotope fractionation. Neither space nor time is an independent variable in any equation in Section 2; changes in either do not independently cause water to change phase and fractionate. The appropriate independent variables through which to understand water-isotope variability are those that influence fractionation: temperature, pressure, and saturation.

In this study we use a simple water-isotope model to understand the relationships of water isotopes in precipitation to temperature boundary conditions. By defining our state space as a temperature grid, we encapsulate the water isotope-temperature relationship. The distinction between temporal and spatial slopes is meaningless in

this context. We investigate the consistency of the water isotope-temperature relationships across this state space. This after all is the heart of the debate surrounding spatial and temporal slopes: is the water isotope-temperature relationship fixed? It is not. But the dimension through which to understand its variability is not space nor time, but temperature. The maps in Figures 23 through 27, show the variability in the relationship between water isotopes to evaporation and condensation temperatures within our self-consistent model. These results are used to reconstruct site and source variability, accounting for the full set of (nonlinear) relationships.

Our nonlinear reconstruction technique allows for the estimation of absolute temperatures in the past, in addition to their variability, and is corroborated by independent temperature constraints. By taking into account the nonlinearities in the water isotope relationships we are better able to constrain evaporation source region changes. Our reconstructions provide insight into the spatial patterns of polar amplification, suggesting that the warming since the Last Glacial Maximum in Antarctica was double that in the mid latitudes. Further our reconstructions reveal a spatial pattern of temperature change across the Antarctic continent.

#### REFERENCES

- Bakhshaii, A. and Stull, R. (2013). Saturated Pseudoadiabats-A Noniterative Approximation. *Journal of Applied Meteorology and Climatology*, 52(1):5–15.
- Barbante, C., Barnola, J.-M., Becagli, S., Beer, J., Bigler, M., Boutron, C., Blunier, T., Castellano, E., Cattani, O., Chappellaz, J., et al. (2006). One-to-one coupling of glacial climate variability in Greenland and Antarctica. *Nature*, 444(7116):195–198.
- Barkan, E. and Luz, B. (2005). High precision measurements of  $^{17}\text{O}/^{16}\text{O}$  and  $^{18}\text{O}/^{16}\text{O}$  ratios in  $\text{H}_2\text{O}$ . *Rapid Communications in Mass Spectrometry*, 19(24):3737–3742.
- Barkan, E. and Luz, B. (2007). Diffusivity fractionations of  $\text{H } ^{216}\text{O}/\text{H } ^{217}\text{O}$  and  $\text{H } ^{216}\text{O}/\text{H } ^{218}\text{O}$  in air and their implications for isotope hydrology. *Rapid Communications in Mass Spectrometry*, 21(18):2999–3005.
- Bintanja, R. and Van de Wal, R. (2008). North American ice-sheet dynamics and the onset of 100,000-year glacial cycles. *Nature*, 454(7206):869–872.
- Brook, E. J., White, J. W., Schilla, A. S., Bender, M. L., Barnett, B., Severinghaus, J. P., Taylor, K. C., Alley, R. B., and Steig, E. J. (2005). Timing of millennial-scale climate change at Siple Dome, West Antarctica, during the last glacial period Siple Dome, West Antarctica, during the last glacial period. *Quaternary Science Reviews*, 24(12):1333–1343.

- Ciais, P. and Jouzel, J. (1994). Deuterium and oxygen 18 in precipitation: Isotopic model, including mixed cloud processes. *Journal of Geophysical Research: Atmospheres*, 99(D8):16793–16803.
- Connolley, W. (1996). The Antarctic temperature inversion. *International Journal of Climatology*, 16(12):1333–1342.
- Craig, H. (1961). Isotopic variations in meteoric waters. *Science*, 133(3465):1702–1703.
- Craig, H. and Gordon, L. I. (1965). Deuterium and oxygen 18 variations in the ocean and the marine atmosphere.
- Criss, R. E. (1999). *Principles of stable isotope distribution*. Oxford University Press.
- Cuffey, K. M., Clow, G. D., Steig, E. J., Buizert, C., Fudge, T., Koutnik, M., Waddington, E. D., Alley, R. B., and Severinghaus, J. P. (2016). Deglacial temperature history of West Antarctica. *Proceedings of the National Academy of Sciences*, 113(50):14249–14254.
- Dahe, Q., Petit, J., Jouzel, J., and Stievenard, M. (1994). Distribution of stable isotopes in surface snow along the route of the 1990 International Trans-Antarctica Expedition. *Journal of Glaciology*, 40(134):107–118.
- Dai, A. (2006). Recent climatology, variability, and trends in global surface humidity. *Journal of Climate*, 19(15):3589–3606.
- Dansgaard, W. (1964). Stable isotopes in precipitation. *Tellus*, 16(4):436–468.
- Dansgaard, W., Johnsen, S. J., Møller, J., and Langway, C. C. (1969). One thousand centuries of climatic record from Camp Century on the Greenland ice sheet. *Science*, 166(3903):377–380.
- Dee, D., Uppala, S., Simmons, A., Berrisford, P., Poli, P., Kobayashi, S., Andrae, U., Balmaseda, M., Balsamo, G., Bauer, P., et al. (2011). The ERA-Interim reanalysis: Configuration and performance of the data assimilation system. *Quarterly Journal of the royal meteorological society*, 137(656):553–597.
- Ellehoj, M., Steen-Larsen, H. C., Johnsen, S. J., and Madsen, M. B. (2013). Ice-vapor equilibrium fractionation factor of hydrogen and oxygen isotopes: Experimental investigations and implications for stable water isotope studies. *Rapid Communications in Mass Spectrometry*, 27(19):2149–2158.
- Epstein, S., Sharp, R. P., and Goddard, I. (1963). Oxygen-isotope ratios in Antarctic snow, firn, and ice. *The Journal of Geology*, 71(6):698–720.
- Fudge, T., Markle, B. R., Cuffey, K. M., Buizert, C., Taylor, K. C., Steig, E. J., Waddington, E. D., Conway, H., and Koutnik, M. (2016). Variable relationship between accumulation and temperature in West Antarctica for the past 31,000 years. *Geophysical Research Letters*, 43(8):3795–3803.
- Gonfiantini, R. (1959). Oxygen isotope variations in Antarctic snow samples. *Nature*, 184:1557–1558.

- Gonfiantini, R. (1965). Some results on oxygen isotope stratigraphy in the deep drilling at King Baudouin Station, Antarctica. *Journal of Geophysical Research*, 70(8):1815–1819.
- Hartmann, D. L. (2015). *Global physical climatology*, volume 103. Newnes.
- Holme, C. (unpublished (2017)). Diffusion lengths at WAIS Divide.
- Hong, S.-Y., Dudhia, J., and Chen, S.-H. (2004). A revised approach to ice microphysical processes for the bulk parameterization of clouds and precipitation. *Monthly Weather Review*, 132(1):103–120.
- Hu, Y., Rodier, S., Xu, K.-m., Sun, W., Huang, J., Lin, B., Zhai, P., and Josset, D. (2010). Occurrence, liquid water content, and fraction of supercooled water clouds from combined CALIOP/IIR/MODIS measurements. *Journal of Geophysical Research: Atmospheres*, 115(D4).
- IAEA (2001). GNIP Maps and Animations. International Atomic Energy Agency, Vienna. Accessible at <http://isohis.iaea.org>.
- Johnsen, S. J., Clausen, H. B., Cuffey, K. M., Hoffmann, G., Schwander, J., and Creyts, T. (2000). Diffusion of stable isotopes in polar firn and ice: the isotope effect in firn diffusion. *Physics of ice core records*, 159:121–140.
- Jouzel, J., Alley, R. B., Cuffey, K., Dansgaard, W., Grootes, P., Hoffmann, G., Johnsen, S. J., Koster, R., Peel, D., Shuman, C., et al. (1997). Validity of the temperature reconstruction from water isotopes in ice cores. *Journal of Geophysical Research: Oceans*, 102(C12):26471–26487.
- Jouzel, J. and Merlivat, L. (1984). Deuterium and oxygen 18 in precipitation: Modeling of the isotopic effects during snow formation. *Journal of Geophysical Research: Atmospheres*, 89(D7):11749–11757.
- Jouzel, J., Merlivat, L., and Lorius, C. (1982). Deuterium excess in an East Antarctic ice core suggests higher relative humidity at the oceanic surface during the last glacial maximum. *Nature*, 299(5885):688–691.
- Kalnay, E., Kanamitsu, M., Kistler, R., Collins, W., Deaven, D., Gandin, L., Iredell, M., Saha, S., White, G., Woollen, J., et al. (1996). The NCEP/NCAR 40-year reanalysis project. *Bulletin of the American meteorological Society*, 77(3):437–471.
- Kavanaugh, J. L. and Cuffey, K. M. (2002). Generalized view of source region effects on  $\delta d$  and deuterium excess of ice sheet precipitation. *Annals of Glaciology*, 35(1):111–117.
- Kavanaugh, J. L. and Cuffey, K. M. (2003). Space and time variation of  $\delta^{18}O$  and  $\delta D$  in Antarctic precipitation revisited. *Global Biogeochemical Cycles*, 17(1).
- Lamb, K. D., Clouser, B. W., Bolot, M., Sarkozy, L., Ebert, V., Saathoff, H., Möhler, O., and Moyer, E. J. (2017). Laboratory measurements of HDO/H<sub>2</sub>O isotopic fractionation during ice deposition in simulated cirrus clouds. *Proceedings of the National Academy of Sciences*, page 201618374.

- Landais, A., Ekaykin, A., Barkan, E., Winkler, R., and Luz, B. (2012). Seasonal variations of  $17\text{O}$ -excess and  $d$ -excess in snow precipitation at Vostok station, East Antarctica. *Journal of Glaciology*, 58(210):725–733.
- Langway, C. C. (1958). A 400 Meter Deep Ice Core in Greenland: Preliminary Report. *Journal of Glaciology*, 3(23):217–217.
- Liu, J., Xiao, C., Ding, M., and Ren, J. (2014). Variations in stable hydrogen and oxygen isotopes in atmospheric water vapor in the marine boundary layer across a wide latitude range. *Journal of Environmental Sciences*, 26(11):2266–2276.
- Luz, B., Barkan, E., Yam, R., and Shemesh, A. (2009). Fractionation of oxygen and hydrogen isotopes in evaporating water. *Geochimica et Cosmochimica Acta*, 73(22):6697–6703.
- Markle, B., Bertler, N., Sinclair, K., and Sneed, S. (2012). Synoptic variability in the Ross Sea region, Antarctica, as seen from back-trajectory modeling and ice core analysis. *Journal of Geophysical Research: Atmospheres*, 117(D2).
- Markle, B. R. (2017). The great atmospheric washing machine. PhD Thesis Chapter, University of Washington.
- Markle, B. R., Steig, E. J., Buizert, C., Schoenemann, S. W., Bitz, C. M., Fudge, T., Pedro, J. B., Ding, Q., Jones, T. R., White, J. W., et al. (2017). Global atmospheric teleconnections during Dansgaard-Oeschger events. *Nature Geoscience*, 10(1):36–40.
- Masson-Delmotte, V., Hou, S., Ekaykin, A., Jouzel, J., Aristarain, A., Bernardo, R., Bromwich, D., Cattani, O., Delmotte, M., Falourd, S., et al. (2008). A review of Antarctic surface snow isotopic composition: Observations, atmospheric circulation, and isotopic modeling. *Journal of Climate*, 21(13):3359–3387.
- Masson-Delmotte, V., Kageyama, M., Braconnot, P., Charbit, S., Krinner, G., Ritz, C., Guilyardi, E., Jouzel, J., Abe-Ouchi, A., Crucifix, M., et al. (2006). Past and future polar amplification of climate change: climate model intercomparisons and ice-core constraints. *Climate Dynamics*, 26(5):513–529.
- Merlivat, L. (1978). Molecular diffusivities of  $\text{H}_2$   $^{16}\text{O}$ ,  $\text{HD}$   $^{16}\text{O}$ , and  $\text{H}_2$   $^{18}\text{O}$  in gases. *The Journal of Chemical Physics*, 69(6):2864–2871.
- Merlivat, L. and Jouzel, J. (1979). Global climatic interpretation of the deuterium-oxygen 18 relationship for precipitation. *Journal of Geophysical Research: Oceans*, 84(C8):5029–5033.
- Merlivat, L. and Nief, G. (1967). Fractionnement isotopique lors des changements d'état solide-vapeur et liquide-vapeur de l'eau à des températures inférieures à  $0^\circ\text{C}$ . *Tellus*, 19(1):122–127.
- Murphy, D. and Koop, T. (2005). Review of the vapour pressures of ice and supercooled water for atmospheric applications. *Quarterly Journal of the Royal Meteorological Society*, 131(608):1539–1565.
- Murray, F. W. (1966). On the computation of saturation vapor pressure.

- Otto-Bliesner, B. L., Brady, E. C., Clauzet, G., Tomas, R., Levis, S., and Kothavala, Z. (2006). Last glacial maximum and Holocene climate in CCSM3. *Journal of Climate*, 19(11):2526–2544.
- Pang, H., Hou, S., Landais, A., Masson-Delmotte, V., Prie, F., Steen-Larsen, H. C., Risi, C., Li, Y., Jouzel, J., Wang, Y., et al. (2015). Spatial distribution of 17 O-excess in surface snow along a traverse from Zhongshan station to Dome A, East Antarctica. *Earth and Planetary Science Letters*, 414:126–133.
- Petit, J.-R., Jouzel, J., Raynaud, D., Barkov, N. I., Barnola, J.-M., Basile, I., Bender, M., Chappellaz, J., Davis, M., Delaygue, G., et al. (1999). Climate and atmospheric history of the past 420,000 years from the Vostok ice core, Antarctica. *Nature*, 399(6735):429–436.
- Pfahl, S. and Wernli, H. (2009). Lagrangian simulations of stable isotopes in water vapor: An evaluation of nonequilibrium fractionation in the Craig-Gordon model. *Journal of Geophysical Research: Atmospheres*, 114(D20).
- Rayleigh, L. (1902). Lix. on the distillation of binary mixtures. *The London, Edinburgh, and Dublin Philosophical Magazine and Journal of Science*, 4(23):521–537.
- Risi, C., Landais, A., Bony, S., Jouzel, J., Masson-Delmotte, V., and Vimeux, F. (2010). Understanding the 17o excess glacial-interglacial variations in Vostok precipitation. *Journal of Geophysical Research: Atmospheres*, 115(D10).
- Schmidt, G., Bigg, G., and Rohling, E. (1999). Global seawater oxygen-18 database—v1. 21. Online at <http://data.giss.nasa.gov/o18data>, online at <http://data.giss.nasa.gov/o18data>.
- Schoenemann, S. W., Steig, E. J., Ding, Q., Markle, B. R., and Schauer, A. J. (2014). Triple water-isotopologue record from WAIS Divide, Antarctica: Controls on glacial-interglacial changes in 17oexcess of precipitation. *Journal of Geophysical Research: Atmospheres*, 119(14):8741–8763.
- Sodemann, H. and Stohl, A. (2009). Asymmetries in the moisture origin of Antarctic precipitation. *Geophysical research letters*, 36(22).
- Steig, E. J., Ding, Q., White, J. W., Küttel, M., Rupper, S. B., Neumann, T. A., Neff, P. D., Gallant, A. J., Mayewski, P. A., Taylor, K. C., et al. (2013). Recent climate and ice-sheet changes in West Antarctica compared with the past 2,000 years. *Nature Geoscience*, 6(5):372–375.
- Steig, E. J., Schneider, D. P., Rutherford, S. D., Mann, M. E., Comiso, J. C., and Shindell, D. T. (2009). Warming of the Antarctic ice-sheet surface since the 1957 International Geophysical Year. *Nature*, 457(7228):459–462.
- Stenni, B., Buiron, D., Frezzotti, M., Albani, S., Barbante, C., Bard, E., Barnola, J., Baroni, M., Baumgartner, M., Bonazza, M., et al. (2011). Expression of the bipolar see-saw in Antarctic climate records during the last deglaciation. *Nature Geoscience*, 4(1):46–49.

- Stenni, B., Jouzel, J., Masson-Delmotte, V., Röthlisberger, R., Castellano, E., Cattani, O., Falourd, S., Johnsen, S., Longinelli, A., Sachs, J., et al. (2004). A late-glacial high-resolution site and source temperature record derived from the EPICA Dome C isotope records (East Antarctica). *Earth and Planetary Science Letters*, 217(1):183–195.
- Stenni, B., Masson-Delmotte, V., Selmo, E., Oerter, H., Meyer, H., Röthlisberger, R., Jouzel, J., Cattani, O., Falourd, S., Fischer, H., et al. (2010). The deuterium excess records of EPICA Dome C and Dronning Maud Land ice cores (East Antarctica). *Quaternary Science Reviews*, 29(1):146–159.
- Tegen, I. and Fung, I. (1994). Modeling of mineral dust in the atmosphere: Sources, transport, and optical thickness. *Journal of Geophysical Research: Atmospheres*, 99(D11):22897–22914.
- Uemura, R., Barkan, E., Abe, O., and Luz, B. (2010). Triple isotope composition of oxygen in atmospheric water vapor. *Geophysical Research Letters*, 37(4).
- Uemura, R., Masson-Delmotte, V., Jouzel, J., Landais, A., Motoyama, H., and Stenni, B. (2012). Ranges of moisture-source temperature estimated from Antarctic ice cores stable isotope records over glacial–interglacial cycles. *Climate of the Past*, 8(3):1109–1125.
- Uemura, R., Matsui, Y., Yoshimura, K., Motoyama, H., and Yoshida, N. (2008). Evidence of deuterium excess in water vapor as an indicator of ocean surface conditions. *Journal of Geophysical Research: Atmospheres*, 113(D19).
- Vimeux, F., Cuffey, K. M., and Jouzel, J. (2002). New insights into Southern Hemisphere temperature changes from Vostok ice cores using deuterium excess correction. *Earth and Planetary Science Letters*.
- WAIS Divide Project Members et al. (2013). Onset of deglacial warming in West Antarctica driven by local orbital forcing. *Nature*, 500(7463):440–444.
- WAIS Divide Project Members et al. (2015). Precise inter-polar phasing of abrupt climate change during the last ice age. *Nature*, 520(7549):661–665.
- Winkler, R., Landais, A., Sodemann, H., Dümbgen, L., Prié, F., Masson-Delmotte, V., Stenni, B., and Jouzel, J. (2012). Deglaciation records of  $17\text{O}$ -excess in East Antarctica: reliable reconstruction of oceanic normalized relative humidity from coastal sites. *Climate of the Past*, 8(1):1–16.
- Xiao, C., Ding, M., Masson-Delmotte, V., Zhang, R., Jin, B., Ren, J., Li, C., Werner, M., Wang, Y., Cui, X., et al. (2013). Stable isotopes in surface snow along a traverse route from Zhongshan station to Dome A, East Antarctica. *Climate dynamics*, 41(9-10):2427–2438.

## Supplemental Materials: Title

### S1. UNCERTAINTY PROPAGATION

**S1.1. Uncorrelated uncertainty.** Assume we have two variables  $x$  and  $y$ , with known uncertainties  $\sigma_x$  and  $\sigma_y$ . We introduce a new parameter  $z$  which is a function of both  $x$  and  $y$ :

$$z = f(x, y) \quad (\text{S1})$$

Assuming the uncertainties in  $x$  and  $y$  are uncorrelated, then the uncertainty in  $z$  is

$$\sigma_z^2 = \left(\frac{\partial f}{\partial x}\right)^2 \sigma_x^2 + \left(\frac{\partial f}{\partial y}\right)^2 \sigma_y^2 \quad (\text{S2})$$

Lets now think about water isotopes. Assume a  $\delta$  value with uncertainty  $\sigma$ . If we take the logarithmic form of the delta value,

$$\delta' = g(\delta) = \log(1 + \delta) \quad (\text{S3})$$

it will have an uncertainty

$$\sigma'^2 = \left(\frac{\partial g}{\partial \delta}\right)^2 \sigma^2 \quad (\text{S4})$$

which reduces to

$$\sigma' = \frac{\sigma}{1 + \delta} \quad (\text{S5})$$

**S1.1.1. Linear deuterium excess.** Now lets consider deuterium excess,  $d_{xs} = h(\delta D, \delta^{18}O)$ , which historically has the form:

$$d_{xs} = \delta D - k \times \delta^{18}O = \delta D - 8 \times \delta^{18}O \quad (\text{S6})$$

Assume a  $\sigma_D$  and  $\sigma_{18}$  and that they are uncorrelated, as would be the case for traditional water isotope measurements. Then,

$$\sigma_{xs}^2 = \left(\frac{\partial h}{\partial \delta D}\right)^2 \sigma_D^2 + \left(\frac{\partial h}{\partial \delta^{18}O}\right)^2 \sigma_{18}^2 \quad (\text{S7})$$

which becomes

$$\sigma_{xs}^2 = \sigma_D^2 + k^2 \sigma_{18}^2 = \sigma_D^2 + 64 \sigma_{18}^2 \quad (\text{S8})$$

S1.1.2. *Logarithmic deuterium excess.* Finally, we can consider the logarithmic (and non-linear) form of the deuterium excess  $d_{ln} = H(\delta' D, \delta^{18} O)$ :

$$d_{ln} = \delta' D - (a(\delta^{18} O)^2 + b\delta^{18} O + c) \quad (\text{S9})$$

and assume, for now, uncertainties  $\sigma'_D$  and  $\sigma'_{18}$ , which we can relate to  $\sigma_D$  and  $\sigma_{18}$ , as above. This logarithmic excess quantity will have uncertainty

$$\sigma_{ln}^2 = \left( \frac{\partial H}{\partial \delta' D} \right)^2 \sigma_D'^2 + \left( \frac{\partial H}{\partial \delta^{18} O} \right)^2 \sigma_{18}'^2 \quad (\text{S10})$$

which becomes,

$$\sigma_{ln}^2 = \sigma_D'^2 + (-2a\delta^{18} O - b)^2 \sigma_{18}'^2 \quad (\text{S11})$$

which, using Equations S3 and S5, becomes

$$\sigma_{ln}^2 = \left( \frac{\sigma_D}{1 + \delta D} \right)^2 + (-2a [\log(1 + \delta^{18} O)] - b)^2 \left( \frac{\sigma_{18}}{1 + \delta^{18} O} \right)^2 \quad (\text{S12})$$

This uncertainty depends on the delta values of the sample for a couple of reasons; first, because of the definition of  $\delta'$  (Equation S3); and second, because of the definition of  $d_{ln}$  (Equation S9). Of course if we assumed we knew  $\sigma'_D$  and  $\sigma'_{18}$ , rather than  $\sigma_D$  and  $\sigma_{18}$ , then  $\sigma_D$  and  $\sigma_{18}$  would depend on the delta values.

However, while  $\sigma_{ln}^2$  is a nonlinear function of the delta values, we can see that it is actually very close to the value of  $\sigma_{xs}^2$ . To the extent that the  $\delta$  values are small,  $\left( \frac{\sigma}{1 + \delta} \right)^2 \approx \sigma^2$ . For normal values of  $\delta D$ ,  $\sigma_D'^2$  is not more than 10% greater than  $\sigma_D^2$ ; while  $\sigma_{18}'^2$  is not more than 1% greater.

The term  $(-2a [\log(1 + \delta^{18} O)] - b)^2$  in Equation S12 expands to

$$4a^2 [\log(1 + \delta^{18} O)]^2 + 4ab [\log(1 + \delta^{18} O)] + b^2 \quad (\text{S13})$$

Because the value of  $a$  is small (of order  $10^{-2}$ ), as is the value of  $\log(1 + \delta^{18} O)$  (on the order of ‰), the first two terms in Equation S13, are very small. Because  $b$  has a value near that of  $k$ , the whole of Equation S13, is actually very close in value to  $k^2$  (as in Equation S8), within 0.1%, for normal values of  $\delta^{18} O$ . Equations S8 and S12 in practice mean that  $\sigma_{ln}^2$  and  $\sigma_{xs}^2$  are very similar.

**S1.2. Correlated uncertainty.** In the case of correlated errors our uncertainty propagation becomes a little more complicated. Let's start by paraphrasing an example from Wikipedia ([https://en.wikipedia.org/wiki/Propagation\\_of\\_uncertainty](https://en.wikipedia.org/wiki/Propagation_of_uncertainty)).

Take our variables  $x$  and  $y$ , and function from Equation S1,  $z = f(x, y)$ , with uncorrelated uncertainties  $\sigma_x$  and  $\sigma_y$ . Now let's assume additional correlated uncertainties which may be quantified as the covariance  $\sigma_{xy}$ . Let's say our function  $z$  has the form:

$$z = f(x, y) = ax - by \quad (\text{S14})$$

The total uncertainty in  $z$ , including both uncorrelated and correlated uncertainty, will be

$$\sigma_z^2 = a^2\sigma_x + b^2\sigma_y - 2ab\sigma_{xy} \quad (\text{S15})$$

**S1.2.1. Linear deuterium excess.** Modern measurements of  $\delta^{18}\text{O}$  and  $\delta D$  are often made on laser instruments and may have correlated uncertainties. This will influence the deuterium excess uncertainty. We can see from Equations S15, S6, and S7, that the uncertainty in the linear definition of deuterium excess will have the form:

$$\sigma_{xs}^2 = \sigma_D^2 + k^2\sigma_{18}^2 - 2k\sigma_{D18} \quad (\text{S16})$$

where  $k$  is the linear scaling factor (with a value of 8, historically), and  $\sigma_{D18}$  is the covariance of  $\delta^{18}\text{O}$  and  $\delta D$ , due to correlated errors.

In practice this uncertainty becomes:

$$\sigma_{xs}^2 = \sigma_D^2 + 64\sigma_{18}^2 - 16\sigma_{D18} \quad (\text{S17})$$

Note that in the case of deuterium excess, correlated uncertainties actually *decrease* the total uncertainty of the parameter. This makes sense. The deuterium excess is the scaled difference between  $\delta D$  and  $\delta^{18}\text{O}$ . Uncertainty that covaries with the two will not influence the difference.

**S1.2.2. Logarithmic deuterium excess.** In the case of the logarithmic definition of deuterium excess, with correlated uncertainties, the situation becomes more complicated still. We will consider our function  $z = f(x, y)$  again, where  $f$  is this time a differentiable but nonlinear function. We can expand  $f$ , and ignore higher order terms,

$$z \approx f_0 + \frac{\partial f}{\partial x}x + \frac{\partial f}{\partial y}y \quad (\text{S18})$$

In this case our uncertainty for  $z$  will be

$$\sigma_z^2 \approx \left| \frac{\partial f}{\partial x} \right|^2 \sigma_x^2 + \left| \frac{\partial f}{\partial y} \right|^2 \sigma_y^2 + 2 \frac{\partial f}{\partial x} \frac{\partial f}{\partial y} \sigma_{xy} \quad (\text{S19})$$

We can now apply this to the logarithmic (and non-linear) definition of deuterium excess accounting for correlated errors.

Recall from Equation S9 above,  $d_{ln} = H(\delta' D, \delta'^{18} O) = \delta' D - (a(\delta'^{18} O)^2 + b\delta'^{18} O + c)$ . In this case,

$$\frac{\partial H}{\partial \delta'^{18} O} = 1 \quad (\text{S20})$$

and

$$\frac{\partial H}{\partial \delta'^{18} O} = -2a\delta'^{18} O - b \quad (\text{S21})$$

Thus, from Equation S19, we see that

$$\sigma_{ln}^2 \approx \sigma_D'^2 + |-2a\delta'^{18} O - b|^2 \sigma_{18}'^2 + (2a\delta'^{18} O - b) \sigma_{D18}' \quad (\text{S22})$$

where  $\sigma_{D18}'$ , is the covariance of  $\delta' D$  and  $\delta'^{18} O$ .

Substituting, Equations S3 and S5 into Equation S22, we see that

$$\sigma_{ln}^2 \approx \left( \frac{\sigma_D}{1 + \delta D} \right)^2 + |-2a [\log(1 + \delta^{18} O)] - b|^2 \sigma_{18}'^2 + (2a [\log(1 + \delta^{18} O)] - b) \sigma_{D18}' \quad (\text{S23})$$

Note again that the correlated uncertainty, *reduces* the total uncertainty in the excess parameter, in this case potentially more so than in the linear definition. Following the same reasoning as in Section S1.1.2, primarily that  $\delta$  values are small, that the value of  $a$  is small, and that the value of  $b$  is very similar to the value of  $k$ , the uncertainty in the logarithmic and linear definitions of deuterium excess, when accounting for both correlated and uncorrelated errors, Equations S16 and S23 are in practice nearly the same. A possible exception is potential differences in  $\sigma_{D18}$  and  $\sigma_{D18}'$ , the covariances. I expect these are extremely similar as well and this can be directly evaluated from data.

Chapter 3

**GLOBAL ATMOSPHERIC TELECONNECTIONS DURING  
DANSGAARD-OESCHGER EVENTS**

# Global atmospheric teleconnections during Dansgaard–Oeschger events

Bradley R. Markle<sup>1\*</sup>, Eric J. Steig<sup>1,2</sup>, Christo Buizert<sup>3</sup>, Spruce W. Schoenemann<sup>1</sup>, Cecilia M. Bitz<sup>2</sup>, T. J. Fudge<sup>1</sup>, Joel B. Pedro<sup>4</sup>, Qinghua Ding<sup>5</sup>, Tyler R. Jones<sup>6</sup>, James W. C. White<sup>6</sup> and Todd Sowers<sup>7</sup>

**During the last glacial period, the North Atlantic region experienced a series of Dansgaard–Oeschger cycles in which climate abruptly alternated between warm and cold periods. Corresponding variations in Antarctic surface temperature were out of phase with their Northern Hemisphere counterparts. The temperature relationship between the hemispheres is commonly attributed to an interhemispheric redistribution of heat by the ocean overturning circulation. Changes in ocean heat transport should be accompanied by changes in atmospheric circulation to satisfy global energy budget constraints. Although changes in tropical atmospheric circulation linked to abrupt events in the Northern Hemisphere are well documented, evidence for predicted changes in the Southern Hemisphere's atmospheric circulation during Dansgaard–Oeschger cycles is lacking. Here we use a high-resolution deuterium-excess record from West Antarctica to show that the latitude of the mean moisture source for Antarctic precipitation changed in phase with abrupt shifts in Northern Hemisphere climate, and significantly before Antarctic temperature change. This provides direct evidence that Southern Hemisphere mid-latitude storm tracks shifted within decades of abrupt changes in the North Atlantic, in parallel with meridional migrations of the intertropical convergence zone. We conclude that both oceanic and atmospheric processes, operating on different timescales, link the hemispheres during abrupt climate change.**

**D**ansgaard–Oeschger (DO) events in the Northern Hemisphere (NH)<sup>1,2</sup> and Antarctic isotope maximum (AIM) events in the Southern Hemisphere (SH) are coupled by variations in meridional oceanic heat transport. The large effective heat capacity of the SH oceans integrates the abrupt changes in oceanic heat transport<sup>3</sup>, leading to the muted, out-of-phase character of Antarctic temperature variations<sup>4</sup>. The Antarctic temperature response systematically lags abrupt DO transitions by about two centuries, a timescale consistent with oceanic processes<sup>5</sup>.

To satisfy the top-of-atmosphere energy budget, interhemispheric oceanic heat flux anomalies must be accommodated by opposing changes in atmospheric heat transport<sup>6</sup> or changes in local radiative processes. While atmospheric models do not necessarily agree on the relative roles of these mechanisms, some responses are robust, such as migration of the Hadley circulation and intertropical convergence zone (ITCZ) toward the warmer hemisphere<sup>6,7</sup>. Recent studies suggest that ITCZ migration can influence the position of the SH eddy-driven jet and surface westerlies<sup>8,9</sup>. The SH mid-latitude westerlies are a key component of the global climate, transporting heat and momentum toward the pole and influencing Southern Ocean wind-driven upwelling<sup>10</sup> and ocean–atmospheric CO<sub>2</sub> exchange<sup>11</sup>. Evidence for abrupt changes in tropical circulation and precipitation, synchronous with NH DO events, comes from sediment cores<sup>12–14</sup> and speleothem records<sup>15</sup>. In contrast, evidence for corresponding millennial-scale changes in the dynamics or meridional position of the SH westerlies is wanting<sup>16</sup>.

## New constraints from ice core records

Here, we use deuterium-excess data from the West Antarctic ice sheet (WAIS) Divide ice core (WDC) to constrain changes in SH atmospheric circulation during DO events. Deuterium excess ( $d_{\text{excess}} = \delta D - 8 \times \delta^{18}\text{O}$ ) of vapour quantifies kinetic fractionation processes and is sensitive to sea surface temperature (SST) and relative humidity at the site of evaporation<sup>17</sup>. Variability in the SST-normalized humidity, the critical moisture source condition driving kinetic fractionation<sup>17</sup>, is probably dominated by changes in SST on millennial timescales, although relative humidity may also be important (Supplementary Information). The  $d_{\text{excess}}$  is also directly affected by SST through the temperature dependence of fractionation at evaporation<sup>17</sup>. The  $d_{\text{excess}}$  of polar precipitation reflects the weighted-mean evaporative conditions of moisture sources, whose spatial distribution is sensitive to changes in atmospheric circulation.

Interpretation of Antarctic  $d_{\text{excess}}$  records has been hampered by the absence of a coherent signal among Antarctic cores<sup>18,19</sup> (Fig. 1a). We find that the lack of coherence is largely an artefact of the linear definition of  $d_{\text{excess}}$ . Equilibrium fractionation alone leads to a nonlinear relationship between  $\delta D$  and  $\delta^{18}\text{O}$  (ref. 20) that is most evident at the very depleted values in East Antarctic precipitation (Supplementary Information). We instead use a logarithmic definition<sup>21</sup> for the parameter,  $d_{\text{in}} = \ln(\delta D + 1) - (8.47 \ln(\delta^{18}\text{O} + 1) - 2.85 \times 10^{-2} (\ln(\delta^{18}\text{O} + 1))^2)$ , which better represents the underlying distillation physics and is a more faithful proxy for moisture source variability (Supplementary Information).

<sup>1</sup>Department of Earth and Space Sciences, University of Washington, Seattle, Washington 98195-1310, USA. <sup>2</sup>Department of Atmospheric Sciences, University of Washington, Seattle, Washington 98195-1640, USA. <sup>3</sup>College of Earth, Oceanic and Atmospheric Sciences, Oregon State University, Corvallis, Oregon 97331, USA. <sup>4</sup>Centre for Ice and Climate, University of Copenhagen, Copenhagen DKK-2100, Denmark. <sup>5</sup>Department of Geography, University of California, Santa Barbara, California 93016, USA. <sup>6</sup>Institute of Arctic and Alpine Research, University of Colorado, Boulder, Colorado 80309, USA. <sup>7</sup>Department of Geosciences, Pennsylvania State University, University Park, Pennsylvania 16802, USA. \*e-mail: marklebr@uw.edu

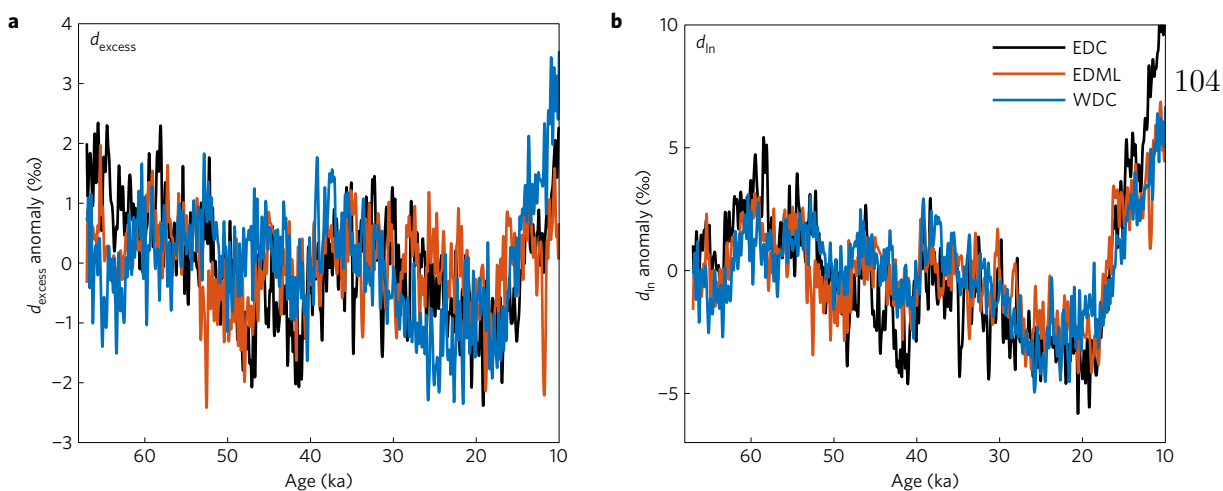


**Figure 1 | Comparison of deuterium-excess definitions for multiple ice cores.** Anomalies are the deviation from the 10 ka to 67 ka mean. A low-pass, fourth-order Butterworth filter with a 1 cycle per 300 yr cutoff frequency has been applied to all curves for visual clarity. **a**, Time series of  $d_{\text{excess}}$  for WDC (blue), EDML (red) and EDC (black). Correlation coefficient for WDC–EDML: 0.13; WDC–EDC: 0.25; EDC–EDML: 0.31. **b**, As above but for the  $d_{\text{in}}$  definition. Correlation coefficient for WDC–EDML: 0.62; WDC–EDC: 0.68; EDC–EDML: 0.74.

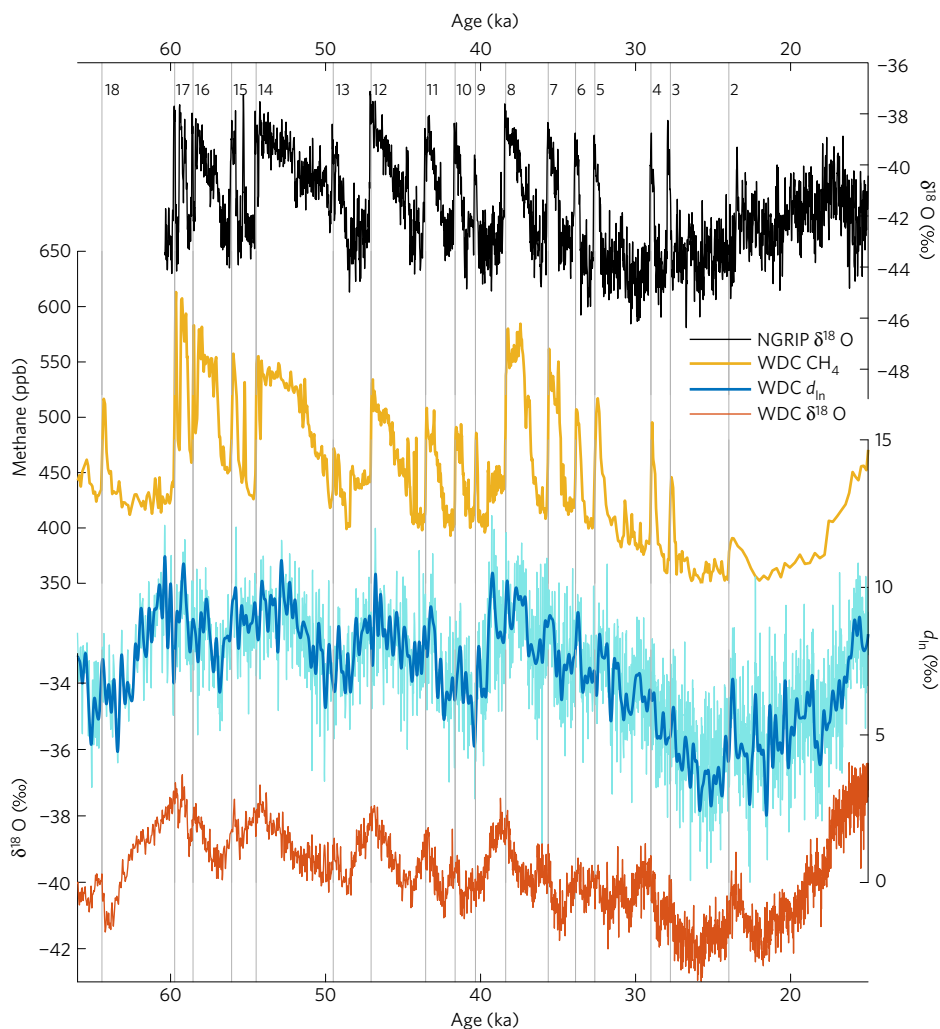


**Figure 2 | Proxy records from the last glacial period.** Greenland  $\delta^{18}\text{O}$  record from NGRIP on  $1.0063 \times \text{GICC05}$  chronology<sup>23</sup> (black). WDC  $\text{CH}_4$  (gold), WDC  $\delta^{18}\text{O}$  (red), WDC  $d_{\text{in}}$  (cyan) and filtered  $d_{\text{in}}$  (blue) on the WD2014 chronology<sup>23</sup>. High-frequency variability ( $>1$  cycle per 300 yr) removed from filtered  $d_{\text{in}}$  by a low-pass Butterworth filter for visual clarity. DO events are numbered and the timings of their midpoints are indicated by vertical grey lines.

While conventionally defined East Antarctic  $d_{\text{excess}}$  records from EPICA Dronning Maud Land (EDML) and EPICA Dome C (EDC)<sup>18</sup> show no significant coherence with WDC  $d_{\text{excess}}$  at any

timescale, the logarithmically defined  $d_{\text{in}}$  records from all three cores are significantly coherent with each other at all periods greater than 3,000 years (Fig. 1). Degradation of coherence at

shorter timescales is expected due to chronological uncertainties. Equilibrium fractionation biases, rather than spatial asymmetries in the climate, clearly dominate the differences among linearly defined  $d_{\text{excess}}$  records, while the  $d_{\text{in}}$  records reveal a coherent signal.

### Analysis of millennial-scale variability

We compare high-resolution WDC  $d_{\text{in}}$  with WDC atmospheric methane ( $\text{CH}_4$ ) concentrations and with WDC  $\delta^{18}\text{O}$ , a proxy for site temperature (Fig. 2). Global  $\text{CH}_4$  variations are in phase with Greenland temperature within a few decades<sup>22</sup> and are thought to reflect changes in tropical precipitation and temperature associated with the north–south migration of the ITCZ during DO events<sup>15,22</sup>, thus serving as an indicator for shifts in tropical circulation<sup>5</sup>. We compare these records (Fig. 2) to establish the phasing between changes in Antarctic moisture sources and SH, tropical and NH climate during DO events. The WDC records are uniquely suited for this purpose owing to the small and well-constrained gas age–ice age difference ( $\Delta\text{age}$ )<sup>5</sup>. The  $\Delta\text{age}$  is calculated continuously through the core and is  $351 \pm 73$  years ( $2\sigma$ ) at 40 thousand years ago (ka), a value representative of the last glacial period<sup>23</sup>.

The  $d_{\text{in}}$  records from WDC, EDC and EDML on average show gradual millennial-scale variability in phase with the AIM events seen in Antarctic  $\delta^{18}\text{O}$  records (Fig. 1b). However, WDC  $d_{\text{in}}$  also exhibits variability that tracks  $\text{CH}_4$  through the DO cycles (Fig. 2). Since the subjective appearance of individual events may be confounded by noise inherent to the proxies and the physical systems they record, we use objective techniques to quantify these relationships across all events.

We first evaluate the WDC data using a multitaper coherency and phase analysis (Methods). The WDC  $\delta^{18}\text{O}$ ,  $d_{\text{in}}$  and  $\text{CH}_4$  records are all significantly coherent with one another across millennial timescales. The WDC  $\delta^{18}\text{O}$  and  $\text{CH}_4$  records have a phase relationship of  $\sim 90^\circ$  at millennial timescales, reflecting integration of the NH DO events by SH climate, and a  $\sim 200$  year lag of WDC  $\delta^{18}\text{O}$  behind  $\text{CH}_4$ . The millennial variability in  $d_{\text{in}}$  is coherent with both  $\delta^{18}\text{O}$  and  $\text{CH}_4$  at phase angles between  $0^\circ$  (in phase) and  $90^\circ$ , consistent with a signal that contains both DO and AIM modes of variability. Indeed, a simple linear combination of the WDC  $\delta^{18}\text{O}$  and  $\text{CH}_4$  signals is coherent and in phase with WDC  $d_{\text{in}}$  at all timescales and is a significantly better predictor of  $d_{\text{in}}$  than either  $\delta^{18}\text{O}$  or  $\text{CH}_4$  individually. Together, the  $\text{CH}_4$  and  $\delta^{18}\text{O}$  signals explain 62% of all variance in  $d_{\text{in}}$  and more than 85% of the variance at relevant timescales (those longer than 500 years).

Next, to investigate the character of DO-like variability recorded in WDC  $d_{\text{in}}$ , we construct composites of the  $d_{\text{in}}$  record during abrupt NH warming and cooling events. We use the stacking procedure described in ref. 5, in which all individual events in all WDC proxies are aligned at the midpoints of the abrupt  $\text{CH}_4$  transitions and averaged to obtain a composite event; this allows direct comparison with DO events from the North Greenland Ice Core Project (NGRIP)  $\delta^{18}\text{O}$  record from Greenland<sup>24</sup> and reduces the noise inherent to any single event. We use objective algorithms<sup>25</sup> to determine the timing of significant change in the WDC  $d_{\text{in}}$ , NGRIP  $\delta^{18}\text{O}$ , WDC  $\text{CH}_4$  and WDC  $\delta^{18}\text{O}$  composites (Methods).

We find that the composite  $d_{\text{in}}$  response at the timing of DO warming and cooling events is step-like and occurs within decades (synchronous within uncertainty) of NH (NGRIP  $\delta^{18}\text{O}$ ) and tropical ( $\text{CH}_4$ ) step changes. The initial change points in the DO warming event stacks of NGRIP  $\delta^{18}\text{O}$ , WDC  $\text{CH}_4$ , and WDC  $d_{\text{in}}$  occur at  $-27 \pm 5$  years ( $1\sigma$ ),  $18 \pm 14$  years, and  $45 \pm 83$  years, respectively, with the timing given relative to the midpoint of the NGRIP  $\delta^{18}\text{O}$  abrupt changes (Fig. 3; see Methods for a full description of uncertainties). For DO cooling events, the initial change points in the NGRIP  $\delta^{18}\text{O}$ , WDC  $\text{CH}_4$ , and WDC  $d_{\text{in}}$  stacks occur at  $-36 \pm 7$  years,  $-24 \pm 14$  years, and  $-27 \pm 70$  years, respectively. In both cases, the change point in WDC  $d_{\text{in}}$  occurs significantly before

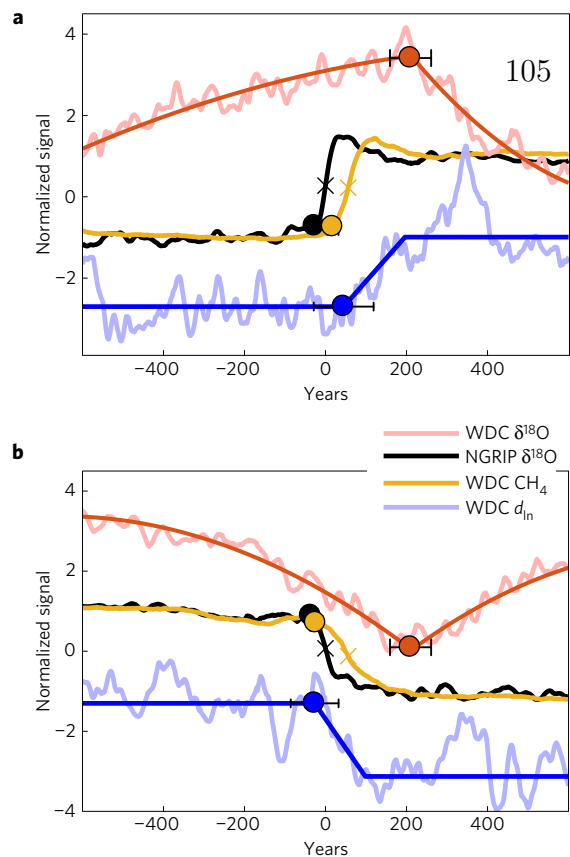


**Figure 3 | DO event compositing analysis.** **a, b**, DO warming (**a**) and cooling (**b**) stacks for NGRIP  $\delta^{18}\text{O}$  (black), WDC  $\text{CH}_4$  (gold), WDC  $\delta^{18}\text{O}$  (red), and WDC  $d_{\text{in}}$  (blue) with fits (bold; see Methods). WDC events are aligned on the midpoint of the abrupt WDC  $\text{CH}_4$  transition (yellow cross), which is set to lag the Greenland  $\delta^{18}\text{O}$  midpoint (black cross) by 56 years (Methods). The timings of initial change points in all stacks (dots) are shown with respect to the Greenland  $\delta^{18}\text{O}$  midpoint, with  $2\sigma$  uncertainty bars that reflect the full combination of age-scale, stacking, and change point detection uncertainties (see Methods).

the change point in WDC  $\delta^{18}\text{O}$ ;  $d_{\text{in}}$  leads  $\delta^{18}\text{O}$  by  $173 \pm 79$  years for DO warming, and  $235 \pm 64$  years for DO cooling.

### Global teleconnections

To elucidate the sources of WDC  $d_{\text{in}}$  variability, we review the processes thought to communicate climate signals between the hemispheres during DO and AIM events. First, variations in northward heat transport by the ocean warm one hemisphere at the expense of the other<sup>4</sup>. The surface temperature response to heating changes in the North Atlantic is abrupt, driving the DO signal. Second, the Southern Ocean integrates the changes in northward heat transport, resulting in the gradual, out-of-phase variations in Southern Ocean and Antarctic temperature<sup>3</sup>: the AIM signal. There is a discrete  $\sim 200$  year lag between the abrupt DO events and the transition between warming and cooling of the AIM events, probably reflecting an oceanic transport timescale<sup>5</sup>. Third, the thermal asymmetry between the hemispheres drives a fast ( $\leq$ decadal) atmospheric response in which the ITCZ migrates toward the warmer hemisphere<sup>6</sup>. Fourth, a related atmospheric teleconnection links migration of the ITCZ to shifts in the meridional position of the storm tracks in the Southern Hemisphere<sup>8</sup>. This teleconnection would link the position of the Southern winds to events in the tropics and high NH latitudes on short atmospheric timescales, despite gradual and lagged changes in mean SH temperatures.

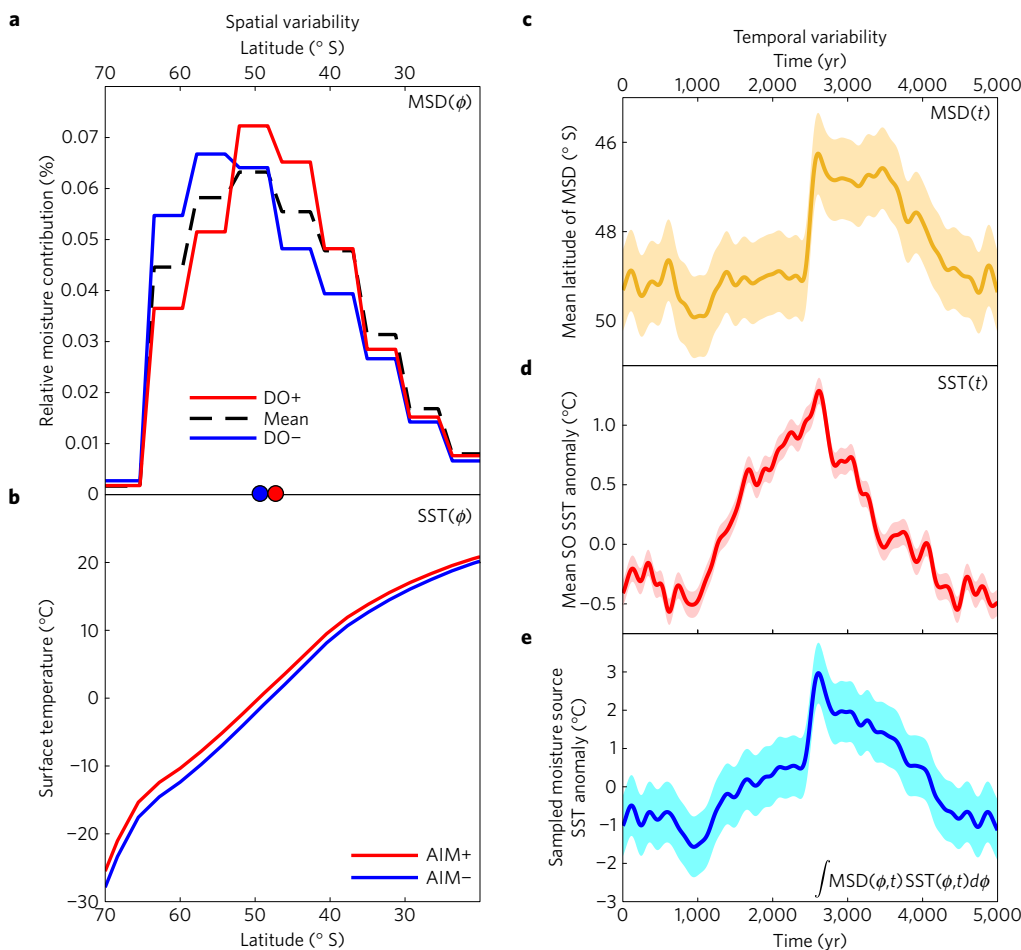


**Figure 4 | Schematic of spatial and temporal variability in moisture sources during an idealized DO/AIM cycle.** **a**, The modelled mean moisture source distribution (MSD( $\phi$ ), black dashed) for WDC (Supplementary Information) is represented as a histogram of the latitude of initial evaporation. Modelled MSDs associated with strongly northward (red) and southward (blue) shifts in the position of the Southern Hemisphere winds are associated with DO warming (+) and cooling (-) events. The weighted-mean latitudes of the displaced MSDs are shown as dots along the bottom axis. **b**, Idealized spatial patterns of surface temperature during warm (AIM+) and cold (AIM-) phases of AIM events, showing the strong meridional gradient of SST( $\phi$ ). **c-e**, Schematics of the temporal evolution of the mean MSD latitude for WDC (**c**), the mean surface temperature anomaly in the Southern Ocean (**d**) and the mean sampled moisture source temperature resulting from the superposition of **c** and **d** (**e**). Shaded bands reflect the expected levels of internal noise for each variable. Details of the schematics are described in the Supplementary Information.

A simple framework reconciles the combined AIM-like and DO-like signals in WDC  $d_{in}$  in light of the above processes. Variability in  $d_{in}$  represents the superposition of two primary mechanisms: changes in moisture source conditions at fixed locations and changes in the spatial distribution of moisture sources for an ice core site. In short, the spatial-temporal pattern of SSTs is weighted by the spatial-temporal pattern of the moisture source distribution (MSD) (Fig. 4). In the zonal mean, and given a linear SST- $d_{in}$  scaling,  $d_{in}(t) \propto \int MSD(\phi, t) SST(\phi, t) d\phi + \nu$ , where  $\phi$  and  $t$  denote dependence on latitude and time, and  $\nu$  denotes other sources of variability.

Owing to the first and second processes above, changes in Southern Ocean heat content are thought to drive the gradual Antarctic surface temperature variability of AIM events<sup>3</sup> via changes in Southern Ocean SSTs<sup>26</sup>. Southern Hemisphere SST( $t$ ) within the moisture source thus drives AIM-like variations in Antarctic  $d_{in}$  (Fig. 4), accounting for the gradual variability observed in the WDC, EDML and EDC records.

A large equator-to-pole gradient dominates the spatial pattern of SST( $\phi$ ) in the SH (Fig. 4). Meridional shifts in the mean location of the moisture source, toward more equatorward or more poleward surface waters, change the sampled mean SST at evaporation due to the steep underlying gradient. Changes in MSD( $\phi$ ) can therefore

change the  $d_{in}$  at an ice core site, independent of any temporal variability in the SSTs themselves. General circulation model simulations (Supplementary Information) show that the latitudinal distribution of moisture sources for WAIS Divide change in parallel with the meridional position of the SH westerly winds and ITCZ, changing the sampled SST and  $d_{in}$  of precipitation (Fig. 4).

The atmospheric teleconnections predicted during abrupt climate change, the third and fourth processes described above, are recorded in the WDC  $d_{in}$  shifts that occur synchronously with NH DO events (Fig. 3). An abrupt DO event shifts the position of the tropical Hadley cell, causing a parallel shift in the SH surface westerlies and storm tracks in the Pacific sector<sup>8,9</sup>, changing the moisture origin for West Antarctica. Thus, abrupt changes in moisture source location superimposed on gradual changes in moisture source temperatures lead to the observed combination of DO-like and AIM-like variability in WDC  $d_{in}$  (Fig. 4).

We calculate the scaling of  $d_{in}$  variations to source-region SSTs in a simple distillation model and an isotope-enabled general circulation model (Supplementary Information). SH SST changes on the order of 1–2 K, in phase with the AIM events, and meridional MSD shifts of 1°–2° latitude, in phase with DO events, together account for the bulk of observed variability in WDC  $d_{in}$  (Fig. 4). Southern Ocean SST changes of this magnitude are in line

with independent estimates from sediment cores<sup>26</sup>. The required MSD shifts are comparable to those associated with westerly wind displacement at the 1–1.5 $\sigma$  level of interannual variability, amounting to 15–20% anomalies in surface winds (Supplementary Information). Storm track shifts of this magnitude during DO events are in good agreement with estimates of ITCZ displacement from proxy data<sup>27</sup> and the modelled relationship between the ITCZ and the SH circulation<sup>8</sup>. Our results are supported by previous modelling showing anti-correlation between Antarctic deuterium excess and the Southern Annular Mode index<sup>28</sup>.

Did the atmospheric circulation shift zonally across the entire SH during DO events<sup>9</sup>, or were changes limited to the Pacific sector (ref. 9)? East Antarctic records may inform this question. EDC  $d_{in}$  shows variability during DO 8 and 12 out of phase with local  $\delta^{18}O$  (ref. 19) and similar to WDC (Supplementary Information). However, unambiguous characterization of the variability in East Antarctic  $d_{in}$  records is currently hampered by uncertainties in East Antarctica  $\Delta$ age, and the lack of synchronization between the WD2014<sup>23</sup> and AICC2012<sup>29</sup> age scales.

## Conclusions

Our new data from WDC demonstrate the importance of both oceanic and atmospheric teleconnections linking the climate of the Northern and Southern hemispheres on millennial timescales. SH SSTs followed the temporal signature of the AIM events, driven by oceanic heat transport changes. SH winds shifted in phase with the NH DO events, reflecting coupled changes in global atmospheric circulation. These atmospheric teleconnections were rapid, shifting the position of the moisture source locations for WDC (recorded in  $d_{in}$ ) within decades of NH DO events and about two centuries before significant Antarctic temperature change (recorded in  $\delta^{18}O$ ). Our findings complement evidence for atmospheric-circulation-imposed variability in Greenland deuterium excess<sup>30</sup>. Atmospheric dynamics link the tropical Hadley circulation to the mid-latitude storm tracks in both hemispheres. A global ‘atmospheric seesaw’ is superimposed on the classic oceanic bipolar seesaw, and may be important to the dynamics of millennial climate change.

## Methods

Methods, including statements of data availability and any associated accession codes and references, are available in the [online version of this paper](#).

Received 28 May 2016; accepted 1 November 2016;  
published online 12 December 2016

## References

- Dansgaard, W. *et al.* A new Greenland deep ice core. *Science* **218**, 1273–1277 (1982).
- Sachs, J. P. & Lehman, S. J. Subtropical North Atlantic temperatures 60,000 to 30,000 years ago. *Science* **286**, 756–759 (1999).
- Stocker, T. F. & Johnsen, S. J. A minimum thermodynamic model for the bipolar seesaw. *Paleoceanography* **18**, 1087 (2003).
- Blunier, T. *et al.* Asynchrony of Antarctic and Greenland climate change during the last glacial period. *Nature* **394**, 739–743 (1998).
- WAIS Divide Project Members. Precise inter-polar phasing of abrupt climate change during the last ice age. *Nature* **520**, 661–665 (2015).
- Kang, S. M., Frierson, D. M. W. & Held, I. M. The tropical response to extratropical thermal forcing in an idealized GCM: the importance of radiative feedbacks and convective parameterization. *J. Atmos. Sci.* **66**, 2812–2827 (2009).
- Broccoli, A. J., Dahl, K. A. & Stouffer, R. J. Response of the ITCZ to Northern Hemisphere cooling. *Geophys. Res. Lett.* **33**, L01702 (2006).
- Ceppi, P., Hwang, Y.-T., Liu, X., Frierson, D. M. W. & Hartmann, D. L. The relationship between the ITCZ and the Southern Hemispheric eddy-driven jet. *J. Geophys. Res.* **118**, 5136–5146 (2013).
- Chiang, J. C. H., Lee, S.-Y., Putnam, A. E. & Wang, X. South Pacific Split Jet, ITCZ shifts, and atmospheric North–South linkages during abrupt climate changes of the last glacial period. *Earth Planet. Sci. Lett.* **406**, 233–246 (2014).

- Marshall, J. & Speer, K. Closure of the meridional overturning circulation through Southern Ocean upwelling. *Nat. Geosci.* **5**, 171–180 (2012).
- Anderson, R. F. *et al.* Wind-driven upwelling in the Southern Ocean and the deglacial rise in atmospheric CO<sub>2</sub>. *Science* **323**, 1443–1448 (2009).
- Deplazes, G. *et al.* Links between tropical rainfall and North Atlantic climate during the last glacial period. *Nat. Geosci.* **6**, 213–217 (2013).
- Peterson, L. C., Haug, G. H., Hughen, K. A. & Röhl, U. Rapid changes in the hydrologic cycle of the tropical Atlantic during the last glacial. *Science* **290**, 1947–1951 (2000).
- Pedro, J. B. *et al.* The spatial extent and dynamics of the Antarctic cold reversal. *Nat. Geosci.* **9**, 51–55 (2016).
- Wang, X. *et al.* Interhemispheric anti-phasing of rainfall during the last glacial period. *Quat. Sci. Rev.* **25**, 3391–3403 (2006).
- Kohfeld, K. E. *et al.* Southern Hemisphere westerly wind changes during the Last glacial maximum: paleo-data synthesis. *Quat. Sci. Rev.* **68**, 76–95 (2013).
- Merlivat, L. & Jouzel, J. Global climatic interpretation of the deuterium-oxygen 18 relationship for precipitation. *J. Geophys. Res.* **84**, 5029–5033 (1979).
- Stenni, B. *et al.* The deuterium excess records of EPICA Dome C and Dronning Maud Land ice cores (East Antarctica). *Quat. Sci. Rev.* **29**, 146–159 (2010).
- Buiron, D. *et al.* Regional imprints of millennial variability during the MIS 3 period around Antarctica. *Quat. Sci. Rev.* **48**, 99–112 (2012).
- Craig, H. Isotopic variations in meteoric waters. *Science* (1961).
- Uemura, R. *et al.* Ranges of moisture-source temperature estimated from Antarctic ice cores stable isotope records over glacial–interglacial cycles. *Clim. Past* **8**, 1109–1125 (2012).
- Baumgartner, M. *et al.* NGRIP CH<sub>4</sub> concentration from 120 to 10 kyr before present and its relation to a  $\delta^{15}N$  temperature reconstruction from the same ice core. *Clim. Past* **10**, 903–920 (2014).
- Buizert, C. *et al.* The WAIS divide deep ice core WD2014 chronology: Part 1: Methane synchronization (68–31 ka BP) and the gas age–ice age difference. *Clim. Past* **11**, 153–173 (2015).
- North Greenland Ice Core Project Members. High-resolution record of Northern Hemisphere climate extending into the last interglacial period. *Nature* **431**, 147–151 (2004).
- Mudelsee, M. Ramp function regression: a tool for quantifying climate transitions. *Comput. Geosci.* **26**, 293–307 (2000).
- Barrows, T. T., Juggins, S., De Deckker, P., Calvo, E. & Pelejero, C. Long-term sea surface temperature and climate change in the Australian–New Zealand region. *Paleoceanography* **22**, PA2215 (2007).
- Wang, X. *et al.* Wet periods in northeastern Brazil over the past 210 kyr linked to distant climate anomalies. *Nature* **432**, 740–743 (2004).
- Schmidt, G. A., LeGrande, A. N. & Hoffmann, G. Water isotope expressions of intrinsic and forced variability in a coupled ocean–atmosphere model. *J. Geophys. Res.* **112**, D10103 (2007).
- Bazin, L. *et al.* An optimized multi-proxy, multi-site Antarctic ice and gas orbital chronology (AICC2012): 120–800 ka. *Clim. Past* **9**, 1715–1731 (2013).
- Masson-Delmotte, V. GRIP deuterium excess reveals rapid and orbital-scale changes in Greenland moisture origin. *Science* **309**, 118–121 (2005).

## Acknowledgements

We thank A. J. Schauer and P. D. Neff for assistance with the measurements, E. J. Brook, V. Gkinis and H. C. Steen-Larsen for insightful discussions, and B. Stenni for sharing data. We acknowledge grants from the US National Science Foundation Division of Polar Programs (0537930, 1043092 to E.J.S.; 0537593, 1043167 to J.W.C.W.; 0538538, 1043500 to T.S.; 0944197 to T.J.F.; 1043518 to E. J. Brook; and 1341497 to C.M.B.). We acknowledge grants from NOAA Climate and Global Change postdoctoral fellowship program, administered by the University Corporation for Atmospheric Research (to C.B.); support from the Joint Institute for the Study of the Atmosphere and Ocean (JISAO Contribution no. 2462) and from a Marie Curie International Incoming Fellowship (to J.B.P.); NASA National Earth and Space Sciences Fellowship (to T.J.F.); and ARCS Foundation scholarship (to B.R.M.).

## Author contributions

B.R.M. and E.J.S. wrote the paper and conducted data analysis with assistance from C.B. and J.B.P. Q.D. and C.M.B. provided climate model output. B.R.M., E.J.S. and S.W.S. produced the water-isotope data with T.R.J. and J.W.C.W. T.S. provided the CH<sub>4</sub> data. All authors contributed to the manuscript.

## Additional information

Supplementary information is available in the [online version of the paper](#). Reprints and permissions information is available online at [www.nature.com/reprints](http://www.nature.com/reprints). Correspondence and requests for materials should be addressed to B.R.M.

## Competing financial interests

The authors declare no competing financial interests.

## Methods

**Data.** Water  $^{18}\text{O}/^{16}\text{O}$  and  $^2\text{H}/^1\text{H}$  composition (expressed as  $\delta^{18}\text{O}$  and  $\delta\text{D}$ , respectively) were measured at IsoLab, University of Washington, Seattle, Washington, USA. Measurement techniques are described in refs 31,32. Measurements were made at 0.5 m depth averaged resolution, using laser spectroscopy (Picarro L2120-i analyzer). Data are reported relative to the VSMOW (Vienna Standard Mean Ocean Water) standard, and normalized to SLAP (Standard Light Antarctic Precipitation,  $\delta^{18}\text{O} = -55.5\text{‰}$ ,  $\delta\text{D} = -428\text{‰}$  relative to VSMOW). Measurement resolution is generally better than 40 years per sample for the 67 kyr record, with a mean temporal resolution of 17.2 years per sample between 10–67 ka. Measurement uncertainties are better than 0.08‰ for  $\delta^{18}\text{O}$  and 0.8‰ for  $\delta\text{D}$ .

Atmospheric methane concentrations were measured on discrete samples at Pennsylvania State University (0–67 ka, 0.5–2 m resolution). Air was extracted from ~50 g ice samples using a melt–refreeze technique, and analysed on a gas chromatograph with a flame-ionization detector. Corrections for gas solubility, blank and gravitational enrichment are described in ref. 32.

**Dansgaard–Oeschger event compositing.** The stacking procedure used in this study is identical to that used in ref. 5. The reader is referred to that study for a complete description of the method and its uncertainties. We summarize and describe additions here. The midpoint of each abrupt DO transition in NGRIP  $\delta^{18}\text{O}$  and WDC  $\text{CH}_4$  is identified following ref. 23 and used as a tie point for each DO/AIM event. A time vector,  $t$ , is defined from –1,200 years to 1,200 years with 1-year spacing. For each DO/AIM event, the NGRIP  $\delta^{18}\text{O}$  and WDC  $\text{CH}_4$ ,  $\delta^{18}\text{O}$  and  $d_{\text{in}}$  data are linearly interpolated onto time vector  $t$ . The midpoints of each DO transition in NGRIP  $\delta^{18}\text{O}$  are fixed to time  $t = 0$  years, and WDC  $\text{CH}_4$  midpoint at time  $t = 56$  years, which is the average lag of atmospheric  $\text{CH}_4$  behind Greenland  $\delta^{18}\text{O}$  as identified by ref. 22. The relative timing of the WDC isotope records to WDC  $\text{CH}_4$  are linked by the small and relatively well-constrained gas age–ice age difference ( $\Delta\text{age}$ ) of the WAIS Divide core<sup>25</sup>. All DO/AIM events are then stacked and averaged creating a composite DO/AIM event for each proxy. Our results are robust to the set of events composited, for example, the dropping of random events from the composite and the exclusion of large or small events.

Before stacking, we filter the WDC  $d_{\text{in}}$  record to reduce noise. WDC  $d_{\text{in}}$  has power at millennial frequencies comparable to that in WDC  $\text{CH}_4$  and  $\delta^{18}\text{O}$  as well as high-frequency noise unrelated to the millennial variability of interest here. We wish to reduce high-frequency noise due to measurement, which is normally distributed in the depth domain. We apply a 1-2-1 filter to the raw  $d_{\text{in}}$  data on the measured depth scale, which is a tapered weighting function similar to a 3-point moving average but twice the weight is given to the central point. Its response function has a relatively sharp frequency cutoff and is never negative (unlike moving averages); thus, no phase shifting of the data occurs. Below, we assess the influence of this light filtering on change point detection.

**Breakpoint determination and uncertainties.** The stacking procedure demonstrates the average response of  $d_{\text{in}}$  to abrupt DO transitions and quantifies lags. To objectively identify change points in the composites we use the RAMPFIT<sup>25</sup> and BREAKFIT<sup>33</sup> algorithms. The use of a modified BREAKFIT change point detection on the WDC  $\delta^{18}\text{O}$  is discussed extensively in ref. 5. RAMPFIT is better suited to this study than BREAKFIT, due to the ramp-like shape of the  $d_{\text{in}}$ ,  $\text{CH}_4$  and NGRIP  $\delta^{18}\text{O}$  composites, although results from both algorithms are comparable (discussed below) and do not affect the conclusions of this study. RAMPFIT has been used previously to detect abrupt change in deuterium-excess records<sup>34</sup>. The RAMPFIT algorithm fits a ramp function, consisting of three linear sections and two break points ( $t_1$  and  $t_2$ ), to the data in a least-squares sense. We let the algorithm search for the initial breakpoint,  $t_1$ , within the bounds –200 to 200 years, and the second break point,  $t_2$ , within the bounds –100 to 350 years on the WDC  $d_{\text{in}}$  composite (recall that the midpoint of the DO transition in NGRIP  $\delta^{18}\text{O}$  is defined at  $t = 0$  years, and the WDC  $\text{CH}_4$  midpoint at time  $t = 56$  years). The algorithm finds the best-fit ramp function defined by the mean of the ‘before’ and ‘after’ line segments, the duration of the ramp, and the timing of  $t_1$  and  $t_2$ . The algorithm uses a Monte Carlo moving block bootstrap (MBB) technique<sup>33</sup> to address uncertainty in the identification of the breakpoints. We report the mean and standard deviation of the initial breakpoint,  $t_1$ , as the timing of initial  $d_{\text{in}}$  change.

We investigate the influence of the choice of smoothing filter applied to the raw  $d_{\text{in}}$  record prior to the stacking procedure. We evaluate three different types of smoothing: a 1-2-1 filter; a 1-1-1 filter, that is, a 3-point symmetrically applied moving average; no filtering. The results are summarized in Supplementary Table 1 and shown in Supplementary Fig. 1. The choice of filter slightly influences the mean timing of the change points as detected by RAMPFIT, but in all cases the initial change points,  $t_1$ , are in agreement within uncertainty. Further, in all cases  $t_1$  is synchronous with the initiation of abrupt change in WDC  $\text{CH}_4$  within uncertainty.

In the stacking procedure, the individual events in all proxies from WDC are aligned at the midpoint of the WDC  $\text{CH}_4$  transitions. However, the exact alignment

of events is subject to uncertainty. We perform a Monte Carlo sensitivity analysis (1,000 realizations) in which random perturbations in timing are applied to the individual  $d_{\text{in}}$  events that make up the  $d_{\text{in}}$  stacks, following ref. 5. These 1,000 uncertainties are discussed in detail in ref. 5. We use the non-systematic errors from that study, which include uncertainty in determining the midpoint of the abrupt shifts in both NGRIP  $\delta^{18}\text{O}$  and WDC  $\text{CH}_4$ ; variability in the stated 56 yr lag of WDC  $\text{CH}_4$  behind shifts in NGRIP  $\delta^{18}\text{O}$ ; and non-systematic errors related to the age-scale construction<sup>5,23</sup>. Random timing errors within the stated uncertainties of ref. 5 are applied to the unfiltered, individual  $d_{\text{in}}$  events. The events are stacked as above and 1,000 realizations are averaged. The resulting composite has a very high signal-to-noise ratio, as uncorrelated variations are heavily reduced. The RAMPFIT routine was performed on the resulting composite  $d_{\text{in}}$  response, yielding an initial  $d_{\text{in}}$  breakpoint at  $t_1 = 51 \pm 33$  yr and  $t_1 = -35 \pm 36$  yr for the DO warming and cooling phases, respectively. Our results are thus robust to timescale uncertainties.

An important source of uncertainty in the timing of the breakpoint relative to the abrupt DO transitions is the gas age–ice age difference ( $\Delta\text{age}$ ). An extensive analysis of this uncertainty is presented in ref. 5. As the  $\delta^{18}\text{O}$  and  $d_{\text{in}}$  are measured on the same ice, the  $2\sigma$  uncertainty bound of 69 years due to  $\Delta\text{age}$ , found by ref. 5, is applicable to the  $d_{\text{in}}$  composite as well. However, the relative timings of breakpoints in the WDC  $\delta^{18}\text{O}$  and  $d_{\text{in}}$  stacks are not subject to any uncertainty associated with  $\Delta\text{age}$ , since they are measured on the same ice samples. Thus, our claim that the breakpoint in the  $d_{\text{in}}$  stack occurs significantly before the  $\delta^{18}\text{O}$  breakpoint relies solely on the identification of the breakpoint, and not  $\Delta\text{age}$  uncertainties. We find that the  $d_{\text{in}}$  change point occurs significantly before that in  $\delta^{18}\text{O}$  by an amount of  $173 \pm 79$  yr for the DO warming, and by  $235 \pm 64$  yr for DO cooling.

As a further test of the robustness of our change point detection, we apply the BREAKFIT algorithm to the  $d_{\text{in}}$  composite of DO warming events (instead of the RAMPFIT routine used above). The  $d_{\text{in}}$  breakpoint as found by the BREAKFIT method ( $t = 23 \pm 38$  yr for raw data, and  $t = 38.4 \pm 25.4$  yr for filtered data) is in good agreement with results from the RAMPFIT method.

**Summary of change point uncertainties.** Here we briefly synthesize the above sensitivity studies and uncertainties in the timing of the  $d_{\text{in}}$  breakpoints. For the phasing of WDC  $d_{\text{in}}$  breakpoints to NGRIP  $\delta^{18}\text{O}$  we consider: the RAMPFIT MBB uncertainty,  $\pm 74$  yr ( $1\sigma$ ) for DO warming and  $\pm 59$  yr for DO cooling; the  $\Delta\text{age}$  uncertainty<sup>5</sup>,  $\pm 69$  yr ( $2\sigma$ ); the systematic uncertainty in the NGRIP  $\delta^{18}\text{O}$ -WDC  $\text{CH}_4$  phasing from ref. 5,  $\pm 27$  yr ( $2\sigma$ ). Adding all uncertainties in quadrature yields  $\pm 83$  yr ( $1\sigma$ ) for DO warming events, and  $\pm 70$  yr ( $1\sigma$ ) for DO cooling events, as reported in the main text.

We can similarly quantify the uncertainty in the WDC  $\text{CH}_4$  and NGRIP  $\delta^{18}\text{O}$  initial break points, as found by the RAMPFIT analysis. In the case of WDC  $\text{CH}_4$ , we consider the RAMPFIT MBB uncertainty,  $\pm 4$  yr ( $1\sigma$ ) for DO warming and  $\pm 2$  yr for DO cooling; and the systematic uncertainty in the NGRIP  $\delta^{18}\text{O}$ -WDC  $\text{CH}_4$  phasing,  $\pm 27$  yr ( $2\sigma$ ). Adding all uncertainties in quadrature yields  $\pm 14$  yr ( $1\sigma$ ) for both DO warming and cooling events (rounding uncertainties to the nearest year). For the NGRIP  $\delta^{18}\text{O}$  change points, we consider only the RAMPFIT MBB uncertainty of  $\pm 5$  yr ( $1\sigma$ ) and  $\pm 7$  yr, for warming and cooling events, respectively. Note that owing to the much higher signal-to-noise ratio of the NGRIP  $\delta^{18}\text{O}$  and WDC  $\text{CH}_4$  stacks, the MBB uncertainties are much lower than those of WDC  $d_{\text{in}}$ .

For the phasing of WDC  $d_{\text{in}}$  to WDC  $\delta^{18}\text{O}$  breakpoints we consider only the RAMPFIT MBB uncertainty for the  $d_{\text{in}}$  breakpoint,  $\pm 74$  yr ( $1\sigma$ ) for DO warming and  $\pm 59$  yr for DO cooling, and the BREAKFIT uncertainty for the  $\delta^{18}\text{O}$  breakpoint<sup>5</sup>,  $\pm 50.8$  yr ( $2\sigma$ ). Adding in quadrature yields phasing uncertainties of  $\pm 79$  yr ( $1\sigma$ ) for DO warming events and  $\pm 64$  yr ( $1\sigma$ ) for DO cooling events.

**Frequency domain methods.** We use the Thompson multitaper method for coherence and phase estimates, correcting for coherence bias and using a Monte Carlo approach to estimate the 95% confidence limits on the phase estimation (for example, ref. 35). We also use the Thompson multitaper method to estimate spectral power density, employing the MATLAB pmtm.m routine with an improved confidence limit estimation that correctly accounts for the degrees of freedom as implemented by P. Huybers (<http://www.people.fas.harvard.edu/~phuybers/Mfiles>). We linearly interpolate the data to even time intervals ( $\Delta t = 10$  yr spacing) before analysis. We perform the analysis on the records over the interval 10–67 ka, 20–67 ka (excluding the deglaciation), 6–67 ka (including the early Holocene), and for different interpolated time spacing ( $\Delta t = 10, 20, 40$  years). These analytical choices do not meaningfully impact the conclusions of this study.

**Characterization of millennial frequencies.** We characterize the WDC  $d_{\text{in}}$ ,  $\text{CH}_4$  and  $\delta^{18}\text{O}$  spectra, providing context for interpreting the phase relationship of WDC  $d_{\text{in}}$  to the AIM and DO patterns of climate variability. Normalized ( $z$ -score over the 10–67 ka period)  $\text{CH}_4$  and  $\delta^{18}\text{O}$  have red power spectra, with increasing power toward lower frequencies through the millennial band; AIM and DO cycles are not

periodic but span a range of timescales from  $\sim 500$  to 5,000 years. Millennial-scale power in normalized  $d_{in}$  is comparable to that of  $CH_4$  and  $\delta^{18}O$ . It is important to note that while the  $\delta^{18}O$  and  $CH_4$  signals are both expressions of millennial variability in the coupled climate system, they do not have the same power distribution across frequency. Specifically, millennial-band power in WDC  $\delta^{18}O$  is weaker than that in  $CH_4$  (or Greenland  $\delta^{18}O$ ). The distribution of millennial power in WDC  $d_{in}$  has similarities to that of both  $CH_4$  and WDC  $\delta^{18}O$ .

The unique nature of the millennial band is shown clearly in the coherence and phase between WDC  $CH_4$  and  $\delta^{18}O$  (Supplementary Fig. 2). The phase relationship transitions from in phase at orbital frequencies, to  $\sim 90^\circ$  out of phase at millennial frequencies ( $\sim 5$  to 1 kyr periods of the DO/AIM cycles). This relationship reflects the integrand–integrator relationship between NH and SH climate: temperature change in the North Atlantic (highly correlated with WDC  $CH_4$ ) is inversely related to the time rate of change of temperature in the Southern Hemisphere<sup>36</sup>. Any signal is  $90^\circ$  out of phase with its derivative across frequency, and has reduced power compared with the derivative. The smoothly decreasing phase angle between WDC  $CH_4$  and  $\delta^{18}O$  at periods below  $\sim 2,000$  yr is equivalent to the discrete  $\sim 200$  yr time lag between the Northern and Southern hemispheres during these events<sup>5</sup>. A discrete time lag between two signals,  $-\Delta\tau$ , is equivalent to a smoothly changing phase angle  $\theta = -\Delta\tau \times \omega \times 360^\circ$  with frequency  $\omega$  (ref. 37).

The  $d_{in}$  record is significantly coherent with both  $CH_4$  and  $\delta^{18}O$  (Supplementary Fig. 2), but shows a distinct phase relationship: at periods  $< 2.5$  kyr,  $d_{in}$  and  $CH_4$  are essentially in phase; at timescales between  $\sim 2.5$  kyr and 5 kyr,  $d_{in}$  is out of phase with both  $\delta^{18}O$  and  $CH_4$ , with a phase angle between  $0^\circ$  (in phase) and  $90^\circ$  (quadrature). One should expect  $d_{in}$  to show phase angles between  $0^\circ$  and  $90^\circ$  with  $\delta^{18}O$  and  $CH_4$ , if its variability were composed of a superposition of two modes of variability, one in phase with  $\delta^{18}O$  and the other in phase with  $CH_4$  (which are  $90^\circ$  to each other). Below we show that the relationship of phase angle to frequency observed among the records is expected if  $d_{in}$  represents a combination of the  $CH_4$  and  $\delta^{18}O$  modes of variability, given the distribution of power in the  $CH_4$  and  $\delta^{18}O$  records.

**Sensitivity of phase relationships to chronological uncertainties.** We investigate the sensitivity of the coherence analysis to chronological uncertainties in the age model and  $\Delta$ age history arising from the dynamical firn densification model on which they are based<sup>23</sup>. We perform a Monte Carlo sensitivity study in which the coherence and phase between WDC  $CH_4$ ,  $\delta^{18}O$  and  $d_{in}$  are calculated for an ensemble of  $10^3$  different possible  $\Delta$ age histories that are generated by varying input parameters to the firn densification model<sup>23</sup> within stated uncertainties, as well as four different depth interpolation schemes<sup>38</sup> for a total of  $4 \times 10^3$  possible WDC chronologies. The mean coherence and phase of the Monte Carlo sensitivity study are shown in Supplementary Fig. 2a,b with  $\pm 1\sigma$  of the spread of results (shading). The results demonstrate that the coherence and phase analysis is insensitive to the small chronological uncertainties of the WDC timescale. The 95% confidence intervals on the estimation of the phase relationship between WDC  $CH_4$ ,  $\delta^{18}O$  and  $d_{in}$  calculated by the cmtm.m routine using an iterative method<sup>35</sup> are shown in Supplementary Fig. 2c.

**Regression model.** WDC  $d_{in}$  variability is related to the variability in both WDC  $CH_4$  and  $\delta^{18}O$ . We illustrate this explicitly by multiple linear regression of the combined  $CH_4$  and  $\delta^{18}O$  signals to WDC  $d_{in}$ ,  $\langle d_{in} \rangle = a\langle \delta^{18}O \rangle + b\langle CH_4 \rangle$ , where  $\langle x \rangle$  indicates that time series  $x$  has been normalized by its z-score over the interval 10–67 ka. The combined regression model ( $a = 0.4589$  and  $b = 0.3951$ ) accounts for 62% of variance of the  $d_{in}$  record at all timescales (Supplementary Fig. 3). The  $F$  statistic of the combined model, 4666.3, has a  $p$  value within rounding error of zero, indicating that the combined regression model is a significantly better predictor of the  $d_{in}$  record than the  $\delta^{18}O$  or  $CH_4$  component alone. Much of the remaining

variance in WDC  $d_{in}$  not described by the combined model can be attributed to high-frequency noise in WDC  $d_{in}$ ; the linear model explains over 87% of the variance in WDC  $d_{in}$  if high-frequency noise ( $< 1$  cycle per 500 yr) is included.

We use a Monte Carlo method to test whether the additional variance explained by the combined linear model is significant over that explained by its components alone, accounting for autocorrelation in the time series. We compare the linear regression model,  $a\langle \delta^{18}O \rangle + b\langle CH_4 \rangle$ , against two dummy regression models,  $M_1 = a_1\langle \delta^{18}O \rangle + b_1\text{noise}_1$ , and  $M_2 = a_2\text{noise}_2 + b_2\langle CH_4 \rangle$ , where  $\text{noise}_{1,2}$  are randomly generated AR-1 time series whose mean, standard deviation, and lag-1 autocorrelation match those of the normalized  $CH_4$  and  $\delta^{18}O$  time series, respectively. We compare the  $r^2$  of the real linear model with the distribution of  $r^2$  values resulting from  $10^3$  random iterations of each dummy model. The distributions of  $r^2$  values for  $M_1$  and  $M_2$  have a greatest-likelihood value equal to that of  $\delta^{18}O$ -only and  $CH_4$ -only models, respectively ( $r^2 = 0.54$  and  $r^2 = 0.51$ ), with a decreasing but non-zero probability of a higher  $r^2$  value due to noise fitting of the additional random, but autocorrelated, time series. The real linear model's  $r^2$  (0.62) exceeds that of 99.95% and 100% of iterations for  $M_1$  and  $M_2$ , respectively. These results demonstrate conclusively that the additional variance in  $d_{in}$  explained by the combined  $\delta^{18}O$  and  $CH_4$  variability is significant and not due to noise fitting.

The linear model analysis is consistent with the observed spectral coherency. An arbitrary linear combination of two normalized signals approximately  $90^\circ$  out of phase with each other can result in a signal with any phase relationship to the components. In this case, approximately equal weighting of the components ( $a = 0.4589$  and  $b = 0.3951$ ) yields a resulting phase relationship of  $\sim 45^\circ$  between WDC  $d_{in}$  and the components of the model ( $CH_4$  and  $\delta^{18}O$ ). WDC  $d_{in}$  is not precisely  $45^\circ$  to  $CH_4$  and  $\delta^{18}O$  at all millennial frequencies. For example,  $d_{in}$  and  $CH_4$  have a phase angle slightly greater than  $45^\circ$  at lower millennial frequencies and closer to  $0^\circ$  at higher millennial frequencies. This reflects differences in the power distribution across millennial frequencies of each proxy and how they combine. The linear model captures the combination of power distribution and phase relationships of  $d_{in}$  to the other proxies: the phase relationship of  $CH_4$  to the linear model is equivalent to the phase relationship of  $CH_4$  to  $d_{in}$ , and likewise for  $\delta^{18}O$  to  $d_{in}$  (Supplementary Fig. 4).

**Data availability.** The data that support the findings of this study are available at <http://dx.doi.org/10.17911/S9MW2F>.

## References

- Steig, E. J. *et al.* Recent climate and ice-sheet changes in West Antarctica compared with the past 2,000 years. *Nat. Geosci.* **6**, 372–375 (2013).
- WAIS Divide Project Members. Onset of deglacial warming in West Antarctica driven by local orbital forcing. *Nature* **500**, 440–444 (2013).
- Mudelsee, M. Break function regression. *Eur. Phys. J. Spec. Top.* **174**, 49–63 (2009).
- Steffensen, J. P. *et al.* High-resolution Greenland ice core data show abrupt climate change happens in few years. *Science* **321**, 680–684 (2008).
- Huybers, P. & Denton, G. Antarctic temperature at orbital timescales controlled by local summer duration. *Nat. Geosci.* **1**, 787–792 (2008).
- Roe, G. H. & Steig, E. J. Characterization of millennial-scale climate variability. *J. Clim.* **17**, 1929–1944 (2004).
- Wunsch, C. Greenland–Antarctic phase relations and millennial time-scale climate fluctuations in the Greenland ice-cores. *Quat. Sci. Rev.* **22**, 1631–1646 (2003).
- Fudge, T. J., Waddington, E. D., Conway, H., Lundin, J. M. D. & Taylor, K. Interpolation methods for Antarctic ice-core timescales: application to Byrd, Siple Dome and Law Dome ice cores. *Clim. Past* **10**, 1195–1209 (2014).

## Global atmospheric teleconnections during Dansgaard-Oeschger events

**Authors:** Bradley R. Markle, Eric J. Steig, Christo Buizert, Spruce W. Schoenemann, Cecilia M. Bitz, T.J. Fudge, Joel B. Pedro, Qinghua Ding, Tyler Jones, James W.C. White, Todd Sowers

### Supplementary Materials:

#### Table of Contents

1. **The definition of deuterium excess**
  - 1.1. Linear vs. logarithmic definition
  - 1.2. Comparison of  $d_{excess}$  and  $d_{in}$  at different Antarctic core sites
  - 1.3. Seawater corrections
2. **Sources of  $d_{in}$  variability**
  - 2.1. GCM fit vs. phenomenological fit
  - 2.2. Correlations of  $d_{in}$  to surface conditions in GCM
  - 2.3. Relationship between  $d_{in}$  and the Southern Westerlies
  - 2.4. Relative humidity
  - 2.5. Moisture source modeling with GCM water tagging
  - 2.6. Summary of mechanisms leading to  $d_{in}$  variability at WDC
  - 2.7. Zonally coherent storm track shifts?
  - 2.8. Additional drivers of  $d_{in}$

### Supplementary References

### Supplementary Figures S1-14; Supplementary Table S1

# 1 The definition of deuterium excess

## 1.1 Linear versus logarithmic definition

The deuterium excess of water quantifies the influence of non-equilibrium (kinetic) fractionation processes<sup>1</sup>, which have differential influence on  $\delta D$  and  $\delta^{18}O$ . Historically, the deuterium excess parameter has been defined as the deviation from a linear slope of 8 between  $\delta D$  and  $\delta^{18}O$  ( $d_{excess} = \delta D - 8 \times \delta^{18}O$ ), from an empirical fit to observational data of the Global Meteoric Water Line (GMWL)<sup>1</sup>. However, the appearance of linearity in the GMWL is fundamentally an artifact<sup>2</sup>. Equilibrium fractionation has a non-linear relative influence on  $\delta D$  and  $\delta^{18}O$ , which becomes increasingly important as the amount of overall fractionation increases, i.e. as  $\delta D$  and  $\delta^{18}O$  are depleted<sup>3</sup>. Fig. S5 shows the isotopic values of precipitation along a temperature gradient calculated by a simple Rayleigh-type isotope distillation model<sup>4</sup> with only equilibrium fractionation processes (kinetic processes are excluded). It is evident that equilibrium fractionation alone drives the isotope content of precipitation away from a linear slope of 8. Note that the magnitudes of  $\delta$  values in this model are not directly comparable to reality since the model lacks known sources of isotopic fractionation.

Because the divergence from a slope of 8 is non-linear, changes in the total degree of fractionation at an ice core site (e.g., due to a temperature change) lead to non-linear temporal variability in the  $d_{excess}$ , even in the absence of kinetic fractionation processes. This non-linear bias will be most problematic at sites with very cold temperatures and high isotopic depletion, such as in East Antarctica. Because of this, the comparison of  $d_{excess}$  records from sites with different absolute temperature histories is complicated<sup>3,5</sup>.

In Figure S5.b we show the same distillation model results plotted in a logarithmic space where values are the natural log of 1 + the delta values, e.g.  $\ln(\delta^{18}O + 1)$ . In this space the results are much nearer to, though not quite, linear. Equilibrium fractionation does not lead to a linear slope of 8 between  $\delta D$  and  $\delta^{18}O$ , but rather a non-linear relationship between  $\ln(\delta D + 1)$  and  $\ln(\delta^{18}O + 1)$ , ref<sup>2,3</sup>. Because the true relationship between  $\ln(\delta D + 1)$  and  $\ln(\delta^{18}O + 1)$  is a ratio of logarithmic functions (this comes from the logarithmic nature of both rainout and isotope distillation), it can be represented to any arbitrary degree of accuracy with a polynomial series expansion. A definition of the deuterium excess parameter as the deviation from a polynomial fit in the logarithmic space will significantly reduce the artifacts due to equilibrium fractionation. The true relationship in the logarithmic space is not known *a priori*; the simple model results shown above are illustrative of the relationship, but are not suitable to define it. Uemura et al.<sup>3</sup> have proposed a phenomenological definition for the excess parameter,  $d_{ln} = \ln(\delta D + 1) - [8.47 \ln(\delta^{18}O + 1) - 2.85 \times 10^{-2} (\ln(\delta^{18}O + 1))^2]$ , based on a 2<sup>nd</sup> order polynomial fit to available global precipitation data. In addition to minimizing the equilibrium fractionation bias of the linearly defined parameter, this logarithmic definition minimizes the influence of kinetic fraction during transport, by fitting the current climatological mean, which reflects the sum of all processes.

## 1.2 Comparison of $d_{excess}$ and $d_{ln}$ at different Antarctic core sites

The differences between the  $d_{excess}$  and  $d_{ln}$  definitions of the deuterium excess parameter are significant at East Antarctic sites (EDC and EDML, Fig. S6). On the other hand, the two definitions are nearly indistinguishable at WDC due to the comparatively limited depletion of water isotopes. The logarithmic definition reduces the non-linear biases evident in the East Antarctic records, revealing shared variability with the less depleted West Antarctic record. At all periods longer than 3000 years,  $d_{ln}$  records are highly coherent across the Antarctic continent (Fig. S7).

The  $\delta^{18}O$  records of EDC, EDML, and WDC have significant coherence at all periods longer than 1000 years, a lower limit which may be in part due to chronological uncertainties. At the longest timescales, Antarctic-wide  $d_{ln}$  variability, like Antarctic-wide  $\delta^{18}O$ , follows a reasonable estimate for orbitally-driven temperature change in the high latitude Southern Hemisphere, e.g. the duration of austral summer<sup>6</sup> (not shown). While orbital scale variations in  $d_{ln}$  and their drivers are beyond the scope of this study, the large-scale (both temporally and spatially) coherence in the logarithmic excess parameter increases our confidence in its utility. The shared, coherent variability in Antarctic  $d_{ln}$  at periods of 3000-5000 years is directly relevant to understanding AIM variability in the WDC record.

## 1.3 Sea water corrections

Changes in the isotopic composition of seawater can influence the deuterium excess of polar precipitation<sup>5</sup>. Following ref<sup>5</sup> we can correct the WDC record for these changes using the seawater isotope record based on marine benthic stacks<sup>7</sup>. Importantly, and in contrast to the linearly defined parameter, seawater corrections do not significantly alter multi-millennial to orbital scale variability of the logarithmically defined excess parameter. Limited resolution and timescale uncertainty of the marine records<sup>7</sup> prevents meaningful corrections from being made at millennial and shorter timescales, and are thus omitted from analyses presented here.

# 2 Sources of $d_{ln}$ variability

## 2.1 GCM fit vs. phenomenological fit

We use the isotope-enabled ECHAM4.6 GCM<sup>8</sup> to assess physical processes that lead to  $d_{ln}$  variability. We compare the phenomenological fit to observations<sup>3</sup> of a 2<sup>nd</sup> order polynomial,  $\ln(\delta D + 1) = a(\ln(\delta^{18}O + 1))^2 + b\ln(\delta^{18}O + 1)$ , with a within-model fit from multiple 30-year control runs of the ECHAM4.6 GCM at T42 resolution. We use fractionation coefficients following ref<sup>9</sup>, and we test two parameterizations of the dependence of supersaturation on temperature,  $T$ , ( $S = 1 - ss \times T$ ;  $ss = 0.002$  and  $ss = 0.007$ ). The coefficients of the in-model fit ( $a = -3.58 \times 10^{-2}$  and  $b = 8.20$  for  $ss = 0.002$ ;  $a = -2.70 \times 10^{-2}$  and  $b = 8.42$  for  $ss = 0.007$ ) are in good agreement the phenomenological fit of ref<sup>3</sup> ( $a = -2.85 \times 10^{-2}$ ,  $b = 8.47$ ). The  $r^2$  values of the in-model fits ( $r^2 = 0.999$  in each case) show that the polynomial relationship is representing the underlying modeled processes well. The similarity of in-model and phenomenological fit coefficients suggests that the distillation processes represented either explicitly or parameterized in the model,

approximate the shape of the real relationship well, and that isotopic fractionation processes not accounted for by the model are not a significant source of interannual variability.

## 2.2 Correlations of $d_{ln}$ to surface conditions in GCM

Here we examine the faithfulness of the logarithmic definition of the deuterium excess parameter to moisture source conditions. We examine the simulated  $d_{ln}$  in precipitation at the WDC site (nearest model grid-point) and relationships to seasonal and interannual climate variability with a 30-year control run of the isotope enabled ECHAM 4.6 GCM under preindustrial boundary conditions. We present correlation results from the  $ss = 0.007$  simulation, though results for  $ss = 0.002$  are qualitatively similar and do not alter our conclusions. In Fig. S8 we show the correlation of WDC site temperature,  $\delta^{18}\text{O}$ ,  $d_{ln}$ , and  $d_{excess}$  to the global surface temperature field. The annual temperature cycle is the largest source of variability in this run. WDC site temperature is well correlated to the surrounding SH high latitude temperatures, as is WDC  $\delta^{18}\text{O}$ ; both share the seasonal cycle of Southern Hemisphere land surfaces. On the other hand, modeled WDC  $d_{ln}$  is highly correlated with Southern Hemisphere ocean surface temperature on the seasonal scale (which are out of phase with that of land surfaces), and is significantly less influenced by Antarctic surface temperature than the historically defined  $d_{excess}$ . This illustrates the higher fidelity to Southern Hemisphere SSTs of  $d_{ln}$  compared to  $d_{excess}$ . Regression of SSTs in the WDC moisture source region (between  $40^\circ$  and  $65^\circ\text{S}$  and  $160^\circ$  and  $280^\circ\text{E}$ , see moisture source modeling below) onto modeled WDC  $d_{ln}$  variability reveals a scaling of  $0.62 \pm 0.12$  ( $1\sigma$ )  $\text{‰}/\text{K}$  for  $d_{ln}$  to source region SST. Importantly, this scaling implicitly includes any contributory drivers of  $d_{ln}$  that happen to covary with SST in the model, such as relative humidity (RH). Applying an isotope-temperature inversion method, ref<sup>3</sup> find a  $d_{ln}$  to moisture-source temperature scaling of  $1.8\text{‰}/\text{K}$ , though this scaling excludes any correlated influence of RH.

To examine the dependence of the  $d_{ln}$ -surface condition relationship to the climate mean state, we additionally analyze isotope-enabled runs of ECHAM4.6 under LGM boundary conditions and LGM with extended sea ice, as described in ref<sup>9</sup>. We investigate the relationship between  $d_{ln}$  and moisture source conditions both at the seasonal and interannual scale, as above. We find very similar correlations between  $d_{ln}$  at WDC and Southern Hemisphere SSTs in LGM and Preindustrial conditions, with slightly higher correlations under LGM conditions, both at the interannual and seasonal scale. Our regression analysis also finds a similar  $d_{ln}$ -SST scaling under LGM ( $0.66 \pm 0.43$  ( $1\sigma$ )  $\text{‰}/\text{K}$ ) and preindustrial conditions ( $0.62 \pm 0.12$   $\text{‰}/\text{K}$ ). Conditions during the last glacial period in general were likely intermediate between LGM and preindustrial. These results are in line with our simple Rayleigh distillation model, in which the source temperature can be varied explicitly. Our Rayleigh model results indicate that the slope of the  $d_{ln}$ -source temperature scaling is not strongly dependent on the mean-state temperature. This is one of the advantages of the logarithmic definition.

## 2.3 Relationship between $d_{ln}$ and the Southern Westerlies.

Isotope enabled GCMs have demonstrated a link between Antarctic deuterium excess and variability in the Southern Hemisphere Westerlies. Schmidt et al.<sup>10</sup> found that the southerly (positive) phase of the Southern Annular Mode (SAM, a feature describing

meridional changes in the SH westerly wind position<sup>11</sup>) is associated with negative deuterium excess anomalies in the GISS GCM. We present new analysis confirming these results. We compare the modeled  $d_{in}$  of precipitation in our 30-year ECHAM4.6 preindustrial and LGM control runs to a within-model index of the Southern Annular Mode to show that more southerly winds (positive SAM) are associated with lower  $d_{in}$  in Antarctica, leading to a negative correlation (Fig. S9). We find nearly identical correlation maps between the preindustrial and LGM runs. Regression of the in-model SAM index to model  $d_{in}$  of precipitation reveals a scaling relationship of  $\sim -0.5\text{‰}$  per standard deviation of the SAM for West Antarctica. Both previous modeling work and the new work presented here demonstrate the link between variability in the Southern Hemisphere storm tracks and Antarctic deuterium excess, strongly supporting our main conclusions. Below we investigate the specific mechanism relating  $d_{in}$  variability in the storm tracks: the location of the moisture source.

The critical factor relating shifts in the moisture source to  $d_{in}$  variability is the meridional surface temperature gradient within the moisture source distribution (the meridional RH gradient is comparatively weaker). While mean state temperature changed significantly between glacial and interglacial, the temperature gradient was likely similar<sup>12</sup>. The modeled mean SST gradient between 30° and 65°S was 0.65 K/°latitude in the preindustrial experiment and 0.89 K/°latitude under LGM conditions. The temperature gradient is steep enough in the high southern latitudes (spanning about 20 degrees within the moisture source) that changes in the steepness of the gradient itself during the AIM events, for example, would have been of 2<sup>nd</sup> order importance on the  $d_{in}$  scaling.

Finally we examine the influence of modern interannual variability on WDC  $d_{in}$  by comparing the most recent section of the record to an reanalysis-based index of SAM variability between 1980 and 2005, the Antarctic Oscillation index (AAO, refs<sup>13,14</sup>). The time series of the AAO and modern  $d_{in}$  show similar interannual variability (Fig. S10), but the short duration of the reliable reanalysis data (on which the AAO index is based) limit the robustness of the correlation. We find that WAIS  $d_{in}$  composited over years when the AAO was in its northward shifted phase has a mean 0.38‰ positive anomaly, while the southward shifted phase is associated with a -0.36‰ negative anomaly in  $d_{in}$ . The sign and magnitude of these anomalies is in excellent agreement with the modeling work presented in the manuscript. The composited  $d_{in}$  distributions are only significantly different at the rather weak level of 70% confidence. However, these composited distributions are for all positive or negative AAO years and only span 30 years in total. If we examine only large positive or negative AAO years (e.g. greater than  $1\sigma$ ), the mean  $d_{in}$  anomalies diverge more strongly, but the smaller number of total years correspondingly impedes the statistics. This analysis also does not isolate fixed location SST changes from shifts in the MSD over the modern interval, unlike the idealized GCM experiments presented in the main text. However, the analyses together are complementary.

## 2.4 Relative humidity

We agree in this study that SSTs are the dominant moisture source variable affecting  $d_{in}$  during millennial climate change, through changes in SSTs at fixed locations and changes in moisture source location. The relative humidity (RH) at the moisture source is also a strong lever on the kinetic fractionation that drives  $d_{in}$ , specifically the RH

normalized to the sea surface temperature (“RH-at-SST”), which quantifies the near-surface vertical moisture gradient<sup>4</sup>. Clearly, variability in both SST and RH result in variability in RH-at-SST. Much of the variability in  $d_{in}$  due to changes in SSTs may be through the influence of RH-at-SST rather than the direct effect of SST on kinetic fractionation<sup>4</sup>, which may be weaker than previously thought<sup>15</sup>. The effective influence of SST on  $d_{in}$  reflects the combination of these effects and is accounted for in our GCM-derived  $d_{in}$  –SST scaling.

There exists a meridional RH gradient over the Southern Ocean, which increases poleward by a few percent within the MSD of WDC. The sign of the RH gradient is such that it amplifies any change in  $d_{in}$  due to spatial shifts in the MSD over the SST gradient; a southward shifted storm track will sample moisture sources that have lower SSTs and higher RH, both of which act to lower  $d_{in}$ . This effect is implicitly included in our scaling of the changes in  $d_{in}$  to variability in the Southern westerlies in the ECHAM4.6 GCM above.

Temporal or spatial changes in RH that are uncorrelated with SSTs could also, in principle, influence the RH-at-SST parameter and drive  $d_{in}$  variability. While we cannot rule out such hypothetical changes in RH *a priori*, there is no evidence that they would be significant. While changes in RH are an important source of  $d_{in}$  variability at diurnal to seasonal timescales<sup>15,16</sup>, RH is strongly homogenous and largely invariant over global oceans at longer timescales<sup>17,18</sup>. The standard deviation of modern marine RH measurements are only 2-4% over most of the globe, which suggests that mixing in the atmosphere acts to maintain RH at a fixed level of saturation and spatial homogeneity<sup>17</sup>. For example, dominant sources of interannual climate variability (e.g. ENSO or SAM) are associated with large anomalies in mid to high latitude SSTs, yet no significant change in RH is seen in NCEP/NCAR reanalysis data<sup>19</sup> during these events. Thus the most likely source for large changes in RH-at-SST, over the millennial and longer timescales of interest here, is changes in the SSTs themselves.

## 2.5 Moisture source modeling with GCM water tagging

Here we examine the spatial pattern of Antarctic moisture sources and assess the sensitivity of the WDC moisture source to atmospheric circulation. We analyze results from the Community Atmosphere Model (CAM) with water tagging. We independently track evaporation from 11 bins: 10 zonal bins over the Southern Hemisphere oceans at 5° intervals from 20°S to the Antarctic continent and one bin over the Antarctic continent itself (re-evaporation) as shown in Fig. S11. We examine output from the last 30 years of a 50-year control run forced by prescribed seasonally varying SSTs and modern boundary conditions. We examine control runs in both CAM3 and CAM5 (presented here), which yield similar results.

We calculate a moisture source distribution (MSD) for a given ice core site as the relative contribution to total annual precipitation at the ice core site by evaporation from each tagged latitudinal bin over the Southern Ocean. Figure S12 shows the mean moisture source distribution calculated for WDC, EDC, and EDML core sites. The MSD for West Antarctica is considerably further south than East Antarctic moisture sources, consistent with previous work<sup>20</sup>. Southern Ocean sources between 40° and 70° South dominate WDC moisture origin, but a non-zero contribution of lower latitude sources is also present.

We create in-model indices of unforced variability in the position of the ITCZ and Southern Westerlies. Following convention, we define a Southern Annular Mode index

(“SAMi”) as the normalized difference in sea level pressure between 50°S and 70°S, to capture north-south (N-S) variability in the Southern Hemisphere westerly winds. An ITCZ index (“ITCZi”) is calculated as the normalized difference in total precipitation between 0°-10°N and 0°-10°S, which captures N-S movement of the tropical precipitation band.

We composite the distribution of moisture sources for WDC for northward and southward shifts in the mean position of the ITCZ and Southern Westerlies based on the sign of the above indices. We find that the northward-shifted phase of the SAM is associated with a significantly northward shifted MSD for WDC, while the southward-shifted phase of SAMi is associated with a southward-shifted MSD. Composited MSDs for all years when SAMi is either negative (northward) or positive (southward) lead to a difference in mean latitude of moisture origin of 0.8° latitude. Owing to the underlying meridional SST gradient, this results in a difference of annually averaged mean SST of evaporation of 0.6 K. The spread of MSD shifts associated with the SAMi variability are shown in Fig. S13: excursions of SAMi greater than  $1\sigma$  of its variability (in either direction) result in a shift of the mean MSD of 1.1° latitude, driving a 1.0 K change in sampled SST; a 2.1° latitude shift and 1.9 K sampled SST change are associated with  $1.5\sigma$  and greater shifts. The MSD of WDC is also sensitive to position of the ITCZ at interannual timescales (Fig. S13). The effect is strongest for large excursions: we find 1.0K and 1.2K changes in SSTs sampled by the MSD associated with  $\pm 1\sigma$  and  $\pm 1.5\sigma$  excursions of ITCZi.

The WDC record shows  $d_{ln}$  anomalies on the order of 1-1.5‰ in phase with DO events. Taking that a 1° latitude shift in the MSD translates to ~1K change in sampled SST, as shown above, and using an  $\sim 0.6\text{‰}/\text{K}$  scaling for the sensitivity of  $d_{ln}$  to SST, our data are consistent with shifts in the MSD on the order of 2° latitude. We can likely rule out shifts of order 10°. Such shifts in the MSD are at about the  $\pm 1$  to  $1.5\sigma$  level of natural variability in our GCM water tagging simulations, but would have been sustained for thousands of years. The associated change in the SH wind field would have had implications for other aspects of the climate system. Using the annular mode in our moisture tagging experiment as an analogy, Figure 4.b shows the mean 10m zonal wind field as well as the difference between the average of years when the SAM index was strongly positive ( $+1\sigma$  SAMi) and years when the SAM was strongly negative ( $-1\sigma$  SAMi). Greater than 1 m/s (>15%) changes in surface winds are seen locally and with strong meridional gradients. Composited by SAM at the  $1.5\sigma$  level, the changes in local 10m zonal winds are over 2m/s (>20%) (Fig. S14). The changes in mean sea level pressure are similar. By any measure, these would have been significant changes in the wind field locally, if sustained for centuries. Such changes in the wind field are the same order as expected from modeling of the proposed teleconnections between the tropics and high southern latitudes<sup>21,22</sup> and consistent with ITCZ displacement of hundreds of kilometers (several degrees latitude) during DO events<sup>23</sup>.

## 2.6 Summary of mechanisms leading to $d_{ln}$ variability at WDC

Here we briefly summarize the above mechanisms that lead to a combination of DO-like and AIM-like variability in the WDC  $d_{ln}$  record, and describe the details of the schematics in Fig. 4 of the main text. Figure 4.a shows the mean MSD for WDC calculated from the CCSM GCM moisture tagging experiment described above. We also show the MSDs

associated with  $>\pm 1.5\sigma$  of internal N-S variability of the westerly winds, which the above scaling analysis suggests are analogous to the displacements during abrupt DO warming (DO+) and cooling (DO-) events. 117

Figure 4.b shows the mean Southern Hemisphere surface temperature from the ECHAM GCM experiment under glacial boundary conditions, which may be typical of cold phases of the AIM events (AIM-). The schematic for the warm phases of AIM events (AIM+) has an anomaly added that is zero at the equator and 2°C over the SO, in line with paleoproxy data described in the text.

The schematic of temporal variability in the mean position of the MSD (Fig. 4.c) is created using the average of several large DO events in the WDC CH<sub>4</sub> record, scaled to reflect the size of the modeled MSD shifts in Fig. 4.a. The expected noise level (shading) is the standard deviation of internal variability in the mean latitude of the MSD in the moisture tagging experiment.

The schematic of temporal variability in the mean Southern Ocean surface temperature (Fig. 4.d) is created using the average of several large AIM events in the WDC  $\delta^{18}\text{O}$  record, scaled to reflect the size of SST anomalies suggested by the above scaling analysis. The noise level (shading) is the standard deviation of interannual Pacific Sector SST variability from NCEP reanalysis<sup>19</sup>.

Shifts in the MSD over a strong meridional gradient in SST, and changes in the mean SSTs themselves, lead to variability in the *sampled* moisture source SSTs that follows a combination of the variability in c) and d). Deuterium excess measured in an ice core is proportional to sampled moisture source conditions.

## 2.7 Zonally coherent storm track shifts?

The WDC  $d_m$  record is consistent with changes in SH atmospheric circulation during DO events. But did these changes occur symmetrically in the Southern Hemisphere, in analogy to the Southern Annular Mode, or were they localized to the Pacific Sector where the WDC site is located? Ceppi et al.<sup>21</sup> find a mechanistic link between the ITCZ and the Southern jet in the zonal mean, though the jet displacement is strongest the Pacific Sector. Chiang et al.<sup>24</sup> investigate a related but separate teleconnection mechanism involving the Pacific Split jet, which is dominantly expressed in the Pacific Sector and would thus most likely influence the moisture sources for just WDC. Modern teleconnections between the tropics and the high Southern latitudes related to ENSO are strongest in the Pacific sector<sup>25</sup> and ENSO-like processes have been proposed to operate during DO events<sup>26</sup>. Mechanisms that would likely influence just West Antarctic moisture sources as well as mechanisms that could influence all Antarctic moisture sources are potentially viable in the context of the DO events.

Our moisture tagging experiments show that the mean MSDs for both EDML and EDC are located further north than that for WDC (Fig. S12). All three MSDs show the same sign of response to interannual variability in the position of the storm tracks, though while the SAM sensitivity of the MSDs for WDC and EDC are similar, the MSD for EDML is less sensitive.

The EDC  $d_m$  record appears to show anomalies during DO 8 and 12 that may result from a shifting moisture source<sup>27,28</sup>. However, neither EDML nor EDC  $d_m$  demonstrate a

consistent relationship during all DO events. The frequency band between 1/1000 to 1/3000 yrs is critical to this question, where WDC  $d_{in}$  and  $CH_4$  are coherent and most nearest to in-phase (0 phase angle, Fig. 3). The timescales and  $\Delta$ age uncertainties in particular prevent similar analysis of the  $d_{in}$  and  $CH_4$  records from the EDML and EDC cores. We can compare the EDML and EDC  $d_{in}$  records directly to the WDC  $d_{in}$  record, though neither show significant coherence with WDC  $d_{in}$  at frequencies lower than 1/3000 years (Fig. S7). While possibly reflecting real zonal asymmetry at these timescales, this lack of coherence likely reflects mismatch in the respective timescales, resolution differences, or even uncertainty in the definition of the parameter.

We also compare the phasing of the  $\delta^{18}O$  and  $d_{in}$  records within each core, thus eliminating the influence of inter-core age scale uncertainty. The  $\delta^{18}O$  to  $d_{in}$  coherence and phase relationship in EDC is similar to the one in WDC over the 3-1 ka band, while the EDML records show less meaningful coherence. The time series of EDC and WDC  $d_{in}$  also show qualitative similarities over some DO intervals (Fig. 1). However, inter-core age scale uncertainties limit confidence in this relationship and without the ability to compare directly to the phasing with  $CH_4$  in each core, we cannot judge whether these relationships arise from systematic differences related to the DO events or random noise. While the suggestion of a similar response of WDC and EDC  $d_{in}$  records is consistent with our moisture tagging results above, the paleo climate data must be judged as inconclusive as to whether storm track shifts occurred outside the Pacific Sector during all events. Synchronization of the WDC age scale with those of other East Antarctic records in the future will improve our ability to answer this question.

## 2.8 Additional drivers of $d_{in}$

While explaining a large portion of the variance, a simple linear combination of the DO-like ( $CH_4$ -like) and AIM-like ( $\delta^{18}O$ -like) signals is not a complete description of the  $d_{in}$  record. We note, for example, that the  $d_{in}$  anomalies coincident with the largest AIM events are larger than would be expected from the linear model. The Clausius–Clapeyron relation should act to amplify these large warming signals since the absolute humidity of the boundary layer, warmed by the underlying SST's, will increase and thus shift the MSD toward the warmer regions. Other mechanisms such as changes in sea ice distribution could act to influence the MSD or the  $d_{in}$  of vapor directly, but are poorly constrained.

Additional sources of  $d_{in}$  variability may include changes in the magnitude of the meridional SST gradient or coupling of the SST gradient to atmospheric circulation and the MSD. Finally, SSTs in the northern-most portion of the MSD of WAIS Divide may not have been AIM-like in character, though paleoclimate constraints on SST variability in these regions is sparse.

The largest differences between the observed WDC  $d_{in}$  and that expected from a simple combination of AIM and DO-like variability appears during the coldest NH stadials (Figure S3), the so-called “Heinrich Stadials”. The WDC  $CH_4$  record shows small step changes during some of these periods that have been suggested to represent extreme southward displacement of the ITCZ<sup>29</sup>. Parallel displacement of the southern westerly winds would be expected to drive  $d_{in}$  anomalies opposite in sign to those observed. Its possible that such changes in the SH atmospheric circulation could drive changes in other moisture source region conditions. We note however that positive SO SST anomalies are

expected to be largest during these stadials<sup>30</sup>, which should drive  $d_{ln}$  anomalies of the observed sign.

We also note an interesting overshoot in the  $d_{ln}$  composite 200 to 400 years after the abrupt baseline shift that is coincident with the DO methane increase (Fig. 3). This feature is robust to the amount of smoothing applied to the data and to the inclusion or exclusion of different AIM events. It is not clear what this anomaly represents. We speculate that after the Northern Hemisphere has warmed to its stable interstadial state, the initiation of cooling in Antarctica and the Southern Hemisphere further increases the inter-hemispheric temperature difference which would continue to push the storm tracks further north for a time. This would increase the sampling of warmer sea surface temperatures and continue the  $d_{ln}$  increase. Additional mechanisms could involve changes in sea ice extent, which could influence the temperature and extent of moisture sources, or perhaps some type of “overshoot warming” related to ocean heat transport changes. Attribution of this feature is challenging without specific hypotheses against which to test the data. In any case, the occurrence of this feature does not affect the statistical assessment of timing of the  $d_{ln}$  shift.

### Supplementary References

1. Dansgaard, W. Stable isotopes in precipitation. *Tellus* **16**, 436–468 (1964).
2. Craig, H. Isotopic variations in meteoric waters. *Science* (1961).
3. Uemura, R. *et al.* Ranges of moisture-source temperature estimated from Antarctic ice cores stable isotope records over glacial–interglacial cycles. *Clim. Past* **8**, 1109–1125 (2012).
4. Merlivat, L. & Jouzel, J. Global climatic interpretation of the deuterium-oxygen 18 relationship for precipitation. *Journal of Geophysical Research: Oceans (1978–2012)* **84**, 5029–5033 (1979).
5. Stenni, B. *et al.* The deuterium excess records of EPICA Dome C and Dronning Maud Land ice cores (East Antarctica). *Quaternary Science Reviews* **29**, 146–159 (2010).
6. Huybers, P. & Denton, G. Antarctic temperature at orbital timescales controlled by local summer duration. *Nature Geoscience* **1**, 787–792 (2008).
7. Bintanja, R., van de Wal, R. S. W. & Oerlemans, J. Modelled atmospheric temperatures and global sea levels over the past million years. *Nature* **437**, 125–128 (2005).
8. Hoffmann, G., Werner, M. & Heimann, M. Water isotope module of the ECHAM atmospheric general circulation model: A study on timescales from days to several years. *Journal of Geophysical Research: Oceans (1978–2012)* **103**, 16871–16896 (1998).
9. Schoenemann, S. W., Steig, E. J., Ding, Q., Markle, B. R. & Schauer, A. J. Triple water-isotopologue record from WAIS Divide, Antarctica: Controls on glacial-interglacial changes in 17Oexcess of precipitation. *J. Geophys. Res. Atmos.* **119**, 8741–8763 (2014).
10. Schmidt, G. A., LeGrande, A. N. & Hoffmann, G. Water isotope expressions of intrinsic and forced variability in a coupled ocean-atmosphere model. *J. Geophys. Res.* **112**, D10103 (2007).
11. Marshall, G. J. Trends in the Southern Annular Mode from Observations and Reanalyses. *J. Climate* **16**, 4134–4143 (2003).
12. Ganopolski, A., Rahmstorf, S., Petoukhov, V. & Claussen, M. Simulation of modern and glacial climates with a coupled global model of intermediate complexity. *Nature* (1998).
13. Mo, K. C. Relationships between Low-Frequency Variability in the Southern Hemisphere and Sea Surface Temperature Anomalies. *J. Climate* **13**, 3599–3610 (2000).
14. Thompson, D. W. J. & Wallace, J. M. Annular Modes in the Extratropical Circulation. Part I: Month-to-Month Variability\*. *J. Climate* **13**, 1000–1016 (2010).
15. Steen Larsen, H. C. *et al.* Moisture sources and synoptic to seasonal variability of North Atlantic water vapor isotopic composition. *J. Geophys. Res. Atmos.* **120**, 5757–5774 (2015).
16. Pfahl, S. & Sodemann, H. What controls deuterium excess in global precipitation? *Clim. Past* **10**, 771–781 (2014).
17. Dai, A. Recent Climatology, Variability, and Trends in Global Surface Humidity. *J. Climate* **19**, 3589–

- 3606 (2006).
18. Vimeux, F., Cuffey, K. M. & Jouzel, J. New insights into Southern Hemisphere temperature changes from Vostok ice cores using deuterium excess correction. *Earth and Planetary Science Letters* (2002).
  19. Kalnay, E. *et al.* The NCEP/NCAR 40-Year Reanalysis Project. [http://dx.doi.org.offcampus.lib.washington.edu/10.1175/1520-0477\(1996\)077<0437:TNYRP>2.0.CO;2](http://dx.doi.org.offcampus.lib.washington.edu/10.1175/1520-0477(1996)077<0437:TNYRP>2.0.CO;2) **77**, 437–471 (1996).
  20. Sodemann, H. & Stohl, A. Asymmetries in the moisture origin of Antarctic precipitation. *Geophys. Res. Lett.* **36**, L22803 (2009).
  21. Ceppi, P., Hwang, Y.-T., Liu, X., Frierson, D. M. W. & Hartmann, D. L. The relationship between the ITCZ and the Southern Hemispheric eddy-driven jet. *J. Geophys. Res. Atmos.* **118**, 5136–5146 (2013).
  22. Staten, P. W. & Reichler, T. On the ratio between shifts in the eddy-driven jet and the Hadley cell edge. *Climate Dynamics* **42**, 1229–1242 (2014).
  23. Wang, X. *et al.* Wet periods in northeastern Brazil over the past 210 kyr linked to distant climate anomalies. *Nature* **432**, 740–743 (2004).
  24. Chiang, J. C. H., Lee, S.-Y., Putnam, A. E. & Wang, X. South Pacific Split Jet, ITCZ shifts, and atmospheric North–South linkages during abrupt climate changes of the last glacial period. *Earth and Planetary Science Letters* **406**, 233–246 (2014).
  25. Steig, E. J. *et al.* Recent climate and ice-sheet changes in West Antarctica compared with the past 2,000 years. *Nature Geoscience* **6**, 372–375 (2013).
  26. Clement, A. C. & Peterson, L. C. Mechanisms of abrupt climate change of the last glacial period. *Rev. Geophys.* **46**, RG4002 (2008).
  27. Buiron, D. *et al.* Regional imprints of millennial variability during the MIS 3 period around Antarctica. *Quaternary Science Reviews* **48**, 99–112 (2012).
  28. Landais, A. *et al.* A review of the bipolar see-saw from synchronized and high resolution ice core water stable isotope records from Greenland and East Antarctica. *Quaternary Science Reviews* **114**, 18–32 (2015).
  29. Rhodes, R. H. *et al.* Enhanced tropical methane production in response to iceberg discharge in the North Atlantic. *Science* **348**, 1016–1019 (2015).
  30. Stocker, T. F. & Johnsen, S. J. A minimum thermodynamic model for the bipolar seesaw. *Paleoceanography* **18**, 1087 (2003).

## Supplementary Figures 1-14 Captions

**Figure S1.** DO warming (A) and cooling (B) stacks are shown for WDC  $\delta^{18}\text{O}$  (red), NGRIP  $\delta^{18}\text{O}$  (black) and WDC  $\text{CH}_4$  (gold) and  $d_{ln}$ . The RAMPFIT results, break points, and uncertainty bounds on the initial break points are shown as solid straight lines and points for different filtering schemes applied to WDC  $d_{ln}$  are shown: a 1-2-1 filter (dark blue, plotted with a 0.5 per mil offset for clarity), a 3 point moving average (1-1-1, purple), and no filter (light blue). This midpoints of abrupt change in NGRIP  $\delta^{18}\text{O}$  (black) and WDC  $\text{CH}_4$  (gold) are shown for reference, as well as the BREAKFIT change point identified for the WDC  $\delta^{18}\text{O}$  (red). Arbitrary offsets are applied to the stacks for visual clarity.

**Figure S2.** Coherence and phasing of WDC records. Multi-taper spectral coherence a) and phase b, c) for WDC  $\delta^{18}\text{O}$  and  $\text{CH}_4$  (orange),  $\text{CH}_4$  and  $d_{ln}$  (green),  $\delta^{18}\text{O}$  and  $d_{ln}$  (purple), and  $d_{ln}$  and the linear regression model of  $\text{CH}_4$  and  $\delta^{18}\text{O}$  (cyan). Coherence is significant (at 95%) above dashed line; a Monte Carlo estimate of the  $2\sigma$  uncertainty in the coherence and phase associated with chronological uncertainties (described in supplementary text) is shown in shading in a) and b). The 95% confidence interval on the phase based on a 1,000 iteration Monte Carlo estimate of the from the MATLAM cmtm.m routine shown in shading in c).

**Figure S3.** Time series of WDC CH<sub>4</sub> (gold),  $\delta^{18}\text{O}$  (red),  $d_{ln}$  (blue) and the linear regression model (orange) anomalies from the interval 10 - 67ka. High frequency variability (period <400 yrs) was removed from  $d_{ln}$  by a low pass Butterworth filter for visual clarity.

**Figure S4.** Multi-taper spectral coherence and phase are shown for  $\delta^{18}\text{O}$  &  $d_{ln}$  (light blue),  $\delta^{18}\text{O}$  & the linear model (dark blue), CH<sub>4</sub> &  $d_{ln}$  (orange), and CH<sub>4</sub> and the linear model (red). Coherence at or above the dashed black line is significant at 95%. Phase values are in degrees and phase uncertainties are omitted for clarity. Large high frequency noise in the WDC  $d_{ln}$  record slightly reduces coherence compared to the linear model but phase angles and their change with frequency are consistent.

**Figure S5.** A) Rayleigh distillation model results due solely to equilibrium fractionation. Note that the lack of all fractionation processes in the model makes the absolute delta values much lower than reality. B) Rayleigh distillation model results for equilibrium fractionation plotted in the logarithmic space. Equivalent results in the linear space are shown in grey for reference.

**Figure S6.** Antarctic  $d_{excess}$  (cyan) and  $d_{ln}$  (blue) from EDC and EDML<sup>5</sup> compared to WDC. Data are plotted as anomalies (standard deviations relative to the mean of each record), with constant offsets for EDC and WDC, and with a weak low pass filter applied (cutoff frequency = 1/250 yrs) for visual clarity. Note a gap in data in the EDML record at ~45 ka. Figures are plotted in anomalies since ‰ values are not directly comparable between the definitions.

**Figure S7.** A) Time series of  $d_{excess}$  for WDC (blue), EDML (red), and EDC (black). Time series anomalies calculated as the standard deviation from the 10ka to 67 ka mean. A low pass, fourth order butterworth filter with a 400 yr cutoff period has been applied to all curves. B) Multi-taper spectral coherence is shown among the three  $d_{excess}$  records. C & D) as above but for the  $d_{ln}$  definition of the parameter.

**Figure S8.** Correlation of monthly SH surface temperature (T) with WDC site temperature (WDC T), and  $\delta^{18}\text{O}$ ,  $d_{ln}$ , and  $d_{excess}$  of precipitation at the nearest grid point to WDC from ECHAM 4.6.

**Figure S9.** Correlation of mean annual  $d_{ln}$  of precipitation to an in-model index of the SAM at every grid point. ECHAM 4.6 model results.

**Figure S10.** Comparison of WDC  $d_{ln}$  with the AAO index of SH westerly wind variability from 1980-2005. a) Anomalies (z-score) of the inverse of the AAO index and monthly WDC  $d_{ln}$  timeseries. Histogram of  $d_{ln}$  anomalies for all months when b) the AAO index is positive (south-ward displace winds) and c) the AAO index is negative. Mean values for each histogram shown in red vertical line.

**Figure S11.** Map of bins used for moisture tagging. Each color represents an individual zonal bin with a width of 5° latitude. The Antarctic continent is a single separate bin. Water evaporated from these bins is tracked independently through the model.

**Figure S12.** The moisture source distribution for the WDC (blue), EDML (red), and EDC (black) core sites, shown as a histogram of latitude. Values reflect the fraction of total moisture that fell at the core site against the latitude of evaporation and sum to unity. The stair-step pattern represents the discrete bins used in the water tagging experiment.

**Figure S13.** The moisture source distribution for WDC composited for phases of the SAMi index (A) and ITCzi index (B), respectively. The mean latitude of each distribution is indicated at bottom.

**Figure S14.** Mean SH 10m zonal wind (contours, 1 m/s interval) from the CAM5 moisture tagging experiment. Shading shows the zonal wind difference (m/s) between strongly northward and southward shifted westerly winds ( $\pm 1\sigma$  of internal Southern Annular Mode variability). WDC site location marked by  $\otimes$ .

**Table S1.** Detecting change-points in stacked records of  $d_m$ . Initial change-points,  $t_1$ , in WDC  $d_m$  as detected by the RAMPFIT method in years after the midpoint of DO transitions in NGRIP  $\delta^{18}\text{O}$ . Two smoothing techniques were applied to the  $d_m$  data to reduce measurement noise, a 1-2-1 filter and a 3-point moving average, which are compared to unsmoothed data (raw). Reported uncertainties are  $1\sigma$ , determined by a Monte Carlo moving block bootstrap (MBB) technique.

	<b>DO Warming</b>		<b>DO cooling</b>	
<b>Smoothing type</b>	<b><math>t_1</math> (yrs)</b>	<b><math>1\sigma</math> MBB Uncertainty (yrs)</b>	<b><math>t_1</math> (yrs)</b>	<b><math>1\sigma</math> MBB Uncertainty (yrs)</b>
<b>1-2-1</b>	45	$\pm 74$	-27	$\pm 59$
<b>3 pt. mo. Avg.</b>	37	$\pm 69$	-20	$\pm 54$
<b>raw</b>	97	$\pm 67$	-17	$\pm 41$

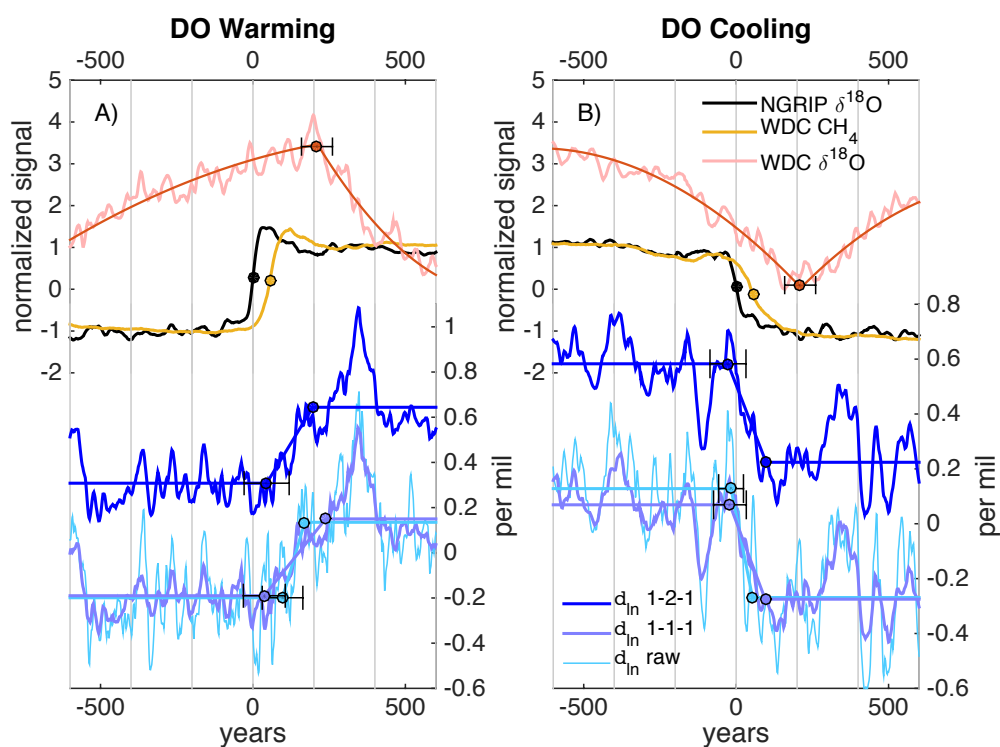


**Figure S1.** DO warming (A) and cooling (B) stacks are shown for WDC  $\delta^{18}\text{O}$  (red), NGRIP  $\delta^{18}\text{O}$  (black) and WDC  $\text{CH}_4$  (gold) and  $d_{in}$ . The RAMPFIT results, break points, and uncertainty bounds on the initial break points are shown as solid straight lines and points for different filtering schemes applied to WDC  $d_{in}$  are shown: a 1-2-1 filter (dark blue, plotted with a 0.5 per mil offset for clarity), a 3 point moving average (1-1-1, purple), and no filter (light blue). This midpoints of abrupt change in NGRIP  $\delta^{18}\text{O}$  (black) and WDC  $\text{CH}_4$  (gold) are shown for reference, as well as the BREAKFIT change point identified for the WDC  $\delta^{18}\text{O}$  (red). Arbitrary offsets are applied to the stacks for visual clarity.

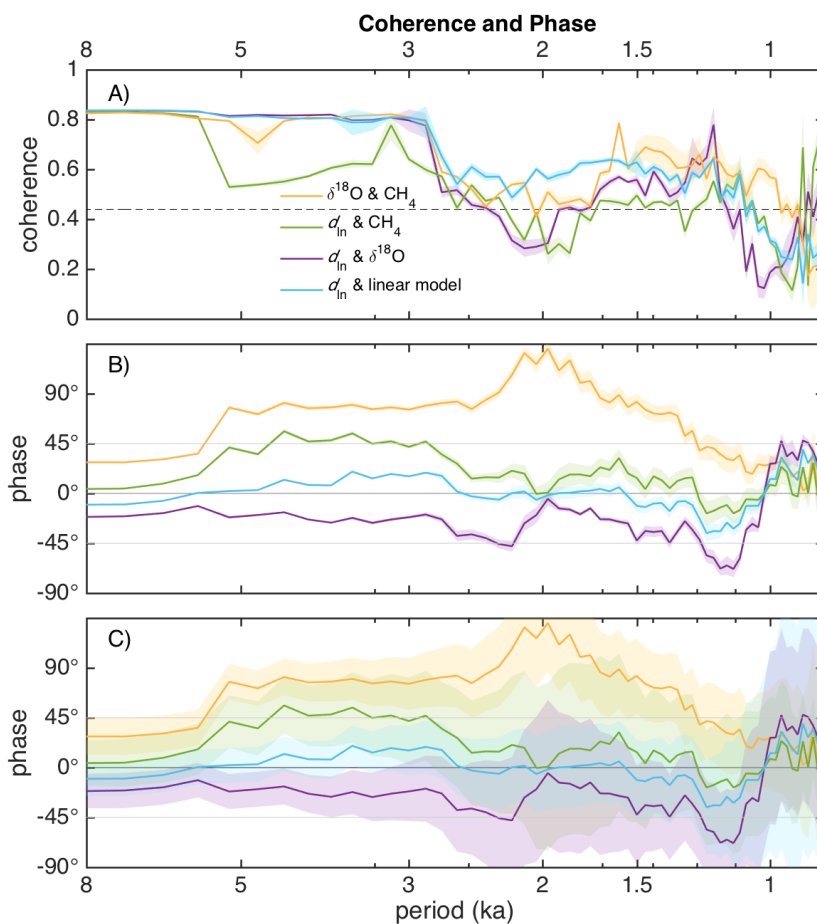


**Figure S2.** Coherence and phasing of WDC records. Multi-taper spectral coherence a) and phase b, c) for WDC  $\delta^{18}\text{O}$  and  $\text{CH}_4$  (orange),  $\text{CH}_4$  and  $d_{in}$  (green),  $\delta^{18}\text{O}$  and  $d_{in}$  (purple), and  $d_{in}$  and the linear regression model of  $\text{CH}_4$  and  $\delta^{18}\text{O}$  (cyan). Coherence is significant (at 95%) above dashed line; a Monte Carlo estimate of the  $2\sigma$  uncertainty in the coherence and phase associated with chronological uncertainties (described in supplementary text) is shown in shading in a) and b). The 95% confidence interval on the phase based on a 1,000 iteration Monte Carlo estimate of the from the MATLAB cmtm.m routine shown in shading in c).

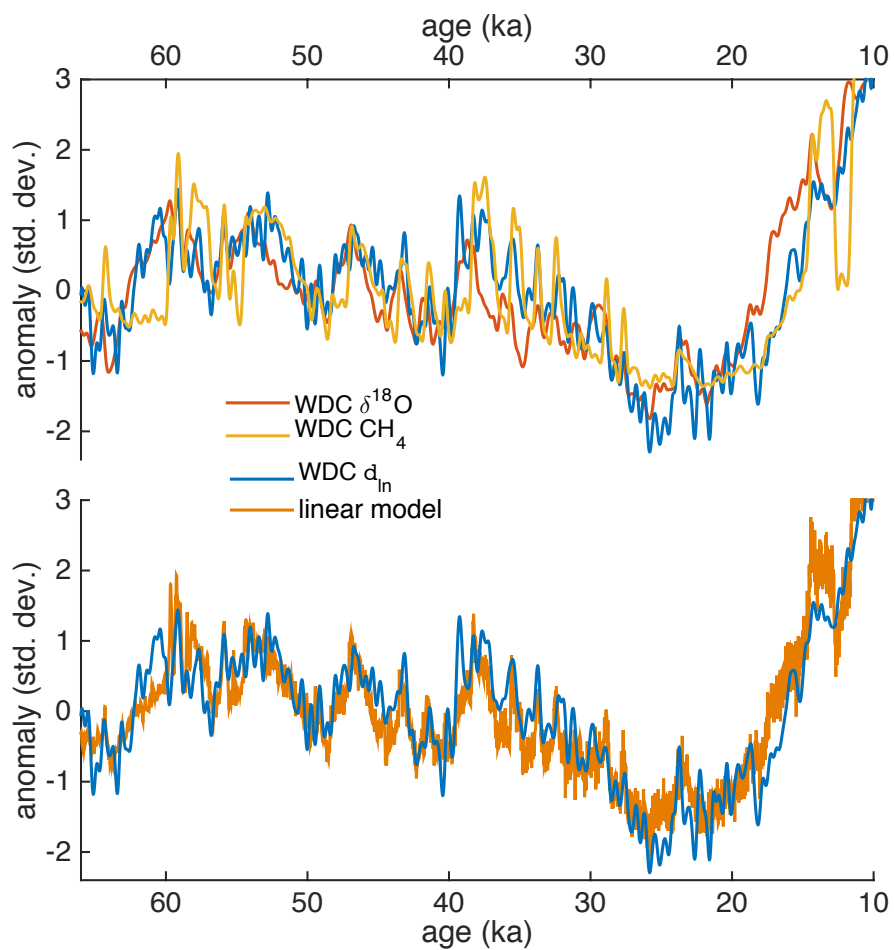


**Figure S3.** Time series of WDC  $\text{CH}_4$  (gold),  $\delta^{18}\text{O}$  (red),  $d_m$  (blue) and the linear regression model (orange) anomalies from the interval 10 - 67ka. High frequency variability (period <400 yrs) was removed from  $d_m$  by a low pass Butterworth filter for visual clarity.

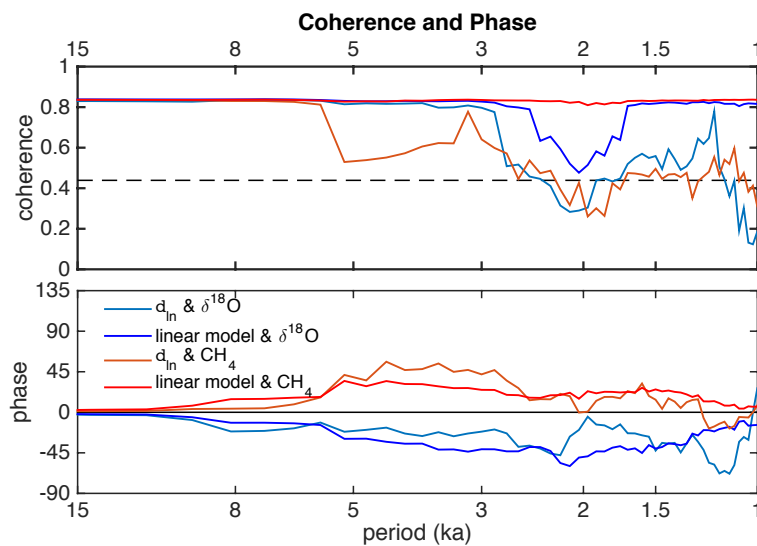


**Figure S4.** Multi-taper spectral coherence and phase are shown for  $\delta^{18}O$  &  $d_{in}$  (light blue),  $\delta^{18}O$  & the linear model (dark blue),  $CH_4$  &  $d_{in}$  (orange), and  $CH_4$  and the linear model (red). Coherence at or above the dashed black line is significant at 95%. Phase values are in degrees and phase uncertainties are omitted for clarity. Large high frequency noise in the WDC  $d_{in}$  record slightly reduces coherence compared to the linear model but phase angles and their change with frequency are consistent.

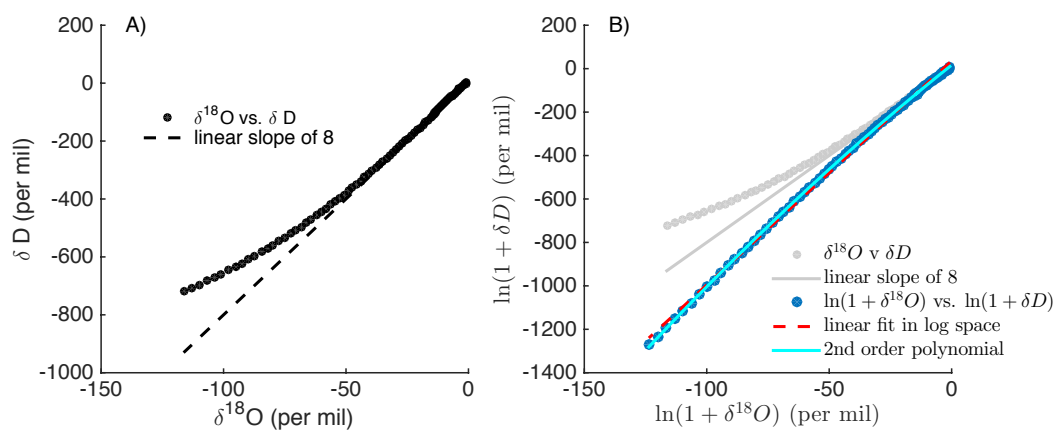


**Figure S5.** A) Rayleigh distillation model results due solely to equilibrium fractionation. Note that the lack of all fractionation processes in the model makes the absolute delta values much lower than reality. B) Rayleigh distillation model results for equilibrium fractionation plotted in the logarithmic space. Equivalent results in the linear space are shown in grey for reference.

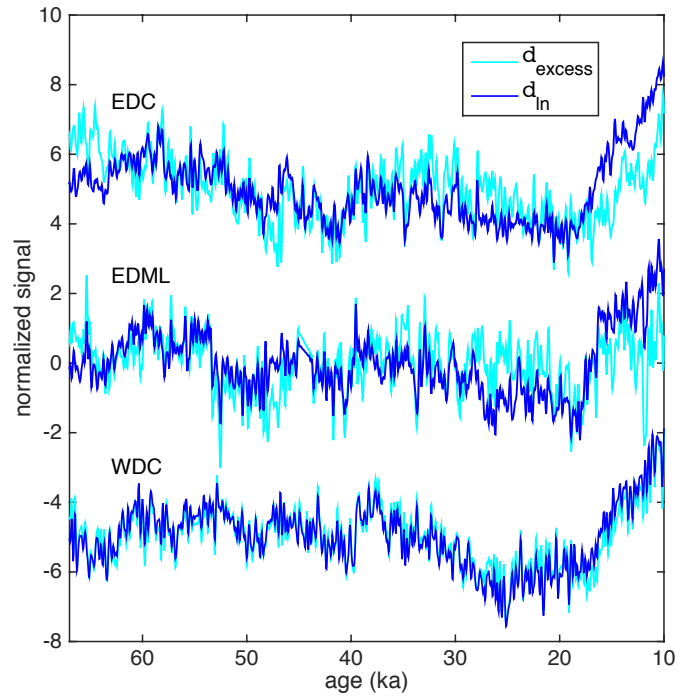


**Figure S6.** Antarctic  $d_{\text{excess}}$  (cyan) and  $d_{\text{in}}$  (blue) from EDC and EDML {Stenni:2010iy} compared to WDC. Data are plotted as anomalies (standard deviations relative to the mean of each record), with constant offsets for EDC and WDC, and with a weak low pass filter applied (cutoff frequency = 1/250 yrs) for visual clarity. Note a gap in data in the EDML record at  $\sim 45$  ka. Figures are plotted in anomalies since ‰ values are not directly comparable between the definitions.

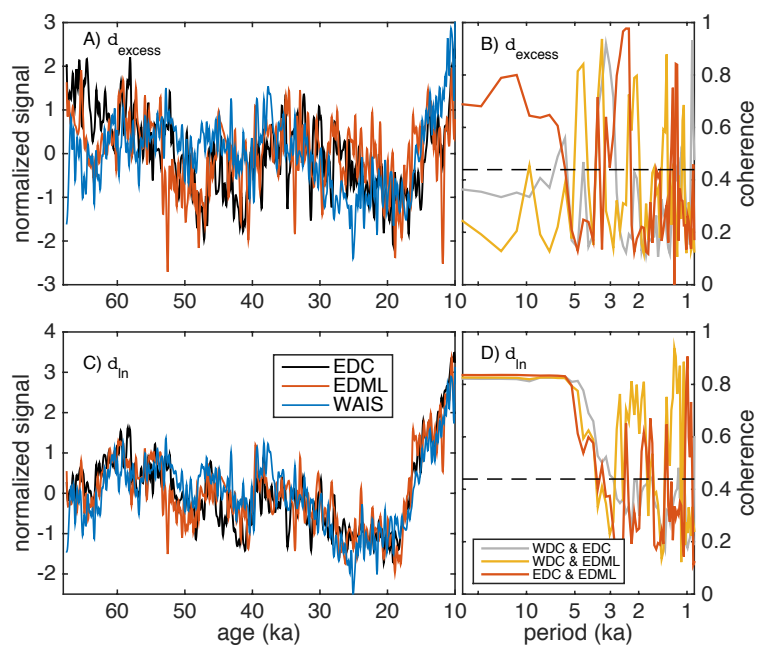


**Figure S7.** A) Time series of  $d_{excess}$  for WDC (blue), EDML (red), and EDC (black). Time series anomalies calculated as the standard deviation from the 10ka to 67 ka mean. A low pass, fourth order butterworth filter with a 400 yr cutoff period has been applied to all curves. B) Multi-taper spectral coherence is shown among the three  $d_{excess}$  records. C & D) as above but for the  $d_{in}$  definition of the parameter.

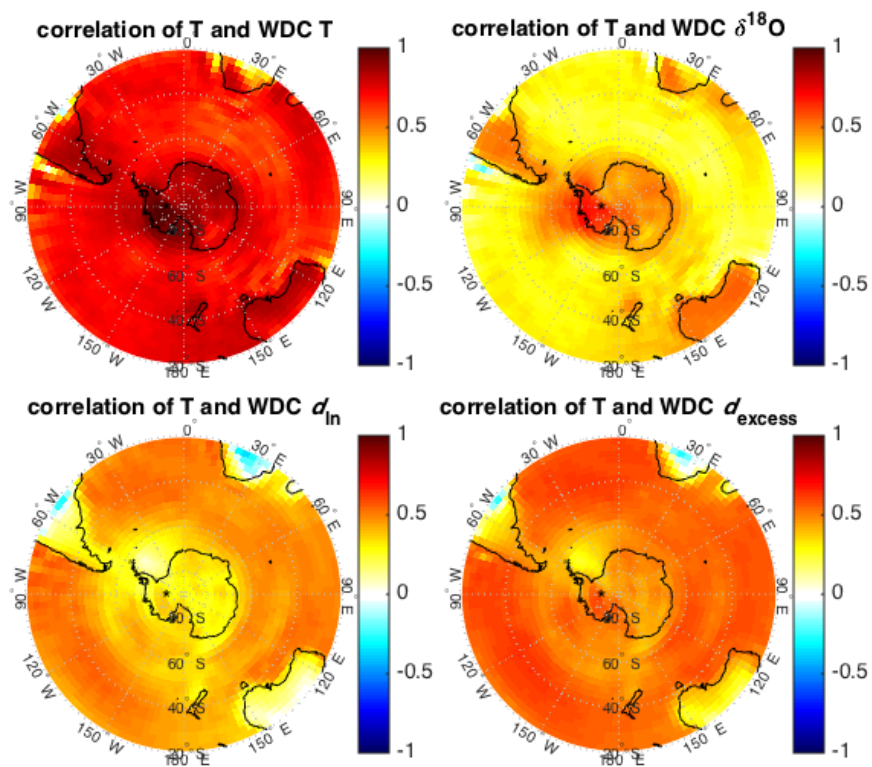


**Figure S8.** Correlation of monthly SH surface temperature (T) with WDC site temperature (WDC T), and  $\delta^{18}\text{O}$ ,  $d_{in}$ , and  $d_{excess}$  of precipitation at the nearest grid point to WDC from ECHAM 4.6.

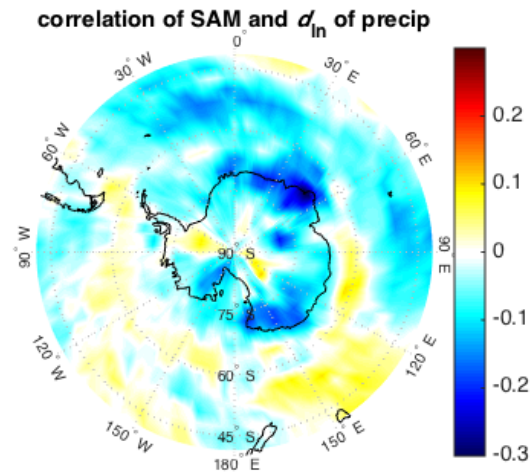


**Figure S9.** Correlation of mean annual  $d_{in}$  of precipitation to an in-model index of the SAM at every grid point. ECHAM 4.6 model results.

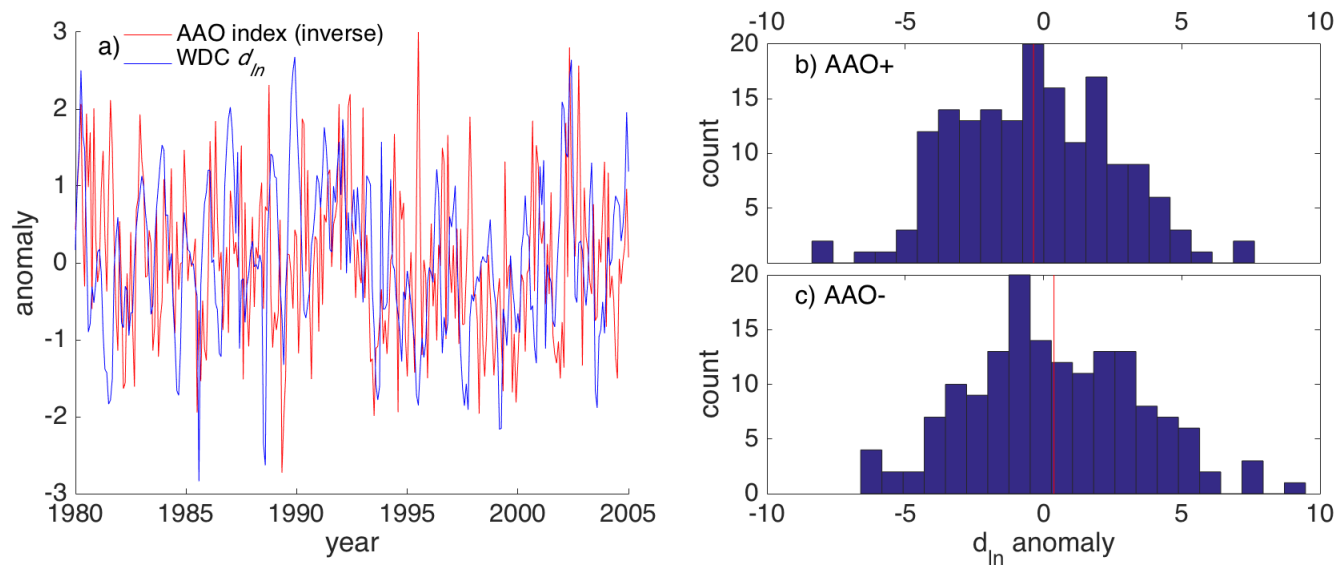


**Figure S10.** Comparison of WDC  $d_{in}$  with the AAO index of SH westerly wind variability from 1980-2005. a) Anomalies (z-score) of the inverse of the AAO index and monthly WDC  $d_{in}$  timeseries. Histogram of  $d_{in}$  anomalies for all months when b) the AAO index is positive (south-ward displace winds) and c) the AAO index is negative. Mean values for each histogram shown in red vertical line.

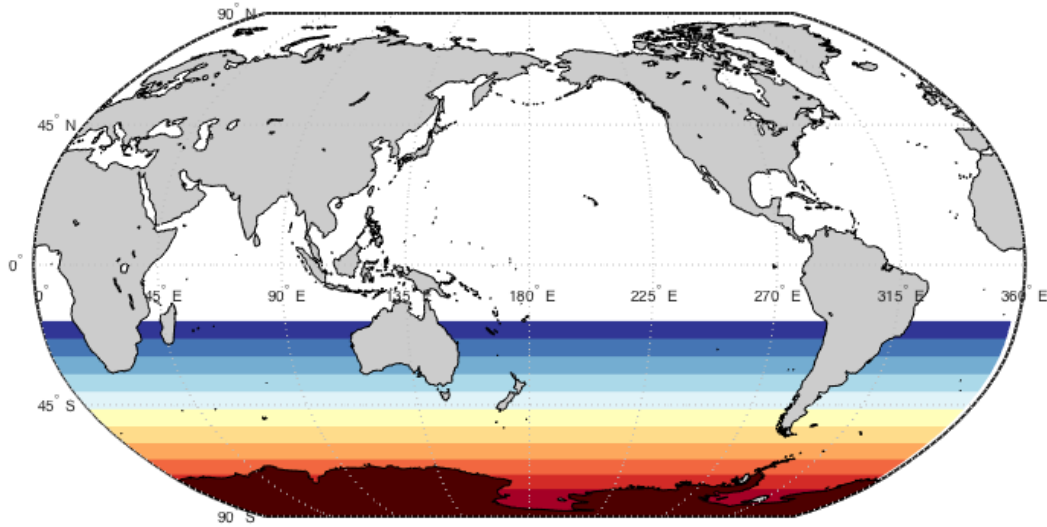


**Figure S11.** Map of bins used for moisture tagging. Each color represents an individual zonal bin with a width of 5° latitude. The Antarctic continent is a single separate bin. Water evaporated from these bins is tracked independently through the model.

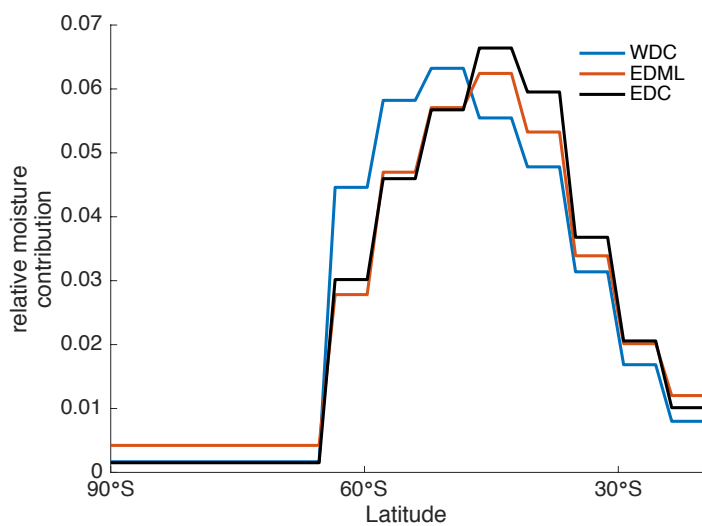


**Figure S12.** The moisture source distribution for the WDC (blue), EDML (red), and EDC (black) core sites, shown as a histogram of latitude. Values reflect the fraction of total moisture that fell at the core site against the latitude of evaporation and sum to unity. The stair-step pattern represents the discrete bins used in the water tagging experiment.

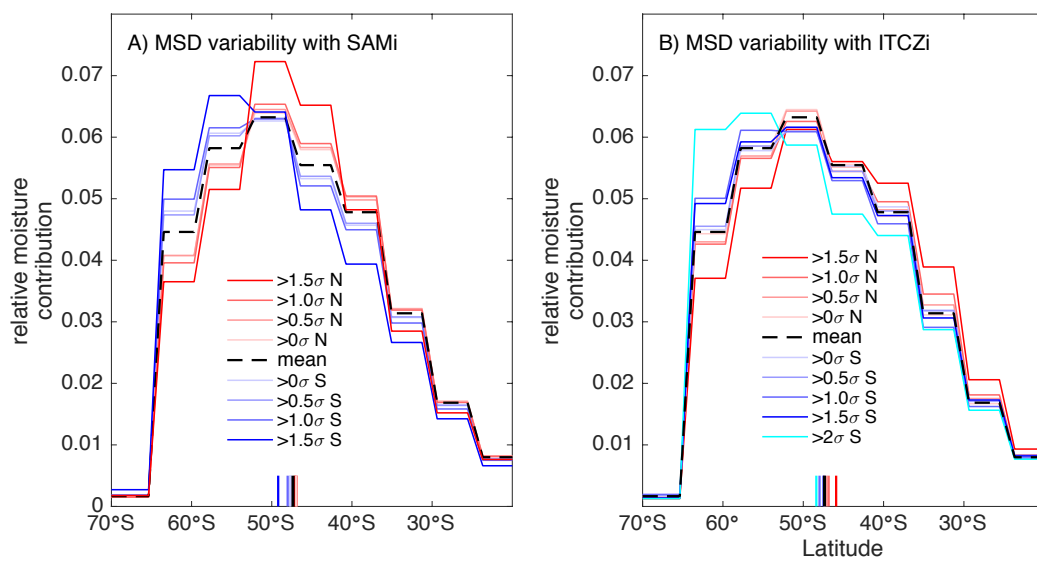


**Figure S13.** The moisture source distribution for WDC composited for phases of the SAMi index (A) and ITCZI index (B), respectively. The mean latitude of each distribution is indicated at bottom.

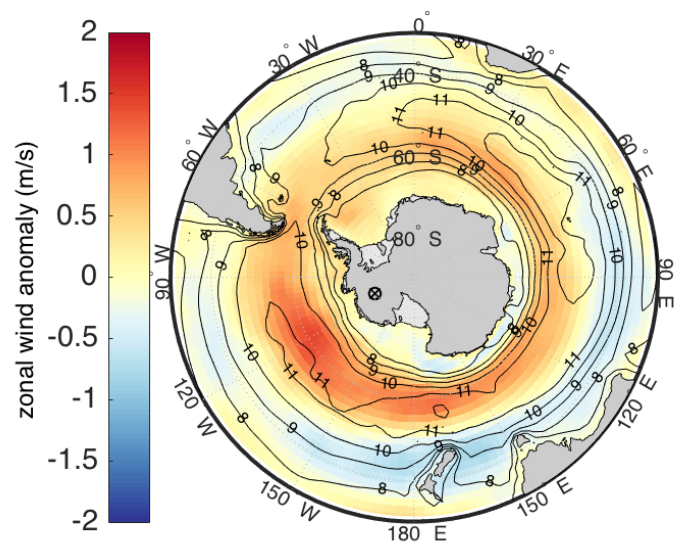


Figure S14. Mean SH 10m zonal wind (contours, 1 m/s interval) from the CAM5 moisture tagging experiment. Shading shows the zonal wind difference (m/s) between strongly northward and southward shifted westerly winds ( $\pm 1\sigma$  of internal Southern Annular Mode variability). WDC site location marked by  $\otimes$ .

Chapter 4

**THE GREAT ATMOSPHERIC WASHING MACHINE:  
RECONCILING WATER, AEROSOLS, AND CLIMATE**

# THE GREAT ATMOSPHERIC WASHING MACHINE: RECONCILING WATER, AEROSOLS, AND CLIMATE

BRADLEY ROSS MARKLE

ERIC STEIG

GERARD ROE

*University of Washington.*

**Ice cores are our most important repositories of past climate history. The interpretation of these records rests on understanding the processes affecting trace constituents of the ice, the foremost of which are rare water isotopes and aerosols. Stable-isotope ratios of water are the classic paleothermometer, and are backed by well-established theory. The interpretation of variability in aerosol proxies, such as mineral dust and sea salts, has remained a topic of debate. Here, we present high-resolution water-isotope and aerosol records from West Antarctica. We show that variations in water isotopes and aerosol concentrations in ice cores may be understood through a single underlying principle. The hydrologic cycle, driven by the thermodynamics of water, dominates the progressive removal of trace atmospheric constituents and their variability at the poles. This framework reconciles our understanding of shared variability in water isotopes and aerosols, as well as changes in the spatial pattern of aerosol concentrations globally, leading to a better understanding of past radiative forcing. Further, we show that this lens reveals how fundamental aspects of climate, like polar amplification, are etched upon these proxy records.**

## 1. INTRODUCTION

The stable isotope ratios of water<sup>1</sup>, such as  $\delta^{18}\text{O}$ , are tracers of the integrated evaporation and condensation history of water in the atmosphere (Dansgaard, 1964). The exponential relationship between atmospheric moisture and temperature means that the poleward transport of moisture drives the progressive distillation of water isotopes, enabling their use as a proxy for condensation temperature over ice sheets (Merlivat and Jouzel, 1979; Jouzel et al., 1997).

In addition to moisture, a variety of aerosols, such as mineral dust and sea salts, are transported to Antarctica from lower latitude sources by the atmospheric circulation (Legrand and Delmas, 1988; Alley et al., 1995). These aerosols are deposited on the ice sheet through wet and dry deposition and preserved as impurities within the ice (Wolff and Bales, 1996). The ice-core records of dust and sea salt show large variability across all time scales, in particular the glacial-interglacial transition (Petit et al., 1981; Fischer et al., 2007a). The source of this variability is debated, and may arise in principle from changes in transport, changes in aerosol lifetimes, the efficacy of wet and dry deposition, and source-emission strength (Fischer et al., 2007a; Alley et al., 1995; Mahowald et al., 2006; Petit and Delmonte, 2009; Lambert et al., 2008).

Terrestrial dust and related ions, such as  $\text{Ca}^{2+}$  or  $\text{Mg}^{2+}$ , recorded in Antarctic ice cores show tenfold to hundredfold changes in concentration between the last glacial period and present. The provenance of this dust is largely South America (Delmonte et al., 2008; Albani et al., 2012). There is a long standing view that the ice-core records of dust deposition reflect variability in dust source emissions (Petit et al., 1981; Delmonte et al., 2002; Wolff et al., 2006; Fischer et al., 2007a; Lambert et al., 2008) suggesting significant changes in environmental conditions in the source regions (Delmonte et al., 2002). The environmental conditions influencing dust emission include wind speeds (Petit et al., 1981), gustiness (McGee et al., 2010), aridity, continental shelf area, soil moisture, land cover, and vegetation (Andersen et al., 1998; Wolff et al., 2006; Li et al., 2010), and glacial activity (Sugden et al., 2009; Bauer and Ganopolski, 2010). Correspondence of Antarctic dust records to other Antarctic and Southern Ocean records of climate has been suggested to reflect broad coupling of the climate system (Lambert et al., 2008; Lamy et al., 2014) in which different aspects of climate, including Antarctic temperature and the combination of factors influencing dust emission, are linked across latitudes, perhaps through the influence of the meridional temperature gradient on circulation (Petit et al., 1981). Further, these links are suggested to change through time possibly in response to threshold-like behavior (Lambert et al., 2008; Petit and Delmonte, 2009). Changes in variables such as transport times or lifetimes of aerosols have also been investigated as sources of variability. However, dust transport times were relatively unchanged between the glacial and present (Fischer et al., 2007a; Petit and Delmonte, 2009). The role of lifetime changes, linked to the water cycle, have been suggested to range from important (Yung et al., 1996; Petit and Delmonte, 2009) to modest or negligible (Lambert et al., 2008; Wolff et al., 2006; Fischer et al., 2007b; Li et al., 2010).

While changes in dust source is the most prevalent interpretation of ice-core dust records, it has explanatory shortfalls. Lower latitude records of dust deposition show orders-of-magnitude less variability than those from Antarctica, in places showing a 2

---

<sup>1</sup>Stable water isotope ratios are reported as delta values:  $\delta^{18}\text{O} = \frac{R_{\text{sample}}^{18} - R_{\text{VSMOW}}^{18}}{R_{\text{VSMOW}}^{18}}$ , where  $R_{\text{sample}}^{18}$  is the number ratio of heavy to light oxygen isotopes in a sample,  $R^{18} = \frac{^{18}\text{O}}{^{16}\text{O}}$ , and  $R_{\text{VSMOW}}^{18}$  is the number ratio in the Vienna Standard Mean Ocean Water (VSMOW) standard.

to 5-fold increase during the last glacial period while other locations show a reduction (Kohfeld and Harrison, 2001; Albani et al., 2012; Lamy et al., 2014; Harrison et al., 2001). Models do not reproduce tenfold to hundredfold changes in source strength and generally underestimate changes in deposition in Antarctica (Albani et al., 2012; Bauer and Ganopolski, 2010; Mahowald et al., 2006; Albani et al., 2014).

The deposition of sea salts and related ions like  $\text{Na}^+$  and  $\text{Cl}^-$ , was at least an order-of-magnitude higher in Antarctica during the glacial period compared to present (Petit et al., 1981; Wolff et al., 2006). This variability is also widely interpreted to represent sea-salt source emission changes (Fischer et al., 2007a; Wolff et al., 2006; WAIS Divide Project Members, 2013, 2015), though the source of those changes remains uncertain. Antarctic sea-salt variability is often linked to sea-ice extent changes, yet the sign of that relationship is debated. Sea-ice extent was expanded during the LGM (Gersonde et al., 2005), which would have reduced the source area of open-ocean sea spray and aerosolized sea salts, though this could have been offset in part by changes in windspeed (Petit et al., 1981). Alternatively, it has been suggested that sea ice itself is an effective source for sea salts due to frost flowers (Rankin et al., 2000; Wolff et al., 2006) and thus increased sea-ice area could have increased emissions. Evidence for a significant contribution of Antarctic sea salts from this source is mixed (Wolff et al., 2006; Curran et al., 2008; Petit and Delmonte, 2009). Further millennial changes in Antarctic Na are subdued at times when sea-ice changes are thought to be large (Fischer et al., 2007a). A semi-empirical model study raises doubts about the relationship of sea-ice extent to Antarctic sodium altogether (Petit and Delmonte, 2009).

In spite of the above shortcomings, ice-core records of both dust and sea salts are widely interpreted to reflect variability in aerosol emissions at the source. Their evolution through time is suggested to reflect the complex combination of source-region variables and their relationships to climate. Any relationships between water isotopes, dust, and sea-salt records thus inferred to arise from relationships between combinations of different aspects of the climate system on disparate parts of the globe (e.g. Antarctic temperature, wind strength over South America, and sea ice extent).

## 2. AN UNDERLYING MECHANISM

A simpler explanation may unite these proxy records. We examine the  $\delta^{18}\text{O}$ , non sea-salt calcium (nssCa, see Methods), and sea-salt sodium (ssNa) records from the West Antarctic Icesheet Divide ice core (WDC)(WAIS Divide Project Members, 2013, 2015), the highest-resolution Antarctic records to span the last deglaciation (Figure 1). The water-isotope variability is strongly anti-correlated with the log of the concentration of both aerosols ( $r = -0.87$ , and  $r = -0.83$ , for nssCa and ssNa, respectively). The variance in the aerosols scale exponentially with the absolute concentration. The covariance resolved among the WDC records is unprecedented, though most Antarctic records show a strong relationship between water isotopes and the log of aerosol variability (Fischer et al., 2007b). The water isotopes and calcium in particular are extremely

coherent, showing significant covariability from multicentennial to orbital timescales (Supplementary Figure S4).

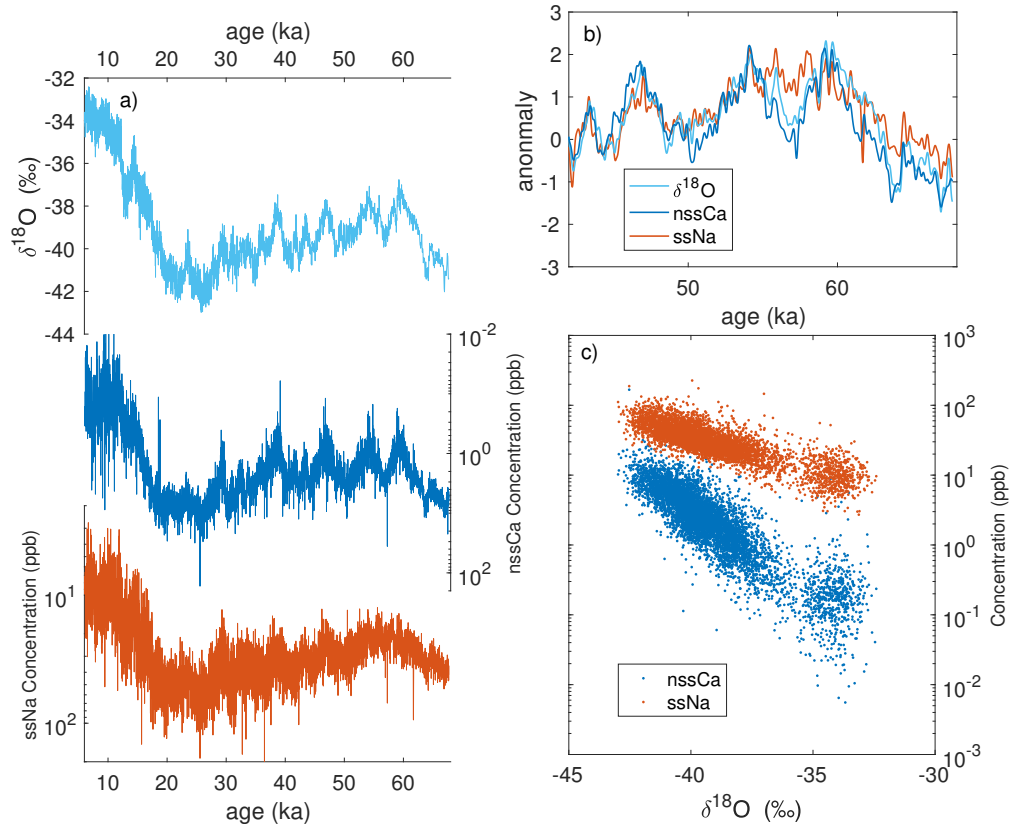


FIGURE 1. Data from the WAIS Divide Ice Core. a) WDC  $\delta^{18}\text{O}$  (top), nssCa (middle), and ssNa (bottom). b) inset of low-pass filtered records, presented as z-score anomalies. High frequency variability ( $> \frac{1}{300\text{yrs}}$ ) removed with a low-pass Butterworth filter. c) WDC  $\delta^{18}\text{O}$  plotted against nssCa (red), and ssNa (blue). Time series are from 6ka to 68ka; aerosol data are only available from below the brittle zone of the core.

We suggest that such a strong correlation must reflect a single dominant physical mechanism. It is intrinsically unlikely to arise spontaneously from concurrent variations among weakly related processes such as Antarctic temperature, distal source strength, and the other processes noted above. For example, the accumulation rate at the WDC site, calculated independently of the other proxies (Fudge et al., 2016), has a weaker statistical relationship to local water-isotope variability (despite a clear mechanistic link), than that

between the water isotopes and nssCa, which purportedly reflects climate and other conditions in South America, some 2,500 miles and 30° of latitude to the north.

The exponential relationship observed in Figure 1, calls for exponential physics. In general such behavior is realized when the rate of change of a quantity varies with the total amount of that quantity. The hydrologic cycle is an obvious candidate to unite variability in water isotopes and aerosols. Two powerful sets of exponential physics link aerosols to the hydrologic cycle.

Aerosols in the atmosphere decay exponentially from the source, owing to progressive removal and dispersion (Wolff and Bales, 1996; Zender et al., 2003). This removal can be quantified by simple exponential decay,

$$C = C_o e^{-\chi} \quad (1)$$

where  $C$  is the atmospheric concentration of aerosol,  $C_o$  is the initial source concentration at emission, and  $\chi$  quantifies the removal. In a simple formulation,  $\chi$  may take the form  $\frac{t}{\tau}$ , (e.g. Fischer et al. (2007a); Petit and Delmonte (2009)) where  $t$  is the transport time from source and  $\tau$  is a characteristic lifetime, though other formulations are possible. Aerosols are removed from the atmosphere in two ways. Dry deposition involves gravitational settling and turbulent interaction with the surface. However the dominant method of aerosol removal globally is wet deposition (Tegen and Fung, 1994). Aerosols act as condensation nuclei, are scavenged by precipitation formation, and are washed-out by falling precipitation (Wolff and Bales, 1996; Albani et al., 2014). The amount of aerosol removed from the atmosphere for a given precipitation event depends on the total concentration of aerosol available.

The characteristic lifetime of aerosols in the atmosphere is affected by the hydrologic cycle (Wolff and Bales, 1996; Yung et al., 1996). The amount of water vapor in the atmosphere varies exponentially with atmospheric temperature, described by the Clausius-Clapeyron relationship. Thus the potential for aerosol removal,  $\chi$ , is nonlinearly dependent on mean state (Yung et al., 1996).

Explanations of long-term high-latitude aerosol variability that rely only on source emission strength,  $C_o$ , are not exponential. Linear changes in source strength,  $C_o$ , lead to linear changes in final concentration,  $C$ , everywhere along the deposition path (Equation 1). Linear changes in removal rate,  $\chi$ , however, lead to exponential changes in  $C$ . Further, we should expect exponential changes in the removal rate with linear changes in the climate's mean temperature, owing to the Clausius-Clapeyron relationship.

Stable-isotope ratios of water are also directly related to the same moisture processes. The  $\delta^{18}\text{O}$  of snow in Antarctica is primarily driven by the integrated condensation history of water between initial evaporation and final precipitation (Dansgaard, 1964). Therefore ice-core water isotopes also depend on precipitation occurring between the evaporative source and the location of deposition.

We construct a simple model of water isotope distillation, aerosol rain-out, and thermodynamic changes in atmospheric moisture, and compare results to the observed

records. Our intent is to estimate the first order response we should expect in the proxy records owing to these processes.

### 3. SIMPLE MODEL

We consider a latitudinal temperature gradient from the mid-latitudes to the pole and assume transport following pseudoadiabatic cooling (Criss, 1999). Moisture is removed from the parcel according to changes in the saturated mixing ratio of air, and the latent heat release of that condensation is the only energy input to cooling process.

Water isotopes are distilled from moisture source latitudes as determined by models (Sodemann and Stohl, 2009; Markle et al., 2017) to the deposition site following well established fractionation equations (Dansgaard, 1964; Merlivat and Jouzel, 1979; Ciais and Jouzel, 1994; Criss, 1999). We use the Simple Water Isotope Model (SWIM) (Markle, 2017) and outlined in the supplement.

Aerosols are injected into the parcel at specified source latitudes. The aerosol concentration of the air parcel decays due to wet removal. The change in concentration of aerosol  $i$  with latitude  $\phi$ , depends on the concentration of the aerosol,  $C_i(\phi)$ , the amount of moisture removed from the atmosphere at that latitude,  $dq$ , and the mass-scavenging ratio for that aerosol,  $\omega_i$ :

$$\frac{dC_i}{d\phi} = \frac{dq}{d\phi} \omega_i C_i = \frac{dr_s}{dT} \frac{dT}{d\phi} \omega_i C_i \quad (2)$$

The mass-scavenging ratio is empirically derived and relates the concentration of an aerosol in precipitation to the concentration in air (Davidson et al., 1989),

$$\omega_i = \frac{C_{i,precip}}{C_{i,air}} \rho_{air} \quad (3)$$

where  $\rho_{air}$  is the density of air. The mass-scavenging ratio has units of (g aerosol/g precipitation)  $\div$  (g aerosol/ g air) (Wolff and Bales, 1996).

In our simple model the amount of moisture removed at each step in the pathway depends on the change in moisture content with latitude,  $\frac{dq}{d\phi}$ , reflecting large scale precipitation, and is determined by the dependence of the saturated mixing ratio,  $r_s$ , on temperature,  $T$ , and the latitudinal temperature gradient,  $\frac{dT}{d\phi}$ . The saturated mixing ratio is derived from the exponential Clausius-Clapeyron relation between the saturated vapor pressure,  $e_s$ , and temperature, and the assumption of pseudoadiabatic cooling which relates temperature and pressure along the pathway. Equation 2 is integrated from initial source latitude  $\phi_0$  and source concentration  $C_0$  to the final deposition latitude, yielding an exponential decay equation similar to Equation 1. By integrating Equation 2, one can see that the log of the final concentration is proportional to the integrated precipitation experienced along the pathway. Although we consider a first order view of precipitation and aerosol removal in our simple model, the explanatory power of the process is

backed up by comparisons to more sophisticated General Circulation Models (GCM, Supplement).

The characteristic source latitude of water for a given ice-core site (Markle et al., 2017) is specified and water isotopes are initialized following those source-region conditions. We use an effective moisture source latitude of  $45^\circ$  S for WDC (Markle et al., 2017). For aerosols we use an effective dust-emission latitude of  $35^\circ$  S, and an effective sea-salt emission latitude of  $60^\circ$  S, corresponding to general South American and Southern Ocean sources, respectively, and in line with satellite observations (Kaufman et al., 2002) and models (e.g. Albani et al. (2012)). The aerosols and water that reach an ice-core site are transported along distinct, though overlapping latitudinal pathways that obey the same thermodynamics.

The general behavior of the model is shown in Figure 2. We consider the modern Southern Hemisphere temperature based on NCEP/NCAR reanalysis (Kalnay et al., 1996) (Figure 2, red lines), as well as the same profile cooled  $5^\circ$  at all latitudes (yellow), and  $10^\circ$  at all latitudes (blue). The gradient in the associated saturated mixing ratio (Figure 2.b) drives integrated precipitation along these paths. Initial aerosol source concentrations are fixed and we assume no changes in transport time and thus total dry deposition. The integrated precipitation along the path in turn drives the exponential removal of aerosol from the initial source to deposition in Antarctica (Figure 2.c). This depletion is several orders of magnitude in concentration and is in good agreement with both observations of atmospheric aerosol burdens and more complex aerosol schemes in GCMs (Albani et al., 2014). This condensation history leads to the familiar poleward depletion of water-isotope ratios (Figure 2.d).

The temperature profiles in Figure 2.a result in largely linear changes in  $\delta^{18}\text{O}$  of precipitation at high latitude sites and exponential changes in aerosol concentration. Because the saturated mixing ratio is a nonlinear function of temperature, the gradient in  $r_s$  changes even with linear changes in temperature and leads to exponential changes in integrated precipitation between points along the path. In warmer mean states, less of the initial aerosol is able to reach the polar regions since the warmer atmosphere has more moisture and thus greater integrated precipitation between the source latitude and deposition site. The model predicts a pattern of aerosol change which increases dramatically toward the pole.

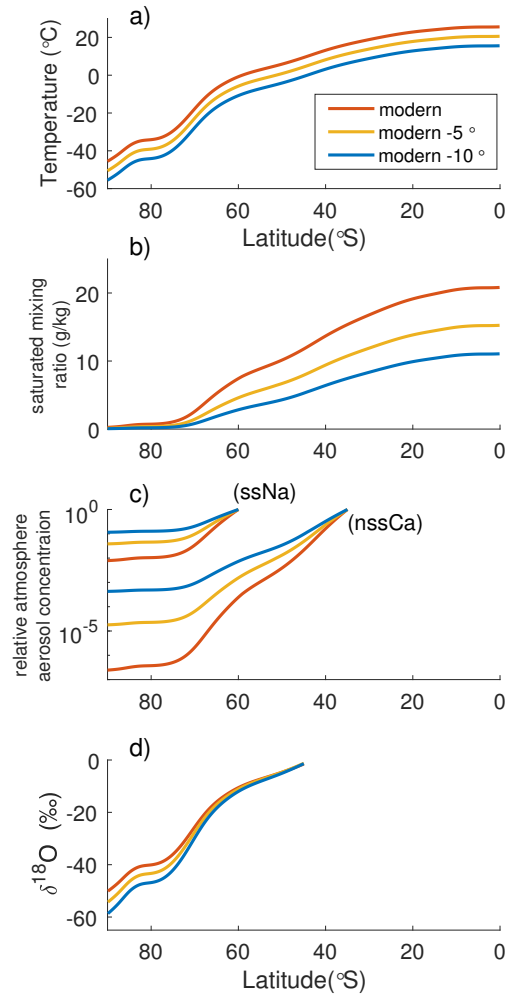


FIGURE 2. a) Zonal mean Southern Hemisphere temperature: modern (red); cooled 5°C (yellow); and cooled 10°C (blue). b) Saturated mixing ratio for the three mean states. c) Atmospheric aerosol concentration along path from initial source for nssCa (35°S) and ssNa (60°S). d)  $\delta^{18}\text{O}$  of precipitation along path from evaporation source (45°S).

#### 4. RESULTS AND SENSITIVITIES

We run the simple model through a range of climate states from modern to LGM to reproduce the range of water-isotope variability observed in the WDC record. The LGM was  $\approx 10^\circ\text{C}$  colder at the WDC site (Cuffey et al., 2016), and we assume polar amplification of  $4^\circ\text{C}$  warming at the pole for every  $1^\circ\text{C}$  warming at the equator (Otto-Bliesner et al., 2006; Masson-Delmotte et al., 2006). We compare the predicted water

isotope, nssCa, and ssNa variability, due only to changes in rain-out (Figure 3). Aerosol changes are presented as amplification factors, the aerosol concentration change with respect to a reference period, in this case the LGM.

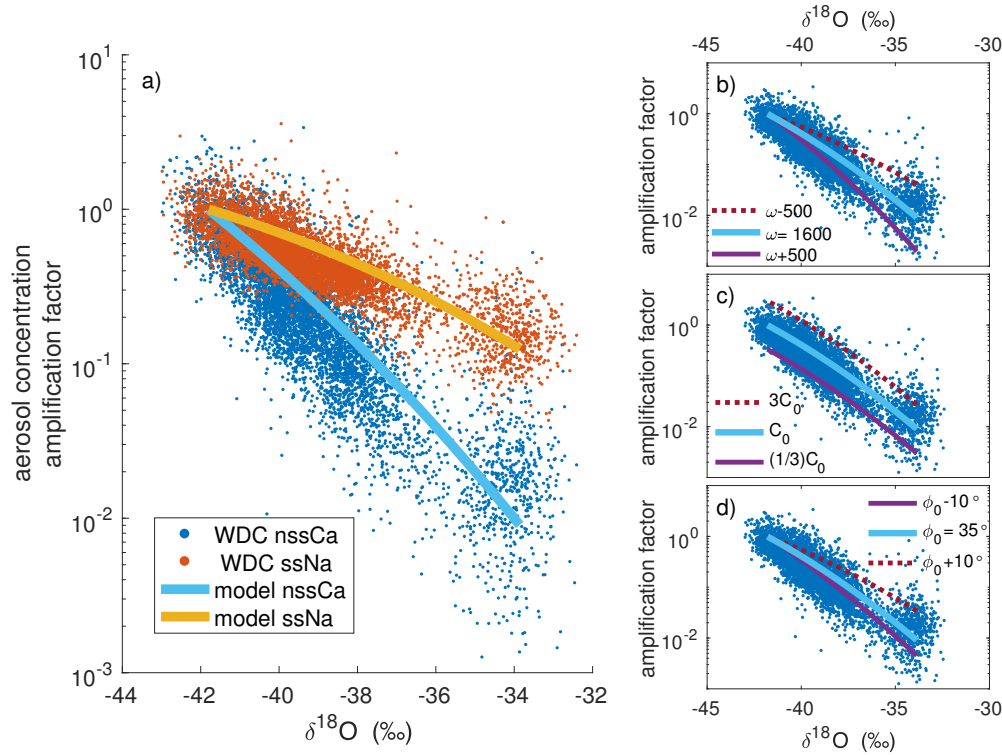


FIGURE 3. a) WDC  $\delta^{18}\text{O}$  vs nssCa (blue) and ssNa (red). Aerosol concentration presented as amplification factors with respect to the mean concentration during the LGM (20 - 25ka). Modeled relationship between  $\delta^{18}\text{O}$  vs nssCa (light blue), and  $\delta^{18}\text{O}$  vs ssNa (yellow). b-d) We test the sensitivity of model results for nssCa to model parameters. Modeled ssNa sensitivity shows similar behavior. b) Sensitivity to scavenging efficiency: WDC  $\delta^{18}\text{O}$  vs nssCa (blue) and modeled relationship (light blue) for our central estimate of  $\omega = 1600$  and the sensitivity to  $\omega \pm 500$ . c) Sensitivity to source concentration: same as panel b) but for a 3 times increase and decrease in source strength,  $C_0$ . d) Sensitivity to initial source latitude: Same as c) but for a  $\pm 10^\circ$  sensitivity of initial source latitude,  $\phi_0$ , from the central estimate of  $35^\circ\text{S}$ .

Temperature-driven changes in the water cycle influence aerosol lifetimes through rain out and by themselves lead to orders-of-magnitude changes in Antarctic aerosol

concentrations. No changes in transport time or in source emission are required to observe orders-of-magnitude variability in aerosols in Antarctica. Further, this process by itself naturally leads to the observed negative, exponential relationship between aerosols and water isotope ratios. This relationship arises not because of coupling between disparate parts of the system for which aerosols and water isotopes are proxies. Rather the relationship reflects the integrated condensation history of the atmosphere shared by water isotopes and aerosols.

How much does the strength of the rain-out process depend on uncertainty or variability in aspects of our model? We explore the sensitivity of the model to several critical variables and parameters in Equation 2 that influence the rainout process and the relationship between aerosols, water isotopes, and a changing climate. These factors include the source emission strength and latitude, the mass-scavenging ratio, and polar amplification.

**4.1. Mass-Scavenging Ratio.** We use an empirically derived mass-scavenging ratio for each aerosol (Davidson et al., 1989), described in Equation 3, which quantifies the efficiency of aerosol scavenging by precipitation. We use estimates based on a compilation of scavenging ratios measured across a range of mid and high latitude environments described in the Supplement and summarized in Table S1. Both calcium and sodium aerosols have a mass-scavenging ratio of magnitude  $1-2 \times 10^3$  (g aerosol/g precipitation)  $\div$  (g aerosol/ g air), though there is uncertainty in the values (Supplementary Materials). Reasonable estimates ( $\approx 1600$  for nssCa and 1700 for ssNa) from our compilation account for the entire range of variability observed in both aerosols in the WDC record. The correspondence of the latitudinal decay of aerosols in our model and observations give confidence that these values are the correct order-of-magnitude. Because the mass-scavenging ratio is in the exponent of Equation 2, our results are sensitive to uncertainty in this parameter. This uncertainty may reflect inherent difficulty in measuring the scavenging parameter or true variance that depends on climate and microphysics. The sensitivity of calcium in our model to a wide range of mass-scavenging ratios ( $1600 \pm 500$ ) is shown in Figure 3, and the sensitivity of sodium is analogous. It is important to note that all interpretations of the variability in high latitude aerosols are subject to the uncertainty of variability in the scavenging efficiency. If the true value of the mass-scavenging ratio were less than our estimates, some amount of variability in the aerosol record may reflect other sources of variability, such as increased dust emission during the glacial period. However, if the true scavenging coefficient were greater, an equally likely scenario, then the implied source change would be of the opposite sign, indicating a decreased source emission during the glacial.

**4.2. Initial source concentration.** Because the source emission strength is outside the exponent in Equation 1, an amplification of source emission leads to a linear amplification of aerosol concentration at all latitudes, and thus a simple translation of the exponential relationship with water isotopes. Figure 3 shows the spread associated with 1/3 to 3 times changes in initial aerosol concentration at the source at any instant in time.

Variability of the emission source for WDC of this magnitude appears within the noise of the ice core data. In Figure S1 we show the time series of measured WDC nssCa variability compared to the nssCa variability predicted solely from the measured  $\delta^{18}\text{O}$  and the expected relationship between  $\delta^{18}\text{O}$  and nssCa from our simple model. The log of the real and modeled WDC nssCa are extremely well correlated,  $r = 0.91$ ,  $p < 0.01$ , indicating the model can explain nearly 83% of the variance in the nssCa record. We also show the time series of predicted nssCa by our simple model if source emissions either doubled or halved from 10ka to the LGM. Such temporal changes in source strength will result in curvature in the relationship between water isotopes and aerosols shown in Figure 3. We cannot rule out such changes in source strength; they are within the spread of observations in Figure 3 and likely within the uncertainty of other model parameters like the scavenging efficiency.

**4.3. Source emission latitude.** Aerosols emitted from a lower latitude source must be transported through more of the latitudinal temperature gradient to reach Antarctica than those emitted from a higher latitude source. They experience more integrated rain-out and greater amplification due to changes in rain-out. Several lines of evidence indicate South America is the dominant source of Antarctic dust (Delmonte et al., 2008; Albani et al., 2012). Albani et al. (2012) identify South American dust production regions between 37°S and 42°S as important Antarctic sources. Similarly, the CESM Large Ensemble Experiment (Kay et al., 2015) shows dust aerosol burdens to peak between 30° and 35°S (see Supplement). For Southern Hemisphere sea salts, satellite observations and models (Kaufman et al., 2002) indicate that the dominant source regions is the Southern Ocean between 50° and 65°S, though there may be contribution from higher latitude sea ice as well (Rankin et al., 2000). We use effective initial source latitudes,  $\phi_0$ , of 35°S for mineral dust and 60°S for sea salt, and explore the sensitivity of the model to uncertainty in  $\phi_0$  below.

The effect of starting latitude on glacial-interglacial change is important. Mineral dust, emitted from the Southern Hemisphere continents, must travel through more of the atmospheric rain-out pathway to reach Antarctica than sea salts emitted from the Southern Ocean and sea ice. The dust will thus also experience greater changes in integrated precipitation between climate states, which is expressed as a steeper slope in Figure 3. Our results are in excellent agreement with the ice core data: while both aerosols show a negative exponential relationship to  $\delta^{18}\text{O}$ , they have different magnitudes of glacial-interglacial change. That difference in magnitude is expressed as the slope with  $\delta^{18}\text{O}$  and is predicted by their differing initial source latitude.

Aerosols are not necessarily emitted from a single point latitude, but rather from a potentially broad distribution of area. The effective aerosol source latitude for an ice-core site is driven by spatial patterns of source region factors, such as wind speeds and arid land area, in the case of terrestrial dust. The effective source latitude for an ice-core site is also determined by the weighting of integrated removal that aerosols experience during transport between sources and the deposition site. This wet removal function quantifies the integrated rain-out experienced by an aerosol between all possible starting

latitudes and the final latitude of deposition at the ice-core site. The wet removal function (see Supplement) leads to a natural explanation for why most Antarctic dust appears to come from South America rather than other potential sources like Australia and South Africa. The function reflects the integrated rain-out between source and site and is exponential with latitude. By the time they reach Antarctica, aerosols emitted from 30°S, for example, may be reduced in concentration by orders-of-magnitude compared to those emitted from 40°S. Because South America extends over 10° of latitude further into the midlatitudes than either Australia or South Africa, dust from South America has an exponentially larger chance of reaching Antarctica, even if their source emissions strengths were identical in magnitude (Albani et al., 2012).

We consider effective emission latitudes for aerosols in Figure 3. However, these effective source latitudes may be uncertain, may be variable within a mean state, and they may change with mean state. Variability in the source latitude will in turn influence the relationship between an aerosol and water isotopes at the deposition site. Figure 3 shows the range of variability associated with a +10° and -10° variation in source latitude.

The effect of source latitude on Antarctic aerosols helps explain several observations about the relationships between nssCa, ssNa, and  $\delta^{18}\text{O}$ . In addition to the difference of slopes in Figure 3, the difference in dust and sea-salt source latitudes, leads to the higher correlation of  $\delta^{18}\text{O}$  to  $\log(\text{nssCa})$  than to  $\log(\text{ssNa})$ . The greater the integrated condensation history shared by two trace constituents of the atmosphere, the more the exponential rainout process will overwhelm other non-shared sources of variance (e.g. different aerosol or water isotope source changes) which may otherwise degrade their correlation. Similarly, the influence of variations in source latitude on Antarctic aerosol concentrations are increasingly damped for aerosols with mean sources farther from Antarctica along the rain-out pathway.

Source latitudes of sea salts, dust, and moisture source for an ice-core site likely change with the mean state (Markle et al., 2017). Such changes will influence the slope of the isotope-to-aerosol relationship. However, given the sensitivity analysis shown in Figure 3.d, small changes in source latitude (e.g.  $< 5^\circ$ ) would likely be difficult to detect as they'd be within the noise of the records and within the uncertainty of other factors.

**4.4. Polar amplification.** Polar amplification, the change in the meridional temperature gradient  $\frac{dT}{d\phi}$  with mean state, is imprinted on the relationship between Antarctic aerosols and water isotopes through time. Estimates from models (Otto-Bliesner et al., 2006) and paleoclimate data (Masson-Delmotte et al., 2006) suggest that, since the LGM, the highest latitudes warmed about 4-5°C for every degree of low latitude warming. Total glacial-interglacial change at WDC is estimated at about 10°C (Cuffey et al., 2016; Markle, 2017). Results in Figure 3 are for a polar amplification of 4°C of high latitude warming per 1°C of equatorial warming, prescribed linearly with latitude. However, polar amplification in the real climate may not have been linear with latitude. Because water, dust, and sea salts share overlapping, but distinct, segments of the rain-out pathway,

the relationships between the aerosols and water isotopes may record the spatial pattern of polar amplification.

We next test the behavior of the simple model to idealized spatial patterns of polar amplification (Figure 4). It is important to note that warming without polar amplification still results in large glacial-interglacial changes in Antarctic aerosols. Because the saturation vapor pressure scales nonlinearly with temperature, even equal temperature change at all latitudes leads to changes in the gradient of moisture and thus condensation and wet removal of aerosols. However, a polar amplification of 4°C of high latitude warming per 1°C of equatorial warming, in line with evidence (Otto-Bliesner et al., 2006; Masson-Delmotte et al., 2006), more faithfully captures the relative slopes between ssNa and  $\delta^{18}\text{O}$  and nssCa and  $\delta^{18}\text{O}$  (Figure 4), compared to warming without polar amplification. We diagnose the pattern of polar amplification from the ECHAM4.6 GCM run under preindustrial and LGM boundary conditions (Markle et al., 2017; Schoenemann et al., 2014), which is consistent with previous GCM modeling experiments (e.g. Otto-Bliesner et al. (2006)). We show that this more complex pattern of polar amplification results in stronger *curvature* in the  $\delta^{18}\text{O}$ -to-log(ssNa) and  $\delta^{18}\text{O}$ -to-log(nssCa) relationships (Figure 4), and that the degree of this curvature depends on the total amount of depletion experienced at an ice-core site. In Figure 4, we shown nssCa flux, ssNa flux, and  $\delta^{18}\text{O}$  records from the East Antarctic EPICA Dome C (EDC) and EPICA Dronning Maud Land (EDML) ice-core records (Fischer et al., 2007b) in addition to the records from WDC. The East Antarctic records in particular show stronger curvature in the  $\delta^{18}\text{O}$ -to-log(ssNa) relationship, similar to that driven by the idealized pattern of polar amplification from ECHAM4.6.

In the Supplement we investigate the influence of temporal variability in the spatial pattern of polar amplification on Antarctic aerosol-water isotope relationships. We use a simple energy balance model (Hwang and Frierson, 2010; Roe et al., 2015) to produce temperature profiles for a range of mean state temperatures. We alter the physics in the model to produce different spatial patterns of polar amplification, as well as spatial patterns of polar amplification that change with time (Figure S2). The latter is achieved by horizontal heat transport and an ice-albedo feedback. This temporal variability in the polar amplification drives additional curvature in the nssCa to  $\delta^{18}\text{O}$  relationship that is similar to that shown in the ice-core records (Figure 4). These results demonstrate that the temporal evolution of polar amplification, in addition to the spatial pattern, influences the water isotope-aerosol relationships at the poles. There is an indication that important feedback processes may be recorded in these proxy records.

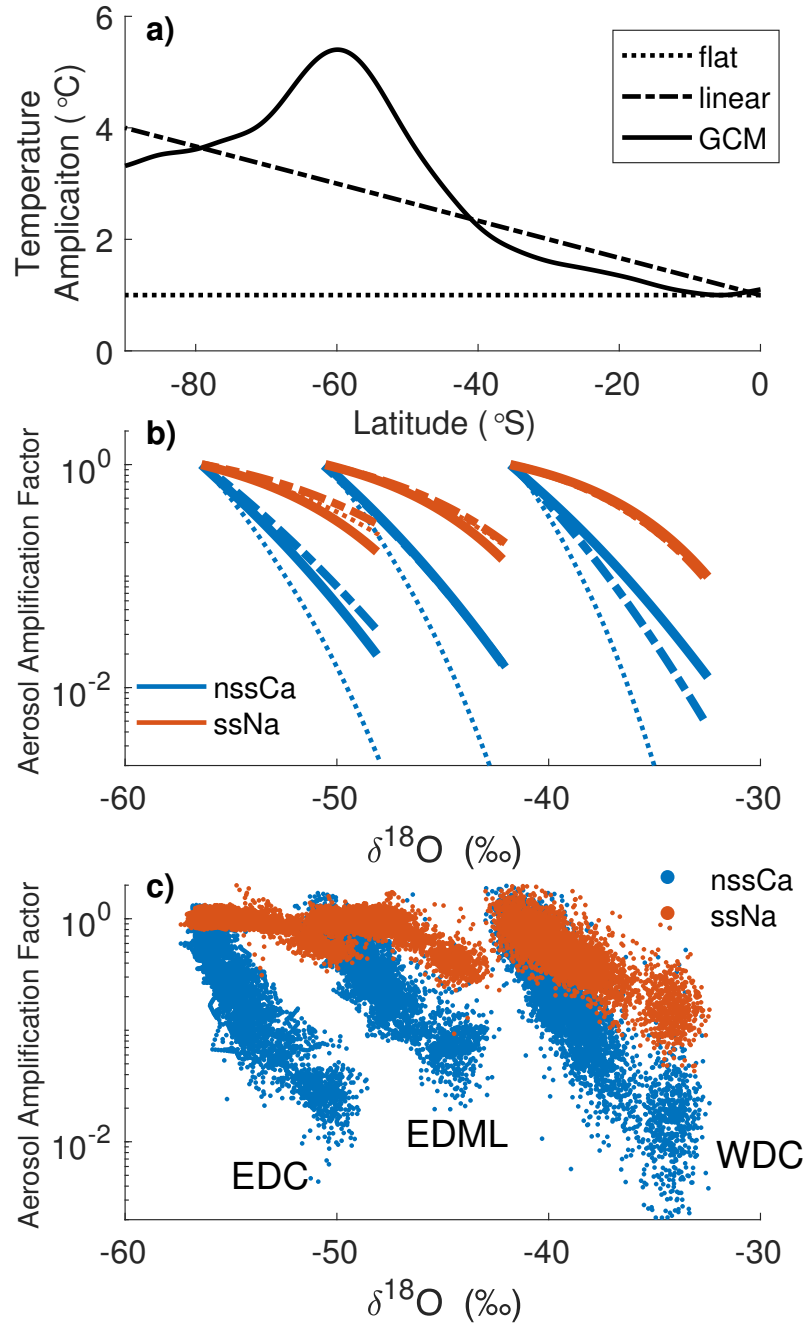


FIGURE 4. a) Three patterns of polar amplification (degree of warming per degree of equatorial warming). "Flat": equal warming at all latitudes. "Linear": linearly increasing amplification toward the pole. "GCM": pattern of warming from preindustrial-LGM ECHAM4.6 control runs. b) Relationship between modeled  $\delta^{18}\text{O}$ , nssCa, and ssNa for three different patterns of polar amplification at three sites with isotope values and ranges representative of WDC, EDML, and EDC. c) Relationship between  $\delta^{18}\text{O}$  and nssCa (blue) and  $\delta^{18}\text{O}$  and ssNa (red), for WDC, EDC, and EDML. Aerosol data are presented as amplification factors from the LGM. Aerosol data are amplification of concentration for WDC, and of flux for EDC and EDML.

## 5. SPATIAL PATTERNS OF AEROSOL VARIABILITY

Because of their impact on the radiative forcing of the climate system, understanding the global extent and spatial pattern of aerosol changes, that of dust in particular, is important to understanding past climate change. How does the rainout model inform us about dust variability outside of Antarctica?

In Figure 5.a we compare the WCD  $\delta^{18}\text{O}$  and nssCa to an equivalent record from the opposite pole; the GRIP ice core record from Greenland (De Angelis et al., 1997). GRIP and WDC are analogous sites with similar modern temperature and accumulation (WAIS Divide Project Members, 2013) and similar modern  $\delta^{18}\text{O}$  and glacial-interglacial changes in  $\delta^{18}\text{O}$ . It is well known that water isotopes and the log of the calcium concentration are well correlated in Greenland ice cores (e.g. Rasmussen et al. (2014)). The LGM amplification of nssCa in the GRIP record is almost identical to that at WDC. Both records show the negative, exponential relationship between nssCa and  $\delta^{18}\text{O}$  and have similar variance around that relationship, despite that the time series themselves are quite distinct between the hemispheres, with different timings of deglaciation and different patterns of millennial variability. Greenland and Antarctica have separate dust sources with different sensitivities to source region conditions such as windiness, aridity, vegetation cover, and continental shelf expansion (Li et al., 2010). If source region changes were the dominant source of polar calcium variability, Figure 5.a, would imply that no matter what set of variables influence different dust production regions around the globe, their changes through time must always combine nonlinearly such that their variability results in a well-defined exponential relationship to water-isotope variability at the nearest pole. That would be remarkable.

The observed symmetry is well described by the rain-out model so long as the atmosphere in the Northern and Southern hemispheres both feature poleward transport of moisture and obey the same thermodynamics. The integrated condensation history that leads to  $\delta^{18}\text{O}$  variability also drives predictable changes in the wet removal of aerosols from the atmosphere.

As seen in Figure 2, the rain out process predicts a spatial pattern of aerosol concentration changes that increases exponentially poleward of the source. In Figure 5 we compare the time series of WDC nssCa, to the East Antarctic records of nssCa and dust flux from EDC (Fischer et al., 2007b; Augustin et al., 2004). We also compare two records of dust flux from midlatitude marine sediment cores from the Atlantic Sector of the Southern Ocean downwind of South American dust sources (Winckler, 2015), as well as a suite of marine sediment core terrestrial dust records from the Pacific Sector of the Southern Ocean (Lamy et al., 2014), north of the WDC site. While the dust flux in sediment cores are amplified in the LGM by factors of 3 to 5, the ice-core records show orders of magnitude more variability, with at least twentyfold and up to hundredfold changes. In Figure 5.c-d, we show the spatial pattern of LGM-Holocene dust amplification for a compilation of dust-flux changes from marine sediment cores and ice cores (Albani et al., 2012), along with the additional records from WDC, EDC, Greenland, and the sediment core records in Figure 5.b. We see distinct amplification of the dust deposition changes

toward both poles. If variation in source-region emissions were primarily responsible for the variability in the ice-core records, we would observe equal amplification at all latitudes between the source and deposition sites, with a magnitude equal to that in the ice-core records. The data do not support this hypothesis.

On the other hand, the spatial pattern of dust amplification predicted by the simple rain-out model accurately predicts the spatial pattern in the global compilation of records (Figure 5). Changes in source strength would simply offset this pattern along the vertical axis. We show the spread that we be expected from no changes in sources, a 3 fold increase in source strength, and a 3 fold *decrease* in source strength. This range of possible source variability spans the paleo climate data well, though a central estimate slightly greater than one is indicated.

It is perhaps likely that aerosol emissions do change in-phase with global climate at the longest timescales. However, the time series of aerosol variability in ice cores are not evidence of this variability. Changes in source strength through time (Figures S1) will emerge as curvature in plots like Figure 3. Indeed, we can see in Figure 3, that factor of 2 to 3 changes are within the noise of the ice core data given the expected changes due to rain out, and that factor of 1/2 to 1/3 changes could be just as likely. While it may be possible to extract source-strength changes (Petit and Delmonte, 2009), other variability and uncertainty, such as source latitude and scavenging efficiencies, may overwhelm our ability to interpret those changes.

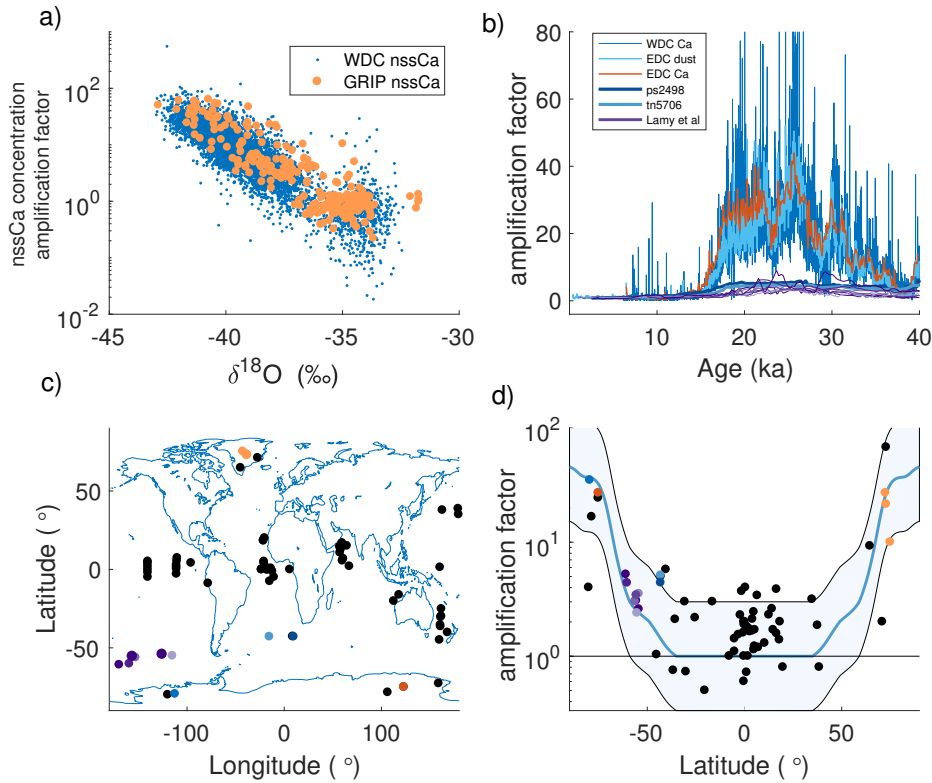


FIGURE 5. a)  $\delta^{18}\text{O}$  and nssCa amplification for WDC (blue) and for the Greenland NGRIP ice core (orange). Note that for visual clarity dust amplification is presented with respect to the early Holocene (6-10ka) in Figure 5. b) Comparison of time series of mid and high latitude southern hemisphere records of dust aerosol amplification records: WDC nssCa (blue), EDC nssCa (red), EDC dust (light blue), and a suite of marine sediment core records (dark blue and purple). Global map of dust amplification factors between LGM and Holocene for a global compilation of marine sediment cores and ice cores (Albani et al., 2012) (black), as well as the additional records from panel (b), colored consistently, and Greenland nssCa records from NGRIP, GRIP, GISP2 (orange). d) Dust amplification against latitude for all records shown in panel (c). The expected global spatial pattern of dust aerosol amplification from the simple model for no change in source strength and rainout poleward of  $35^\circ\text{S}$  (dark blue line). Shading shows the expected spatial pattern of dust aerosol between a 3x increase of aerosol sources between  $35^\circ\text{S}$  and  $35^\circ\text{N}$ , and a 3x decrease in those source strengths.

## 6. IMPLICATIONS FOR GLOBAL RADIATIVE FORCING

Aerosols affect the radiation budget of the climate system both directly through scattering and absorption and indirectly through interaction with clouds (Stier et al., 2007). The aerosol optical depth quantifies the extinction of incoming solar radiation by dust in the atmosphere and scales with the atmospheric dust burden (Supplement). Uncertainty in the magnitude of dust aerosol forcing in the past, is one of the largest sources of uncertainty in estimating climate sensitivity from paleoclimate data (Friedrich et al., 2016). Spatial heterogeneity in that forcing is especially uncertain (Köhler et al., 2010).

The interpretation of the cause of aerosol variability in ice cores has important implications for the magnitude and spatial pattern of past changes in the atmospheric dust burden, optical depth, and radiative forcing. If dust-emission strength is the primary driver of ice-core aerosol variability, this implies order-of-magnitude changes in the aerosol optical depth everywhere between the midlatitude source and the high latitudes. If on the other hand, the rain-out process is the dominant driver of ice-core variability, there may have been order-of-magnitude changes at the poles, but comparatively little or no change at middle and lower latitude sources (Figure S5). This has important implications for changes in the magnitude and variability of past radiative forcing and its spatial pattern, which in turn has implications for feedbacks and poleward heat transport. Studies which take ice-core aerosol records to reflect the temporal variability of aerosol radiative forcing (e.g. Köhler et al. (2010); Friedrich et al. (2016)) may overestimate the aerosol influence on glacial-interglacial radiative forcing changes and may miss important changes in the spatial pattern of that forcing. Studies ignoring changes in aerosol radiative forcing (e.g. Otto-Bliesner et al. (2006)) likely underestimate changes in the global mean forcing and spatial pattern. In the Paleoclimate Model Intercomparison Project, for example, models either compute aerosols on-line or use the preindustrial aerosol loading (Schmidt et al., 2011), for past climate scenarios. The preindustrial pattern likely underestimates changes in forcing in the middle and high latitudes. While on-line aerosols may be preferable, the extent to which models underestimate the rain-out effect (Albani et al., 2014), will bias the simulated spatial pattern of aerosol loading and associated radiative forcing. The paleoclimate data support a spatial pattern of aerosol optical depth during the LGM that had modest and potentially variable amplification at the middle and low latitudes, but exponential amplification of aerosol optical depth toward the poles (Figure 5 and Figure S7). This pattern should be the basis of future paleoclimate simulations of the Last Glacial Maximum.

## 7. CONCLUSION

We have shown that the rainout process naturally leads to the observed exponential relationship between water isotopes and aerosols. Expected thermodynamically driven changes in the hydrologic cycle between the LGM and Holocene lead to order-of-magnitude changes in aerosol concentrations reaching the poles. In addition to explaining the variability between mean states, our model also predicts the scaling of aerosol

variance within mean states. The expected spatial pattern of aerosol changes due to rain-out is consistent with the global spatial pattern of LGM dust amplification, from both poles to the equator.

Identification of the source of dust variability in ice-core records helps us better understand the past magnitude and global spatial patterns of aerosol radiative forcing. We have reconciled our understanding of simultaneous variability in both terrestrial dust and marine sea-salts in Antarctic records, and helped resolve the debated source of glacial-interglacial variability in Antarctic sea salts. The nature of aerosol relationship to water-isotope variability, their difference in slopes and curvature in those slopes, are direct consequences of changes in the hydrologic cycles. Our results suggest that rather than failing to represent the complex dynamics of aerosol emissions, GCM studies actually represent source region changes well, but may underrepresent changes in precipitation or, perhaps more likely, the efficiency of aerosol scavenging by that precipitation. Our model, while simple, rests on first-order thermodynamics and has few degrees of freedom with all parameters constrained by independent estimates.

While other sources of aerosol variability undoubtedly exist, and may dominate the records on shorter timescales, the water cycle carries a big lever. Precipitation in the midlatitudes is the principal barrier to aerosols reaching the poles. The intensity of that hydrologic machinery is linked, exponentially, to the climate's temperature. Changes in integrated precipitation dominates the variability in the amount of trace atmospheric constituents reaching the poles and unites the interpretation of dust, sea-salt, and water-isotope records. Other sources of variability are surely important, but their attribution must contend the exponential lever of the water cycle, its variability, and its uncertainties.

While driven by the same underlying process, it is not the case that these water-isotope and aerosol records are redundant. The poleward transport of water is a fundamental aspect of our climate system, accounting for over half of the atmospheric heat transport in the Southern extratropics (Hartmann, 2015), and itself a source of polar amplification (Roe et al., 2015). Being transported through different but overlapping segments of the equator to pole temperature gradient, and responding to atmospheric distillation in distinct ways, these proxies together provide greater insight into past changes in moisture transport than any alone. Imprinted upon their relationship is unique information about fundamental aspects of the climate system such as the spatial and temporal patterns of polar amplification.

## 8. METHODS

### 8.1. Data.

8.1.1. *Water Isotopes.* WDC water  $\frac{^{18}O}{^{16}O}$  composition (expressed as  $\delta^{18}O$ ) was measured at  $\Delta^*$  IsoLab, University of Washington, Seattle WA, USA. Measurement techniques are described in Markle et al. (2017). Measurements were made at 0.5 m depth averaged resolution, using laser spectroscopy (Picarro L2120-i analyzer). Data are reported relative to the VSMOW (Vienna Standard Mean Ocean Water) standard, and normalized

to SLAP. Measurement resolution is generally better than 40 years/sample for the 67 ka record, with a mean temporal resolution of 17.2 years/sample between 10-67 ka. Measurement uncertainties are better than 0.08‰ for  $\delta^{18}O$ .

8.1.2. *Aerosols.* As their names imply sea salt sodium (ssNa) and non sea salt calcium (nssCa) are the marine-sourced and non marine-sourced components of the sodium and calcium impurities of ice, respectively. WDC ice impurities were measured at the Trace Chemistry Laboratory at the Desert Research Institute using a continuous flow system and inductively coupled plasma mass spectrometry (McConnell et al., 2002) and published previously (WAIS Divide Project Members, 2013, 2015). The effective sampling resolution is  $\approx 1$ cm. Because the elements Ca and Na appear in both mineral dust and sea salts, those ions alone are not unique identifiers of the aerosols of interest. We use standard calculations to isolate the sea salt component of the sodium and the non sea salt component of the Calcium records. These are calculated by accounting for Na/Ca mass ratios of 26.3 for marine aerosols and 0.562 for average crust composition (Bowen, 1984; Röthlisberger et al., 2002).

Aerosol amplification factors, presented throughout, represent normalized changes in concentration for WDC record. We also present amplification factors of aerosol fluxes for EDC and EDML. Because of its high accumulation rate, WDC aerosol concentrations are a better representation of past changes in the overlying atmospheric aerosol concentration, whereas the flux is a more appropriate quantification for atmospheric concentration at low accumulation sites like EDC and EDML (Alley et al., 1995; Fischer et al., 2007b). The difference between flux and concentration is at most a factor of two at all sites, owing to changes in accumulation (WAIS Divide Project Members, 2013; Fischer et al., 2007b), a minor consideration given the orders-of-magnitude change observed in the records. It is interesting to note however that at WDC the correlation between  $\delta^{18}O$  and accumulation is shown to degrade at millennial and lower timescales (Fudge et al., 2016). This relationship is largely assumed to be fixed at many East Antarctic sites where accumulation cannot be calculated independently from water isotope records. East Antarctic accumulation records are largely not independent of water-isotope variability and are used to calculate aerosol fluxes. This assumption may obscure real millennial variability in East Antarctic aerosol fluxes, though is likely unimportant for the timescales of variability investigated here.

**8.2. Simple Atmospheric Transport, Water Isotope, and Aerosol Models.** We use a simple model to test the influence of hydrologic cycle changes on both water isotopes and aerosols. We consider isolated air parcels which are cooled following a temperature gradient between the midlatitudes and high latitudes. In our simple model we consider isolated pseudoadiabatic pathways. Moisture removal ( $-\nabla q$ ) from the parcel follows changes in the saturated mixing ratio,  $r_s$ , which is derived from the saturated vapor pressure,  $e_s$ , and the Clausius-Clapeyron (CC) relationship, Equation 4, where  $L$  is the latent heat and  $R$  is the specific gas constant.

$$\frac{d \ln e_s}{dT} = \frac{L}{RT^2} \quad (4)$$

Cooling is pseudoadiabatic and we account for mixed ice and liquid in the atmosphere and the difference in the associated vapor pressures (Markle, 2017). Our results are robust to the details of the mixed phase nature of the pathway, as well as the pseudoadiabatic assumption; an isobaric assumption leads to the same conclusions.

We are interested in understanding centennial and longer scale variability in the water isotopes and aerosols. All the relevant climate variables are well mixed and generally zonally symmetric over the Southern Ocean at these timescales. As such we are not concerned with the particular details of any single air parcel pathway, but rather the statistics of those pathways over suitably long timescales. We assume only that the mean transport depends on the climate mean state and that these statistics are reasonably stationary.

Were we to consider the entire atmosphere, rather than isolated pathways, it would be appropriate to account for the addition of moisture to the atmosphere by evaporation,  $-\nabla q = (P - E)$ , and changes in  $(P - E)$  with mean state. To first order, the quantity  $(P - E)$  scales with CC, about  $7\%K^{-1}$ , while changes in E show a far smaller scaling with mean state, about  $2\%K^{-1}$  Held and Soden (2006). Considering changes between mean states and polar amplification, the largest changes in temperature will occur toward the midlatitudes and poles, where evaporation is very low in the control state. Our simplification, that changes in  $(P - E)$  are dominated by changes in P, is thus useful to first order, though it may somewhat *underestimate* changes in integrated mid and high latitude precipitation. If E changes at a rate less than the CC-scaling of  $(P - E)$ , in regions of positive  $(P - E)$ , P must have a greater scaling (Held and Soden, 2006). Our estimate of changes in the rain-out process, and associated changes in aerosols from the simplified model are thus likely conservative.

The Simple Water Isotope Model is described in detail in Markle (2017). In short, it is a Rayleigh-type distillation model (Dansgaard, 1964; Merlivat and Jouzel, 1979) that accounts for equilibrium and non-equilibrium fractionation of water isotopes, mixed ice and liquid phases, source region conditions, and uses a parameterized supersaturation. While similar to previous models (Ciais and Jouzel, 1994; Kavanaugh and Cuffey, 2003) it has several improvements including updated fractionation factors (Markle et al., 2017; Uemura et al., 2008), consistent saturation and supersaturation conditions between the water isotope fractionation and physical moisture pathway, temperature dependence of liquid/ice phase mixing based on satellite measurements, and fidelity to modern  $\delta^{18}O$ ,  $\delta D$ , and temperature observations.

The aerosol removal model is incapsulated in Equation 2 which is integrated from a specified initial latitude (or distribution of latitudes) to the deposition site. The moisture removal, water isotope distillation, and aerosol removal equations are integrated along temperature profiles and projected onto a latitudinal grid. We use Euler numerics in both the water isotope and aerosol models,  $\frac{dy_i}{dx_i} \approx \frac{y_i - y_{i-1}}{x_i - x_{i-1}}$ , with sufficiently small

$\Delta x = x_i - x_{i-1}$ , where  $y$  is the variable of interest and  $x$  is the grid variable such as latitude or temperature.

Because the initial aerosol source concentration is outside the exponent in all the distillation equations, changes in source strength lead to linear changes in deposition site concentrations both along a trajectory and through time. By setting all initial source strengths to unity, aerosol concentrations along a path length may be thought of as fractions of source concentration. When examining changes in aerosol concentration through time at a given ice-core site, it is useful to consider amplification factors, changes in concentration at the site with respect to a reference period, such as the Holocene or the Last Glacial period.

Our model ignores dry deposition of aerosols, which contributes to the total removal. While wet deposition far exceeds dry deposition along most of the transport path, dry deposition is important at the highest latitudes (Alley et al., 1995). Considering only wet deposition, the model likely underestimates the total fractional change from source to deposition site for some aerosols. Dry deposition is easily added to the model by considering a dry deposition rate, and climatological wind speeds which lead to a characteristic transport time. Dry deposition likely accounts for some of the differences between core sites that have similar latitudes but different longitudes and thus different transport times from fixed sources, like EDC and EDML (Fischer et al., 2007b). Because we are interested in understanding how much variability in the ice-core records may be explained by changes in wet deposition alone, we assume no changes to either the dry deposition rate nor transport time. Other authors have investigated changes in transport time which would effect total removal by dry deposition, and find that likely changes in dry deposition are small (Fischer et al., 2007b; Petit and Delmonte, 2009).

By considering amplification factors between mean states for a given ice-core site, the inclusion or exclusion of constant dry deposition in the model is inconsequential. Consider Equation 1,  $C = C_o e^{-\chi}$ , in which the removal,  $\chi$ , may be expressed as the dependence of wet ( $W$ ) and dry ( $D$ ) removal,  $-\chi = -(W + D)$ . Assuming the dry removal rate and initial concentration are constant, the concentration for two mean states may be written  $C_1 = C_o e^{-(W_1+D)}$  and  $C_2 = C_o e^{-(W_2+D)}$ . The amplification factor between the two states is then  $\frac{C_2}{C_1} = \frac{C_o e^{-(W_2+D)}}{C_o e^{-(W_1+D)}} = e^{(W_1-W_2)}$ , showing no dependence on initial concentration nor dry deposition.

**Supplemental Materials:**  
**The great atmospheric washing machine: reconciling water, aerosols, and climate**

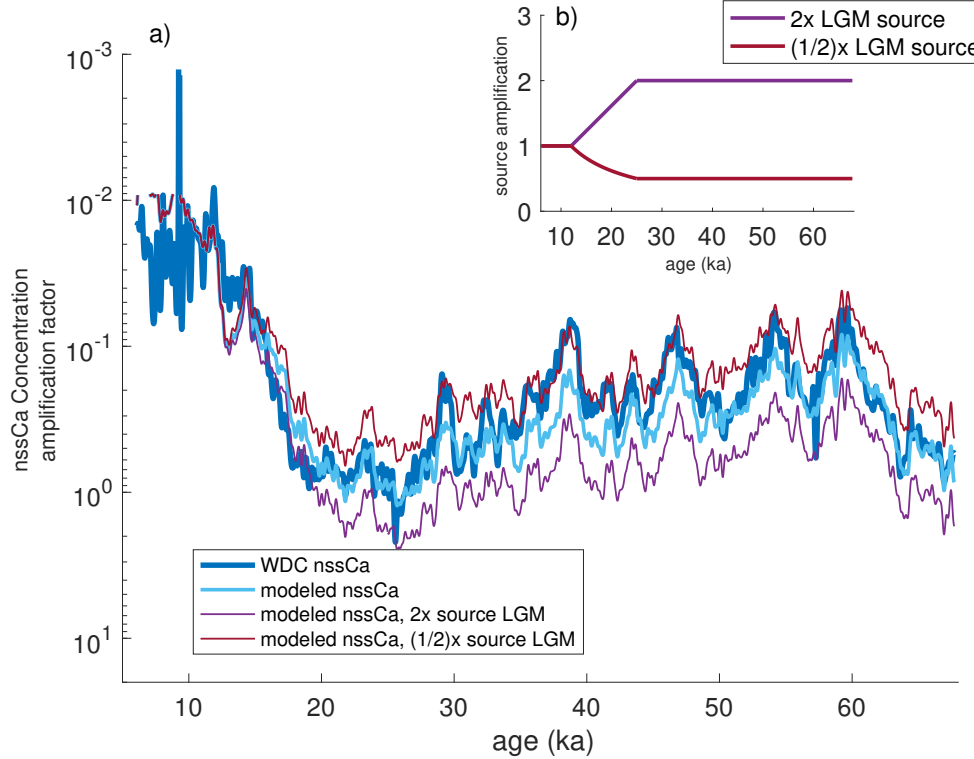


FIGURE S1. WDC nssCa record compared to the predicted variability based solely from the WDC  $\delta^{18}O$  (low pass filtered, frequencies  $> \frac{1}{300\text{yrs}}$  removed) and the simple rainout model. We also show the expected variability in the predicted in nssCa associated with a temporal increase or decrease in the initial source strength,  $C_0$ .

### S1. ENERGY BALANCE MODELS

To investigate the influence of polar amplification on the relationship between water isotopes and aerosols, we use an energy balance model (EBM) (Hwang and Frierson, 2010; Roe et al., 2015) to produce self consistent temperature profiles with polar amplification for a range mean state temperatures. The spatial pattern of downward radiative forcing is specified, upward emission is parameterized based on a linearization with temperature, and horizontal heat transport is based on heat diffusion, though the physics of this transport is varied in our experiments. All scenarios are initialized to match the modern meridional temperature gradient. The top of atmosphere radiative forcing is

repeatedly perturbed and the model allowed to come to equilibrium to produce different mean states. We examine the addition of physical processes to the model that contribute to polar amplification: 1) we allow horizontal heat transport to be achieved through dry thermal diffusion (e.g. Paltridge (1975)); 2) heat transport is driven by the down gradient diffusion of moist static energy (MSE) (Hwang and Frierson, 2010) rather than dry thermal energy; and 3) heat transport is driven by MSE diffusion and we impose an ice-albedo feedback. The ice-albedo feedback is represented by changing surface albedo following the hemispheric  $0^{\circ}\text{C}$  isotherm. We then use the resulting suite of pole to equator temperature gradients from each scenario as the base for the simple water isotope and aerosol rainout model.

Due to their physics, both scenarios 2) and 3) result in spatial patterns of polar amplification that change with the mean state temperature and thus time. These scenarios are progressively more realistic, though still substantial simplifications of the real climate system, and lead to different spatial and temporal patterns of polar amplification (Figure S2). Note for example simple dry diffusion leads to polar damping; for every degree of equatorial warming the poles experience a fraction of a degree. The simple energy balance model lacks the total set of feedbacks that lead to the full extent of polar amplification in reality or even a GCM. The mean state temperature changes in our EBM scenarios are not meant to simulate changes between the LGM and present, nor indeed any historical climate change. We simply aim to test the sensitivity of the relationships between polar water isotopes and aerosols under transient conditions with different patterns of polar amplification. Such a test would be computationally expensive and impractical with a GCM.

The influence of the polar amplification scenarios on the relationship between water isotopes and nssCa and ssNa aerosols for an ice-core site at  $80^{\circ}\text{S}$  is shown in Figure S2. All patterns of polar amplification drive rainout processes that leads to a exponential relationship between aerosols and water isotopes. Further, we see that the nature of polar amplification and its temporal evolution is imprinted upon the nssCa-water isotope and ssNa-water isotope relationships. For example, in the third scenario (Figure S2), the moving sea ice edge shifts the peak of polar amplification equatorward with a cooling climate. In our simple test, this evolving polar amplification drives additional curvature in the exponential  $\delta^{18}\text{O}$ -to- nssCa relationship, in fact inverting the slight curvature seen in Scenario 1. The calcium records in the WDC, EDC, and EDML ice core all show curvature of this shape (Figure 4.c). While it is not yet possible to diagnose the source of curvature in the ice-core records from these tests alone, our results demonstrate that in principle the spatial and temporal patterns of polar amplification may be imprinted upon the relationships between these proxies.

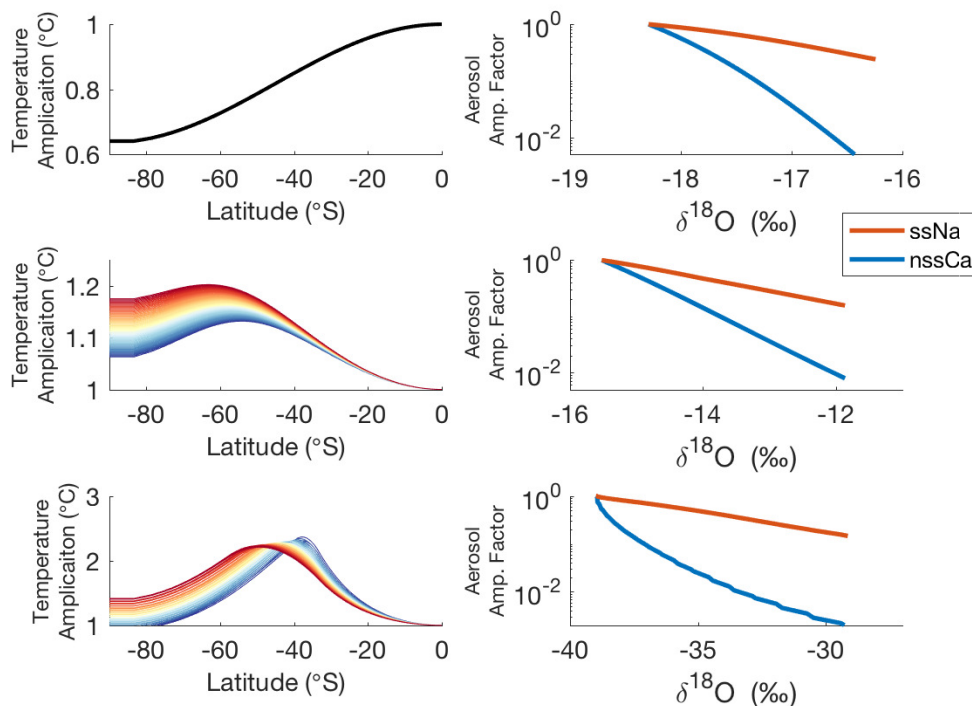


FIGURE S2. Influence of polar amplification from a simple energy balance model on polar aerosol-water isotope relationships. The left panels show spatial patterns (degree of warming with latitude per degree of equatorial warming) from three different energy balance scenarios. Top: dry thermal diffusion (note this actually leads to polar damping of temperature change). Middle: moist thermal diffusion. The different colored lines reflect how the spatial pattern of polar amplification changes with relative changes in global mean temperature. Red colors are warmer mean state temperatures while blue colors are colder mean state temperatures. Bottom: moist thermal diffusion with and ice albedo feedback. Again colors represent relative change in global mean temperature. The right column shows the associated patterns of ssNa (red) and nssCa (blue) change at 80°S on the model grid. Note the changing curvature, particularly of the nssCa line.

## S2. TIMESCALES

Here we investigate the timescale dependence of the relationship between water isotopes and aerosols. In Figure S3, we show the relationship between the WDC  $\delta^{18}\text{O}$  and  $\log(\text{nssCa})$  records filtered for different frequency bands of variability. We examine

the following times scales: the full record (>40,000 to 10 yr variability); >10,000 yr; >1,000 yr; 10,000-1,000 yr; 5,000-1,000 yr; 2,000-500 yr; and <1,000 yr variability. At all but the highest frequency bands of variability (<1,000 yr),  $\delta^{18}O$  and  $\log(\text{nssCa})$  are similarly correlated with similar slopes. This suggests that both millennial and orbital variability is driven by the same underlying process, and consistent with the rainout mechanism. There is some indication of a higher slope at the longest timescales which could represent additional sources of variance such as source region changes, but the differences in slope between timescales are small.

The spectral coherence of WDC  $\delta^{18}O$  and  $\log(\text{nssCa})$ , as well as  $\delta^{18}O$  and  $\log(\text{ssNa})$  (interpolated to even 10 yr/sample spacing), are shown in Figure S4. The records are significantly coherent from orbital to multi-centennial timescales. By comparison WDC  $\delta^{18}O$  and accumulation are not significantly coherent at timescales shorter than multi-millennial (Fudge et al., 2016). At frequencies higher than multi-centennial the water isotope and aerosol records cease to be significantly correlated. This suggests that on shorter timescales, the rainout process that drives correlation in these records is overwhelmed by other sources of non shared variability like source region variability or climate noise.

This analysis suggests that the same processes that drive the relationship between water isotopes and aerosols on glacial-interglacial timescales are the same as the process driving their relationship on millennial timescales. This leaves only a limited role for sources of aerosol variance that may have specific long timescales associated with them, such as Southern Hemisphere glacial activity or large-scale biome changes. To be clear, this analysis does not suggest those processes do not affect source strength, only that their variance is not the dominant driver of the variance in the ice core record.

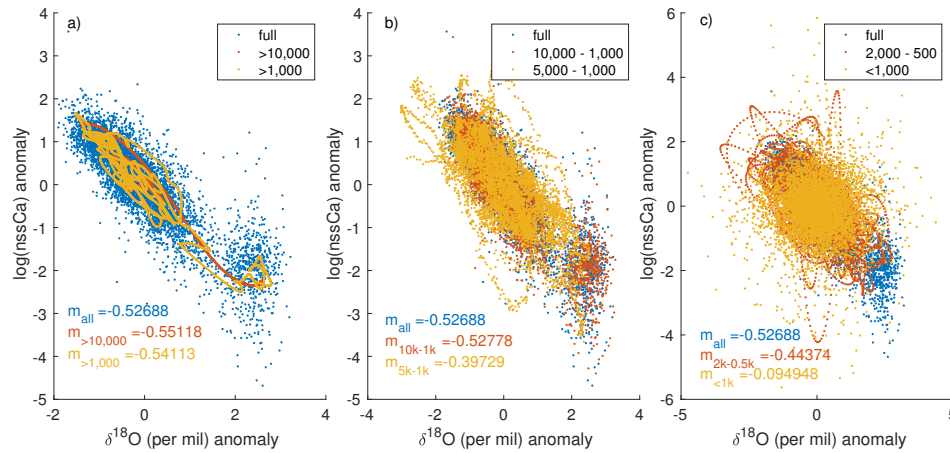


FIGURE S3. Comparison of WDC water isotope and aerosol records at different timescales of variability. a) The full WDC  $\delta^{18}\text{O}$  and  $\log(\text{nssCa})$  record (blue); low pass filtered records with periods  $>10,000$  yr (red); and low pass filtered records with periods  $>1,000$  yr. b) Same as a) but for the full records (blue); band pass filtered records with 10,000-1,000 yr periods (red); and 5,000-1,000 yr periods. c) Same as a) but for the full records (blue); band pass filtered records with 2,000-500 yr periods; and high pass filtered records with  $<1,000$  yr periods. All filtering was done with a fourth order Butterworth filter. Data are presented as z-score anomalies.

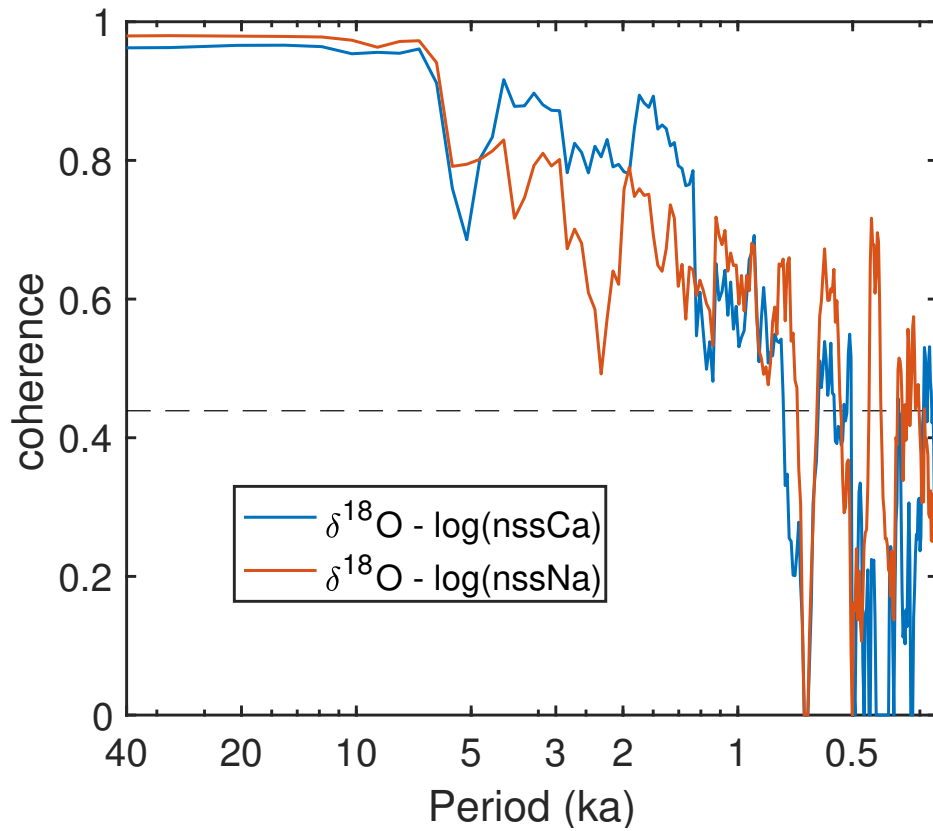


FIGURE S4. Multitaper spectral coherence of WDC  $\delta^{18}\text{O}$  and  $\log(\text{nssCa})$  (blue) and  $\log(\text{ssNa})$  (red). Coherence above the dashed black line is significantly coherent at the 95% confidence limit.

### S3. IMPLICATIONS FOR AEROSOL INFLUENCE ON PAST RADIATIVE FORCING

We here examine the zonal-mean dust burden and the 500 nm aerosol optical depth from the 100 year preindustrial experiment from the CESM Large Ensemble (Kay et al., 2015), shown in Figure S5.a. The two variables are well correlated, particularly in the mid and high latitudes of the Northern Hemisphere (NH) and Southern Hemisphere (SH), Figure S5.b, reflecting the well-known link between dust aerosols and radiative forcing (Stier et al., 2007). In Figure S5.c and d, we show schematics of possible past spatial patterns of aerosol optical depth, on an exponential scale (c) and linear scale (d), based on the correlation of aerosol optical depth to aerosol burden in the model (shown in panels a and b). In red, we show the preindustrial pattern from the CESM Large Ensemble. In light blue, we show the same pattern but multiplied by an order of magnitude across all latitudes, a pattern that might be expected if ice core variability primarily reflects source emission changes ( $LGM_{source}$ ). In contrast we also show a schematic that might be expected if ice-core records predominantly reflect variability in the rain-out process as described in this study ( $LGM_{rainout}$ , dark blue). As emphasized in Figure S5.d, the interpretations of ice-core records has significant implications for past aerosol influence on the radiative budget.

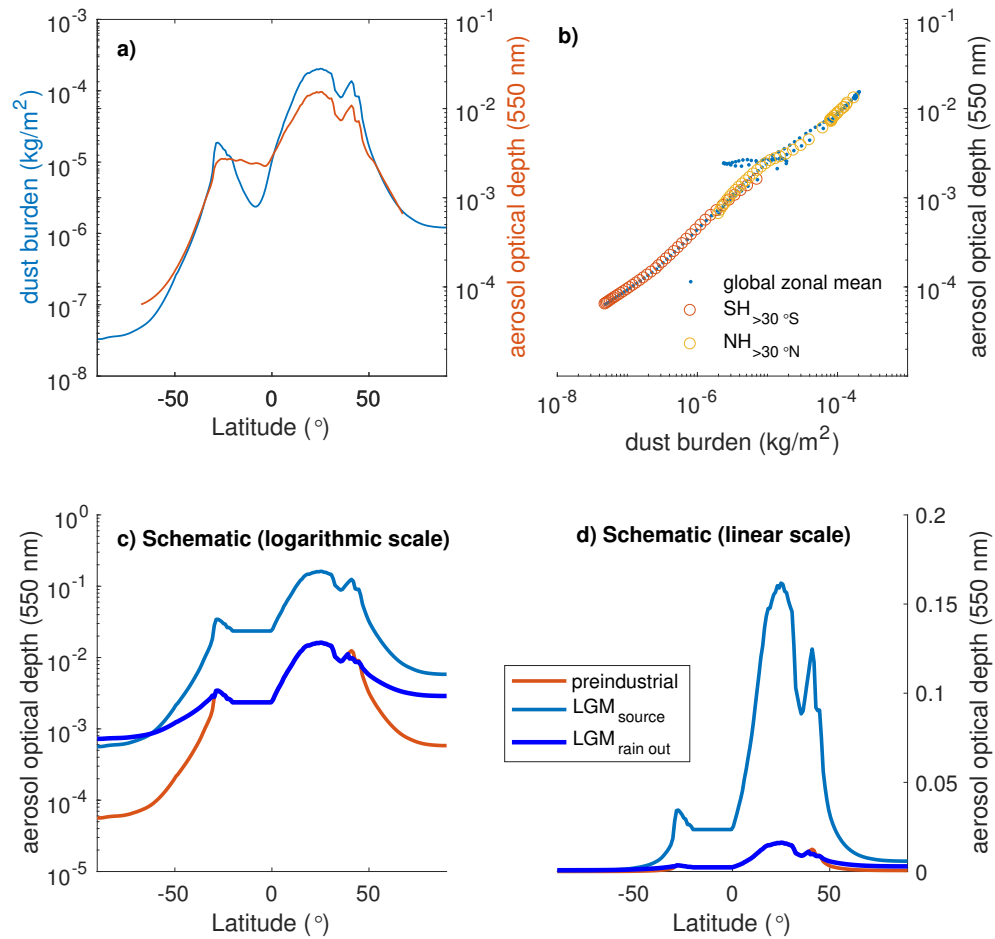


FIGURE S5. a) and b) Comparison of the zonal mean dust burden and the 500nm aerosol optical depth from the 100 year preindustrial experiment from the CESM Large Ensemble. c) and d) Schematic of aerosol optical depth for the preindustrial (red), and two hypothetical LGM-like scenarios: one in which preindustrial dust burdens are amplified by an order of magnitude at all latitudes ( $LGM_{source}$ , light blue), in line with large dust-emission changes; and another in which dust burdens show no change at the source but are amplified toward the pole due to changes in the rain-out process ( $LGM_{rainout}$ , light blue).

#### S4. AEROSOLS AND RAINOUT IN COMPLEX MODELS

Aerosols like dust and seasalts are simulated in GCMs (Zender et al., 2003; Li et al., 2008; Albani et al., 2014). However comparisons of paleoclimate records and simulations of past changes in dust production and deposition have yielded mixed results. In

general the simulations do not reproduce orders-of-magnitude changes in dust source emissions (Mahowald et al., 2006; Bauer and Ganopolski, 2010; Albani et al., 2012; Li et al., 2010). Many models do reproduce 2-3 fold changes in low-latitude dust emissions during the LGM (Mahowald et al., 2006; Bauer and Ganopolski, 2010; Albani et al., 2012) in agreement with low-latitude proxy records (Albani et al., 2014). Some models do not find significant changes in dust lifetime in the LGM compared to modern but also underestimate changes in Antarctic deposition of dust by orders of magnitude (Mahowald et al., 2006; Bauer and Ganopolski, 2010; Li et al., 2010). It has been suggested that early global dust models lacked the necessary complexity in source region variables required to reproduce the variability recorded in ice cores, but thorough investigations of many dust production mechanisms are still unable to yield 10-100 fold changes in production (Li et al., 2010). There is some indication that models may have underestimate the efficiency of aerosol rainout and thus the changes in aerosol lifetime for a given change in precipitation. Albani et al. (2014) doubled dust solubility and below-cloud scavenging, which improved the spatial patterns of dust variability compared to modern observations and significantly increased LGM changes in Antarctic dust deposition compared to previous studies (Albani et al., 2012, 2014).

We examine model results from the CESM Large Ensemble Experiment (Kay et al., 2015), run under different sets of boundary conditions. We examine mean fields from 100 years of an 1850 control run and the means of the first 94 years of an RCP8.5 forcing scenario. The nature of the change in boundary conditions aren't important in this test, we are simply interested in the change in hydrological cycle and aerosols for a given change in mean state. In Figure S6 we show that between boundary conditions, changes in temperature lead to changes in integrated precipitation that increase toward the poles. These changes in integrated precipitation are in turn associated with exponential changes in high latitude aerosols, both dust and sea salts, between their sources and deposition sites, in agreement with the results of our simplified model. The change in aerosols are shown as amplification from their initial source strength, identified as the peak aerosol burden in the zonal mean (about 35°S for dust and 60°S for sea salts in this model). Changes in sea salts are muted compared to those of dust, just as in our simple model. It is interesting to note that the source strengths of both aerosols are actually increased in the warmer mean state (the RCP 8.5 scenario) in this model compared to the colder mean state (the 1850 scenario). While we do not diagnose the source of this source region aerosol burden change, this is of the opposite sign of source region changes that would be required to explain Antarctic aerosols between LGM and Holocene. However changes in the hydrologic cycle are strong enough to overwhelm this source effect for both aerosols, leading to absolute aerosol burdens over Antarctica in the warm scenario that are less than the cold scenario, in spite of stronger emissions. This analysis demonstrates that the underlying physics of the simple model, while surely a simplification of more complex dynamics, is robust.

While the GCM displays poleward changes in aerosols as predicted by the simple model, the magnitude of those changes are less than those of the simple model when

run with the zonal mean temperature profiles from the 1850 and RCP 8.5 scenarios. There may be several sources for this discrepancy including the rudimentary estimation of precipitation and aerosol rainout in the simple model. However, there is a strong indication that CESM is actually underestimating the strength of the scavenging process in these control runs. As seen in figure Figure S6, dust burden decays by about 1.5 orders of magnitude from the midlatitudes to the pole in the control run. Modern observations however suggest this decay should be on the scale of 3-4 orders of magnitude (Albani et al., 2012, 2014). If the model is underestimating the current strength of the rainout process, that is the amount of aerosol removed for a given amount of precipitation, it will also underestimate the changes in aerosols driven by the rainout process, perhaps by orders of magnitude. As noted above, Albani et al. (2014) find that by significantly increasing the strength of scavenging in CAM (the atmosphere component of CESM) they are better able to match modern observations and past changes.

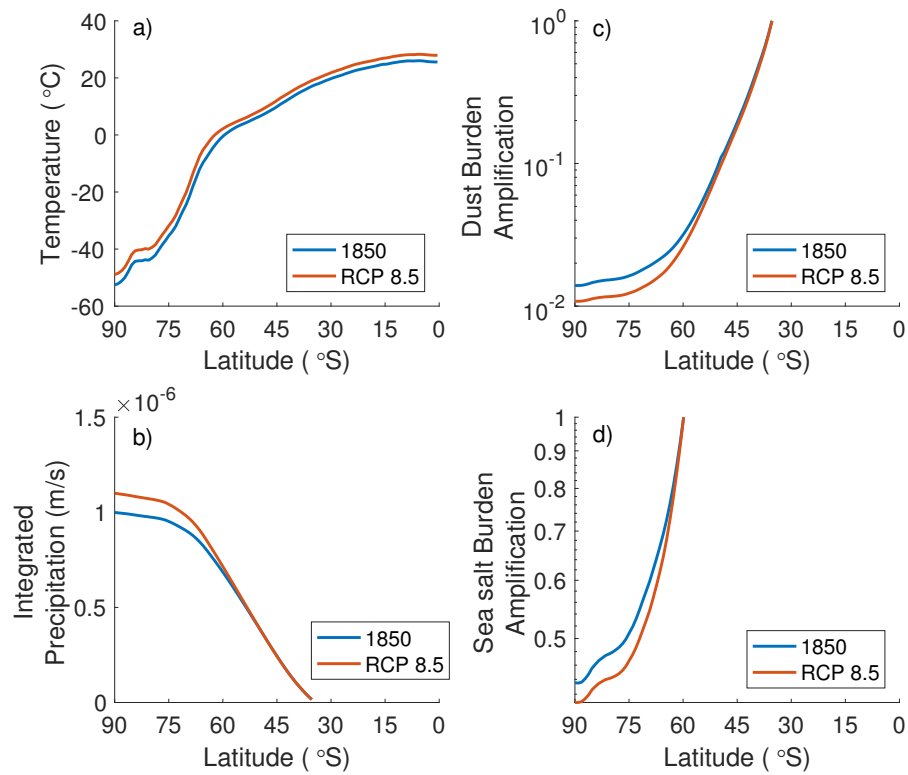


FIGURE S6. a) Zonal mean, century mean Southern Hemisphere surface temperature for the 1850 (blue) and RCP 8.5 (red) scenarios. b) Integrated precipitation between  $40^{\circ}$ S and the pole for both scenarios. c) Dust aerosol burden ( $\text{kg m}^{-2}$ ) as a fraction of source strength for both scenarios. Sea salt aerosol burden ( $\text{kg m}^{-2}$ ) as a fraction of source strength for both scenarios.

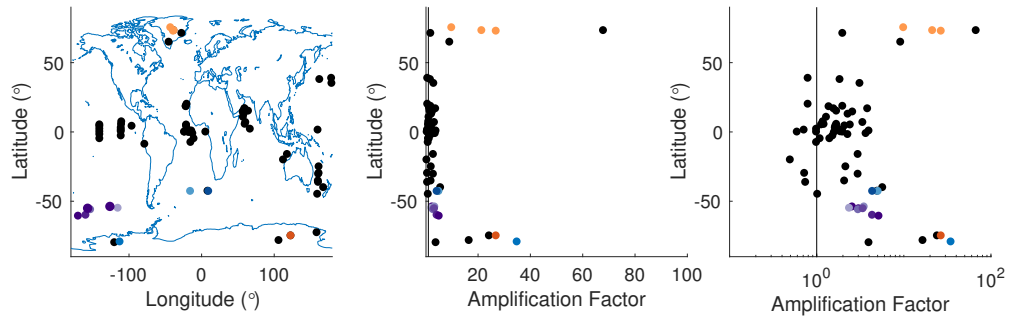


FIGURE S7. a) Global map of dust amplification factors between LGM and Holocene for a global compilation of marine sediment cores and ice cores (Albani et al., 2012) (black), and WDC nssCa (blue), EDC nssCa (red), EDC dust (light blue), and a suite of marine sediment core records (dark blue and purple), colored consistently, and Greenland nssCa records from NGRIP, GRIP, GISP2 (orange). Dust amplification against latitude for all records shown in panel (a) on a linear scale (b) and log scale (c). Vertical black line in b) and c) at amplification of 1 (i.e. no change).

## S5. CONTRASTING VARIABILITY RESULTING FROM SOURCE CHANGES AND FROM RAINOUT

In this section we contrast differences in Antarctic aerosol variability expected due to changes in initial concentration in the source region and due to changes in rainout. Equation 1,  $C = C_0 e^{\frac{t}{\tau}}$ , has significant implications for potential sources of aerosol variability. Order of magnitude variability in  $C$  in Antarctica would require equal orders-of-magnitude variability in  $C_0$ . On the other hand only modest changes in the aerosol lifetime,  $\tau$ , which is a direct result of the strength of rainout, achieves the same result if a site is sufficiently far from the source like Antarctica.

The high resolution WDC records shown in Figure 1 require that whatever the source of aerosol variability, it must be intimately linked to Antarctic climate and the processes governing water isotope fractionation. The rainout process leads to this result naturally and must be operating regardless of other sources of variability. Source emissions on the other hand are unlikely to share this close relationship. In the source emission hypothesis, the Antarctic data require that all the source region variables influencing emissions (such as wind speed, aridity, land cover, shelf area, etc) would have to combine through time such that their logarithm always varied inversely with Antarctic  $\delta^{18}\text{O}$ . This would require a very specific set of nonlinear physics which, to our knowledge, have not yet been articulated. Another set, relating the completely distinct combination of climate variables driving sea salt emission, would also be required to lead to a similar relationship with Antarctic water isotopes. The coincidence would be required yet again in the Northern Hemisphere, whose dust source region conditions must also combine to vary inversely with the exponent of  $\delta^{18}\text{O}$  in Greenland. The rainout process, on the other hand, unites all of these observations, with well known thermodynamics.

Further, as can be seen in Figure 1, the aerosol concentrations plotted against the water isotope data have a log-normal distribution. The spread of the concentration data along the y-axis is similar across climate states in the log scale indicating that the variance in concentration scales with the absolute concentration. This, again is a natural result of the rainout model and the thermodynamics of moisture in the atmosphere; even linear changes in temperature lead to exponential changes in integrated precipitation. On the other hand, if source emissions were the dominant source of variance it would require a log-normal distribution in their variability. There are no obvious *a priori* expectations about how the variance of the full set of source region factors might combine through time or how they might depend on mean state.

Entrainment of dust in the atmosphere at the source is parameterized to depend cubically with surface wind speeds (Bauer and Ganopolski, 2010). This nonlinear relationship has been proposed to help explain the orders-of-magnitude changes in aerosols, perhaps in addition to changes in the statistics of wind speeds (McGee et al., 2010). Such a relationship does not however explain the exponential relationship to Antarctic  $\delta^{18}\text{O}$ , still requiring additional non-linear changes in wind speeds during the deglaciation. While possible, such a picture has shortcomings.

The variance in source emission predicted by a cubic relation to windspeed is also inconsistent with the spread shown in Figure 1. Assuming equal variance in the wind between mean states, the variance in entrainment will scale with the cube of windspeed, which when viewed on a log of concentration plot, the resultant variance will decrease dramatically with increasing concentration. This would require a change in variance of the windspeed that also changes with mean state in such a way that the log of its cube scales with the  $\delta^{18}\text{O}$  in Antarctica, indicating not only a shift in the mean distribution of wind speeds, but a specific change in the character of their probability distribution function.

Finally, global dust deposition records, and those from mid latitude sediment cores in the Southern Hemisphere in particular, do not show the large changes in dust emissions required to account for the variability in ice-core records. The rain out process on the other hand naturally explains the global spatial pattern observed in the records (Figure 5). The global compilation does suggest the possibility of modest changes in dust emission, perhaps 2-3 fold changes, about  $1/10^{\text{th}}$  the total ice core variance. If they occurred, such changes would have certainly influence Antarctic aerosols. But they would not be a large source variability in the record, and due to the influence of the intervening stormy atmosphere, ice cores are not particularly good record of that variability. We cannot rule out dust-emission increases of those magnitudes during the LGM, but nor can we rule out equal changes of the opposite sign. The global picture of dust depositions changes in Figure S7 in fact supports variable changes in dust source emissions between the LGM and Holocene in the low latitudes.

#### S6. COMPILATION OF MASS SCAVENGING EFFICIENCIES

The mass-scavenging ratio,  $\omega$ , quantifies the efficiency of wet removal. It is a dimensionless ratio with units  $\frac{\text{g aerosol}}{\text{g precipitation}} \div \frac{\text{g aerosol}}{\text{g air}}$ . Measured empirically, this ratio is influenced by both in-cloud and below-cloud processes. We here compile measurements of the mass-scavenging ratio for calcium and sodium from several previous compilations (Jaffrezo and Colin, 1988; Tegen and Fung, 1994; Wolff and Bales, 1996; He and Balasubramanian, 2008), and the references therein. The summary statistics for calcium and sodium are presented in Table S1. The measurements compiled in Table S1 are predominantly from Northern Hemisphere midlatitude and polar environments. There is considerable variance in the measured mass-scavenging ratios, likely reflecting both environmental variability and the difficulty of the measurements. For both calcium and sodium, the data indicate central values in the range of  $1\text{-}2 \times 10^3$ . Values within this range may be equally likely. As presented above, our results are robust to uncertainty of  $\omega$  within this range.

Empirical Mass-Scavenging ratio, $\omega$							
aerosol	$n$	minimum	maximum	mean	median	25 <sup>th</sup> percentile	75 <sup>th</sup> percentile
Calcium	14	320	3983	1528	1267	892	1815
Sodium	16	360	7106	1910	1002	523	2300

TABLE S1. Compilation of mass-scavenging ratios from Jaffrezo and Colin (1988), Wolff and Bales (1996), and He and Balasubramanian (2008). Summary statistics for both calcium and sodium include the number of independent measurements,  $n$ ; the minimum, maximum, mean and median of those measurements; as well as the 25<sup>th</sup> to 75<sup>th</sup> percentile bounds of those measurements.

### S7. WET REMOVAL WEIGHTING FUNCTION

The “wet removal weighting function” quantifies how much aerosol emitted from any latitude will reach a final deposition latitude owing to integrated rainout along the way. In Figure S8.a and b we show the wet removal weighting function for Southern Hemisphere aerosols reaching 75°S, in linear and log-scale axes, respectively. The function is calculated assuming equal initial concentrations ( $C_0 = 1$ ) at all latitudes. Aerosols are then transported from initial latitude to 75°S, with integrated wet removal occurring along the way. Aerosol with hypothetical initial source latitude at 75°S will have a weighting of 1, i.e. no removal. The weighting function decreases exponentially toward the equator. For reference, the latitudinal histogram of land area of the Southern Hemisphere continents (South America, Africa, and Australia) are shown in Figure S8.c and the area of the Southern Hemisphere Oceans shown in Figure S8.d. Emissions of terrestrial dust and marine sea salts depend on the available area of their respective sources, as well as other factors including windspeed.

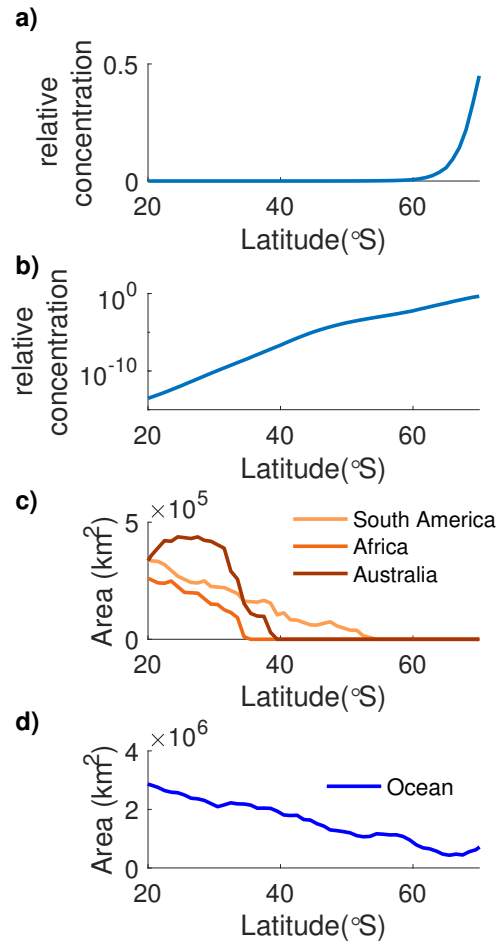


FIGURE S8. a) The wet removal weighting function for equal emission from all Southern Hemisphere latitudes for aerosols reaching 75°S. b) same as a) but on a log axis. c) The land area as a function of latitude for the major Southern Hemisphere continents. d) Surface area as a function of latitude for the Southern Hemisphere ocean.

#### REFERENCES

- Albani, S., Mahowald, N., Perry, A., Scanza, R., Zender, C., Heavens, N., Maggi, V., Kok, J., and Otto-Bliesner, B. (2014). Improved dust representation in the Community Atmosphere Model. *Journal of Advances in Modeling Earth Systems*, 6(3):541–570.

- Albani, S., Mahowald, N. M., Delmonte, B., Maggi, V., and Winckler, G. (2012). Comparing modeled and observed changes in mineral dust transport and deposition to Antarctica between the Last Glacial Maximum and current climates. *Climate dynamics*, 38(9-10):1731–1755.
- Alley, R., Finkel, R., Nishiizumi, K., Anandakrishnan, S., Shuman, C., Mershon, G., Zielinski, G., and Mayewski, P. A. (1995). Changes in continental and sea-salt atmospheric loadings in central Greenland during the most recent deglaciation: model-based estimates. *Journal of Glaciology*, 41(139):503–514.
- Andersen, K. K., Armengaud, A., and Genthon, C. (1998). Atmospheric dust under glacial and interglacial conditions. *Geophysical Research Letters*, 25(13):2281–2284.
- Augustin, L., Barbante, C., Barnes, P. R., Barnola, J. M., Bigler, M., Castellano, E., Cattani, O., Chappellaz, J., Dahl-Jensen, D., Delmonte, B., et al. (2004). Eight glacial cycles from an Antarctic ice core. *Nature*, 429(6992):623–628.
- Bauer, E. and Ganopolski, A. (2010). Aeolian dust modeling over the past four glacial cycles with CLIMBER-2. *Global and Planetary Change*, 74(2):49–60.
- Bowen, H. J. M. (1984). *Environmental chemistry*, volume 3. Royal Society of Chemistry.
- Ciais, P. and Jouzel, J. (1994). Deuterium and oxygen 18 in precipitation: Isotopic model, including mixed cloud processes. *Journal of Geophysical Research: Atmospheres*, 99(D8):16793–16803.
- Criss, R. E. (1999). *Principles of stable isotope distribution*. Oxford University Press.
- Cuffey, K. M., Clow, G. D., Steig, E. J., Buizert, C., Fudge, T., Koutnik, M., Waddington, E. D., Alley, R. B., and Severinghaus, J. P. (2016). Deglacial temperature history of West Antarctica. *Proceedings of the National Academy of Sciences*, 113(50):14249–14254.
- Curran, M., Wong, G., Goodwin, I., van Ommen, T., and Vance, T. (2008). Estimate of sea salt sources to Antarctica: An alternative interpretation of the EPICA sea salt record? In *European Geosciences Union (EGU) General Assembly 2008*, page 1.
- Dansgaard, W. (1964). Stable isotopes in precipitation. *Tellus*, 16(4):436–468.
- Davidson, C., Harrington, J., Stephenson, M., Small, M., Boscoe, F. P., and Gandley, R. (1989). Seasonal variations in sulfate, nitrate and chloride in the Greenland ice sheet: relation to atmospheric concentrations. *Atmospheric Environment (1967)*, 23(11):2483–2493.
- De Angelis, M., Steffensen, J. P., Legrand, M., Clausen, H., and Hammer, C. (1997). Primary aerosol (sea salt and soil dust) deposited in Greenland ice during the last climatic cycle: Comparison with east Antarctic records. *Journal of Geophysical Research: Oceans*, 102(C12):26681–26698.
- Delmonte, B., Andersson, P., Hansson, M., Schöberg, H., Petit, J.-R., Basile-Doelsch, I., and Maggi, V. (2008). Aeolian dust in East Antarctica (EPICA-Dome C and Vostok): Provenance during glacial ages over the last 800 kyr. *Geophysical Research Letters*, 35(7).
- Delmonte, B., Petit, J., and Maggi, V. (2002). Glacial to Holocene implications of the new 27000-year dust record from the EPICA Dome C (East Antarctica) ice core.

- Climate Dynamics*, 18(8):647–660.
- Fischer, H., Fundel, F., Ruth, U., Twarloh, B., Wegner, A., Udisti, R., Becagli, S., Castellano, E., Morganti, A., Severi, M., et al. (2007a). Reconstruction of millennial changes in dust emission, transport and regional sea ice coverage using the deep EPICA ice cores from the Atlantic and Indian Ocean sector of Antarctica. *Earth and Planetary Science Letters*, 260(1):340–354.
- Fischer, H., Siggaard-Andersen, M.-L., Ruth, U., Röthlisberger, R., and Wolff, E. (2007b). Glacial/interglacial changes in mineral dust and sea-salt records in polar ice cores: Sources, transport, and deposition. *Reviews of Geophysics*, 45(1).
- Friedrich, T., Timmermann, A., Tigchelaar, M., Timm, O. E., and Ganopolski, A. (2016). Nonlinear climate sensitivity and its implications for future greenhouse warming. *Science Advances*, 2(11):e1501923.
- Fudge, T., Markle, B. R., Cuffey, K. M., Buizert, C., Taylor, K. C., Steig, E. J., Waddington, E. D., Conway, H., and Koutnik, M. (2016). Variable relationship between accumulation and temperature in West Antarctica for the past 31,000 years. *Geophysical Research Letters*, 43(8):3795–3803.
- Gersonde, R., Crosta, X., Abelmann, A., and Armand, L. (2005). Sea-surface temperature and sea ice distribution of the southern ocean at the epilog last glacial maximum—a circum-antarctic view based on siliceous microfossil records. *Quaternary Science Reviews*, 24(7):869–896.
- Harrison, S. P., Kohfeld, K. E., Roelandt, C., and Claquin, T. (2001). The role of dust in climate changes today, at the last glacial maximum and in the future. *Earth-Science Reviews*, 54(1-3):43–80.
- Hartmann, D. L. (2015). *Global physical climatology*, volume 103. Newnes.
- He, J. and Balasubramanian, R. (2008). Rain-aerosol coupling in the tropical atmosphere of southeast asia: distribution and scavenging ratios of major ionic species. *Journal of atmospheric chemistry*, 60(3):205–220.
- Held, I. M. and Soden, B. J. (2006). Robust responses of the hydrological cycle to global warming. *Journal of Climate*, 19(21):5686–5699.
- Hwang, Y.-T. and Frierson, D. M. W. (2010). Increasing atmospheric poleward energy transport with global warming. *Geophysical Research Letters*, 37(24):n/a–n/a.
- Jaffrezo, J.-L. and Colin, J.-L. (1988). Rain-aerosol coupling in urban area: scavenging ratio measurement and identification of some transfer processes. *Atmospheric Environment (1967)*, 22(5):929–935.
- Jouzel, J., Alley, R. B., Cuffey, K., Dansgaard, W., Grootes, P., Hoffmann, G., Johnsen, S. J., Koster, R., Peel, D., Shuman, C., et al. (1997). Validity of the temperature reconstruction from water isotopes in ice cores. *Journal of Geophysical Research: Oceans*, 102(C12):26471–26487.
- Kalnay, E., Kanamitsu, M., Kistler, R., Collins, W., Deaven, D., Gandin, L., Iredell, M., Saha, S., White, G., Woollen, J., et al. (1996). The NCEP/NCAR 40-year reanalysis project. *Bulletin of the American meteorological Society*, 77(3):437–471.

- Kaufman, Y. J., Tanré, D., and Boucher, O. (2002). A satellite view of aerosols in the climate system. *Nature*, 419(6903):215–223.
- Kavanaugh, J. L. and Cuffey, K. M. (2003). Space and time variation of  $\delta^{18}\text{O}$  and  $\delta\text{D}$  in Antarctic precipitation revisited. *Global Biogeochemical Cycles*, 17(1):n/a–n/a.
- Kay, J., Deser, C., Phillips, A., Mai, A., Hannay, C., Strand, G., Arblaster, J., Bates, S., Danabasoglu, G., Edwards, J., et al. (2015). The Community Earth System Model (CESM) large ensemble project: A community resource for studying climate change in the presence of internal climate variability. *Bulletin of the American Meteorological Society*, 96(8):1333–1349.
- Kohfeld, K. E. and Harrison, S. P. (2001). DIRTMAP: the geological record of dust. *Earth-Science Reviews*, 54(1):81–114.
- Köhler, P., Bintanja, R., Fischer, H., Joos, F., Knutti, R., Lohmann, G., and Masson-Delmotte, V. (2010). What caused Earth's temperature variations during the last 800,000 years? Data-based evidence on radiative forcing and constraints on climate sensitivity. *Quaternary Science Reviews*, 29(1):129–145.
- Lambert, F., Delmonte, B., Petit, J.-R., Bigler, M., Kaufmann, P. R., Hutterli, M. A., Stocker, T. F., Ruth, U., Steffensen, J. P., and Maggi, V. (2008). Dust-climate couplings over the past 800,000 years from the EPICA Dome C ice core. *Nature*, 452(7187):616–619.
- Lamy, F., Gersonde, R., Winckler, G., Esper, O., Jaeschke, A., Kuhn, G., Ullermann, J., Martínez-García, A., Lambert, F., and Kilian, R. (2014). Increased dust deposition in the Pacific Southern Ocean during glacial periods. *Science*, 343(6169):403–407.
- Legrand, M. R. and Delmas, R. J. (1988). Soluble impurities in four Antarctic ice cores over the last 30 000 years. *Annals of Glaciology*, 10(1):116–120.
- Li, F., Ginoux, P., and Ramaswamy, V. (2008). Distribution, transport, and deposition of mineral dust in the Southern Ocean and Antarctica: Contribution of major sources. *Journal of Geophysical Research: Atmospheres*, 113(D10).
- Li, F., Ramaswamy, V., Ginoux, P., Broccoli, A. J., Delworth, T., and Zeng, F. (2010). Toward understanding the dust deposition in Antarctica during the Last Glacial Maximum: sensitivity studies on plausible causes. *Journal of Geophysical Research: Atmospheres*, 115(D24).
- Mahowald, N. M., Muhs, D. R., Levis, S., Rasch, P. J., Yoshioka, M., Zender, C. S., and Luo, C. (2006). Change in atmospheric mineral aerosols in response to climate: Last glacial period, preindustrial, modern, and doubled carbon dioxide climates. *Journal of Geophysical Research: Atmospheres*, 111(D10).
- Markle, B. (2017). Nonlinear temperature reconstruction with a Simple Water-Isotope Model. *in preparation*.
- Markle, B. R., Steig, E. J., Buizert, C., Schoenemann, S. W., Bitz, C. M., Fudge, T., Pedro, J. B., Ding, Q., Jones, T. R., White, J. W., et al. (2017). Global atmospheric teleconnections during Dansgaard-Oeschger events. *Nature Geoscience*, 10(1):36–40.
- Masson-Delmotte, V., Kageyama, M., Braconnot, P., Charbit, S., Krinner, G., Ritz, C., Guilyardi, E., Jouzel, J., Abe-Ouchi, A., Crucifix, M., et al. (2006). Past and future

- polar amplification of climate change: climate model intercomparisons and ice-core constraints. *Climate Dynamics*, 26(5):513–529.
- McConnell, J. R., Lamorey, G. W., Lambert, S. W., and Taylor, K. C. (2002). Continuous ice-core chemical analyses using inductively coupled plasma mass spectrometry. *Environmental science & technology*, 36(1):7–11.
- McGee, D., Broecker, W. S., and Winckler, G. (2010). Gustiness: The driver of glacial dustiness? *Quaternary Science Reviews*, 29(17):2340–2350.
- Merlivat, L. and Jouzel, J. (1979). Global climatic interpretation of the deuterium-oxygen 18 relationship for precipitation. *Journal of Geophysical Research: Oceans*, 84(C8):5029–5033.
- Otto-Bliesner, B. L., Brady, E. C., Clauzet, G., Tomas, R., Levis, S., and Kothavala, Z. (2006). Last glacial maximum and Holocene climate in CCSM3. *Journal of Climate*, 19(11):2526–2544.
- Paltridge, G. W. (1975). Global dynamics and climate—a system of minimum entropy exchange. *Quarterly Journal of the Royal Meteorological Society*, 101(429):475–484.
- Petit, J. R., Briat, M., and Royer, A. (1981). Ice age aerosol content from East Antarctic ice core samples and past wind strength. *Nature*.
- Petit, J.-R. and Delmonte, B. (2009). A model for large glacial–interglacial climate-induced changes in dust and sea salt concentrations in deep ice cores (central Antarctica): Palaeoclimatic implications and prospects for refining ice core chronologies. *Tellus B*, 61(5):768–790.
- Rankin, A., Auld, V., and Wolff, E. (2000). Frost flowers as a source of fractionated sea salt aerosol in the polar regions. *Geophysical Research Letters*, 27(21):3469–3472.
- Rasmussen, S. O., Bigler, M., Blockley, S. P., Blunier, T., Buchardt, S. L., Clausen, H. B., Cvijanovic, I., Dahl-Jensen, D., Johnsen, S. J., Fischer, H., et al. (2014). A stratigraphic framework for abrupt climatic changes during the Last Glacial period based on three synchronized Greenland ice-core records: refining and extending the INTIMATE event stratigraphy. *Quaternary Science Reviews*, 106:14–28.
- Roe, G. H., Feldl, N., Armour, K. C., Hwang, Y.-T., and Frierson, D. M. (2015). The remote impacts of climate feedbacks on regional climate predictability. *Nature Geoscience*, 8(2):135–139.
- Röthlisberger, R., Mulvaney, R., Wolff, E. W., Hutterli, M. A., Bigler, M., Sommer, S., and Jouzel, J. (2002). Dust and sea salt variability in central East Antarctica (Dome C) over the last 45 kyrs and its implications for southern high-latitude climate. *Geophysical Research Letters*, 29(20).
- Schmidt, G. A., Jungclaus, J., Ammann, C., Bard, E., Braconnot, P., Crowley, T., Delaygue, G., Joos, F., Krivova, N., Muscheler, R., et al. (2011). Climate forcing reconstructions for use in PMIP simulations of the last millennium (v1. 0). *Geoscientific Model Development*, 4(1):pp33–45.
- Schoenemann, S. W., Steig, E. J., Ding, Q., Markle, B. R., and Schauer, A. J. (2014). Triple water-isotope record from WAIS Divide, Antarctica: Controls on glacial–interglacial changes in  $17\text{O}$  excess of precipitation. *Journal of Geophysical Research:*

- Atmospheres*, 119(14):8741–8763.
- Sodemann, H. and Stohl, A. (2009). Asymmetries in the moisture origin of Antarctic precipitation. *Geophysical research letters*, 36(22).
- Stier, P., Seinfeld, J. H., Kinne, S., and Boucher, O. (2007). Aerosol absorption and radiative forcing. *Atmospheric Chemistry and Physics*, 7(19):5237–5261.
- Sugden, D. E., McCulloch, R. D., Bory, A. J. M., and Hein, A. S. (2009). Influence of Patagonian glaciers on Antarctic dust deposition during the last glacial period. *Nature Geoscience*, 2(4):281–285.
- Tegen, I. and Fung, I. (1994). Modeling of mineral dust in the atmosphere: Sources, transport, and optical thickness. *Journal of Geophysical Research: Atmospheres*, 99(D11):22897–22914.
- Uemura, R., Matsui, Y., Yoshimura, K., Motoyama, H., and Yoshida, N. (2008). Evidence of deuterium excess in water vapor as an indicator of ocean surface conditions. *Journal of Geophysical Research: Oceans (1978–2012)*, 113(D19):D19114.
- WAIS Divide Project Members (2013). Onset of deglacial warming in west antarctica driven by local orbital forcing. *Nature*, 500(7463):440–444.
- WAIS Divide Project Members (2015). Precise inter-polar phasing of abrupt climate change during the last ice age. *Nature*, 520(7549):661–665.
- Winckler, G. (2015). South Atlantic Ocean Dust Records. Personal Communication.
- Wolff, E. and Bales, R. (1996). Chemical exchange between the atmosphere and polar snow: proceedings of the NATO advanced research workshop "Processes of chemical exchange between the atmosphere and polar snow", held at Il Ciocco, Italy, March 19-23, 1995]. *NATO ASI series (Series I, Global environmental change)*, 43.
- Wolff, E. W., Fischer, H., Fundel, F., Ruth, U., Twarloh, B., Littot, G. C., Mulvaney, R., Röthlisberger, R., De Angelis, M., Boutron, C. F., et al. (2006). Southern Ocean sea-ice extent, productivity and iron flux over the past eight glacial cycles. *Nature*, 440(7083):491–496.
- Yung, Y. L., Lee, T., Wang, C.-H., and Shieh, Y.-T. (1996). Dust: A diagnostic of the hydrologic cycle during the Last Glacial Maximum. *Science*, 271(5251):962.
- Zender, C. S., Bian, H., and Newman, D. (2003). Mineral Dust Entrainment and Deposition (DEAD) model: Description and 1990s dust climatology. *Journal of Geophysical Research: Atmospheres*, 108(D14).

Appendix A

**ONSET OF DEGLACIAL WARMING IN WEST ANTARCTICA  
DRIVEN BY LOCAL ORBITAL FORCING**

# Onset of deglacial warming in West Antarctica driven by local orbital forcing

WAIS Divide Project Members\*

**The cause of warming in the Southern Hemisphere during the most recent deglaciation remains a matter of debate<sup>1,2</sup>. Hypotheses for a Northern Hemisphere trigger, through oceanic redistributions of heat, are based in part on the abrupt onset of warming seen in East Antarctic ice cores and dated to 18,000 years ago, which is several thousand years after high-latitude Northern Hemisphere summer insolation intensity began increasing from its minimum, approximately 24,000 years ago<sup>3,4</sup>. An alternative explanation is that local solar insolation changes cause the Southern Hemisphere to warm independently<sup>2,5</sup>. Here we present results from a new, annually resolved ice-core record from West Antarctica that reconciles these two views. The records show that 18,000 years ago snow accumulation in West Antarctica began increasing, coincident with increasing carbon dioxide concentrations, warming in East Antarctica and cooling in the Northern Hemisphere<sup>6</sup> associated with an abrupt decrease in Atlantic meridional overturning circulation<sup>7</sup>. However, significant warming in West Antarctica began at least 2,000 years earlier. Circum-Antarctic sea-ice decline, driven by increasing local insolation, is the likely cause of this warming. The marine-influenced West Antarctic records suggest a more active role for the Southern Ocean in the onset of deglaciation than is inferred from ice cores in the East Antarctic interior, which are largely isolated from sea-ice changes.**

Exceptional records of Southern Hemisphere climate change come from Antarctic ice cores<sup>2,6,7</sup>. Most of these records are from high-altitude sites on the East Antarctic plateau. Questions about the reliability of the two previous deep West Antarctic ice-core records result in those records often being excluded from reconstructions of Antarctic climate<sup>4,8</sup>. Because the climate of West Antarctica is distinct from that of interior East Antarctica, the exclusion of West Antarctic records may result in an incomplete picture of past Antarctic and Southern Ocean climate change. Interior West Antarctica is lower in elevation and more subject to the influence of marine air masses than interior East Antarctica, which is surrounded by a steep topographic slope<sup>9,10</sup>. Marine-influenced locations are important because they more directly reflect atmospheric conditions resulting from changes in ocean circulation and sea ice. However, ice-core records from coastal sites are often difficult to interpret because of complicated ice-flow and elevation histories. The West Antarctic Ice Sheet (WAIS) Divide ice core (WDC), in central West Antarctica, is unique in coming from a location that has experienced minimal elevation change<sup>11</sup>, is strongly influenced by marine conditions<sup>9</sup> and has a relatively high snow-accumulation rate, making it possible to obtain an accurately dated record with high temporal resolution.

Drilling of WDC was completed in December 2011 to a depth of 3,405 m. Drilling was halted ~50 m above the bedrock to avoid contaminating the basal water system. WDC is situated 24 km west of the Ross–Amundsen ice-flow divide and 160 km east of the Byrd ice-core site (Supplementary Fig. 1). The elevation is 1,766 m; the present-day snow accumulation rate is 22 cm yr<sup>-1</sup> (ice equivalent) and the average temperature is approximately -30 °C. The age of the oldest recovered ice is ~68 kyr. The WDC06A-7 timescale is based on the identification of annual layers to 29.6 kyr ago using primarily electrical measurements

(Methods). To validate WDC06A-7, we compare times of abrupt changes in atmospheric methane concentration (Supplementary Information) with the Greenland Ice Core Chronology 2005<sup>12</sup> (GICC05). We also compare the methane variations in WDC with abrupt changes in a speleothem  $\delta^{18}\text{O}$  record from Hulu Cave, China. The difference in age between the ice and gas at a given depth is calculated using a steady-state firn-densification model and is always less than 500 yr. The age differences between WDC06A-7 and GICC05 and between WDC06A-7 and the Hulu Cave timescale are much less than the independent timescale uncertainties (Supplementary Fig. 6).

We interpret  $\delta^{18}\text{O}$  of ice (Methods) as annual-mean surface air temperature, as supported by independent estimates of temperature from borehole thermometry<sup>13</sup>. WDC has many similarities with other records (Fig. 1) and resolves Antarctic Isotope Maximum (AIM) events clearly. The late Holocene WDC record shows cooling, suggesting that the increase in  $\delta^{18}\text{O}$  at Byrd over the past few thousand years resulted from ice advection and thinning<sup>11</sup>. The abrupt increase in  $\delta^{18}\text{O}$  ~22 kyr ago at Siple Dome is not observed at WDC. The AIM1 peak and the subsequent Antarctic Cold Reversal (ACR; 14.5–12.9 kyr ago) are more pronounced in WDC than at Byrd and Siple Dome, possibly owing to discontinuous sampling of the Byrd core and thinning of Siple Dome.

The most rapid warming at WDC occurred after the ACR and culminated at AIM0. The timing of AIM0 is difficult to define because it is composed of two peaks, one 11.95 kyr ago and the other 11.6 kyr ago. The ice accumulation rate at WDC increased abruptly by 37% in the 400 yr between 12.0 and 11.6 kyr ago (Supplementary Fig. 2). The increase in ice accumulation with little change in  $\delta^{18}\text{O}$  shows that the accumulation rate is not controlled strictly by temperature. Abrupt changes in accumulation cannot be recognized in most other Antarctic ice cores because their timescales lack sufficient resolution; it is thus unknown whether this event is specific to WDC or whether accumulation increased abruptly over a larger portion of Antarctica.

The coldest period at WDC was between 28 and 22 kyr ago and was interrupted by AIM2, a 1,000-yr warm period between 24 and 23 kyr ago. AIM2 is also prominent in the EPICA Dronning Maud Land (EDML) ice core<sup>7</sup> but is muted or nearly absent in other East Antarctic records<sup>14</sup> (Fig. 1). Other West Antarctic cores also record AIM2, although the low resolution of the Byrd core and the abrupt  $\delta^{18}\text{O}$  increase 22 kyr ago in the Siple Dome core have made this feature difficult to discern. AIM2 illustrates the spatial heterogeneity of Antarctic climate variability during the coldest part of the glacial period.

To investigate deglacial warming across the Antarctic continent, we use a sliding Wilcoxon rank-sum test (Fig. 2) to identify times of significant change in the  $\delta^{18}\text{O}$  records of WDC, EDML and the EPICA Dome C ice core<sup>6</sup> (EDC); we convert the EDC  $\delta\text{D}$  record to  $\delta^{18}\text{O}$  using  $\delta^{18}\text{O} = (\delta\text{D} - 10)/8$ . The WDC and EDC timescales can be aligned at a ~150-yr-long acid deposition event<sup>15,16</sup>, which eliminates the relative age uncertainty at 18 kyr ago. The rank sum test reveals three important features: gradual deglacial warming at WDC was punctuated by periods of more rapid change; the most abrupt warming

\*Lists of participants and their affiliations appear at the end of the paper.

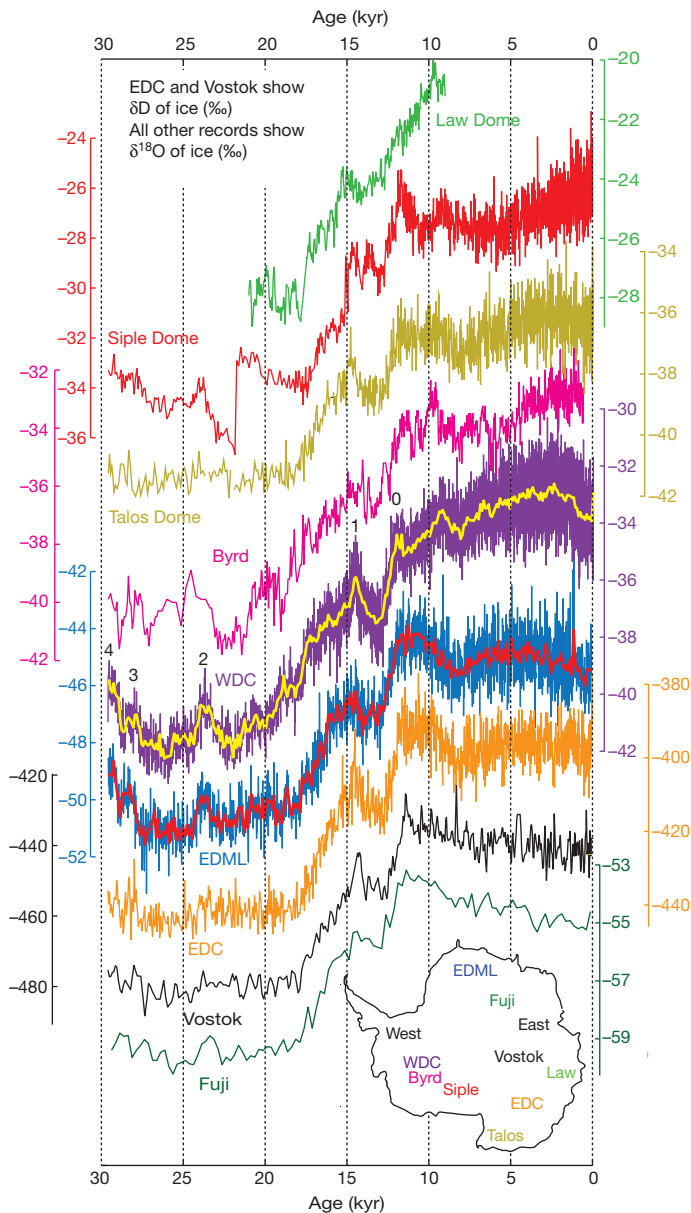


**Figure 1 | Antarctic Isotope Records.** Water isotope ratios from nine Antarctic ice cores. Inset, outline of Antarctica with the ice-core locations: Law Dome<sup>27</sup> (light green), Siple Dome<sup>28</sup> (red), Byrd<sup>29</sup> (pink), Talos Dome<sup>14</sup> (khaki), WDC (purple, WDC06A-7 timescale), EDML<sup>7</sup> (blue), EDC<sup>6</sup> (orange), Dome Fuji<sup>2</sup> (dark green), Vostok<sup>30</sup> (black). Taylor Dome is not plotted because of timescale uncertainties. All records are at original resolution. Thick lines for WDC and EDML are 50-yr averages. EDML, EDC and Vostok use the Lemieux-Dudon<sup>31</sup> timescale. Numbers above the WDC curve indicate AIM events. ( $\delta^{18}\text{O} = (^{18}\text{O}/^{16}\text{O})_{\text{sample}} / (^{18}\text{O}/^{16}\text{O})_{\text{VSMOW}} - 1$  and  $\delta\text{D} = ({}^2\text{H}/{}^1\text{H})_{\text{sample}} / ({}^2\text{H}/{}^1\text{H})_{\text{VSMOW}} - 1$ .)

began at the 18-kyr-ago acid deposition event; and significant warming at WDC began by 20 kyr ago, at least 2,000 yr before significant warming at EDML and EDC.

Further insight into deglacial warming at WDC is gained by investigating the sea-salt sodium (ssNa) record (Methods). Debate remains about whether ssNa on millennial timescales reflects primarily sea-ice production or the strength of atmospheric circulation<sup>17</sup>. In the Amundsen and Ross seas, changes in sea ice and atmospheric circulation are coupled because atmospheric forcing is the dominant control on sea-ice concentration<sup>18</sup>. We interpret ssNa as a proxy for sea-ice extent and a marker of marine changes (Supplementary Information). The rank-sum test reveals that each rapid increase in  $\delta^{18}\text{O}$ , indicating warming, was accompanied by a decrease in ssNa, suggesting less sea ice (Fig. 2).

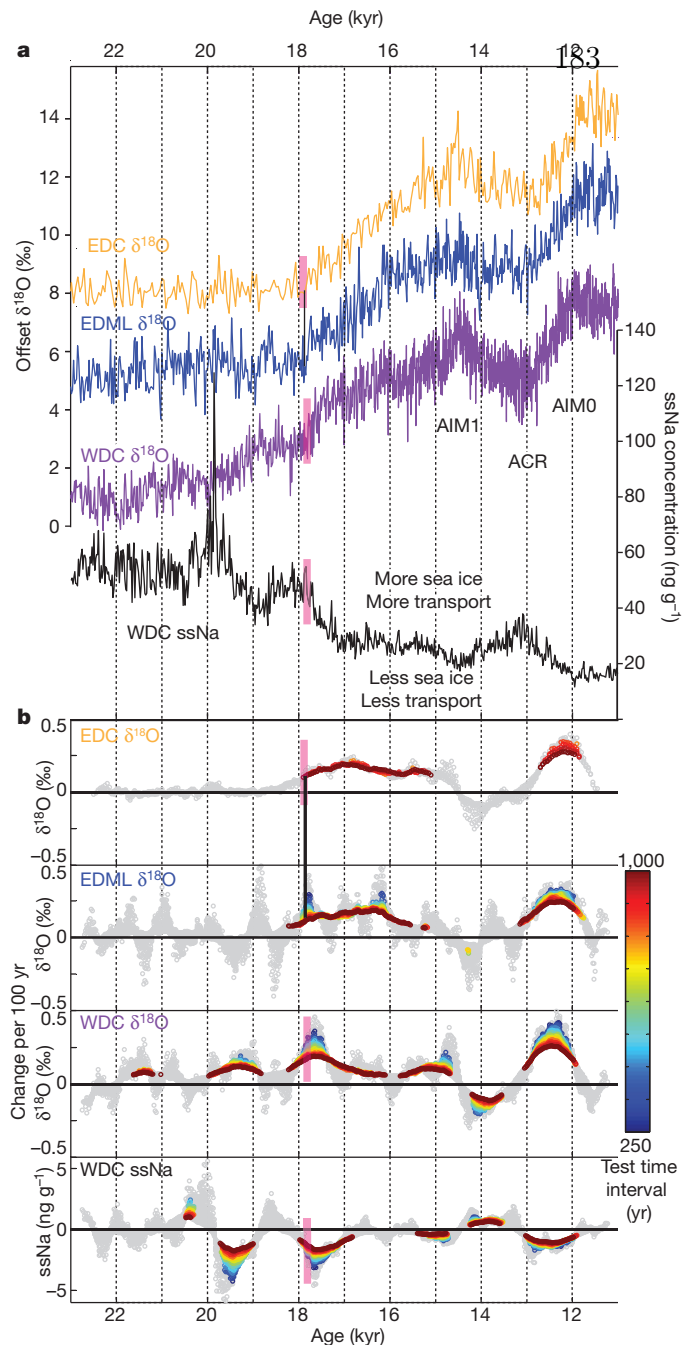


**Figure 2 | Timing of rapid change in Antarctica.** **a**, Water isotope ratios ( $\delta^{18}\text{O}$ , purple) and ssNa concentrations (black) from WDC on WDC06A-7. EDML<sup>7</sup> (blue) and EDC<sup>6</sup> (orange)  $\delta^{18}\text{O}$  use the Lemieux-Dudon<sup>31</sup> timescale. Constants have been subtracted from  $\delta^{18}\text{O}$  records for plotting. Magenta boxes indicate a volcanic tie point (Methods). ssNa is plotted as 25-yr median values. **b**, Rate of change for  $\delta^{18}\text{O}$  at WDC, EDML, and EDC and ssNa at WDC. A Wilcoxon rank-sum test (Methods) is used to determine significance. Significant rates of change are coloured by test time interval; rates of change that are not significant are coloured grey.

Consistent with this, the decrease in  $\delta^{18}\text{O}$  during the ACR was accompanied by an increase in ssNa.

The accumulation rate at WDC was inferred without assuming a relationship with  $\delta^{18}\text{O}$  or temperature (Methods). Although uncertainty in the annual-layer interpretation and ice-flow history used to determine the accumulation rate precludes a statistical assessment comparable to that used for the  $\delta^{18}\text{O}$  and ssNa records, results suggest that an initial increase in accumulation occurred between 18.5 and

17 kyr ago (Fig. 3), consistent with the rapid warming 18 kyr ago. This also coincides with evidence for changes in Southern Ocean upwelling<sup>19</sup>, atmospheric carbon dioxide concentration<sup>8,20</sup> and Atlantic meridional overturning circulation<sup>5</sup> (AMOC). The accumulation increase probably results from more frequent or stronger moisture-bearing storms penetrating into West Antarctica. This supports a southward shift<sup>21</sup> or intensification<sup>22</sup> of the mid-latitude westerly storm track, and is consistent with the hypothesis of a decrease in AMOC leading to Southern Hemisphere warming and Northern Hemisphere cooling<sup>3</sup>—the ‘bipolar seesaw’.

Both the WDC and the lower-resolution Byrd ice-core records show that warming in West Antarctica began before the decrease in AMOC that has been invoked to explain Southern Hemisphere warming<sup>4,19</sup>. The most significant early warming at WDC occurred between 20 and 18.8 kyr ago, although a period of significant warming also occurred between 22 and 21.5 kyr ago. The magnitude of the warming at WDC before 18 kyr ago is much greater than at EDML or EDC; linear regression of  $\delta^{18}\text{O}$  between 22 and 18 kyr ago shows that it increased by

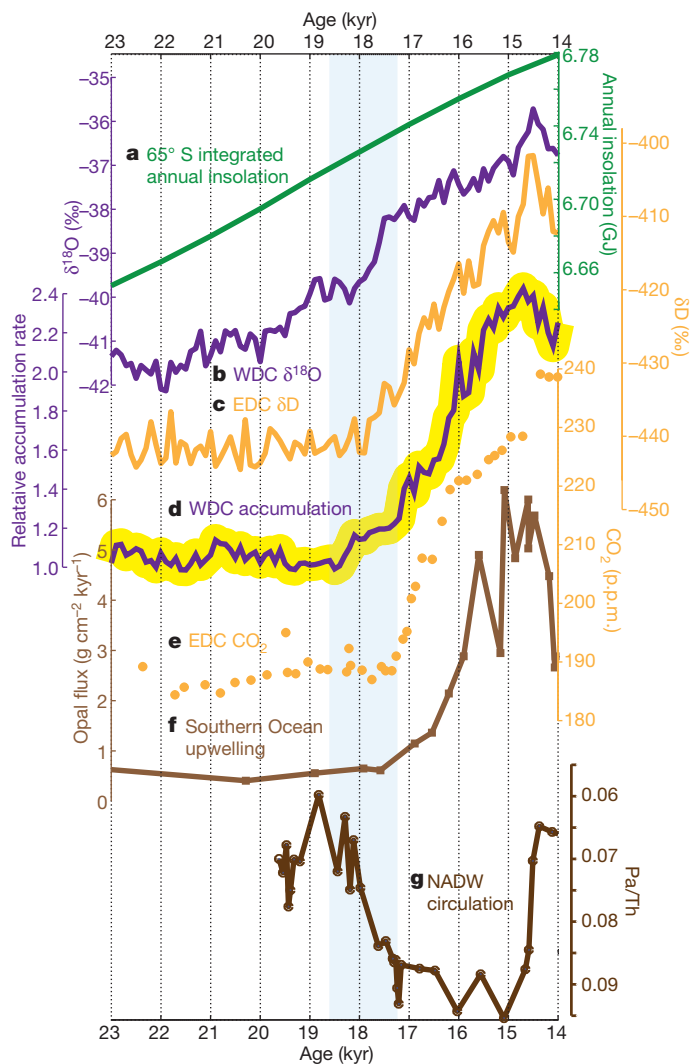


**Figure 3 | Global records of deglaciation.** **a**, Integrated annual insolation at latitude  $65^{\circ}\text{S}$ . **b**, 100-yr averages of  $\delta^{18}\text{O}$  at WDC on WDC06A-7. **c**, 100-yr averages of  $\delta\text{D}$  at EDC<sup>6</sup> on the Lemieux-Dudon<sup>31</sup> timescale. **d**, Relative accumulation rate (normalized to the mean value between 19.5 and 18.5 kyr ago) at WDC. Yellow shading indicates the uncertainty in identifying annual layers (Methods). **e**, Atmospheric  $\text{CO}_2$  concentration<sup>20</sup> from EDC on the Lemieux-Dudon<sup>31</sup> timescale. **f**, Opal flux<sup>19</sup>, a proxy for upwelling, from ocean sediment core TNO57-13-4PC in the South Atlantic. **g**, Pa/Th, a proxy for North Atlantic Deep Water (NADW) circulation<sup>5</sup>, from sediment core GCC5. Blue shading indicates a period with relatively abrupt changes in all palaeoclimate records (**b–g**).

2.2‰ at WDC, by 0.4‰ at EDML and by 0.1‰ at EDC (Fig. 2). It is very unlikely that the 2.2‰ increase at WDC can be attributed to elevation change; this magnitude of isotope change would require more than 200 m of ice-sheet thinning, twice the amount of thinning that occurred during the Holocene epoch when the grounding line retreated hundreds of kilometres (Supplementary Information). The subdued warming at EDML and the lack of warming at EDC are consistent with the lack of clear AIM2 signals in some East Antarctic cores, and suggest that cores from the East Antarctic plateau do not capture the full magnitude of Southern Hemisphere climate variability.

There is evidence that warming at WDC before 18 kyr ago is due to decreasing sea ice. The ssNa at WDC began to decrease 20 kyr ago, probably as a result of both decreasing sea-ice extent and decreasing strength of transport from changes in atmospheric circulation. A marine record from the southwest Atlantic Ocean indicates that significant summer and winter sea-ice retreat began before 22 kyr ago<sup>23</sup>. Furthermore, a reduction in sea-ice extent can explain the different magnitude of warming among ice-core sites before 18 kyr ago. The high East Antarctic plateau is largely isolated from coastal changes because the local marine air masses do not have the energy to rise above the steep coastal escarpment<sup>10</sup>.

To illustrate the variable sensitivity of different areas in Antarctica to changes in sea-ice extent, we used an atmospheric general circulation model<sup>24</sup>. Using Last Glacial Maximum (LGM) sea surface temperature and sea-ice boundary conditions from a fully coupled model run<sup>25</sup>, we performed a control run of the ECHAM4.6 atmospheric model with the LGM sea-ice extent and a comparison run with reduced sea-ice extent (Supplementary Information). Sea surface temperatures are prescribed; the atmospheric circulation therefore responds to the change in sea-ice extent but the sea-ice extent is not further affected by the changes in atmospheric circulation. The magnitude of sea-ice retreat is consistent with evidence for reduced sea ice in the southwest Atlantic between 22 and 18 kyr ago<sup>23</sup>. In response to the sea-ice retreat, all of West Antarctica and coastal East Antarctica is enriched in precipitation-weighted  $\delta^{18}\text{O}$ , whereas interior East Antarctica is little changed or is depleted (Fig. 4). The positive  $\delta^{18}\text{O}$  anomalies probably extend unrealistically far into the East Antarctic interior because of the low-resolution topography in the climate model. Although the details of the spatial pattern of  $\delta^{18}\text{O}$  anomalies are dependent on model resolution and on the specified boundary conditions, the greater

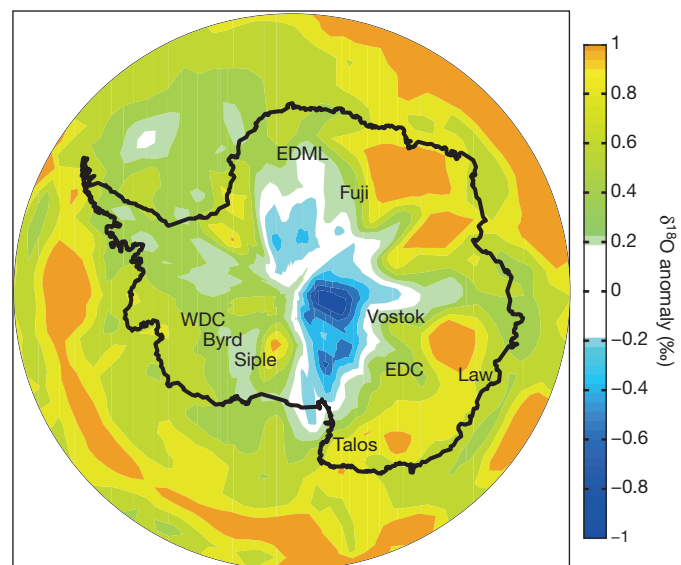


**Figure 4 | Antarctic  $\delta^{18}\text{O}$  response to sea-ice decrease.** Response of precipitation-weighted  $\delta^{18}\text{O}$  to an approximately zonally symmetric southward displacement of the sea-ice edge (Supplementary Fig. 9) in the ECHAM4.6 climate model run with LGM boundary conditions.

sensitivity of the WAIS Divide region to sea-ice decline compared with locations in interior East Antarctica is clear.

Local orbital forcing is a likely cause of the inferred sea-ice change. Integrated annual insolation at latitude 65° S increased by 1% between 22 and 18 kyr ago. The additional annual insolation is 60 MJ m<sup>-2</sup>, which is enough to melt 5 cm m<sup>-2</sup> of sea ice assuming an albedo of 0.75. The increase in integrated summer insolation, where summer is defined as days with insolation above a threshold<sup>26</sup> of 275 W m<sup>-2</sup>, is greater than the total annual increase (Supplementary Fig. 10). Thus, the increase comes in summer, when it is most likely to be absorbed by low-albedo open water. The summer duration also begins increasing at 23 kyr ago; longer summers and shorter winters may also contribute to the decrease in sea-ice extent<sup>1</sup>. The effect of an increase in insolation would be amplified by the sea-ice/albedo feedback.

The abrupt onset of East Antarctic warming<sup>4,8</sup>, increasing CO<sub>2</sub> (ref. 20) and decreasing AMOC<sup>5</sup> 18 kyr ago has supported the view that deglaciation in the Southern Hemisphere is primarily a response to changes in the Northern Hemisphere<sup>3</sup>. Yet the evidence of warming in West Antarctica and corresponding evidence for sea-ice decline in the southeast Atlantic<sup>23</sup> show that climate changes were ongoing in the Southern Ocean before 18 kyr ago, supporting an important role for local orbital forcing<sup>1</sup>. Warming in the high latitudes of both hemispheres before 18 kyr ago implies little change in the interhemispheric temperature gradient that largely determines the position of the intertropical convergence zone and the position and intensity of the mid-latitude westerlies<sup>21,22</sup>. We propose that when Northern Hemisphere cooling occurred ~18 kyr ago, coupled with an already-warming Southern Hemisphere, the intertropical convergence zone and mid-latitude westerlies shifted southwards in response. The increased wind stress in the Southern Ocean drove upwelling, venting of CO<sub>2</sub> from the deep ocean<sup>19</sup> and warming in both West Antarctica and East Antarctica. The new WDC record thus reveals an active role for the Southern Hemisphere in initiating global deglaciation.

## METHODS SUMMARY

The WDC06A-7 timescale is based on measurements of sulphur, sodium, black carbon and electrical conductivity above 577 m (to 2,358 yr before AD 1950), and primarily on electrical measurements below 577 m. Using atmospheric methane as a stratigraphic marker, WDC06A-7 and GICC05 agree to within 100 ± 200 yr at the three abrupt changes between 14.7 and 11.7 kyr ago; WDC06A-7 is older by 500 ± 600 yr at 24 kyr ago, by 250 ± 300 yr at 28 kyr ago and by 350 ± 250 yr at 29 kyr ago (Supplementary Fig. 6). WDC06A-7 agrees within the uncertainties with the Hulu Cave timescale and is older by 50 ± 300 yr at 28 kyr ago and by 100 ± 300 yr at 29 kyr ago.

We measured δ<sup>18</sup>O at a resolution of 0.5 m using laser spectroscopy with calibration to Vienna Standard Mean Ocean Water (VSMOW). We report ssNa concentration rather than flux because wet deposition dominates at higher accumulation rates. The accumulation-rate record was derived independently from the stable-isotope record using a one-dimensional ice-flow model to calculate the thinning function.

Periods of significant change in δ<sup>18</sup>O and ssNa are identified with a sliding, non-parametric Wilcoxon rank-sum test. The data were averaged to 25-yr resolution for WDC and EDML, and to 50-yr resolution for EDC. We tested pairs of adjacent blocks of data against the null hypothesis of equal medians, performing the test at all points along the record. We assessed change on multiple timescales using a range of block sizes corresponding to time intervals of 250–1,000 yr for WDC and EDML and 500–1,000 yr for EDC. We used an effective 95% a-posteriori confidence requirement; the critical significance level (*p*) was determined as 1 – 0.95<sup>1/N</sup> where *N* is the number of test realizations.

We used the ECHAM4.6 atmospheric general circulation model at T42 resolution (2.8° by 2.8°) with 19 vertical levels and glacial sea surface temperature boundary conditions.

**Full Methods** and any associated references are available in the online version of the paper.

Received 4 January; accepted 12 June 2013.

Published online 14 August 2013.

- Huybers, P. & Denton, G. Antarctic temperature at orbital timescales controlled by local summer duration. *Nature Geosci.* **1**, 787–792 (2008).

- Kawamura, K. *et al.* Northern Hemisphere forcing of climatic cycles in Antarctica over the past 360,000 years. *Nature* **448**, 912–916 (2007).
- Clark, P. U., Pisias, N. G., Stocker, T. F. & Weaver, A. J. The role of the thermohaline circulation in abrupt climate change. *Nature* **415**, 863–869 (2002).
- Shakun, J. D. *et al.* Global warming preceded by increasing carbon dioxide concentrations during the last deglaciation. *Nature* **484**, 49–54 (2012).
- McManus, J. F., Francois, R., Gherardi, J. M., Keigwin, L. D. & Brown-Leger, S. Collapse and rapid resumption of Atlantic meridional circulation linked to deglacial climate changes. *Nature* **428**, 834–837 (2004).
- EPICA community members. Eight glacial cycles from an Antarctic ice core. *Nature* **429**, 623–628 (2004).
- EPICA Community Members. One-to-one coupling of glacial climate variability in Greenland and Antarctica. *Nature* **444**, 195–198 (2006).
- Parrenin, F. *et al.* Synchronous change of atmospheric CO<sub>2</sub> and Antarctic temperature during the last deglacial warming. *Science* **339**, 1060–1063 (2013).
- Nicolas, J. P. & Bromwich, D. H. Climate of West Antarctica and influence of marine air intrusions. *J. Clim.* **24**, 49–67 (2011).
- Noone, D. & Simmonds, I. Sea ice control of water isotope transport to Antarctica and implications for ice core interpretation. *J. Geophys. Res.* **109**, D07105 (2004).
- Steig, E. J. *et al.* in *The West Antarctic Ice Sheet: Behavior and Environment* Vol. 77 (eds Alley, R. & Bindshadler, R.) 75–90 (American Geophysical Union, 2001).
- Svensson, A. *et al.* A 60,000 year Greenland stratigraphic ice core chronology. *Clim. Past* **4**, 47–57 (2008).
- Steig, E. J. *et al.* Recent climate and ice-sheet changes in West Antarctica compared with the past 2,000 years. *Nature Geosci.* **6**, 372–375 (2013).
- Stenni, B. *et al.* Expression of the bipolar see-saw in Antarctic climate records during the last deglaciation. *Nature Geosci.* **4**, 46–49 (2011).
- Hammer, C. U., Clausen, H. B. & Langway, C. C. 50,000 years of recorded global volcanism. *Clim. Change* **35**, 1–15 (1997).
- Schwander, J. *et al.* A tentative chronology for the EPICA Dome Concordia ice core. *Geophys. Res. Lett.* **28**, 4243–4246 (2001).
- Wolff, E. W., Rankin, A. M. & Rothlisberger, R. An ice core indicator of Antarctic sea ice production? *Geophys. Res. Lett.* **30**, 2158 (2003).
- Holland, P. R. & Kwok, R. Wind-driven trends in Antarctic sea-ice drift. *Nature Geosci.* **5**, 872–875 (2012).
- Anderson, R. F. *et al.* Wind-driven upwelling in the Southern Ocean and the deglacial rise in atmospheric CO<sub>2</sub>. *Science* **323**, 1443–1448 (2009).
- Monnin, E. *et al.* Atmospheric CO<sub>2</sub> concentrations over the last glacial termination. *Science* **291**, 112–114 (2001).
- Toggweiler, J. R., Russell, J. L. & Carson, S. R. Midlatitude westerlies, atmospheric CO<sub>2</sub>, and climate change during the ice ages. *Paleoceanography* **21**, PA2005 (2006).
- Lee, S. Y., Chiang, J. C. H., Matsumoto, K. & Tokos, K. S. Southern Ocean wind response to North Atlantic cooling and the rise in atmospheric CO<sub>2</sub>: modeling perspective and paleoceanographic implications. *Paleoceanography* **26**, PA1214 (2011).
- Collins, L. G., Pike, J., Allen, C. S. & Hodgson, D. A. High-resolution reconstruction of southwest Atlantic sea-ice and its role in the carbon cycle during marine isotope stages 3 and 2. *Paleoceanography* **27**, PA3217 (2012).
- Roeckner, E. *et al.* *The Atmospheric General Circulation Model ECHAM-4: Model Description and Simulation of Present-Day Climate*. Report No. 218 90 (Max-Planck-Institut für Meteorologie, 1996).
- Braconnot, P. *et al.* Results of PMIP2 coupled simulations of the Mid-Holocene and Last Glacial Maximum - Part 1: experiments and large-scale features. *Clim. Past* **3**, 261–277 (2007).
- Huybers, P. Early Pleistocene glacial cycles and the integrated summer insolation forcing. *Science* **313**, 508–511 (2006).
- Pedro, J. B. *et al.* The last deglaciation: timing the bipolar seesaw. *Clim. Past* **7**, 671–683 (2011).
- Brook, E. J. *et al.* Timing of millennial-scale climate change at Siple Dome, West Antarctica, during the last glacial period. *Quat. Sci. Rev.* **24**, 1333–1343 (2005).
- Blunier, T. & Brook, E. J. Timing of millennial-scale climate change in Antarctica and Greenland during the last glacial period. *Science* **291**, 109–112 (2001).
- Petit, J. R. *et al.* Climate and atmospheric history of the past 420,000 years from the Vostok ice core, Antarctica. *Nature* **399**, 429–436 (1999).
- Lemieux-Dudon, B. *et al.* Consistent dating for Antarctic and Greenland ice cores. *Quat. Sci. Rev.* **29**, 8–20 (2010).

**Supplementary Information** is available in the online version of the paper.

**Acknowledgements** This work was supported by US National Science Foundation (NSF). The authors appreciate the support of the WAIS Divide Science Coordination Office (M. Twickler and J. Souney) for the collection and distribution of the WAIS Divide ice core; Ice Drilling and Design and Operations (K. Dahnert) for drilling; the National Ice Core Laboratory (B. Bencivengo) for curating the core; Raytheon Polar Services (M. Kippenhan) for logistics support in Antarctica; and the 109th New York Air National Guard for airlift in Antarctica. We also thank C. Buizert and S. Marcott for discussions. The following individual NSF grants supported this work: 0944197 (E.D.W., H. Conway); 1043092, 0537930 (E.J.S.); 0944348, 0944191, 0440817, 0440819, 0230396 (K.C.T.); 0538427, 0839093 (J.R.M.); 1043518 (E.J.B.); 1043500 (T.S.); 05379853, 1043167 (J.W.C.W.); 1043528, 0539578 (R.B.A.); 0539232 (K.M.C., G.D.C.); 1103403 (R.L.E., H. Conway); 0739780 (R.E.); 0637211 (G.H.); 0538553, 0839066 (J.C.-D.), 0538657, 1043421 (J.P.S.); 1043313 (M.K.S.); 0801490 (G.J.W.). Other support came from a NASA NESSF award (T.J.F.), the USGS Climate and Land Use Change Program (G.D.C., J.J.F.), the National Natural Science Foundation of China (41230524 to H. Cheng) and the Singapore National Research Foundation (NRFF2011-08 to X.W.).

**Author Contributions** The manuscript was written by T.J.F., E.J.S. and B.R.M. K.C.T. organized the WAIS Divide Project. T.J.F., K.C.T. and T.J.P. made the electrical measurements and developed the electrical timescale with K.C.M. E.J.S., J.W.C.W., A.J.S., P.N., B.H.V. and S.W.S. measured the stable-isotope record. J.R.M., M.S., O.J.M. and R.E. developed the chemistry timescale and measured Na. E.J.B., T.S., L.E.M., J.S.E. and J.E.L. made the methane measurements. G.D.C. and K.M.C. measured the borehole temperature profile. J.C.-D. and D.F. provided an independent timescale for the brittle ice. Q.D., S.W.S. and E.J.S. performed the climate modelling. T.J.F., E.D.W., H. Conway and K.M.C. performed the ice-flow modelling to determine the accumulation rate. H. Cheng, R.L.E., X.W., J.P.S. and T.J.F. made comparisons with the Hulu cave timescale. M.K.S., J.J.F., J.M.F., D.E.V. and R.B.A. examined the physical properties of the core. W.M., J.J. and N.M. designed the drill. G.H. designed core-processing techniques. A.J.O., B.H.V., D.E.V., K.C.T., T.J.P. and G.J.W. led collection and processing of the core in the field.

**Author Information** Reprints and permissions information is available at [www.nature.com/reprints](http://www.nature.com/reprints). The authors declare no competing financial interests. Readers are welcome to comment on the online version of the paper. Correspondence and requests for materials should be addressed to T.J.F. ([tjfudge@uw.edu](mailto:tjfudge@uw.edu)).

**WAIS Divide Project Members** T. J. Fudge<sup>1</sup>, Eric J. Steig<sup>1,2</sup>, Bradley R. Markle<sup>1</sup>, Spruce W. Schoenemann<sup>1</sup>, Qinghua Ding<sup>1,2</sup>, Kendrick C. Taylor<sup>3</sup>, Joseph R. McConnell<sup>3</sup>, Edward J. Brook<sup>4</sup>, Todd Sowers<sup>5</sup>, James W. C. White<sup>6,7</sup>, Richard B. Alley<sup>5,8</sup>, Hai Cheng<sup>9,10</sup>, Gary D. Clow<sup>11</sup>, Jihong Cole-Dai<sup>12</sup>, Howard Conway<sup>1</sup>, Kurt M. Cuffey<sup>13</sup>, Jon S. Edwards<sup>4</sup>, R. Lawrence Edwards<sup>10</sup>, Ross Edwards<sup>14</sup>, John M. Fegyveresi<sup>5,8</sup>, David Ferris<sup>12</sup>, Joan J. Fitzpatrick<sup>15</sup>, Jay Johnson<sup>16</sup>, Geoffrey Hargreaves<sup>17</sup>, James E. Lee<sup>4</sup>, Olivia J. Maselli<sup>3</sup>, William Mason<sup>18</sup>, Kenneth C. McGwire<sup>3</sup>, Logan E. Mitchell<sup>4</sup>, Nicolai Mortensen<sup>16</sup>, Peter Neff<sup>1,19</sup>, Anais J. Orsi<sup>20</sup>, Trevor J. Popp<sup>21</sup>, Andrew J. Schauer<sup>1</sup>,

Jeffrey P. Severinghaus<sup>20</sup>, Michael Sigl<sup>3</sup>, Matthew K. Spencer<sup>22</sup>, Bruce H. Vaughn<sup>7</sup>, Donald E. Voigt<sup>5,8</sup>, Edwin D. Waddington<sup>1</sup>, Xianfeng Wang<sup>23</sup> & Gifford J. Wong<sup>24</sup>

186

Affiliations for participants: <sup>1</sup>Department of Earth and Space Sciences, University of Washington, Seattle, Washington 98195, USA. <sup>2</sup>Quaternary Research Center, University of Washington, Seattle, Washington 98195, USA. <sup>3</sup>Desert Research Institute, Nevada System of Higher Education, Reno, Nevada 89512, USA. <sup>4</sup>College of Earth, Ocean and Atmospheric Sciences Oregon State University, Corvallis, Oregon 97331, USA. <sup>5</sup>Earth and Environmental Systems Institute, Pennsylvania State University, University Park, Pennsylvania 16802, USA. <sup>6</sup>Department of Geological Sciences and Department of Environmental Studies, Boulder, Colorado 80309, USA. <sup>7</sup>INSTAAR, University of Colorado, Boulder, Colorado 80309, USA. <sup>8</sup>Department of Geosciences, Pennsylvania State University, University Park, Pennsylvania 16802, USA. <sup>9</sup>Institute of Global Environmental Change, Xi'an Jiaotong University, Xi'an 710049, China. <sup>10</sup>Department of Earth Sciences, University of Minnesota, Minneapolis, Minnesota 55455, USA. <sup>11</sup>US Geological Survey, Geosciences and Environmental Change Science Center, Lakewood, Colorado 80225, USA. <sup>12</sup>Department of Chemistry and Biochemistry, South Dakota State University, Brookings, South Dakota 57007, USA. <sup>13</sup>Department of Geography, University of California-Berkeley, Berkeley 94720, USA. <sup>14</sup>Department of Imaging and Applied Physics, Curtin University, Perth, Western Australia 6102, Australia. <sup>15</sup>US Geological Survey, Denver, Colorado 80225, USA. <sup>16</sup>Ice Drilling Design and Operations, Space Science Engineering Center, University of Wisconsin-Madison, Madison, Wisconsin 53706, USA. <sup>17</sup>US Geological Survey, National Ice Core Laboratory, Denver, Colorado 80225, USA. <sup>18</sup>EMECH Designs, Brooklyn, Wisconsin 53521, USA. <sup>19</sup>Antarctic Research Centre, Victoria University of Wellington, Wellington 6012, New Zealand. <sup>20</sup>Scripps Institution of Oceanography, University of California, San Diego, La Jolla, California 92037, USA. <sup>21</sup>Centre for Ice and Climate, Niels Bohr Institute, University of Copenhagen, Juliane Maries Vej 30, 2100 Copenhagen, Denmark. <sup>22</sup>Department of Geology and Physics, Lake Superior State University, Sault Ste Marie, Michigan 49783, USA. <sup>23</sup>Earth Observatory of Singapore, Nanyang Technological University, Singapore 639798. <sup>24</sup>Department of Earth Sciences, Dartmouth College, Hanover, New Hampshire 03755, USA.

## METHODS

**Stable-isotope measurements of ice.** Water isotope analyses were by laser spectroscopy<sup>32</sup> at the University of Washington. Values of  $\delta^{18}\text{O}$  represent the deviation from Vienna Standard Mean Ocean Water (VSMOW) normalized<sup>11</sup> to the VSMOW-SLAP standards and reported in per mil (‰). The precision of the measurements is better than 0.1‰. The data have not been corrected for advection, elevation, or mean seawater  $\delta^{18}\text{O}$ .

**Accumulation rates.** The accumulation-rate record was derived independently from the stable-isotope record using an ice-flow model to calculate the thinning function. We use a transient one-dimensional ice-flow model to compute the vertical-velocity profile:

$$w(z) = -\left(\dot{b} - \dot{m} - \dot{H}\right)\psi(z) - \dot{m} - \left(\frac{\rho_i}{\rho(z)} - 1\right)\dot{b} \quad (1)$$

Here  $z$  is the height above the bed,  $\dot{b}$  is the accumulation rate,  $\dot{m}$  is the melt rate,  $\dot{H}$  is the rate of ice-thickness change,  $\rho_i$  is the density of ice,  $\rho(z)$  is the density profile and  $\psi(z)$  is the vertical velocity shape function computed as

$$\psi(z) = \frac{(f_B z + (1/2)(1 - f_B)(z^2/h))}{(H - (h/2)(1 - f_B))} \quad \text{for } h \geq z > 0$$

$$\psi(z) = \frac{(z - (h/2)(1 - f_B))}{(H - (h/2)(1 - f_B))} \quad \text{for } H \geq z > h$$

following ref. 33. Here  $h$  is the distance above bedrock of the Dansgaard–Johnsen<sup>34</sup> kink height,  $f_B$  is the fraction of the horizontal surface velocity due to sliding over the bed and  $H$  is the ice thickness. Firn compaction is incorporated through the rightmost term in equation (1) and assumes a density profile that does not vary with time.

A constant ice thickness was specified because the thickness change near the divide was probably small ( $\sim 100$  m) and the timing of thickening and thinning is not well constrained; a 100-m thickness change would alter the inferred accumulation rate by  $\sim 3\%$ . A constant basal melt rate of  $1 \text{ cm yr}^{-1}$  and non-divide flow conditions, represented by a Dansgaard–Johnsen kink height of  $0.2H$ , were assumed. We also prescribed a sliding fraction of 0.5 of the surface velocity, which approximates effects of both basal sliding and enhanced shear near the bed, neither of which is well constrained. To assess the possible range of inferred accumulation rates, we also used sliding fractions of 0.15 and 0.9 (Supplementary Fig. 2). The inferred accumulation rate was only slightly affected for the Holocene part of the record but differed by up to 16% for the oldest part of the record (29.6 kyr ago). Because the thinning function varies smoothly, the uncertainty in the timing of the changes in accumulation rate is only weakly affected by the uncertainty in the magnitude of the accumulation rate. The main uncertainty in identifying the timing of accumulation rate changes is the uncertainty in the timescale itself. During the deglacial transition, the uncertainty in the interpretation is estimated at 8%. The yellow shading in Fig. 3 shows this uncertainty.

**WDC06A-7 timescale.** The WDC06A-7 timescale is based on high-resolution ( $< 1$  cm) measurements of sulphur, sodium, black carbon and electrical conductivity (ECM) above 577 m (2,358 yr before present (BP; AD 1950); ref. 35). Below 577 m, WDC06A-7 is based primarily on electrical measurements: di-electrical profiling was used for the brittle ice from 577 to 1,300 m (to 6,063 yr BP). Alternating-current ECM measurements were used from 1,300 to 1,955 m (to 11,589 yr BP) and both alternating-current and direct-current ECM measurements were used below 1,955 m. The interpretation was stopped at 2,800 m because the expression of annual layers becomes less consistent, suggesting that all years may not be easily recognized.

The upper 577 m of the timescale has been compared with volcanic horizons dated on multiple other timescales<sup>35</sup>; the uncertainty at 2,358 yr BP is  $\pm 19$  yr. For the remainder of the timescale, we assigned an uncertainty based on a qualitative assessment of the clarity of the annual layers. For ice from 577 to 2,020 m (2–12 kyr ago), we estimated a 2% uncertainty based on comparisons between the ECM and chemical (Na,  $\text{SO}_4$ ) interpretations between 577 and 1,300 m, which agreed to within 1% (Supplementary Fig. 4). The estimated uncertainty increased during the deglacial transition owing to both thinner layers and a less pronounced seasonal cycle. We compared the annual-layer interpretation of the ECM records in an 800-yr overlap section (1,940–2,020-m depth, corresponding to 11.4–12.2 kyr ago) with various high-resolution chemistry records (sodium and sulphur). We found overall good agreement (19 yr more in the ECM-only interpretation) but did observe a tendency for the ECM record to ‘split’ one annual peak into two small peaks. We used this knowledge in the annual-layer interpretation of the ECM record. We increased the uncertainty to 4% between 2,020 and 2,300 m (12.2–15.5 kyr ago) and to 8% between 2,300 and 2,500 m (15.5–20 kyr ago). The glacial period had a stronger annual-layer signal than the transition, and we estimate a 6%

uncertainty for the rest of the glacial. The 150-yr acid deposition event, first identified in the Byrd ice core<sup>15</sup>, was found in WDC at depths of 2,421.75 to 2,427.25 m. Because there is consistently high conductance without a clear annual signal, we used the average annual layer thickness of the 10 m above and below this section to determine the number of years within it. There are periods of detectable annual variations within this depth range, and they have approximately the same annual-layer thickness as the 10-m averages. A 10% uncertainty was assumed.

We assess the accuracy of WDC06A-7 by comparing it with two high-precision timescales: GICC05 and a new speleothem timescale from Hulu Cave. Because the age of the gas at a given depth is less than that of the ice surrounding it, we first need to calculate the age offset ( $\Delta\text{age}$ ). We use the inferred accumulation rates and surface temperatures estimated from the  $\delta^{18}\text{O}$  record constrained by the borehole temperature profile (Supplementary Information) in a steady-state firn-densification model<sup>36</sup>. The model is well-suited to WDC because it was developed using data from modern ice-core sites that span the full range of past WDC temperatures and accumulation rates. We calculate  $\Delta\text{age}$  using 200-yr smoothed histories of surface temperature and accumulation rate, a surface density of  $370 \text{ kg m}^{-3}$  and a close-off density of  $810 \text{ kg m}^{-3}$  (Supplementary Fig. 5a). The calculated present-day  $\Delta\text{age}$  is 210 yr, which is similar to the value, 205 yr, measured for WDC<sup>37</sup>. The steady-state model is acceptable for WDC because the surface temperature and accumulation rate vary more slowly than in Greenland. Because our primary purpose is to assess the accuracy of the WDC06A-7 timescale, calculation of  $\Delta\text{age}$  to better than a few decades is not necessary. The  $\Delta\text{age}$  uncertainty between 15 and 11 kyr ago is estimated to be 100 yr. The  $\Delta\text{age}$  uncertainty is estimated to be 150 yr for times before 20 kyr ago because of the colder temperatures and lower and less certain accumulation rates.

Because methane is well mixed in the atmosphere and should have identical features in both hemispheres, we use atmospheric methane measurements from WDC and the Greenland composite methane record<sup>33</sup> to compare WDC06A-7 and GICC05 at six times. The age differences are summarized in Supplementary Fig. 6 and the correlation and  $\Delta\text{age}$  uncertainties are shown in Supplementary Table 1. In Greenland, methane and  $\delta^{18}\text{O}$  changes are nearly synchronous<sup>38–40</sup> and we therefore assume no  $\Delta\text{age}$  uncertainty in the Greenland gas timescale at times of abrupt change. An exception is at 24 kyr ago (Dansgaard–Oeschger event 2), when methane and  $\delta^{18}\text{O}$  changes do not seem to be synchronous. We estimate the correlation uncertainty from the agreement of the methane records in Supplementary Fig. 5.

Speleothems can be radiometrically dated with U/Th and have smaller absolute age uncertainties than do annually resolved timescales in the glacial period<sup>37</sup>. Records of speleothem  $\delta^{18}\text{O}$  show many abrupt changes that have been tied to the Greenland climate record<sup>41,42</sup>. However, the physical link between  $\delta^{18}\text{O}$  variations in the caves and methane variations is not fully understood. Therefore, there is an additional and unknown correlation uncertainty in these comparisons. We compare WDC06A-7 with the new record from Hulu Cave, China, which is the best-dated speleothem record during this time interval. Comparisons can be made at only three times; our best estimate of the age differences is 100 yr or less.

The EDC timescale can be compared with the WDC06A-7 at a  $\sim 150$ -yr-long acid deposition event<sup>15,16</sup>. The two timescales agree within 100 yr, and we therefore do not adjust either timescale. The EDM1 timescale has been synchronized with the EDC timescale using sulphate matches<sup>43</sup>. The sulphate match that occurs during the 150-yr acid deposition event is marked in Fig. 2.

**Sea-salt sodium measurements.** Sea-salt sodium (ssNa) is the amount of Na that is of marine origin. The Na record was measured at the Trace Chemistry Laboratory at the Desert Research Institute. Na is one of many elements measured on the continuous-flow analysis system, which is coupled to two inductively coupled plasma mass spectrometers. The effective sampling resolution is  $\sim 1$  cm. Details of the analytical set-up are described elsewhere<sup>35,44–47</sup>. Sea-salt Na is calculated assuming Na/Ca mass ratios of 26.3 for marine aerosols and 0.562 for average crust composition<sup>48</sup>. Sea-salt Na can be influenced by volcanic activity if the ratio of Na to Ca is different from the sea water and crustal ratios; the spike 20 kyr ago is part of an Na-rich but Ca-poor volcanic event. We present ssNa concentration in the main text instead of ssNa flux because wet deposition dominates at higher accumulation rates<sup>49</sup>. For comparison, the ssNa flux is shown in Supplementary Fig. 7.

**Methane measurements.** The methane concentration was measured in discrete samples at Oregon State University (OSU) and Pennsylvania State University (PSU) using automated melt–refreeze extraction and gas chromatography, with final concentration values reported on the NOAA04 concentration scale<sup>50</sup>. OSU data are corrected for gravitational fractionation, solubility and blanks as described in ref. 37. The gravitation fractionation correction assumes that  $\delta^{15}\text{N}$  of  $\text{N}_2$  is 0.3‰, a value based on late-Holocene measurements.

PSU methods were modelled on the basis of the OSU melt–refreeze system. The major difference between the OSU and PSU methods is the extraction cylinders; glass at OSU and stainless steel at PSU. Using stainless steel cylinders carries the

added problem of a blank associated with CH<sub>4</sub> outgassing, which we have estimated to be  $19 \pm 8$  p.p.b. We have used a calculation similar to that derived in ref. 37, to estimate the amount of CH<sub>4</sub> left in the vessel after refreezing; we verified this using artificially degassed ice samples over which standard air was introduced and processed. These results indicate a 3.8% reduction in the measured headspace CH<sub>4</sub> value relative to the original trapped air, owing to solubility effects. The constant solubility and blank corrections were applied to all PSU data. In general, replicate samples from each depth were run on separate days to ensure that the final averaged data were not aliased by day-to-day instrument drifts. The average difference between replicate analyses of 1,316 individual depths run over 4 yr was  $7 \pm 8$  p.p.b. ( $1\sigma$ ). Finally, the PSU data were also corrected for gravitational fractionation by assuming that  $\delta^{15}\text{N}$  of N<sub>2</sub> is 0.3‰ throughout.

To ensure that the PSU and OSU CH<sub>4</sub> data sets can be accurately merged into a single record, we performed an inter-calibration exercise involving a 100-m section of the WDC06A core (400–500 m) where both labs sampled for CH<sub>4</sub> every 2 m. By interpolating the OSU data to compare with the PSU data, we determined the average difference between the two labs over this 100 m interval to be  $0.2 \pm 9.9$  p.p.b. ( $1\sigma$ ). This result implies that we can merge CH<sub>4</sub> data from the two labs without correcting for inter-laboratory offsets.

**Wilcoxon rank-sum test.** Initial inspection of the WDC isotope record showed that warming was pulsed. We applied a sliding Wilcoxon rank-sum statistical test<sup>51</sup> to identify periods of significant change. A figure of the *P* values, for each individual Wilcoxon rank-sum test, is shown in Supplementary Fig. 8. A dashed line indicates the effective critical *P* value. Insignificant *P* values are plotted in grey, and significant *P* values are plotted in colours that correspond to timespan (block size) as in Fig. 2. The Wilcoxon rank-sum test makes no assumption of normality within the data and has been shown to be robust when used in windowing algorithms for the identification of periods of significant change in climate data<sup>52</sup>. Our windowing algorithm can also be applied using the more common Student's *t*-test. Though parametric, such an implementation has the benefit of a well-established method for correcting the degrees of freedom for autocorrelation within the data<sup>53</sup>. Applying either statistical test, we identify nearly identical periods of significant change in the data sets.

**Climate modelling.** To assess the effects of changing sea-ice conditions on precipitation-weighted  $\delta^{18}\text{O}$  in Antarctica, we used the ECHAM4.6 climate model<sup>24</sup>, implemented with the water isotope module<sup>54</sup>. Model simulations used a horizontal resolution of T42 (2.8° latitude by 2.8° longitude) with 19 vertical levels. The ECHAM4.6 model has been shown to reproduce Antarctic conditions realistically in the modern climate<sup>13,55</sup>. We used the sea surface temperatures from the PMIP2 fully coupled model experiments<sup>25</sup> for LGM conditions ~21 kyr ago. Those sea surface temperatures are prescribed as a model boundary condition for the atmospheric model runs with ECHAM4.6. We used a modern Antarctic ice-sheet configuration because the LGM configuration remains poorly known.

Model experiments were designed to test the sensitivity of  $\delta^{18}\text{O}$  to changes in sea-ice extent. In the control experiment, sea ice forms at  $-1.7^\circ\text{C}$  and the model grid cell is set to 100% concentration below this threshold. The latitude of sea-ice coverage is decreased by lowering the ocean surface temperature threshold at which sea ice forms in the model. For the run with decreased sea ice, the freezing point was lowered from  $-1.7$  to  $-3.7^\circ\text{C}$ . The amount of sea-ice reduction is not zonally uniform around Antarctica because of asymmetric gradients in the prescribed sea surface temperature. We note that model sea surface temperatures do not change whether model sea ice is present or not. Newly formed open water in the run with reduced sea ice is below the freezing point.

**Integrated insolation.** We calculate integrated annual insolation at latitude  $65^\circ\text{S}$  following the tables prepared in ref. 26. We also calculate integrated 'summer' and 'winter' insolation using a cut-off of  $275\text{ W m}^{-2}$  (ref. 26; Supplementary Fig. 10).

32. Crosson, E. R. A cavity ring-down analyzer for measuring atmospheric levels of methane, carbon dioxide, and water vapor. *Appl. Phys. B* **92**, 403–408 (2008).
33. Dahl-Jensen, D., Gundestrup, N., Gogineni, S. P. & Miller, H. Basal melt at NorthGRIP modeled from borehole, ice-core and radio-echo sounder observations. *Ann. Glaciol.* **37**, 207–212 (2003).
34. Dansgaard, W. & Johnsen, S. J. A flow model and a time scale for the ice core from Camp Century, Greenland. *J. Glaciol.* **8**, 215–223 (1969).
35. Sigl, M. *et al.* A new bipolar ice core record of volcanism from WAIS Divide and NEMM and implications for climate forcing of the last 2000 years. *J. Geophys. Res.* **118**, 1151–1169 (2013).
36. Herron, M. M. & Langway, C. C. Firn densification: an empirical model. *J. Glaciol.* **25**, 373–385 (1980).
37. Mitchell, L. E., Brook, E. J., Sowers, T., McConnell, J. R. & Taylor, K. Multidecadal variability of atmospheric methane, 1000–1800 CE. *J. Geophys. Res.* **116**, G02007 (2011).
38. Huber, C. *et al.* Evidence for molecular size dependent gas fractionation in firn air derived from noble gases, oxygen, and nitrogen measurements. *Earth Planet. Sci. Lett.* **243**, 61–73 (2006).
39. Kobashi, T., Severinghaus, J. P., Brook, E. J., Barnola, J. M. & Grachev, A. M. Precise timing and characterization of abrupt climate change 8200 years ago from air trapped in polar ice. *Quat. Sci. Rev.* **26**, 1212–1222 (2007).
40. Severinghaus, J. P., Sowers, T., Brook, E. J., Alley, R. B. & Bender, M. L. Timing of abrupt climate change at the end of the Younger Dryas interval from thermally fractionated gases in polar ice. *Nature* **391**, 141–146 (1998).
41. Fleitmann, D. *et al.* Timing and climatic impact of Greenland interstadials recorded in stalagmites from northern Turkey. *Geophys. Res. Lett.* **36**, L19707 (2009).
42. Cheng, H. *et al.* Ice age terminations. *Science* **326**, 248–252 (2009).
43. Ruth, U. *et al.* "EDML1": a chronology for the EPICA deep ice core from Dronning Maud Land, Antarctica, over the last 150,000 years. *Clim. Past* **3**, 475–484 (2007).
44. Bisiaux, M. M. *et al.* Changes in black carbon deposition to Antarctica from two high-resolution ice core records, 1850–2000 AD. *Atmos. Chem. Phys.* **12**, 4107–4115 (2012).
45. McConnell, J. R. Continuous ice-core chemical analyses using inductively coupled plasma mass spectrometry. *Environ. Sci. Technol.* **36**, 7–11 (2002).
46. McConnell, J. R. *et al.* 20th-century industrial black carbon emissions altered arctic climate forcing. *Science* **317**, 1381–1384 (2007).
47. Pasteris, D. R., McConnell, J. R. & Edwards, R. High-resolution, continuous method for measurement of acidity in ice cores. *Environ. Sci. Technol.* **46**, 1659–1666 (2012).
48. Röthlisberger, R., Crosta, X., Abram, N. J., Armand, L. & Wolff, E. W. Potential and limitations of marine and ice core sea ice proxies: an example from the Indian Ocean sector. *Quat. Sci. Rev.* **29**, 296–302 (2010).
49. Alley, R. B. *et al.* Changes in continental and sea-salt atmospheric loadings in central Greenland during the most recent deglaciation: model-based estimates. *J. Glaciol.* **41**, 503–514 (1995).
50. Dlugokencky, E. J. *et al.* Conversion of NOAA atmospheric dry air CH<sub>4</sub> mole fractions to a gravimetrically prepared standard scale. *J. Geophys. Res.* **110**, D18306 (2005).
51. Wilcoxon, F. Individual comparisons by ranking methods. *Biom. Bull.* **1**, 80–83 (1945).
52. Mauget, S. A. Intra- to multidecadal climate variability over the continental United States: 1932–99. *J. Clim.* **16**, 2215–2231 (2003).
53. Bretherton, C. S., Widmann, M., Dymnikov, V. P., Wallace, J. M. & Blade, I. The effective number of spatial degrees of freedom of a time-varying field. *J. Clim.* **12**, 1990–2009 (1999).
54. Hoffmann, G., Werner, M. & Heimann, M. Water isotope module of the ECHAM atmospheric general circulation model: a study on timescales from days to several years. *J. Geophys. Res.* **103**, 16871–16896 (1998).
55. Ding, Q. H., Steig, E. J., Battisti, D. S. & Kuttel, M. Winter warming in West Antarctica caused by central tropical Pacific warming. *Nature Geosci.* **4**, 398–403 (2011).

## Contents

1. Modern climate and glaciological setting
2. Non-climate effects on the  $\delta^{18}\text{O}$  record
  - a. Ice sheet elevation change
  - b. Ice sheet advection
3. Ice and heat flow modeling
  - a. Calculation of basal melt rate
  - b. Inference of past accumulation rates
  - c. Inference of past surface temperatures
4. Sea-salt sodium
5. Climate modeling
6. Insolation

### 1. Modern climate and glaciological setting

The WAIS Divide ice core (WDC) was drilled at 79° 28.058' S, 112° 05.189' W, ~160 km east from the Byrd ice-core drilling site and ~24 km towards the Ross Sea from the current Ross-Amundsen ice-flow divide (Figure S1). The elevation is 1766 meters above sea level, average annual ice accumulation<sup>1</sup> is ~0.22 m, ice thickness is 3455 m, and the average annual surface temperature<sup>2</sup> is -30°C. The modern climate conditions are similar to those in central Greenland. Compared with the interior of East Antarctica, central West Antarctica is strongly influenced by intrusions of marine air<sup>3</sup>. There is a strong gradient in accumulation across the ice divide, with higher accumulation towards the Amundsen Sea and lower accumulation towards the Ross Sea<sup>4,5</sup>. This reflects the prevailing pattern of cyclonic activity over the Amundsen Sea<sup>3</sup>. There is no apparent climate divide corresponding to the physical ice divide<sup>4,6</sup>, so variations in the location of the ice divide through time should not significantly influence the climate at WDC.

Measurements of oxygen stable-isotope ratios ( $\delta^{18}\text{O}$ ) in multiple firn and ice cores from across West Antarctica show that WDC is well-situated to represent West Antarctic climate conditions as a whole; interannual  $\delta^{18}\text{O}$  variations in ice cores west and east of the ice divide are most highly correlated with other cores from their respective regions, while  $\delta^{18}\text{O}$  at WDC is equally well correlated with cores from both regions<sup>6</sup>. Annual isotope variations at WDC are significantly correlated ( $r=0.44$ ;  $p=0.004$ ) with local mean annual temperature, and decadal-scale trends show the same  $\delta^{18}\text{O}$ -temperature scaling<sup>7</sup>. Comparison with borehole temperature data<sup>2,7</sup> and independent estimates from bubble-number densities<sup>8</sup> further support the interpretation of low frequency  $\delta^{18}\text{O}$  variations as a measure of temperature. Investigation of the seasonal  $\delta^{18}\text{O}$  variations in the nearby ITASE 2000-01 ice core and other cores from West Antarctica show that sea-ice variations over the Amundsen Sea contribute significantly to  $\delta^{18}\text{O}$  variability<sup>6</sup>, consistent with the prevailing wind pattern and the strong marine influence at this site<sup>3</sup>.

## 2. Non-climate effects on the $\delta^{18}\text{O}$ record

### 2a. Ice Sheet Elevation Change

The site for WDC was selected near the ice-flow divide to minimize the influence of ice-sheet elevation change on the climate record; interior locations experience smaller ice thickness changes than coastal locations<sup>9,10</sup>. The best evidence for ice-sheet elevation change in the interior of the West Antarctic ice sheet comes from the Ohio Range, to the south of the WDC site at 1600 m elevation, and from Mt. Waesche to the north at 2000 m elevation<sup>9,11,12</sup>. Moraines at Mt. Waesche were ~50 m higher and trimlines in the Ohio Range were ~125 m higher, between 12 and 10 ka. The ~100 m of thinning throughout the Holocene occurred as the grounding line retreated by hundreds of km<sup>13,14</sup> and the accumulation rates were relatively stable. The elevation changes are much smaller than early model estimates<sup>15,16</sup> and comparable to the amount of elevation change inferred for interior East Antarctic sites<sup>17</sup>.

While there are no direct constraints on elevation changes prior to ~12 ka, the ice sheet either had to be at its high stand during the last glacial maximum or thicken in response to increasing accumulation rates during the deglaciation<sup>11,12</sup>. A thinner ice sheet in the interior during the Last Glacial Maximum (LGM) is difficult to reconcile with the large advance in the grounding line position. Numerical modeling of the WAIS suggests little ice-thickness change in the interior<sup>18,19</sup>.

Rapid changes in  $\delta^{18}\text{O}$  are particularly unlikely to have been caused by changes in ice sheet elevation. For instance, the 1.5‰ increase in  $\delta^{18}\text{O}$  between 20 and 18.8 ka would require >150 m of thinning in only 1200 years. This is a rate of ~0.12 m a<sup>-1</sup>. In comparison, the accumulation rate at the time was ~0.1 m a<sup>-1</sup> and had been reasonably constant for thousands of years (Figure S2). A rapid thinning of the ice sheet at the divide is also unlikely because of the long distance that perturbations at the grounding line need to propagate inland. There is also no evidence of large grounding line retreat at the LGM. Rates of thinning in response a retreat of the grounding line are highest near the coast and decrease inland<sup>9-11</sup>.

### 2b. Ice Advection

The modern divide is 1‰ enriched in  $\delta^{18}\text{O}$  relative to the ice-core site<sup>6</sup>. The divide position likely varied through time because no Raymond bump is observed in the internal radar stratigraphy<sup>4</sup> and it is currently migrating<sup>20</sup>. Using the modern horizontal ice flow velocity<sup>20</sup> of 3 m a<sup>-1</sup> at the core site and the modern isotope gradient (~0.005‰/km), we estimate the effect of ice advection to be ~0.15‰ per 1000 years over the last one to two thousand years. This rate was likely smaller in the past because the ice would have been closer to the divide where the ice velocity is lower. The ice-flow velocity was also likely smaller in the glacial period when accumulation rates were lower. While ice advection is unlikely to substantially affect the glacial-interglacial changes, the advection effect may be important during periods of relatively stable isotopic values, such as the Holocene.

## 3. Ice and heat flow modeling

Although a full analysis of past surface temperature and accumulation rate is beyond the scope of this Letter, we make quantitative estimates of both to calculate the gas-age ice-age difference ( $\Delta\text{age}$ ) and compare the accuracy of the annually resolved portion of the WDC06A-7 timescale

to Greenland and speleothem timescales. Two features unique to WDC among Antarctic ice<sup>191</sup> cores allow our temperature and accumulation histories to have good accuracy:

- 1) The magnitude of the glacial-interglacial temperature change is preserved in the borehole temperature profile, allowing a first-order calibration of the isotope-temperature relationship.
- 2) The annually-resolved timescale can be used to directly infer the accumulation rate without assuming a particular relationship with temperature.

We use a transient one-dimensional ice-flow model to compute the vertical-velocity profile:

$$w(z) = -(\dot{b} - \dot{m} - \dot{H})\psi(z) - \dot{m} - \left(\frac{\rho_i}{\rho(z)} - 1\right)\dot{b} \quad (1)$$

where  $z$  is the height above the bed,  $\dot{b}$  is the accumulation rate,  $\dot{m}$  is the melt rate,  $\dot{H}$  is the rate of ice-thickness change,  $\rho_i$  is the density of ice,  $\rho(z)$  is the density profile and  $\psi(z)$  is the vertical velocity shape function computed as:

$$\psi(z) = \left(f_B z + \frac{1}{2}(1 - f_B)\frac{z^2}{h}\right) / \left(H - \frac{1}{2}h(1 - f_B)\right) \quad \text{for } h \geq z > 0 \quad (2a)$$

$$\psi(z) = \left(z - \frac{1}{2}h(1 - f_B)\right) / \left(H - \frac{1}{2}h(1 - f_B)\right) \quad \text{for } H \geq z > h \quad (2b)$$

following Dahl-Jensen et al.<sup>21</sup> where  $h$  is the distance above bedrock of the Dansgaard-Johnsen<sup>22</sup> kink height,  $f_B$  is the fraction of the horizontal surface velocity due to sliding over the bed, and  $H$  is the ice thickness. Firn compaction is incorporated through the right hand term in equation 1 and assumes a density profile that does not vary with time.

The heat equation following Cuffey and Paterson<sup>23</sup> is:

$$\rho c_p \frac{\partial T}{\partial t} = \frac{\partial}{\partial z} \left( k \frac{\partial T}{\partial z} \right) - \rho c_p w \frac{\partial T}{\partial z} + Q \quad (3)$$

where  $c_p$  is the heat capacity,  $T$  is temperature,  $k$  is the thermal conductivity, and  $Q$  is the heat production term. The firn density profile is modeled using the Herron and Langway<sup>27</sup> model matched to modern measurements<sup>28</sup> to assure a smooth vertical velocity profile. Values of  $c_p$  and  $k$  are calculated at each time step following standard relationships in Cuffey and Paterson<sup>23</sup>.

The ice-flow and heat-flow models are not explicitly coupled; the ice-flow model is used to calculate the vertical velocity for the heat-flow model but the temperature profile is not incorporated in the calculation of the vertical velocity. The ice thickness was held constant. The basal melt rate is prescribed and does not vary in time; the ice/bed interface is always at the melting point. Any water produced by melt at the bed is assumed to drain away instantaneously.

### 3a. Basal Melt Rate

The first indication of a high basal melt rate at WDC was the young ice at depth and the correspondingly thick (~1cm) annual layers. Similar to the situation at North GRIP<sup>21</sup>, the basal melting reduces the vertical strain of layers as ice is removed through melting rather than horizontal shear. The melting also steepens the basal temperature gradient as the colder ice near

the surface is advected towards the bed more quickly. The borehole temperature gradient, measured in December 2011, allows an estimate of basal melting. Rearranging equation 3 to solve for  $w$ :

$$w = \left[ \kappa \left( \frac{\partial T^2}{\partial z^2} \right) - b\kappa \left( \frac{\partial T}{\partial z} \right)^2 - \frac{\partial T}{\partial t} + \frac{1}{\rho c_p} Q \right] / \frac{\partial T}{\partial z} \quad (4)$$

where  $\kappa$  is the thermal diffusivity and  $b$  is an exponent that relates the thermal conductivity to temperature<sup>23</sup>. We evaluate these terms at 3300 m. The first two terms in the brackets can be measured from the borehole temperature profile:  $\partial T/\partial z$  is  $34.8 \times 10^{-3} \text{ K}^{-1}\text{m}$  and  $\partial^2 T/\partial z^2$  is  $0.029 \times 10^{-3} \text{ K}^{-1}\text{m}^2$ . A model must be used to estimate the second two terms; both are small compared to the first two terms. At 3300 m depth, the vertical velocity is  $2.1 \text{ cm a}^{-1}$ . It is unlikely this large of a vertical flux can be removed through horizontal shear in the remaining  $\sim 160 \text{ m}$  of the ice column, and we therefore conclude that the basal melt rate is likely between  $0.7$  and  $1.5 \text{ cm a}^{-1}$ .

### 3b. Accumulation Rates

The accumulation rate is calculated from the depth-age relationship using the ice-flow model described above. A constant ice thickness was specified because the thickness change near the divide was probably small ( $\sim 100 \text{ m}$ ) and the timing of thickening and thinning is not well constrained; a  $100 \text{ m}$  thickness change would alter the inferred accumulation rate by  $\sim 3\%$ . A constant basal melt rate of  $1 \text{ cm a}^{-1}$  and non-divide flow conditions, represented by a Dansgaard-Johnsen kink height of  $0.2H$ , are assumed. We also prescribe a sliding fraction of  $0.5$  of the surface velocity, which approximates effects of both basal sliding and enhanced shear near the bed, neither of which are well constrained. To assess the possible range of inferred accumulation rates, we also use sliding fractions of  $0.15$  and  $0.9$  (Figure S2). The inferred accumulation rate is only slightly affected for the Holocene part of the record but is up to  $16\%$  different for the oldest part of the record ( $29.6 \text{ ka}$ ). Because the thinning function varies smoothly, the uncertainty in the timing of the changes in the accumulation rate is only weakly affected by the uncertainty in the magnitude of the accumulation rate. The main uncertainty in identifying the timing of accumulation rate changes is the uncertainty in the timescale itself. During the deglacial transition, the uncertainty in the interpretation is estimated at  $8\%$  (section 4b). The yellow shading in Figure 3 of the main text shows this uncertainty.

The inferred accumulation rate is an “ice-core accumulation rate” rather than a “climate accumulation rate.” Because ice at depth originated upstream from the core site, the annual layer thicknesses record both temporal and spatial gradients in the accumulation rate. The current divide receives approximately  $30\%$  more accumulation than the ice core site<sup>5</sup>. Assuming that the accumulation gradient was similar in the past, this results in a gradient of  $1.3\%$  per km. Modern ice-flow velocities at the ice-core site are  $\sim 3 \text{ m a}^{-1}$  and were likely lower in the past. Therefore, accumulation changes from ice-advection may amount to  $\sim 2\%$  per 1000 years. However, the effect is cumulative so the snow that fell at the LGM could have been at a location, such as the modern divide, that received  $\sim 30\%$  more accumulation than the core site without any change in climate.

We do not develop an accumulation rate derived from the temperature estimated from  $\delta^{18}\text{O}$ . The relationship between stable isotopes and accumulation rate in West Antarctica does not follow a

simple relationship that would justify such a calculation. For instance, in the modern climate<sup>193</sup> Byrd is 2‰ lighter in  $\delta^{18}\text{O}$  than WAIS Divide but receives 40% less accumulation. While the accumulation record from WDC does show a general correspondence to  $\delta^{18}\text{O}$  and thus local temperature at orbital timescales, there are significant differences between the isotope and accumulation records. Foremost is the abrupt accumulation increase of  $37\pm 10\%$  between 12.0 and 11.6 ka during the double isotope peak of Antarctic Isotope Maximum (AIM) 0 (Figure S2). The uncertainty bounds are the additive effects of possible ice-thickness change (3%), ice advection through an accumulation gradient (3%), and annual-layer interpretation (4%). Abrupt changes in accumulation cannot be recognized in other Antarctic cores because their timescales lack sufficient resolution. The timing of the abrupt accumulation increase is coincident within uncertainty with a minimum in dust concentration at three sites on the East Antarctic plateau<sup>24</sup> (EDC, Dome B, Komosmolskaia) raising the possibility that the atmospheric circulation changed during this period across much of Antarctica.

### 3c. Surface temperature:

The surface temperature history is derived as a linear function of the  $\delta^{18}\text{O}$  record, with calibration coefficients determined by optimizing the match between model and measured borehole temperature profiles. For a range of ice-dynamical scenarios, results suggest that the Last Glacial Maximum was 7 to 9 °C colder than present. Work on this topic is in progress and full results and analyses will be reported in a future publication. Figure S3 illustrates results for simplified scenarios with a range of temperature-change magnitudes.

## 4. Sea-salt sodium

The concentration of sea-salt Sodium (ssNa) in surface snow decreases with distance from the ocean and elevation above sea level<sup>25</sup>. However, concentrations also vary regionally indicating the importance of both the source region and the intensity of transport on the ssNa concentration at a specific location<sup>26</sup>. While ssNa is clearly a proxy for oceanic and atmospheric conditions, it is debated whether ssNa is a better indicator of sea-ice production or atmospheric circulation. Increasing ssNa concentrations at Siple Dome throughout the Holocene have been interpreted to indicate increasing incursions of marine air as the grounding line of the Ross ice sheet retreated<sup>27</sup>. The large Holocene increase at Siple Dome (modern levels are higher than glacial levels) is unique among long ice-core records (WDC, EDC<sup>28,29</sup>, EDML<sup>30</sup>, and Taylor Dome<sup>27</sup>); however, the glacial record is quite similar to that at WDC, with a large decrease during the deglaciation.

Different interpretations of ssNa may be due to both different locations of ice cores and different timescales of analysis. The use of ssNa as a sea-ice proxy has focused on interior ice-core sites at multi-millennial timescales; the use of ssNa as an atmospheric-circulation proxy has focused on coastal ice-core sites at annual to decadal timescales. At the centennial to millennial timescales we are investigating at WDC, we favor the interpretation of ssNa as a sea-ice proxy<sup>29,31</sup>. The large decrease in ssNa during the deglaciation is difficult to explain on the basis of decreased strength of atmospheric circulation; model results do not support a large change in wind strength<sup>32</sup> and instead predict decreased ssNa deposition at the LGM due to the increased distance to open water<sup>33</sup>. Atmospheric circulation undoubtedly is also important. In fact, sea ice and atmospheric circulation are strongly correlated in the modern climate of the Ross and

Amundsen Seas<sup>34</sup>. Because of the uncertainties in  $\delta^{18}\text{O}$  as a sea-ice proxy, we do not attempt a detailed sea-ice reconstruction. The strong relationship with  $\delta^{18}\text{O}$  at times of abrupt change may indicate significant sea-ice decreases, changes in atmospheric circulation and transport, or both.<sup>194</sup>

## 5. Climate Modeling

To assess the effects of changing sea-ice conditions on the  $\delta^{18}\text{O}$  of Antarctica, we used the ECHAM 4.6 climate model<sup>35</sup>, implemented with the water isotope module<sup>36</sup>. Model simulations used a horizontal resolution of T42 (2.8° latitude by 2.8° longitude) with 19 vertical levels. The ECHAM 4.6 model has been shown to realistically reproduce variability in Antarctic climate and water isotope ratios in precipitation given observed sea surface temperature boundary conditions<sup>7,37</sup>. In this paper, we use sea surface temperatures from the PMIP2 fully-coupled model experiments<sup>38</sup> for LGM ~21 ka conditions. Those sea surface temperatures are prescribed as a model boundary condition for the atmospheric model runs with ECHAM4.6. We used a modern Antarctic Ice Sheet configuration because the LGM configuration remains poorly known; for example, the ICE-5g reconstruction<sup>39</sup> has greatly increased elevations at interior locations in West Antarctica that exceed estimates from geological observations and recent modeling work<sup>40</sup>. Using the modern topography underestimates the ice sheet elevation in the Ross Sea sector but, the effect of a thinner Ross Ice Sheet on WDC is relatively small because the precipitation received at WDC is predominantly from the Amundsen Sea<sup>3</sup>.

Model experiments were designed to test the sensitivity of  $\delta^{18}\text{O}$  to changes in the sea-ice extent. In the control experiment, sea ice forms at  $-1.7\text{ }^\circ\text{C}$  and the model grid cell is set to 100% concentration below this threshold. The latitude of sea ice coverage is decreased by lowering the ocean surface temperature threshold at which sea ice forms in the model. For the decreased sea ice run, the freezing point was artificially lowered from  $-1.7\text{ }^\circ\text{C}$  to  $-3.7\text{ }^\circ\text{C}$ . The amount of sea ice reduction is not zonally uniform around Antarctica because of asymmetric gradients in the prescribed sea surface temperature (SST). It is important to note that model SSTs do not change whether model sea ice is present or not; newly formed open water in the reduced sea-ice run is below the freezing point. We have refrained from modeling the change in sea ice due to orbital forcing because of the known limitations in modeling sea ice correctly. Roche et al.<sup>41</sup> show that different models simulate very different amounts of sea-ice for both the modern and LGM conditions. Furthermore, they show that the amplitude of the seasonal cycle of sea-ice growth for the LGM is underestimated by all models.

The difference between 30-year integrations of the control run and the sea-ice reduction run are shown in Figure 4. In West Antarctica, the  $\delta^{18}\text{O}$  is enriched across the entire ice sheet. In East Antarctica, there is a sharp contrast between the enriched  $\delta^{18}\text{O}$  along the coast and unchanged or depleted  $\delta^{18}\text{O}$  in the interior. The deep ice core positions are also shown in Figure 4. WDC is located in the enriched  $\delta^{18}\text{O}$  signal initiating from the Amundsen Sea region, just as expected from the modern trajectory of marine air masses into West Antarctica<sup>3</sup>.

The magnitude of the  $\delta^{18}\text{O}$  anomalies in East Antarctica vary inversely with measures of a site's isolation from marine influence, such as elevation and distance from the coast. Most of the East Antarctic core sites are located in the strong gradient between positive coastal anomalies and zero or negative interior anomalies. The inland extent of the positive anomalies depends on the

horizontal resolution in the model, which smoothes the steep coastal topography. The anomalies at any given position are also model dependent, but higher-resolution (T106) model experiments show that the pattern of coastal enrichment and little interior change is robust. Law Dome is the lone East Antarctic core not in the interior and seemingly well-positioned to record coastal changes; however the accumulation rate during the LGM was inferred to be less than 10% of the modern value<sup>42</sup>. This suggests that the climate during the LGM was more similar to the East Antarctic plateau than to the current maritime climate<sup>42</sup>. Like Siple Dome, Law Dome highlights the difficulties associated with interpreting the climate records of coastal domes.

## 6. Insolation

Figure 3 shows integrated annual insolation as calculated by Huybers<sup>43</sup>. Figure S10 shows the integrated insolation on “summer” and “winter” days, as defined by a threshold of 275 W m<sup>-2</sup> of insolation following Huybers<sup>43</sup>. At ~28 ka, the integrated annual insolation begins increasing as the integrated summer insolation increases and integrated winter insolation decreases. Therefore, not only is integrated annual insolation increasing, it is increasing more in the summer when there is the greatest potential to warm the ocean and melt sea ice because of the lower albedo. The increase in integrated summer insolation is related to the increasing summer duration as discussed by Huybers and Denton<sup>44</sup>. They primarily discuss the impact of the lengthening summer on radiative equilibrium, which is a mechanism for increasing surface temperature, but note that sea ice may be affected as well. Future work is needed to determine what forcing sea ice is most sensitive too, but both integrated summer insolation and summer duration show that local forcing were increasing significantly at the onset of warming at WDC.

## References

- 1 Banta, J. R., McConnell, J. R., Frey, M. M., Bales, R. C. & Taylor, K. Spatial and temporal variability in snow accumulation at the West Antarctic Ice Sheet Divide over recent centuries. *Journal of Geophysical Research-Atmospheres* **113**, doi:D23102 (2008).
- 2 Orsi, A. J., Cornuelle, B. D. & Severinghaus, J. P. Little Ice Age cold interval in West Antarctica: Evidence from borehole temperature at the West Antarctic Ice Sheet (WAIS) Divide. *Geophysical Research Letters* **39**, doi:10.1029/2012gl051260 (2012).
- 3 Nicolas, J. P. & Bromwich, D. H. Climate of West Antarctica and Influence of Marine Air Intrusions. *Journal of Climate* **24**, 49-67, doi:10.1175/2010jcli3522.1 (2011).
- 4 Neumann, T. A. *et al.* Holocene accumulation and ice sheet dynamics in central West Antarctica. *Journal of Geophysical Research-Earth Surface* **113**, doi:F02018 (2008).
- 5 Morse, D. L., Blankenship, D. D., Waddington, E. D. & Neumann, T. A. A site for deep ice coring in West Antarctica: results from aerogeophysical surveys and thermo-kinematic modeling. *Annals of Glaciology, Vol 35* **35**, 36-44, doi:10.3189/172756402781816636 (2002).
- 6 Küttel, M., Steig, E. J., Ding, Q. H., Monaghan, A. J. & Battisti, D. S. Seasonal climate information preserved in West Antarctic ice core water isotopes: relationships to temperature, large-scale circulation, and sea ice. *Climate Dynamics* **39**, 1841-1857, doi:10.1007/s00382-012-1460-7 (2012).
- 7 Steig, E. J. *et al.* Recent climate and ice-sheet changes in West Antarctica compared with the past 2,000 years. *Nature Geoscience* **6**, 372-375, doi: 10.1038/NGEO1778 (2013).
- 8 Fegyveresi, J. M. *et al.* Late-Holocene climate evolution at the WAIS Divide site, West Antarctica: bubble number-density estimates. *Journal of Glaciology* **57**, 629-638 (2011).

- 9 Ackert, R. P., Mukhopadhyay, S., Parizek, B. R. & Borns, H. W. Ice elevation near the West Antarctic Ice Sheet divide during the Last Glaciation. *Geophysical Research Letters* **34**, 6, doi:L21506 10.1029/2007gl031412 (2007).
- 10 Stone, J. O. *et al.* Holocene deglaciation of Marie Byrd Land, West Antarctica. *Science* **299**, 99-102 (2003).
- 11 Ackert, R. P. *et al.* Measurements of past ice sheet elevations in interior West Antarctica. *Science* **286**, 276-280, doi:10.1126/science.286.5438.276 (1999).
- 12 Steig, E. J. *et al.* in R. Alley and R. Bindshadler Vol. **77** (ed The West Antarctic Ice Sheet: Behavior and Environment) 75-90 (Antarctic Research Series, 2001).
- 13 Anderson, J. B., Shipp, S. S., Lowe, A. L., Wellner, J. S. & Mosola, A. B. The Antarctic Ice Sheet during the Last Glacial Maximum and its subsequent retreat history: a review. *Quaternary Science Reviews* **21**, 49-70, doi:10.1016/s0277-3791(01)00083-x (2002).
- 14 Conway, H., Hall, B. L., Denton, G. H., Gades, A. M. & Waddington, E. D. Past and future grounding-line retreat of the West Antarctic Ice Sheet. *Science* **286**, 280-283 (1999).
- 15 Huybrechts, P. Sea-level changes at the LGM from ice-dynamic reconstructions of the Greenland and Antarctic ice sheets during the glacial cycles. *Quaternary Science Reviews* **21**, 203-231, doi:10.1016/s0277-3791(01)00082-8 (2002).
- 16 Denton, G. H. & Hughes, T. J. Reconstructing the Antarctic Ice Sheet at the Last Glacial Maximum. *Quaternary Science Reviews* **21**, 193-202, doi:10.1016/s0277-3791(01)00090-7 (2002).
- 17 Parrenin, F. *et al.* 1-D-ice flow modelling at EPICA Dome C and Dome Fuji, East Antarctica. *Climate of the Past* **3**, 243-259 (2007).
- 18 Pollard, D. & DeConto, R. M. Modelling West Antarctic ice sheet growth and collapse through the past five million years. *Nature* **458**, 329-U389, doi:10.1038/nature07809 (2009).
- 19 Whitehouse, P. L., Bentley, M. J. & Le Brocq, A. M. A deglacial model for Antarctica: geological constraints and glaciological modelling as a basis for a new model of Antarctic glacial isostatic adjustment. *Quaternary Science Reviews* **32**, 1-24, doi:10.1016/j.quascirev.2011.11.016 (2012).
- 20 Conway, H. & Rasmussen, L. A. Recent thinning and migration of the Western Divide, central West Antarctica. *Geophysical Research Letters* **36**, doi:L12502 10.1029/2009gl038072 (2009).
- 21 Dahl-Jensen, D., Gundestrup, N., Gogineni, S. P. & Miller, H. Basal melt at NorthGRIP modeled from borehole, ice-core and radio-echo sounder observations. *Annals of Glaciology, Vol 37* **37**, 207-212, doi:10.3189/172756403781815492 (2003).
- 22 Dansgaard, W. & Johnsen, S. J. A flow model and a time scale for the ice core from Camp Century, Greenland. *Journal of Glaciology* **8**, 215-223 (1969).
- 23 Cuffey, K. M. & Paterson, W. S. B. *The Physics of Glaciers*. Fourth Edition edn, (2010).
- 24 Delmonte, B. *et al.* Dust size evidence for opposite regional atmospheric circulation changes over east Antarctica during the last climatic transition. *Climate Dynamics* **23**, 427-438, doi:10.1007/s00382-004-0450-9 (2004).
- 25 Bertler, N. *et al.* Snow chemistry across Antarctica. *Annals of Glaciology, Vol 41, 2005* **41**, 167-179 (2005).
- 26 Kaspari, S., Dixon, D. A., Sneed, S. B. & Handley, M. J. Sources and transport pathways of marine aerosol species into West Antarctica. *Annals of Glaciology, Vol 41 2005* **41**, 1-9, doi:10.3189/172756405781813221 (2005).
- 27 Mayewski, P. A. *et al.* West Antarctica's Sensitivity to Natural and Human Forced Climate Change over the Holocene. *Journal of Quaternary Science* (in press).
- 28 Rothlisberger, R. *et al.* Dust and sea salt variability in central East Antarctica (Dome C) over the last 45 kyrs and its implications for southern high-latitude climate. *Geophysical Research Letters* **29**, doi:10.1029/2002gl015186 (2002).

- 29 Wolff, E. W. *et al.* Southern Ocean sea-ice extent, productivity and iron flux over the past eight  
glacial cycles. *Nature* **440**, 491-496, doi:10.1038/nature04614 (2006).
- 30 Fischer, H. *et al.* Reconstruction of millennial changes in dust emission, transport and regional  
sea ice coverage using the deep EPICA ice cores from the Atlantic and Indian Ocean sector of  
Antarctica. *Earth and Planetary Science Letters* **260**, 340-354, doi:10.1016/j.epsl.2007.06.014  
(2007).
- 31 Rothlisberger, R., Crosta, X., Abram, N. J., Armand, L. & Wolff, E. W. Potential and limitations of  
marine and ice core sea ice proxies: an example from the Indian Ocean sector. *Quaternary  
Science Reviews* **29**, 296-302, doi:10.1016/j.quascirev.2009.10.005 (2010).
- 32 Rojas, M. *et al.* The Southern Westerlies during the last glacial maximum in PMIP2 simulations.  
*Climate Dynamics* **32**, 525-548, doi:10.1007/s00382-008-0421-7 (2009).
- 33 Mahowald, N. M., Lamarque, J. F., Tie, X. X. & Wolff, E. Sea-salt aerosol response to climate  
change: Last Glacial Maximum, preindustrial, and doubled carbon dioxide climates. *Journal of  
Geophysical Research-Atmospheres* **111**, doi:10.1029/2005jd006459 (2006).
- 34 Holland, P. R. & Kwok, R. 2012. Wind-driven trends in Antarctic sea-ice drift. *Nature Geoscience*,  
**5** 872-875.
- 35 Roeckner, E. *et al.* Vol. 218 (Max Planck Institut für Meteorologie Report, 1996).
- 36 Hoffmann, G., Werner, M. & Heimann, M. Water isotope module of the ECHAM atmospheric  
general circulation model: A study on timescales from days to several years. *Journal of  
Geophysical Research-Atmospheres* **103**, 16871-16896, doi:10.1029/98jd00423 (1998).
- 37 Ding, Q. H., Steig, E. J., Battisti, D. S. & Kuttel, M. Winter warming in West Antarctica caused by  
central tropical Pacific warming. *Nature Geoscience* **4**, 398-403, doi:10.1038/ngeo1129 (2011).
- 38 Braconnot, P. *et al.* Results of PMIP2 coupled simulations of the Mid-Holocene and Last Glacial  
Maximum - Part 1: experiments and large-scale features. *Climate of the Past* **3**, 261-277 (2007).
- 39 Peltier, W. R. Global glacial isostasy and the surface of the ice-age earth: The ice-5G (VM2)  
model and grace. *Annual Review of Earth and Planetary Sciences* **32**, 111-149,  
doi:10.1146/annurev.earth.32.082503.144359 (2004).
- 40 Ackert, R. P. *et al.* Controls on interior West Antarctic Ice Sheet Elevations: inferences from  
geologic constraints and ice sheet modeling. *Quaternary Science Reviews* **65**, 26-38 (2013).
- 41 Roche, D. M., Crosta, X. & Renssen, H. Evaluating Southern Ocean sea-ice for the Last Glacial  
Maximum and pre-industrial climates: PMIP-2 models and data evidence. *Quaternary Science  
Reviews* **56**, 99-106, doi:10.1016/j.quascirev.2012.09.020 (2012).
- 42 Van Ommen, T. D., Morgan, V. & Curran, M. A. J. Deglacial and Holocene changes in  
accumulation at Law Dome, East Antarctica. *Annals of Glaciology, Vol 39, 2005* **39**, 359-365,  
doi:10.3189/172756404781814221 (2004).
- 43 Huybers, P. Early Pleistocene glacial cycles and the integrated summer insolation forcing.  
*Science* **313**, 508-511, doi:10.1126/science.1125249 (2006).
- 44 Huybers, P. & Denton, G. Antarctic temperature at orbital timescales controlled by local summer  
duration. *Nature Geoscience* **1**, 787-792, doi:10.1038/ngeo311 (2008).

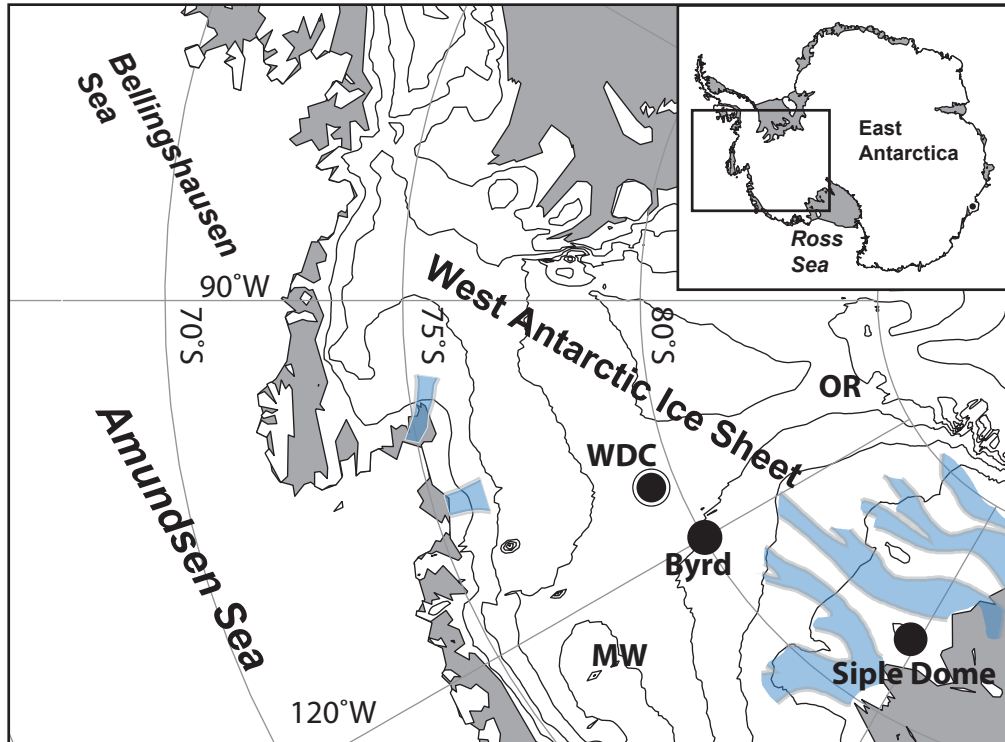


Figure S1. Map of West Antarctica.

Locations of the WDC, Byrd, and Siple Dome ice cores and the Ohio Range (OR) and Mt. Waesche (MW). Ice shelves are shown in gray; Siple Coast and Amundsen Sea ice streams are shown by blue shading. Contour interval is 500 m.

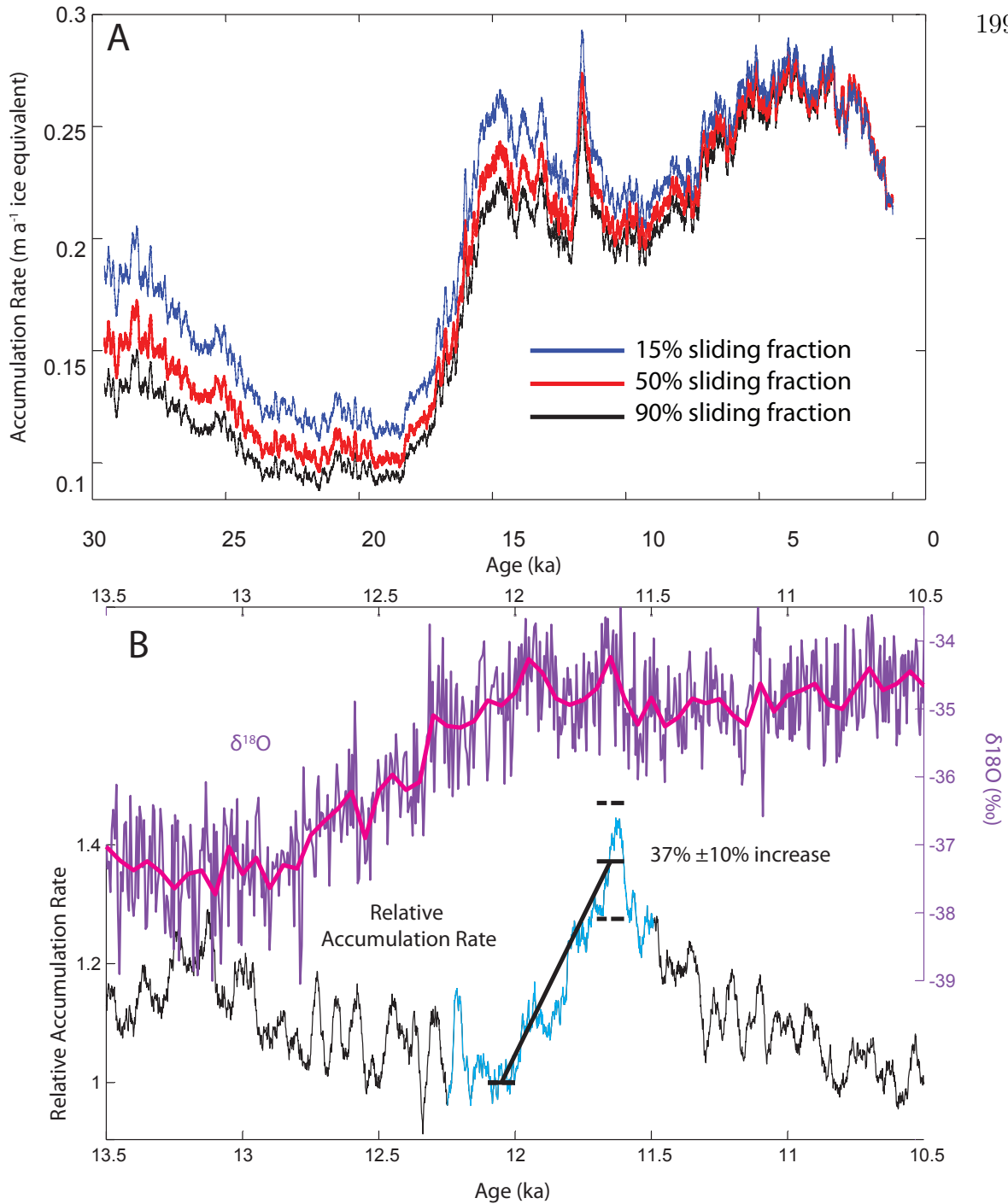


Figure S2: Accumulation Rate History.

(A) Inferred accumulation rate using a one-dimensional ice-flow model and three different vertical-strain profiles. The red profile is preferred. Accumulation rates shown are the 100-year running average.

(B) 31-year running average of accumulation rate relative to 100-year average between 12.1 and 12.0 ka. The relative accumulation rate increase between 12.1 to 12.0 ka and 11.7 to 11.6 ka is shown with the thick black line. The uncertainty bounds are the additive effects of possible ice-thickness change (3%), ice advection through an accumulation gradient (3%), and annual-layer interpretation uncertainties (4%). The annual-layer interpretation for the section in light blue (1940 to 2020 m) was confirmed with multi-parameter chemistry measurements; black is from ECM only. The ECM-only interpretation from 1940 to 2020 m found 19 fewer years (2.5%) and the same magnitude of accumulation rate change. Note that trends in relative accumulation rate are less certain away from the abrupt increase.

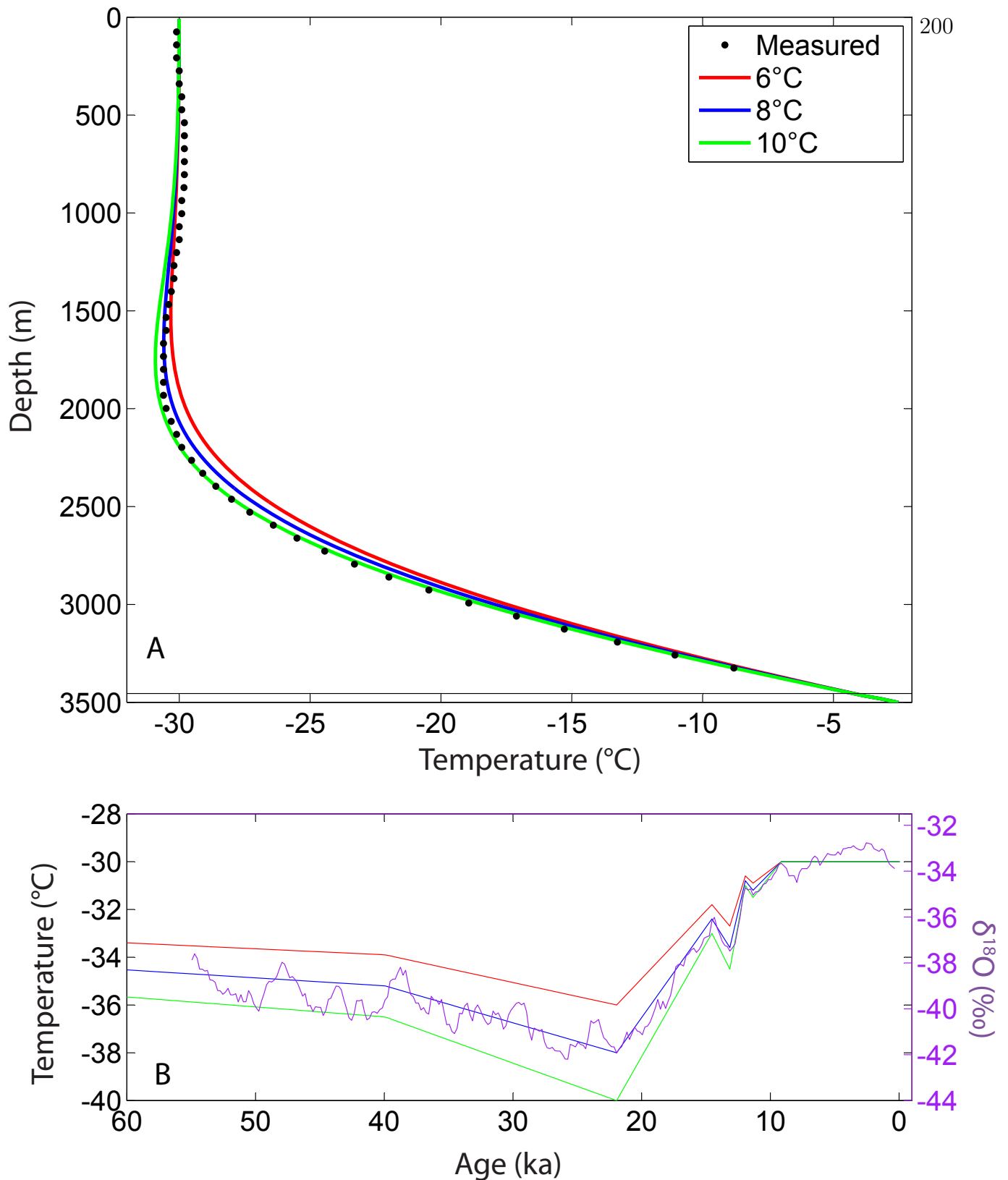


Figure S3. Borehole Temperature Profile and Surface Temperature History.

Match of modeled temperature profiles (A) with surface temperature histories shown in (B) to the measured borehole temperature profile. Legends in (A) indicate the magnitude of the glacial-interglacial temperature change used in the model runs.

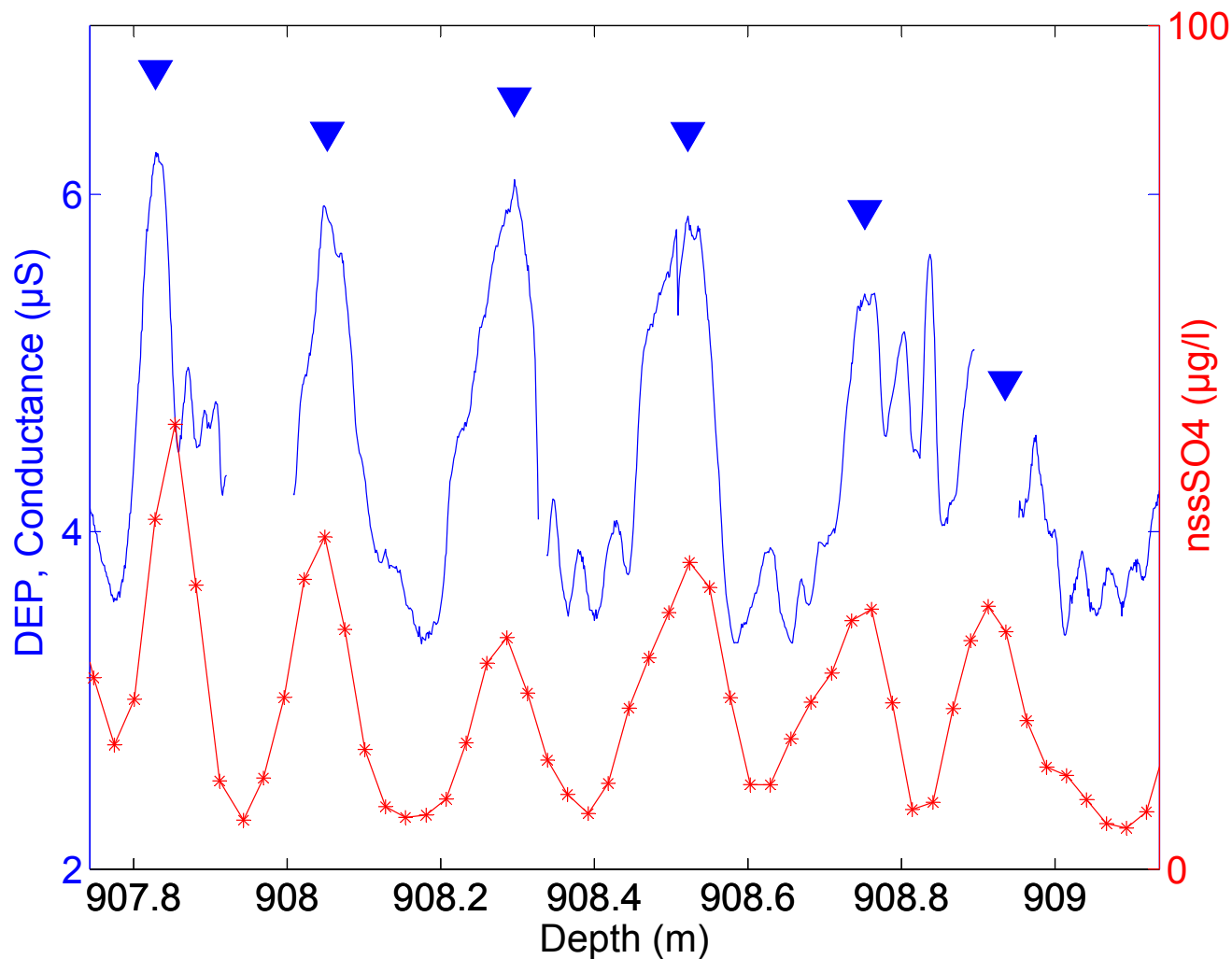


Figure S4. Brittle Ice Annual Signals

Comparison of electrical (dielectric profiling) and chemical (non-sea-salt sulfate) annual signals in a section of brittle ice that was rated “very poor,” the worst rating for ice quality. Blue triangles are annual layer picks.

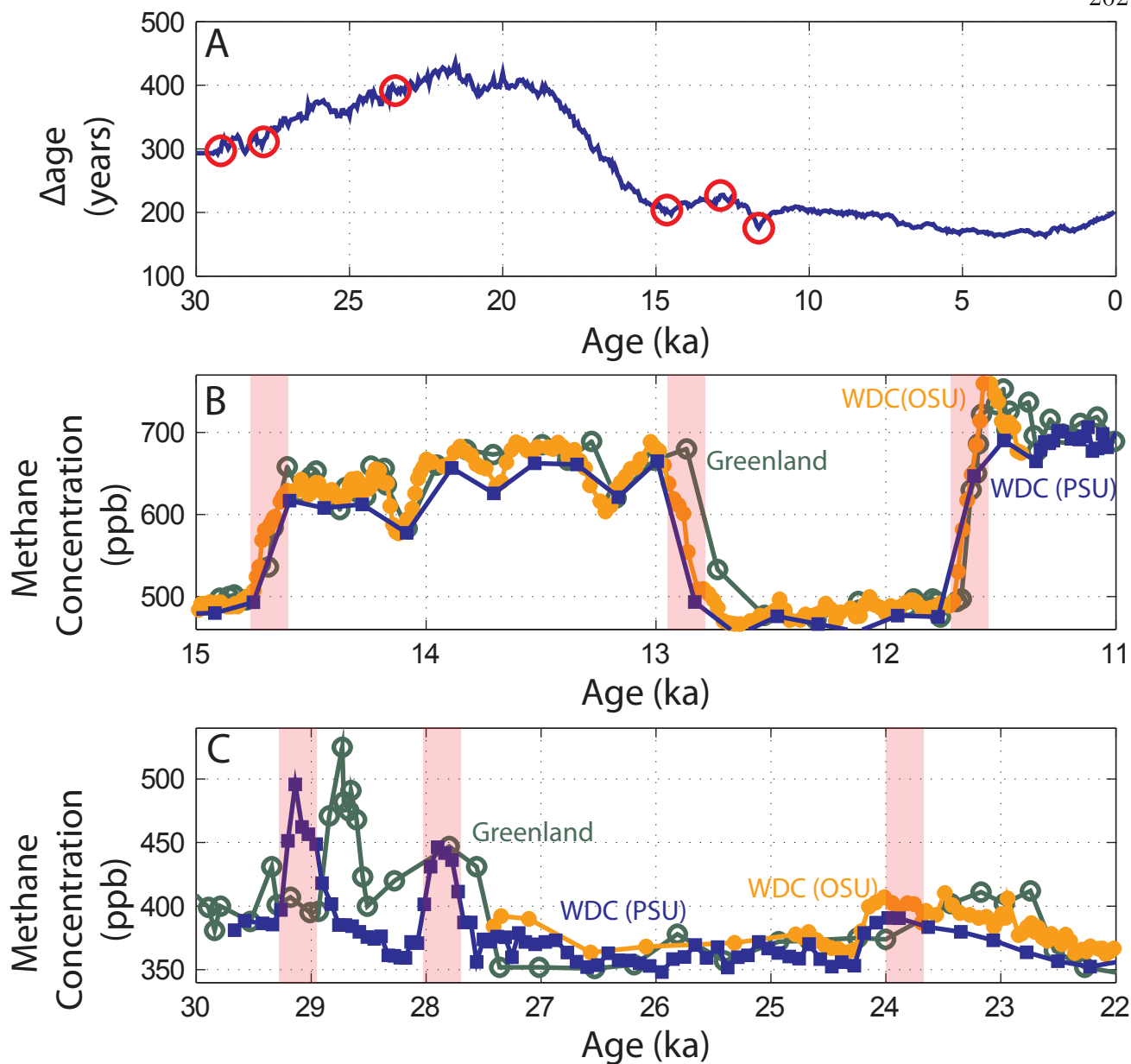


Figure S5: Assessment of WDC06A-7 Timescale via atmospheric methane.

A)  $\Delta$ age for WDC calculated with Herron and Langway<sup>27</sup> firn densification model using the inferred accumulation rate and temperature histories. Circles are the  $\Delta$ age values at the times of abrupt variations in methane used to compare timescales.

B and C) WDC methane on WDC06A-7 minus  $\Delta$ age and Greenland methane composite on GICC05 gas timescale<sup>33</sup>. Red vertical bars correspond to the times of the red circles in A where the  $\Delta$ age was calculated. The age differences between the WDC and Greenland timescales are shown in Figure S6.

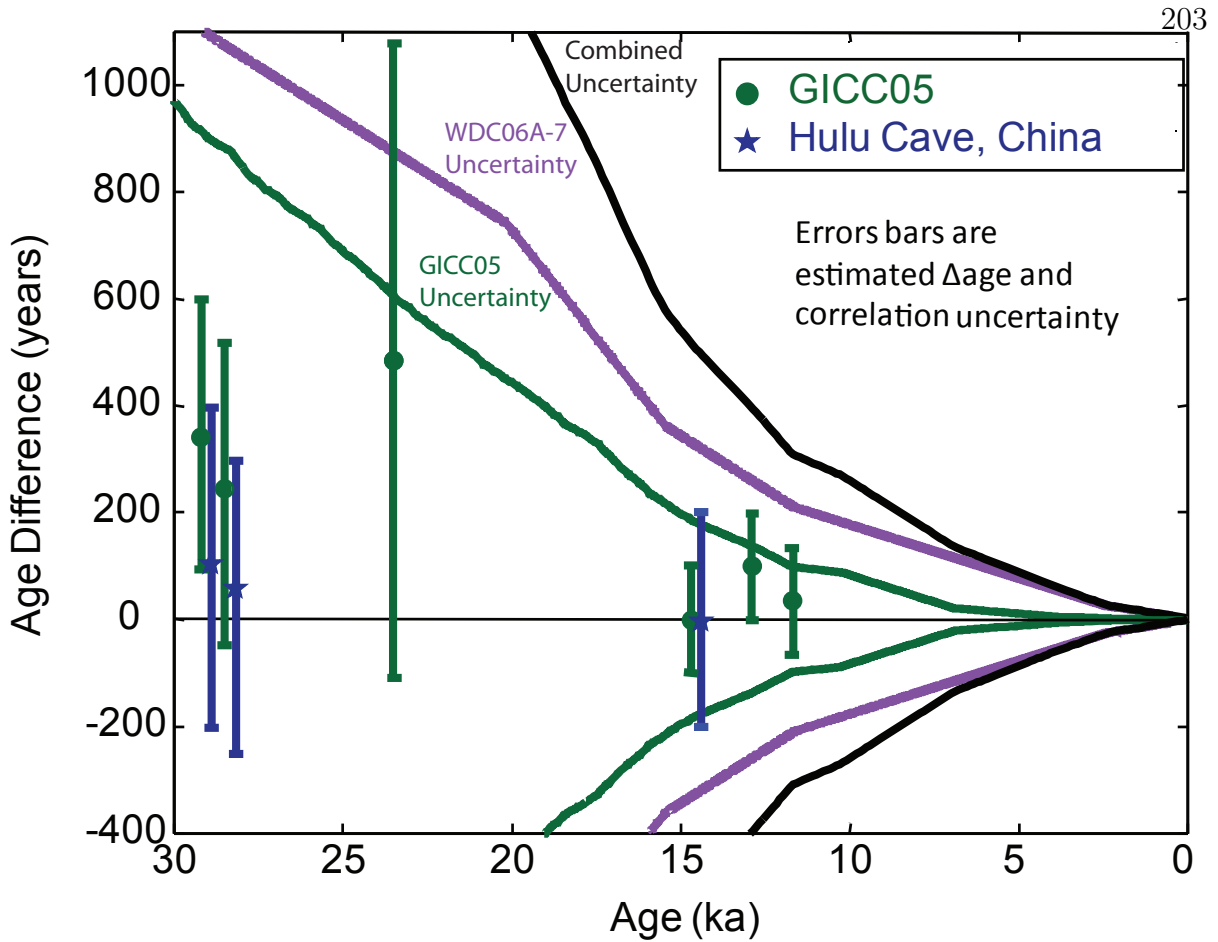


Figure S6: Timescale Comparison

Age differences between methane records shown in Figure S5 for WDC06A-7 and GICC05<sup>33,40</sup> and age differences between WDC methane and stalagmite  $\delta^{18}\text{O}$  from Hulu Cave<sup>41</sup>. Uncertainty of age comparisons is the  $\Delta$  age and correlation uncertainties and does not include timescale uncertainties.

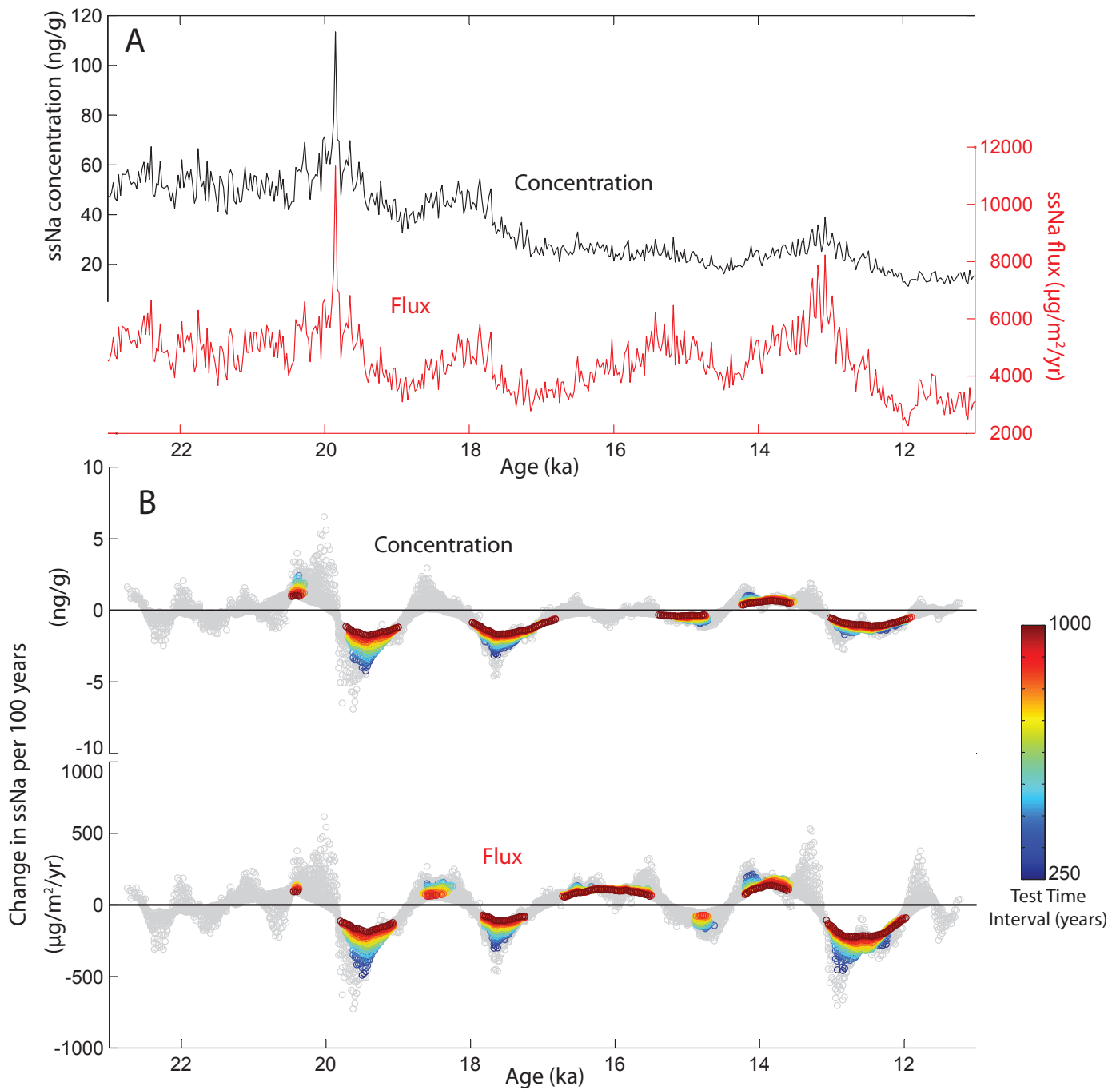


Figure S7: Sea-salt sodium (ssNa) concentration and flux.

Results of rank sum test shown in (B) are described in methods. Colored circles indicate times of significant change.

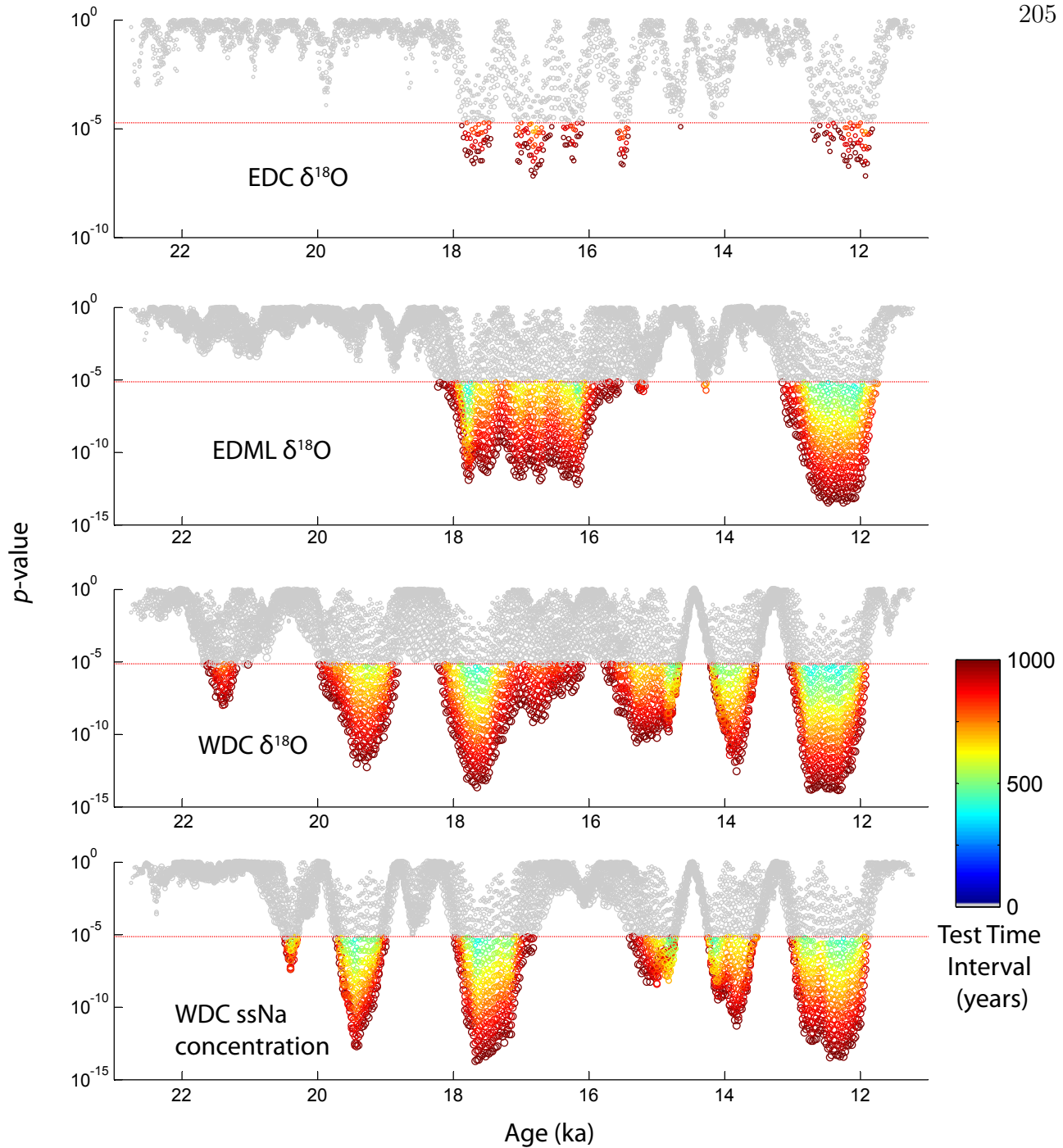


Figure S8. Significance levels for Wilcoxon Rank Sum tests. The four plots show the  $p$ -values of the sliding Wilcoxon Rank Sum test for the difference of medians shown in Figure 2. The test algorithm and interpretation is described in Methods. The 95% a posteriori confidence level, that accounts for the large number of test realizations, is shown with the red line. Each point is a test realization and is colored by the test time interval.

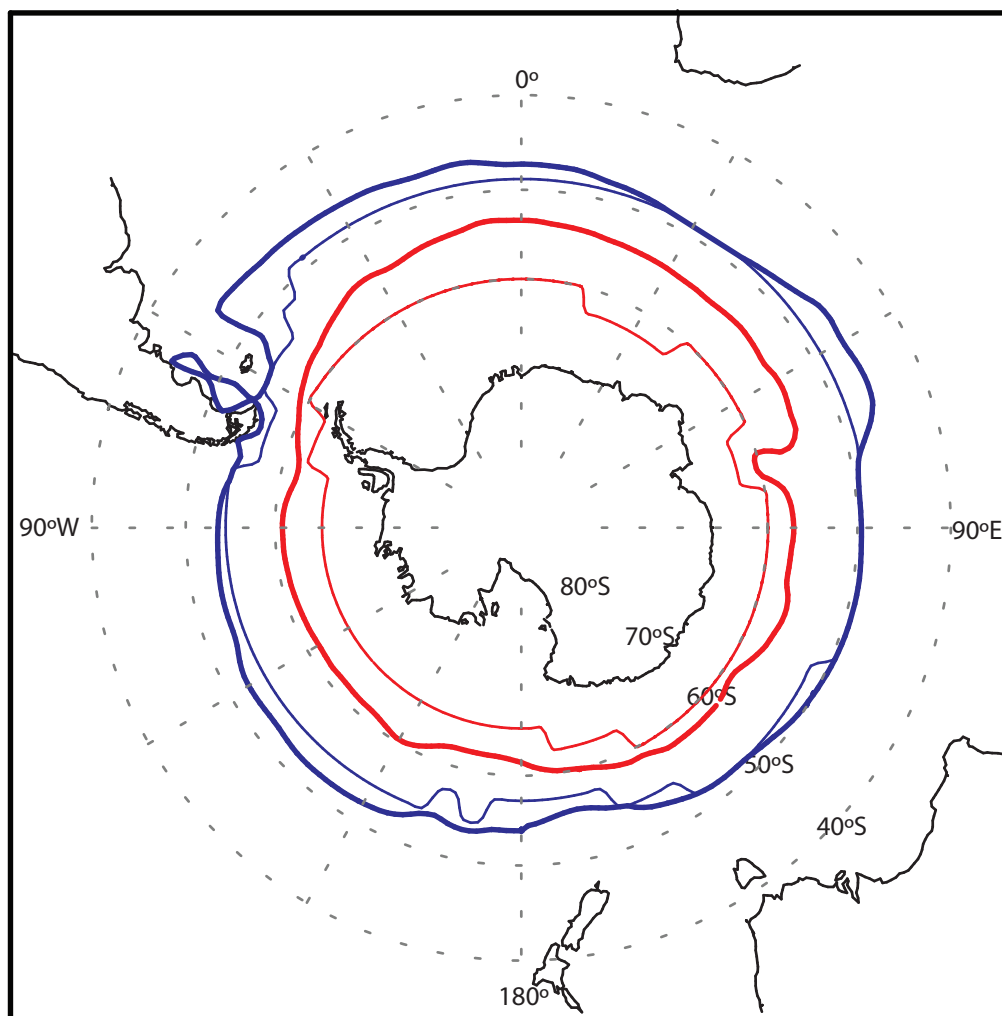


Figure S9: Sea-ice reduction in climate model experiments. Thick line is control run; thin line is reduced sea-ice run. Blue is winter (July) and red is summer (January) sea-ice extent.

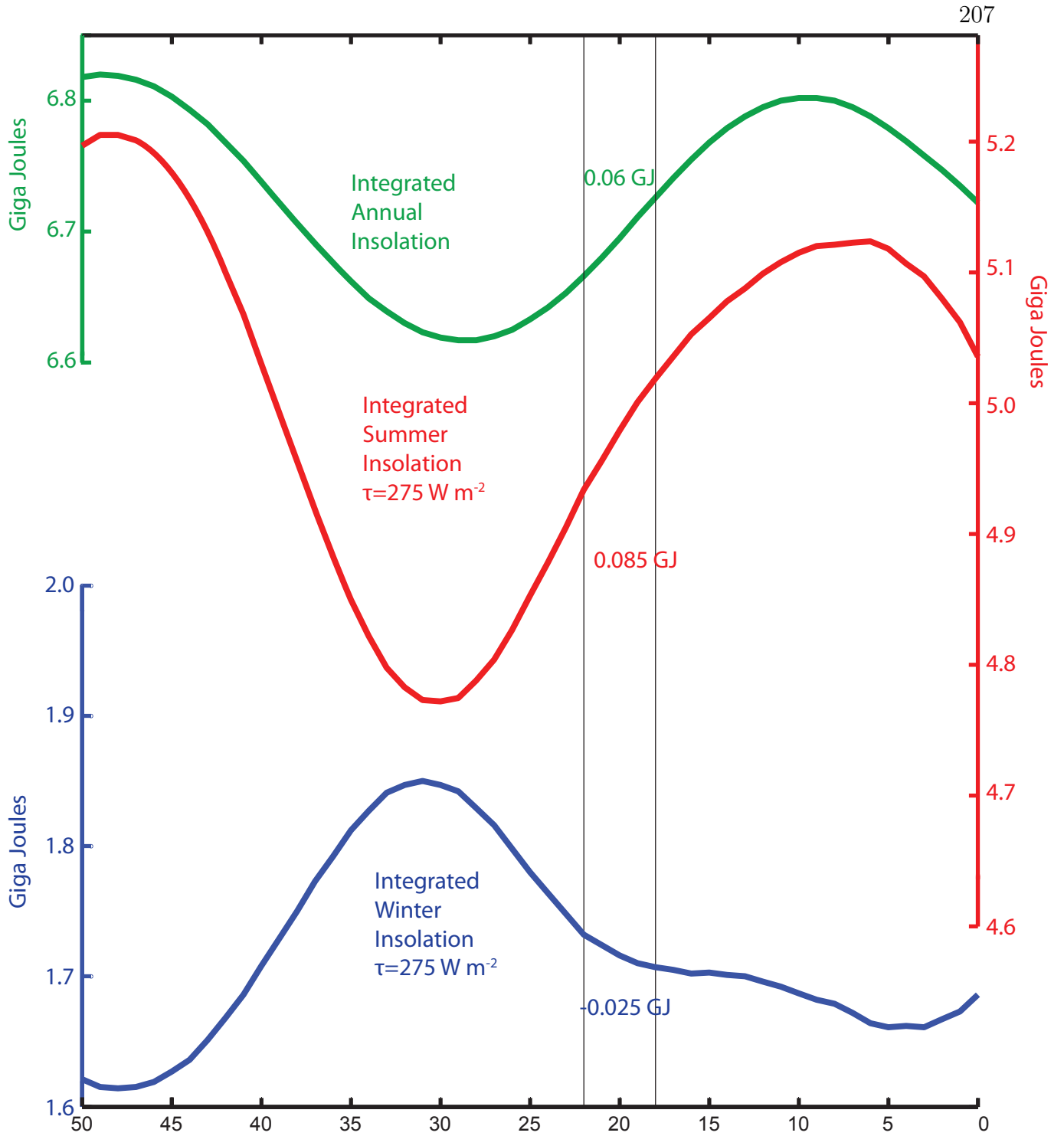


Figure S10. Integrated insolation. Integrated insolation at 65°S from Huybers<sup>71</sup>. Values are the increase in insolation between 22 and 18 ka (black lines).

## VITA

Bradley Markle is a climate scientist, living in Seattle, WA, USA. He has a Bachelor of Arts in Geology with a minor in Physics from Pomona College, CA, USA. He received a Master of Science from Victoria University of Wellington, in Wellington, New Zealand, where he studied Antarctic climatology with the support of a Fulbright Fellowship from the U.S. Department of State. He will receive a Doctor of Philosophy from the Department of Earth and Space Sciences at the University of Washington, WA, USA.

He welcomes your comments to [marklebr@uw.edu](mailto:marklebr@uw.edu).